

---

# F

---

## Fabrication of 3D Microfluidic Structures

Ji Fang<sup>1</sup>, Weisong Wang<sup>2</sup> and Shihuai Zhao<sup>3</sup>

<sup>1</sup>Institute for Micromanufacturing, Louisiana Tech University, Ruston, LA, USA

<sup>2</sup>Department of Astronomy, University of Texas at Austin, Austin, TX, USA

<sup>3</sup>Center for Microfibrous Materials Manufacturing, Department of Chemical Engineering, Auburn University, Auburn, AL, USA

### Synonyms

3D microfabrication; 3D micromachining; Fabrication of 3D microfluidic channels; Microfabrication of three-dimensional microstructures; Three-dimensional patterning

### Definition

The fabrication of 3D microfluidic structures is related to the microfabrication or micro-electromechanical systems (MEMS) processes, which produce the microscale structures (or microchannels) involving or relating to three dimensions ( $x$ ,  $y$ , and  $z$ ) or aspects and giving the illusion of depth, for the handling of fluids in biomedical, chemical, biological devices, etc. It is specifically referred to in the fabrication of

microstructures with complex lateral contours using a 2D mask layout. These 3D microstructures may be sculpted in a bulk substrate or created on the surface of a substrate.

### Overview

3D microstructures have been highlighted in microfluidic devices and systems and typically used to improve the properties of fluidic handling, such as micro-mixers, valves, pumps, and micro total analysis systems ( $\mu$ -TAS). For instance, the microchannel geometry in a micromixer plays an important role in mixing, because only laminar flow is present in the straight microchannels. Well-defined three-dimensional microchannels or microstructures can generate a heterogeneous mixture with a finely dispersed structure, and the diffusion of the fluid molecules in the adjacent domains produces a homogenous mixture at the molecular level. As one of the key microfluidic devices, the conventional micropump has been designed and fabricated using two-dimensional or planar structures due to crystallographic orientation of the substrate. These pumps have intrinsic limitations such as dead volume, impedance mismatch in interconnects, and low back pressure. The 3D fabrication technology provides a new design concept for the micropump and improves its performance. Over the last two decades, microfluidic handling and analysis have been emerging in

the interdisciplinary research field of fluidics. The applications have also expanded to microarray, sample preparation, cell cultivation and detection, DNA sequencing, and environmental monitoring. Using 3D microfabrication technologies could potentially enhance the efficiency, reliability, and overall performance of various microfluidic devices. With the continually high demands of microfluidics applications, 3D microstructure fabrication technology becomes more interesting to researchers and industries.

Lithography, as a traditional pattern transfer technology, is normally the first step in top-down microfabrication. Several lithographic techniques offer intrinsic 3D structuring capabilities. For example, electron-beam lithography (EBL) can generate grayscale profiles by controlling the exposure dose. Grayscale lithography can transfer 3D structure from a 2D grayscale mask. X-ray lithography (XRL) is capable to replicate multilevel masks by amplifying the thickness profile and can generate complex 3D structures with multiple exposures at tilted angles. Moreover, focused ion beam (FIB) lithography has shown the capability for direct milling and growth of hard materials. Holographic lithography can generate large volume periodic 3D structures with submicrometer resolution. However, lithographic techniques have their own peculiarities and potentialities that in many cases cannot be exploited to completely cover the entire spectrum of fabrication needs for 3D microstructures. The main disadvantages of these technologies include low speed processes and difficulty moving into mass production. On the other hand, these technologies can be used to fabricate reverse 3D microstructures in the form of molds to produce the final devices by casting, hot embossing, imprinting, and soft lithography at low cost.

Most micromachined structures applied in MEMS are fabricated on silicon substrate. Silicon patterning with chemical and/or plasma etching has been extensively studied in the last two decades. Using wet chemical etching, one can define the 3D geometry profile into the silicon substrate by choice of mask geometry, etchant, and crystallographic cutting of the substrate.

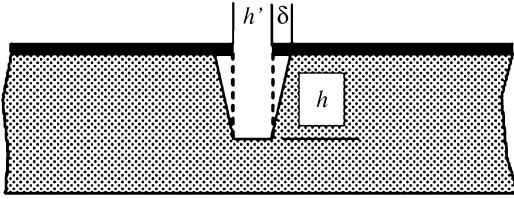
Isotropic silicon etching can generate rounded sidewall profiles, and anisotropic etching can produce more complicated profiles like V-shape channel, square and rectangular hole, frustum of a pyramid, and other shapes. Plasma dry silicon etching makes it possible to etch controllable profiles without limitations due to crystal orientation. It also provides high etch rate and selectivity between substrate and masking material. Dry plasma etching is becoming a standard tool in microfabrication.

Recently, patterning of polymers, proteins, and cells has been intensively studied for 3D polymer structure. In contrast to silicon, polymers show several major advantages that are currently not available in silicon or glass, including a wide range of material characteristics, biochemical compatibility, ease of fabrication and prototyping, and low cost. These benefits make polymers the most promising substrate materials for biomedical and biological applications. Poly(dimethylsiloxane) (PDMS), poly(methylmethacrylate) (PMMA), and SU-8 have been broadly used in microfluidic devices and systems. New technologies for polymer 3D micro-/nanostucture fabrication such as soft lithography, hot embossing, and different replica moldings are also developed as low-cost approaches to fabricate microfluidic devices.

## Basic Methodology

### Wet Chemical Etching

Wet chemical etching has its genesis in the semiconductor industry. In this process, the feature structures are sculpted in bulk substrates such as silicon, quartz, SiC, GaAs, Ge, and glass by orientation-dependent (anisotropic) or orientation-independent (isotropic) wet etchants. The first use of silicon as a substrate can be traced back to mid-1950s and early 1960s. Although this process has a long history, it is still a main conventional microfabrication technology. It not only is low cost and suitable for mass production but also provides the ability of controlling the etching profile and the well-defined geometries of etched features.



**Fabrication of 3D Microfluidic Structures, Fig. 1** Example of an etching profile

Wet chemical etching can be considered as a sequence of three steps: transport of the reactant to the surface of substrate, reaction with the surface, and movement of reaction product into the etchant solution. Therefore, it includes three components: mask, etchant, and substrate. Two important figures for the etching process are selectivity and directionality. Selectivity is the degree to which the etchant can differentiate between the masking layer and the layer to be etched. Directionality has to do with the etch profile under the mask. In isotropic etching, the etchant removes the substrate materials in all directions at the same etch rate and creates a semicircular profile under the mask. In anisotropic etching, the etch rate depends on the substrate’s crystallographic orientation by which one can obtain straight sidewalls or other noncircular profiles. To describe the etching processes including wet and dry etching, the following terms are defined (Fig. 1).

**Etch Rate (ER)**

It is the ratio of etch depth ( $h$ ) and actual etching time ( $t$ ).

$$ER = \frac{h}{t}$$

**Selectivity (S)**

During the etching process, the mask layer and the substrate are both immersed in the etching media which can be a wet chemical etching bath or plasma. Although the etchant mainly reacts with the substrate, the mask layer is also attacked. The relationship between the etching of the substrate and the mask layer is the

selectivity  $S$  which is given as the ratio of the etch rate of the substrate ( $r$ ) to the etch rate of the mask ( $r'$ ):

$$S = \frac{r}{r'}$$

It is a critical parameter where deep etching is required.

**Aspect Ratio (AR)**

It is defined as the ratio of the etch depth ( $h$ ) with the channel opening width ( $h'$ ).

$$AR = \frac{h}{h'}$$

**Undercut Rate (UR)**

Undercut rate is defined as the ratio of the undercut ( $\delta$ ) to the etch depth ( $h$ ).

$$UR = \frac{\delta}{h}$$

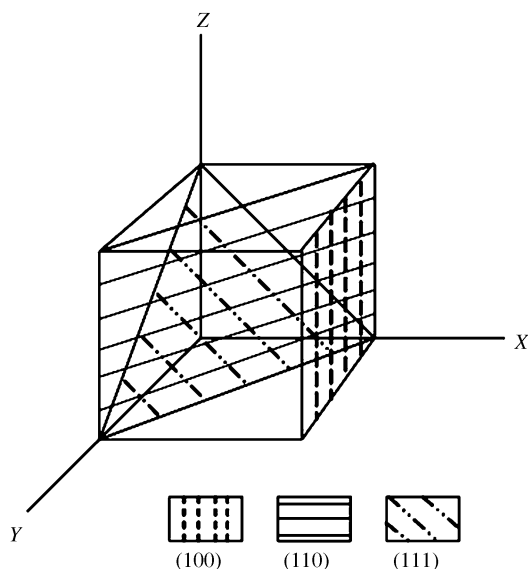
Since the etch rate in isotropic etching is the same in all directions, its undercut rate is  $\sim 1$ . For orientation-dependent anisotropic wet etching, the undercut rate is basically  $< 1$ . If the undercut rate can be controlled in the etching process, the lateral contours along the  $z$  direction will be changed, and a special 3D structure can be created with a 2D mask pattern.

**Theory**

The majority of substrate used for MEMS and microfluidic devices or systems is silicon. Crystalline silicon forms a covalently bonded structure and has the same atomic arrangement as carbon in diamond. The crystallographic orientation in crystals of the cubic class is described in terms of Miller notation [1]. Any plane in the space satisfies the equation

$$\frac{x}{a} + \frac{y}{b} + \frac{z}{c} = 1$$

where  $a$ ,  $b$ , and  $c$  are the intercepts made by the plane at the  $x$ ,  $y$ , and  $z$  axes, respectively. A set of



**Fabrication of 3D Microfluidic Structures, Fig. 2** Three main planes in a cubic lattice

integers of  $h$ ,  $k$ , and  $l$  can be used, and then the equation can be written as

$$hx + ky + lz = 1$$

The integer  $h$ ,  $k$ , and  $l$  are called Miller indices. To identify a plane or direction, a series of three numbers are used. Figure 2 shows three planes in a cubic lattice nestled into the origin of the  $x$ ,  $y$ , and  $z$  coordinate system which illustrate the important planes (100), (110), and (111) in the conventional microfabrication process. Each plane is unique, differing in atom count and binding energy between the atoms. Each plane also has different mechanical, chemical, and electrical properties. The etch rate is strongly affected by the crystallographic orientation of silicon. For example, the etch rate of the (100) plane is  $\sim 0.6 \mu\text{m}/\text{min}$  in 40% KOH at 70 °C, while the etch rate is 1.3  $\mu\text{m}/\text{min}$  for the (110) plane and 0.009  $\mu\text{m}/\text{min}$  for the (111) plane. The (110) plane is the fastest etching primary surface. The ideal (110) surface has a more corrugated atomic structure than the (100) and (111) primary surfaces. The (111) plane is an extremely slow etching plane that is tightly packed, has a singling bond per atom, and is overall atomically flat.

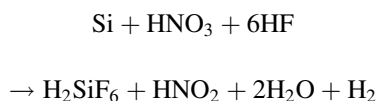
**Fabrication of 3D Microfluidic Structures, Table 1** Silicon etch rate at different crystal orientations in KOH

Crystallographic Orientation	Etch rate at different KOH concentrations ( $\mu\text{m}/\text{min}$ )		
	30 %	40 %	50 %
(100)	0.797	0.599	0.539
(110)	1.455	1.294	0.870
(210)	1.561	1.233	0.959
(211)	1.319	0.950	0.621
(221)	0.714	0.544	0.322
(310)	1.456	1.088	0.757
(311)	1.436	1.067	0.746
(320)	1.543	1.287	1.013
(331)	1.160	0.800	0.489
(530)	1.556	1.280	1.033
(540)	1.512	1.287	0.914
(111)	0.005	0.009	0.009

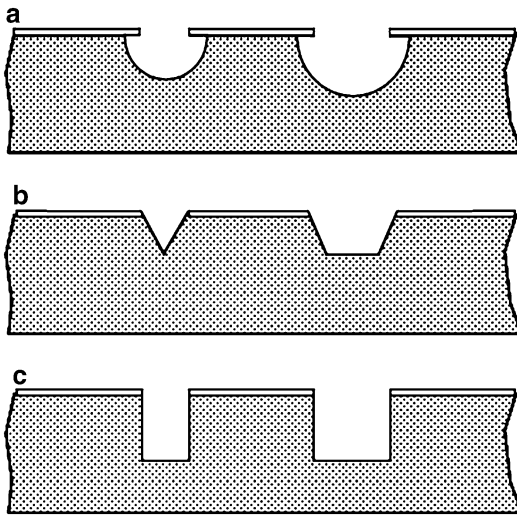
Table 1 lists the etch rates for some crystallographic orientations of silicon in KOH etchant with different concentrations. By understanding and using these orientation-dependent properties, 3D microstructures in a silicon substrate can be well defined.

### Experimental

For wet isotropic etching of silicon, the commonly used etchant is a mixture of nitric acid ( $\text{HNO}_3$ ), hydrofluoric acids (HF), and water or acetic acid ( $\text{CH}_3\text{COOH}$ ). The reaction of silicon with acids suggests that chemical etching in aqueous solution occurs via the oxidation of the silicon surface by  $\text{HNO}_3$  oxidation agent, followed by the dissolution of the silicon oxidation products in HF. The overall reaction mechanism for silicon etching in HF/ $\text{HNO}_3$  mixture is [2]



The mixing weight ratio of HF to  $\text{HNO}_3$  greatly affects the silicon etch rate. The highest etch rate is observed at the weight ratio of 2:1. Figure 3a shows the etching profile for this wet isotropic etching process. The etch rate is the same in all directions.



**Fabrication of 3D Microfluidic Structures, Fig. 3** Etching profiles in wet chemical etching

Anisotropic etchants are alkaline solutions, and the etching process is characterized by a high etch rate and an excellent selectivity dominated by the substrate's crystal orientation. There are a wide variety of etchants available for anisotropic etching including KOH, NaOH, LiOH, CsOH, and RbOH. The most commonly used ones are KOH and EDP (ethylenediamine/pyrocatechol with water). The normal etching temperature for KOH etchant is in the range of 20–80 °C, and it strongly influences the etch rate. Raising the etching temperature will increase the etch rate, but decrease the anisotropic degree (etching selectivity in different crystallographic directions). After several hours of the etching process at such temperatures, the concentration of the alkali solution will be changed. Therefore, closed vessels are recommended and the safety issue must be a concern. Since the photoresist will be quickly dissolved in an alkaline etching media, SiO<sub>2</sub> and Si<sub>3</sub>N<sub>4</sub> are the common materials for mask layer. The etching selectivity ratio of silicon is ~ 100 to SiO<sub>2</sub> and >500 to Si<sub>3</sub>N<sub>4</sub>. Si<sub>3</sub>N<sub>4</sub> as a mask layer is necessary if an etch depth of over 200 μm is required. A SiO<sub>2</sub> film may be deposited on the Si<sub>3</sub>N<sub>4</sub> film as a mask to pattern the Si<sub>3</sub>N<sub>4</sub> film. Figure 3b illustrates the etching result for a V-groove in a (100) silicon wafer.

The etching bond at (111) planes is generally at 54.74 °C to the (100) surface of silicon. Figure 3c shows a straight sidewall feature using a properly aligned mask on a (110) silicon wafer.

### Dry Plasma Etching

Dry etching is referred to as plasma processing, which was first introduced in the 1960s. During the past 40 years, a number of plasma sources have been developed for dry etching, including reactive ion etching (RIE), sputter etching, magnetically enhanced RIE (MERIE), electron cyclotron resonance (ECR), inductively coupled plasma (ICP), etc. It has been shown that ICP etching is the most suitable and efficient plasma source for deep anisotropic silicon etching with high etch rate and provides the capability of creating 3D microstructures.

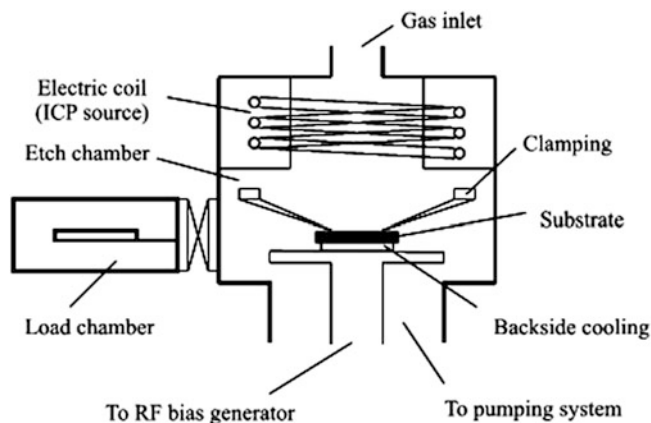
### Plasma Physics and Chemistry of ICP Etching

In general, the plasma for dry etching is produced by the dissipation of electrical power in a gaseous medium at radio frequency (RF). Electrons gain sufficient energy during oscillation in the RF field to initiate collisions with atoms and molecules to generate the etching species and to initiate processes such as excitation, ionization, and dissociation. The inductively coupled plasma can be generated by using a time-varying axial magnetic field to induce an azimuthal electrical field which effectively confines the plasma current. The current path minimizes contaminants or particles resulting from direct ICP etching and chamber wall sputtering. The highest plasma intensity region is located close to the etching chamber sidewalls, and ambipolar diffusion results in a highly uniform plasma inside the chamber.

Figure 4 is a schematic diagram of a typical ICP etching system. The sample is loaded into the etching chamber via a load chamber and either mechanically or electrostatically clamped to the lower electrode. Helium or nitrogen backside cooling provides good thermal conductance between the electrode and the sample. Process gases are admitted to the etching chamber and controlled to a pressure usually in the range of 2.5–13 Pa. The 13.56 MHz RF power is applied to the ICP coil to generate the high-density etching plasma.

### Fabrication of 3D Microfluidic Structures,

**Fig. 4** Schematic of a typical ICP etching system

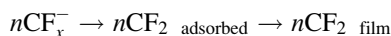
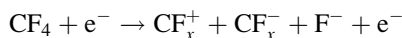


The RF power is also applied to the lower electrode for independent control of substrate bias power. Unused feed gases and volatile etch products are pumped away by a backed turbo pump.

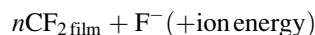
The chemistries of ICP etching mainly include fluorinated, chlorinated, or bromine-based gases. When silicon substrates are dry-processed with fluorinated chemistry, the etch rate is a combination of contributions from spontaneous or thermal reactions between fluorine and silicon, ion bombardments, and a small effect of physical sputtering. A chlorinated chemistry allows easier control of the etching profiles as compared to fluorinated chemistry due to the lack of spontaneous etching of silicon. In general, a higher silicon etch rate as well as a higher etch selectivity of substrate to masking material is expected when using fluorinated chemistry. Moreover, fluorine-based compounds cause fewer health hazards and corrosion concerns than their chlorinated and brominated counterparts.

Among the available anisotropic process schemes and recipes, the Bosch process which is named after the German company that developed and patented the technique is recognized as a standard process for ICP system. The Bosch approach is based on a variation of the Teflon-film sidewall passivation technique which avoids the recombination of active species in the gas phase. The deposition and etching steps are performed subsequently to control the sidewall profile of the 3D structures. In the deposition step, the precursor gas ( $\text{CF}_4$ ,  $\text{C}_4\text{F}_8$ ,  $\text{CHF}_3$ ,  $\text{C}_2\text{F}_6$ , or

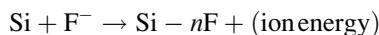
higher molecular gas) is dissociated by the plasma. The ion and radical species undergo polymerization reactions. A passivation layer of  $n\text{CF}_2$  is deposited on the etched pattern surface. A possible reaction scheme using  $\text{CF}_4$  as an example is



The deposited polymer film can be removed by ion bombardment with low energy. In the etching step, the etching gas (for instance,  $\text{SF}_6$ ) is dissociated by the plasma, liberating high amounts of etching species. These species are necessary to remove the polymer film at the bottom of the pattern and to effectively react with the silicon. The etching reactions involve the removal of the passivation layer



and silicon etching



Since the bombardment and etching reaction with the passivation film on the bottom of pattern

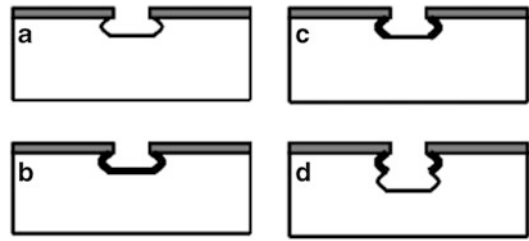
are faster than on the sidewall, the silicon surface on the sidewall can be protected by the passivation layer during the etching step. Hence, a straight sidewall for the etched feature can be obtained. The kinetics of etching silicon, based on the Langmuir type surface kinetics model, in fluorocarbon discharges using ICP reactors has been developed successfully and can be found in [3].

#### Time-Multiplexed Deep Etching (TMDE)

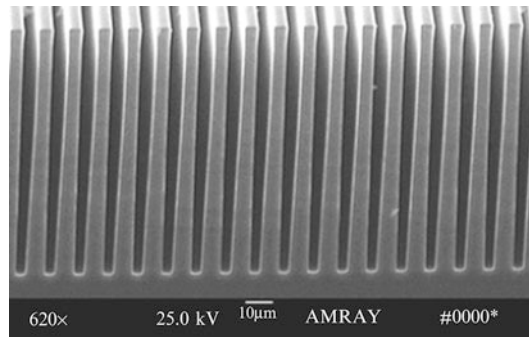
Various 3D microstructures can be created by ICP etching utilizing two gas-feeding methods, continuous etching and time multiplexing. For the continuous etching technique, all gas species (passivation and etching) are flowed into the etching chamber simultaneously. The etching results depend on the presence of radicals in the glow discharge to proceed with the etching and on other radicals for protecting the sidewalls during operation.

In time-multiplexed deep etching (TMDE), the etching and passivation gas monomers are flowed independently one at a time during operation. First, the etch step (normally  $\leq 12$  s) forms a shallow isotropic trench in the silicon substrate. Second, the passivation cycle (normally  $\leq 10$  s) forms a protective film on all the surfaces. In the subsequent etching step, ion bombardment promotes the preferential removal of the film on the horizontal surface and further isotropic etching of silicon, allowing the profile to evolve in a highly anisotropic structure (Fig. 5).

In a typical configuration,  $\text{SF}_6$  is the etching gas and  $\text{C}_4\text{F}_8$  is the deposition gas for the sidewall protection. By adjusting etch parameters (such as gas flow rates and durations, plasma source power, substrate bias power, chamber pressure, and substrate temperature) in each process step, etch rate, surface roughness, sidewall profile, and etch selectivity can be controlled and optimized to achieve designed 3D microfluidic structures. Figure 6 shows a scanning electron microscopy (SEM) image of microfluidic channels fabricated using TMDE process and Alcatel 601E ICP system. The feature size of the microchannels is a  $5\ \mu\text{m}$  width with  $100\ \mu\text{m}$  depth. The process recipe is source power 1,800 W, bias power



**Fabrication of 3D Microfluidic Structures, Fig. 5** Four process steps for time-multiplexed deep etching: (a) isotropic etching of silicon; (b) polymer passivation; (c) removal of formed polymer film on the horizontal surfaces; (d) further isotropic etching of silicon



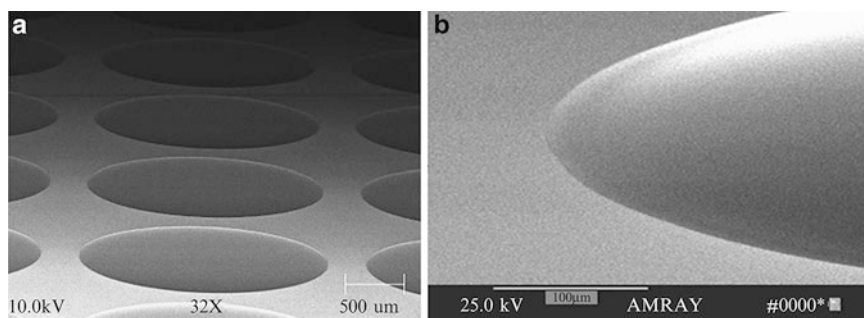
**Fabrication of 3D Microfluidic Structures, Fig. 6** SEM image of microfluidic channels with high aspect ratio of 20:1 ( $5\ \mu\text{m}$  width and  $100\ \mu\text{m}$  depth) fabricated using TMDE process

50 W,  $\text{SF}_6$  flow rate 300 sccm and pulse duration 4 s,  $\text{C}_4\text{F}_8$  flow rate 180 sccm and pulse duration 2 s, chamber pressure 5 Pa, substrate temperature  $20\ ^\circ\text{C}$ , and process time 20 min.

Besides the continuous and the TMDE process, single feeding gas (such as  $\text{SF}_6$ ) has been utilized in fabrication of 3D microfluidic structures with isotropic features for special applications. At the present time, commercial ICP etchers are available from Alcatel, San Jose, CA; Surface Technology Systems, Ltd. (STS), Redwood City, CA; and Plasma-Therm, Inc., St. Petersburg, FL.

#### Polymer-Based 3D Microstructure Fabrication

Polymer materials are widely used in the current research involving microfluidic devices because



**Fabrication of 3D Microfluidic Structures, Fig. 7** SEM images of 3D structure of a mold fabricated by photoresist reflow: (a) well or cell array; (b) the enlarged edge of a single well mold

they are chemically and biologically compatible, easy to handle, and low material and manufacturing cost. The devices made by polymer materials are also disposable.

The concept of polymer-based 3D microstructure utilizes replica molding. Therefore, the key fabrication processes include 3D mold fabrication and pattern transfer. The material property is a very important factor when choosing the polymer and mold materials for special applications. For easy handling and accurate shape transfer, the mold requires smooth surface and relatively low thermal expansion coefficient since the curing of the polymer often involves heat. Nowadays, several polymer materials such as PDMS, PMMA, and SU-8 are popular choices for microfluidic applications.

Replica molding is a method to reproduce the desired structures by filling the mold with the particular material. It is used to create structures on the materials that are not easy to have patterns created. It has the advantages of low cost and the capability of mass production. Replica molding involves two steps: 3D mold fabrication and mold transfer.

### 3D Mold Fabrication

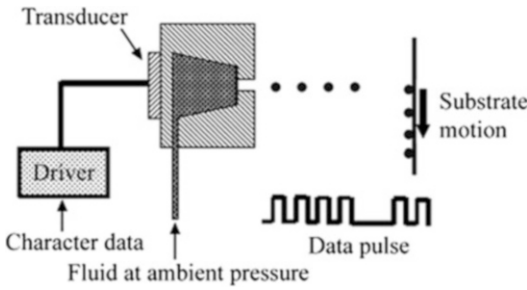
In recent decades, a number of technologies have been developed to fabricate 3D molds. These include photoresist reflow, inkjet printing, conventional lithography, and hybrids of those methods with conventional lithography.

**Photoresist Reflow** Photoresist reflow is a method to generate 3D hemispheric structures for

microfluidic applications. First, a photoresist will be patterned by conventional lithography to generate cylindering or rectangular bars on a substrate. Then, the photoresist pattern is thermally treated for reflowing to form the hemispheric 3D shape. When temperature is higher than the glass transition temperature of the photoresist, it begins to melt and reflows around the pattern. Due to the surface tension of the liquid resist on the substrate and the surface property of the substrate, the liquid resist always tends to form a convex shape. This method was first suggested by Popovic in 1988. Figure 7a shows the photoresist reflow result of a mold for well or cell array. A well with smooth edge is shown in Fig. 7b.

**Inkjet Printing** Inkjet printing technology is familiar to most people in the form of desktop printers. Repeatable generation of small droplets of a fluid (polymers) can be used to make 3D structures directly on a substrate for MEMS manufacturing applications.

In a drop-on-demand inkjet printer, the fluid is maintained at ambient pressure, and a transducer is used to create a drop only when needed. The transducer creates a volumetric change in the fluid which creates pressure waves. The pressure waves travel to an orifice and are converted to fluid velocity, which results in a drop being ejected from the orifice. Figure 8 shows a schematic of a drop-on-demand-type inkjet system which can generate 60  $\mu\text{m}$  diameter drops of butyl carbitol (an organic solvent) from a device with a 50  $\mu\text{m}$  orifice at 4,000 drops per second.

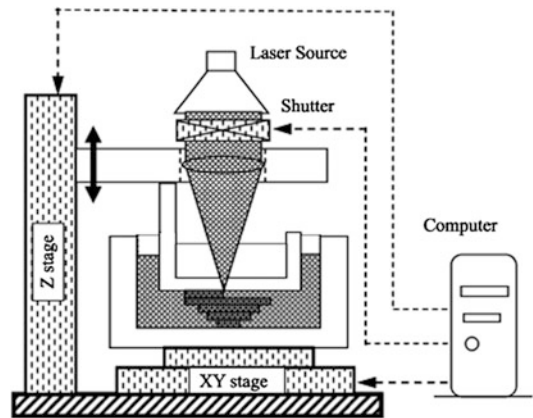


**Fabrication of 3D Microfluidic Structures, Fig. 8** Schematic of a drop-on-demand-type inkjet system

Therefore, various molds for microfluidic applications could be created by this method.

**Unconventional Lithography Methods** Sometimes a mold can be generated directly by unconventional lithography methods such as e-beam, grayscale, and stereo laser lithography. Electron-beam direct-write lithography (EBL) has been widely used for creating masks with sub-100 nm resolution. To generate 3D structures, controlling the exposure dose during beam scanning is very important in e-beam lithography. E-beam lithography creates patterns by serially exposing the resist beam spot by the beam spot. The differential levels of exposure dose determine the pattern depth of the exposed area after developing. By adjusting the dose of each exposed spot, lateral contours can be controlled, and 3D structures can be created.

Grayscale lithography utilizes locally modulated exposure doses to develop 3D structures in photoresist. Differentially exposed doses lead to multiple depths of exposed photoresist across the surface. This is due to the ultraviolet (UV) light energy being absorbed by the photoactive compound as it travels in the depth of the photoresist. From the differentially exposed doses, a gradient height photoresist structure corresponding to the designed silicon structure will remain once the resist is developed. There are two primary techniques to generate an optical mask capable of modulating the UV intensity passing through to the photoresist surface. One such method uses a high-energy-beam-sensitive glass as an optical mask, in which the UV light transmission of the



**Fabrication of 3D Microfluidic Structures, Fig. 9** Schematic of a micro stereo lithography system

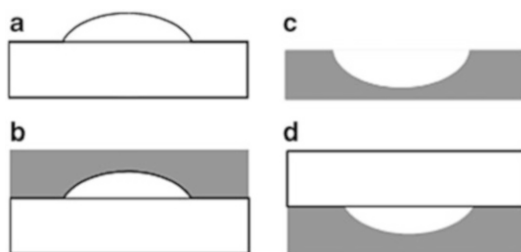
glass is changed by an e-beam direct-write system. Thus, when using this mask to expose the photoresist, the exposed pattern will form 3D structures due to the different exposure levels. The second method utilizes projection lithography to induce diffraction by using a conventional chrome-on-glass (COG) mask.

Micro stereo lithography is a rapid prototyping method to generate 3D molds. It is a maskless process with layer-by-layer fabrication of microstructures via the projection of sliced images of 3D objects, as shown in Fig. 9.

A laser beam directs to the photocurable resin which can be classified as an epoxy, vinyl ether, or acrylate. The 3D structure or mold is built on a platform which can be controlled by an XYZ positioner. When one layer is complete, the platform drops lower into the vat of resin, fresh resin washes over the part, and the laser proceeds to build the next layer. The 3D microstructure is built up in this additive process. When all layers are complete, the part is cleaned and post-cured. The major drawback of this technique is the considerable capital investment. Also, only photocurable resins can be used which can be a limitation if a special material is required.

#### Mold Transfer

After generating a mold, the next step is to transfer the 3D structure from the mold into the polymer. There are several technologies available.



**Fabrication of 3D Microfluidic Structures, Fig. 10** Direct casting process: (a) making a 3D mold; (b) casting a polymer structure; (c) peeling off the 3D polymer structure; (d) bonding to form sealed microfluidic structure

**Direct Casting** The direct method is to cast the polymer material onto the mold and then peel off the 3D structure after the material is polymerized.

Figure 10 illuminates this simple process. The reverse 3D structure is first prepared by microfabrication techniques as a mold. Then, a prepolymer with cross-link is cast onto the mold. After the polymer is well cured by heat or UV, the 3D polymer structure is produced by peeling off the polymer structure from the mold. To construct a microfluidic device, bonding the 3D polymer structure with a substrate is the next step to seal the fluidic channels and reservoirs.

**Soft Lithography** Soft lithography represents a non-photolithographic strategy based on self-assembly and replica molding for carrying out micro and nanofabrication [4]. It has been mostly developed in recent years. It is a favorable process for researchers to build nanometer-scale structures. It includes the following techniques:

**Replica Molding (REM)** A PDMS stamp is cast against a conventionally patterned master. Polyurethane is then molded against the secondary PDMS master. In this way, multiple copies can be made without damaging the original master. The technique can replicate features as small as 30 nm.

**Micromolding in Capillaries (MIMIC)** Continuous channels are formed when a PDMS stamp is brought into conformal contact with

a solid substrate. Capillary action fills the channels with a polymer precursor. The polymer is cured and the stamp is removed. MIMIC is able to generate feature sizes as small as 1  $\mu\text{m}$ .

**Microtransfer Molding ( $\mu\text{TM}$ )** A PDMS stamp is filled with a prepolymer or ceramic precursor and placed on a substrate. The material is cured and the stamp is removed. The technique is able to create multilayer systems and features as small as 250 nm.

**Solvent-Assisted Microcontact Molding (SAMIM)** A small amount of solvent (e.g., methanol, ethanol, or acetone) is spread on a patterned PDMS stamp which is placed on a polymer, such as photoresist. The solvent swells the polymer and causes it to expand to fill the surface relief of the stamp. Feature size as small as 60 nm can be reached.

**Microcontact Printing ( $\mu\text{CP}$ )** An ink of alkanethiols is spread on a patterned PDMS stamp. The stamp is then brought into contact with a substrate, which can range from coinage metals to oxide layers. The thiol ink is transferred to the substrate where it forms a self-assembled monolayer that can act as a resist against etching. Features can be made as small as 300 nm in this method.

**Hot Embossing** Hot embossing is essentially the stamping of a pattern into a polymer that is softened by raising the polymer's temperature just above its glass transition temperature. Some parameters such as loading pressure, demolding force, and temperature play important roles in quality of the molded parts. Hot embossing often requires high loading pressure to stamp the polymer material in a vacuum chamber. However, the pressure should be controlled within a limit to avoid damaging the mold. And at the end of hot embossing, the demolding process requires fast release without damaging the stamped pattern. The surface roughness of the mold affects the demolding and the roughness of the stamped pattern as well. The stamp used to define the pattern in the polymer can be made

in a variety of ways including micromachining from silicon, LIGA, and the methods that have been discussed above. A wide variety of polymers have been successfully hot embossed including polycarbonate and PMMA. The feature size can be in micro- or submicroscale. This technique is used primarily for defining microchannels and wells for microfluidic devices. The benefits of this approach are the ability to take advantage of the wide range of the properties of polymers, as well as the potential to economically mass produce parts with micron-scale features.

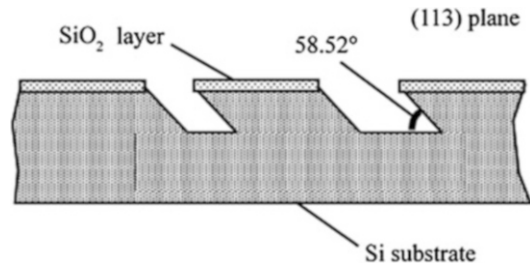
### Key Research Findings

Figure 11 shows the possible wet etching profile with (113) crystallographic orientation of a silicon wafer. The mask pattern is parallel stripes and aligned at an angle  $\varphi$ , relative to the substrate crystallographic orientation. The angle  $\varphi$  was estimated from the geometrical relationship including the inclination of the  $(hkl)$  plane in relation to the (110) plane, equal to  $(90^\circ - \alpha)$ . The angle of  $\alpha$  represents the angle of inclination of  $(hkl)$  planes toward the (100) plane.

$$\varphi = \arctan[0.707 \cos(90^\circ - \alpha)]$$

The substrate used in this experiment was (113) silicon wafer with  $1 \mu\text{m}$   $\text{SiO}_2$  layer. The  $\text{SiO}_2$  was used to be the mask material for silicon wet etching. The first step was to use optical lithography and buffered HF wet etching to pattern the  $\text{SiO}_2$  layer with a mask and an align angle  $\varphi = 16.78^\circ$ . Then the silicon etching was carried out in 10 M KOH solution at  $75^\circ \text{C}$  to create an anisotropic 3D structure [5].

The complex 3D structures with desired cross-section for special microfluidic applications can be realized by modifying three classes of ICP etching processes [6]. Figure 12 shows the resulting profiles of the 3D structures. The first patterning was carried out using an anisotropic continuous etching process ( $\text{SF}_6$ + polymer-forming gas, high-density plasma, and intensive

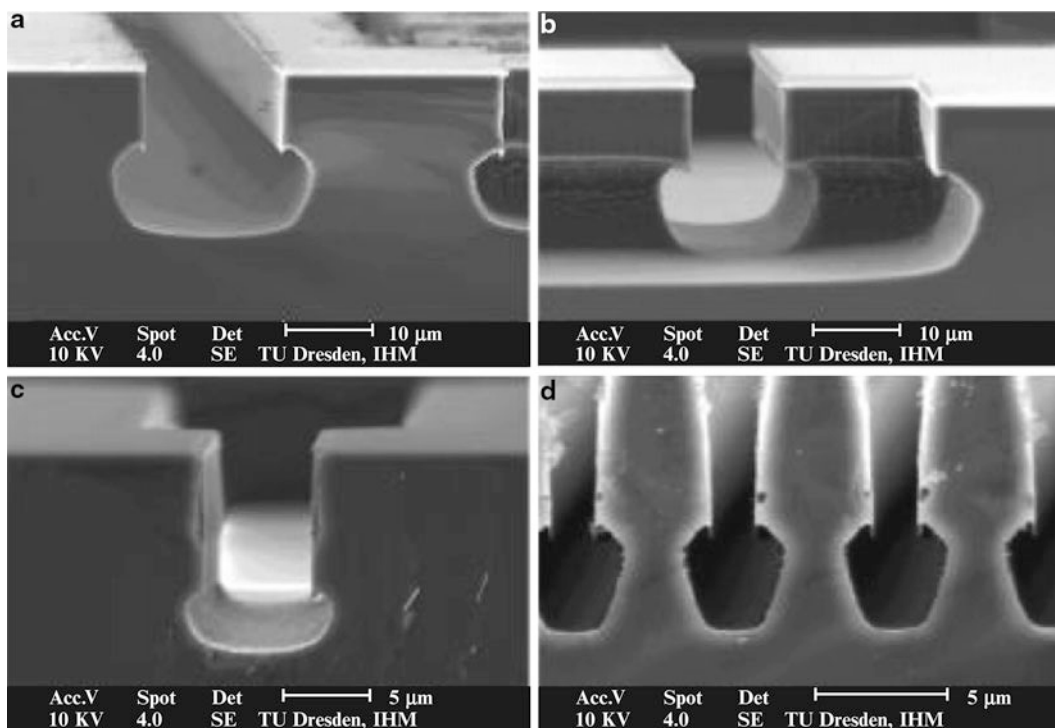


**Fabrication of 3D Microfluidic Structures, Fig. 11** Wet etch profile in a (113) silicon wafer

ion bombardment). Afterwards, a polymer layer was deposited under the same conditions of the deposition step in a TMDE process. The deposition rate is  $\sim 85 \text{ nm/min}$ , and the uniformity of the thickness is  $\sim 4\%$ . After deposition of the polymer, isotropic silicon etching using  $\text{SF}_6$  plasma was carried out. The minimum pattern created in this way has a lateral width of  $11 \mu\text{m}$  (Fig. 12a, b).

In addition to realize smaller patterns with the same cross-sectional area, a silicon nitride layer was deposited on the surface after anisotropic etching of the deep trenches. The polymer was then deposited, and the silicon was etched by the isotropic process (only  $\text{SF}_6$ ). The results are shown in Fig. 12c, d. In this case, the patterns with a minimum lateral width of  $5 \mu\text{m}$  are realized.

The combination of conventional photolithography and photoresist reflow is an effective method to smoothly integrate microfluidic chambers with microchannels. To fabricate a PDMS 3D microstructure joined with the microchannel by mold transfer, a master mold is needed. The photoresist reflow method was adopted to make the master mold for the 3D chambers, and a negative photoresist SU-8 was used to generate the microstructure master mold for the microchannels. Since SU-8 is an epoxy-based photoresist and has good chemical stability and withstands temperatures up to  $200^\circ \text{C}$ , the channel pattern cannot be damaged during the whole processing. The processing schematic is shown in Fig. 13. First, negative photoresist SU-8 was used to form high bars for the microchannels' mold.

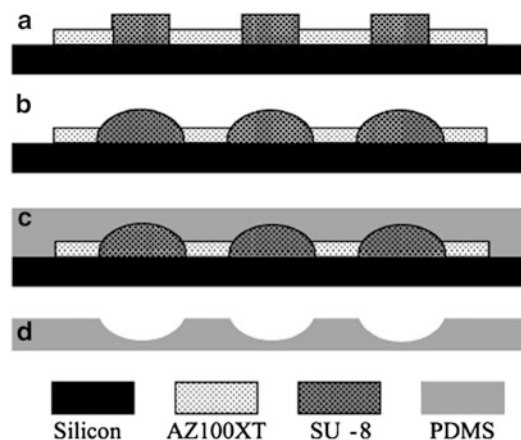


**Fabrication of 3D Microfluidic Structures, Fig. 12** SEM images of the composed etching profiles: (a), (b) patterns realized by anisotropic silicon etching, deposition of passivation polymer layer, and isotropic

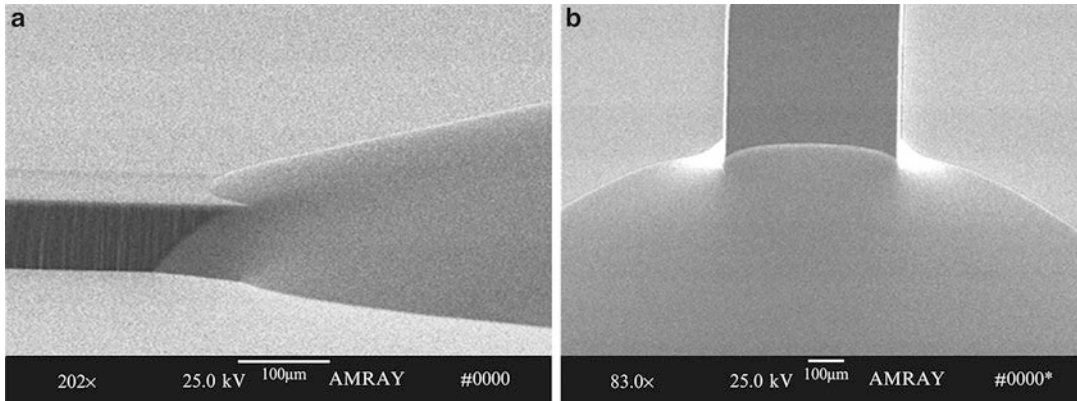
silicon etching; (c), (d) patterns etched like (a) and (b), passivation with polymer and additional  $\text{Si}_3\text{N}_4$  layer (5) (With permission from Elsevier)

Photoresist cylinders were then separately built by conventional lithography. In order to achieve large fluidic volume, thick photoresist AZ100XT was chosen, and its patterned cylinders on the substrate were thermally treated on a hot plate. The reflow occurred at  $120^\circ\text{C}$  in a period of 60 s. Sometimes, the organic solvent vapor surrounding the photoresist pattern can promote the reflow process. Figure 14a shows the SEM image for the photoresist mold, which smoothly joins hemispherical structure  $2,200\ \mu\text{m}$  in diameter and  $167\ \mu\text{m}$  in depth with the microchannel.

After completing the mold, the next step was to transfer from the photoresist microstructure to PDMS by casting. The PDMS, Dow Corning Sylgard 184 silicone, was chosen as the casting material because of its high-dimensional accuracy and easy fabrication. After the PDMS substrate was cured in a vacuum oven for 2 h at 5 mTorr of pressure at  $75^\circ\text{C}$ , it was then peeled



**Fabrication of 3D Microfluidic Structures, Fig. 13** Schematic of fabrication process of 3D polymer microstructures by combination of conventional photolithography and photoresist reflow: (a) photoresist patterned on the silicon wafer; (b) photoresist mold after thermal treatment; (c) PDMS casting on the photoresist mold; (d) PDMS with desired structures



**Fabrication of 3D Microfluidic Structures, Fig. 14** SEM images of 3D microstructures fabricated by combination of conventional photolithography and

photoresist reflow: (a) the photoresist mold; (b) the PDMS 3D microstructure of the hemispherical chamber joined smoothly with the microchannel

off from the photoresist mold. The PDMS substrate consists of 3D structure joined smoothly together with the microchannel as shown in Fig. 14b.

### Future Directions for Research

3D microfabrication being one of the most promising areas of microfabrication technologies has been extensively studied and developed over the last two decades. New technologies have been discovered and developed to design and fabricate a variety of microfluidic devices and systems [7, 8]. The demand for high-precision 3D microfluidic devices and efficient manufacturing technologies is rapidly growing in recent years, particularly in the application areas of drug discovery and delivery, diagnostics, biotelemetry, and genomics. It creates an obvious need for modular, non-silicon approaches to build inexpensive, disposable, and biocompatible sensors and systems. To continually explore 3D fabrication methods using the extremely developed lithography technologies, new materials are expected, which are photosensitive, wet or dry etchable, and biocompatible. To precisely control 3D microstructures, it is highly desirable to develop the analog 3D fabrication technologies or tools which can produce complex 3D structures without masks. Most microfluidic devices

need to be sealed in order to perform certain liquid handling functions. Packaging for sealing a device with a lid or bonding with an additional layer is always a challenging issue in the fabrication of polymer-based microfluidic devices. New technologies and materials which are suitable to integrate 3D fabrication and sealing or bonding will promote rapid prototyping and commercialization for microfluidic devices and systems.

### Cross-References

- ▶ [Photolithography](#)
- ▶ [Photoresist Reflow](#)
- ▶ [Photoresist SU-8](#)
- ▶ [Plasma Etching](#)
- ▶ [Reactive Ion Etching \(RIE\)](#)
- ▶ [Simulating Migration of Polymer Chains, Methods](#)
- ▶ [Thick Resist Lithography](#)

### References

1. Ghandhi SK (1994) VLSI fabrication principles (second version). Wiley, New York
2. Madou M (2004) Fundamentals of microfabrication. RCA Press LLC, Boca Raton
3. Kim MT (2004) Kinetics of etching in inductively coupled plasmas. Appl Surf Sci 228:245–256

- Xia Y, Whitesides G (1998) Soft lithography. *Annu Rev Mater Sci* 28:153–184
- Zubel I, Kramkowska M (2005) Possibility of extension of 3-D shapes by bulk micromachining of different Si (hkl) substrates. *J Micromech Microeng* 15:485–493
- Richter K, Orfert M, Schührer H (2001) Variation of etch profile and surface properties during patterning of silicon substrates. *Surf Coat Technol* 142–144:797–802
- Shaikh K, Ryu KS, Goluch E, Nam JM, Liu J, Thaxton CS, Chiesl T, Barron A, Lu Y, Mirkin C, Liu C (2005) A modular microfluidic architecture for integrated biochemical analysis. *Proc Natl Acad Sci U S A* 102:9745–9750
- Thorsen T, Maerkl S, Quake S (2002) Microfluidic large-scale integration. *Science* 298:580–584

---

## Fabrication of Self-Assembled Catalytic Nanostructures

Michael Cross<sup>1</sup>, W. J. Varhue<sup>1</sup> and  
Darren L. Hitt<sup>2</sup>

<sup>1</sup>Electrical and Computer Engineering Program,  
School of Engineering, The University of  
Vermont, Burlington, VT, USA

<sup>2</sup>Mechanical Engineering Program, School of  
Engineering, The University of Vermont,  
Burlington, VT, USA

### Synonyms

Nanocatalyst; Nanorods; Nanostructures

### Definition

A nanocatalyst is a material which performs the role of chemical catalysis while confined to a physical size of 10–1,000 nm. More important, the nanometer size of the catalyst material affords these materials access to unique physical and chemical properties which makes them capable of delivering enhanced catalytic performance. Most nanostructures are obtained as a result of self-assembly, governed by the physical and chemical nature of the material systems.

### Overview

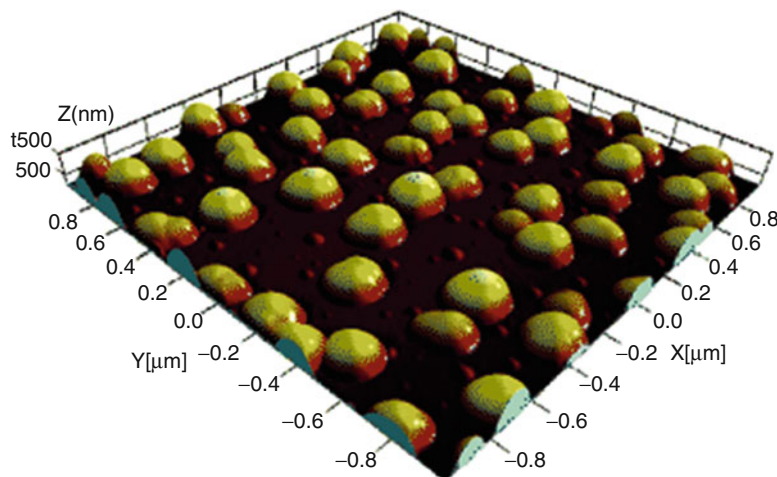
A catalyst is a material entity which participates in a chemical reaction in such a way as to reduce the activation energy required to change one chemical species, *reactants*, into a second chemical species, *products*. Ideally the catalyst material can emerge at the end of the desired chemical reaction unaltered after performing this function. If the catalyst material is in a different phase than the reactants (e.g., a gas-phase reaction occurring on a solid-state surface), the solid is characterized as a heterogeneous catalyst. From an economical point of view, there is a desire to use catalyst materials that are not consumed in the planned chemical reaction. The performance of a catalytic material will improve when:

- The surface area exposed to the reacting species is large.
- The catalyst material is specifically suited to perform a desired chemical reaction.

The emergence of nanotechnology offers potential enhancement in both criteria. One of the fundamental advantages of a nanocatalyst is that it offers a large potential surface area of catalyst per mass of material. Prior to the advent of nanotechnology, a large surface area could always be realized through the use of a finely divided powders or meshes. In a heterogeneous reactor environment, the act of reclaiming the catalytic material would, however, impose certain difficulties. With regard to the specificity of a chemical catalyst, this ability relies on chemical and physical phenomena that can best be described as depending on the steric and/or quantum mechanical nature of the catalyst. Nanotechnology permits one to design physical structures endowed with specific geometric and electronic properties. There is currently great interest in growing nanostructured materials, attached to a substrate, into structures that are commonly referred to as nanorods, nanoribbons, quantum dots, etc. These intriguing structures occur as the result of processing conditions used to form these materials with a variety of physical and chemical processes. The act of formation of these material structures is referred to as

### Fabrication of Self-Assembled Catalytic Nanostructures,

**Fig. 1** Atomic force microscope image of GaSb quantum dots formed on a Si substrate. Dots formed as a result of self-assembly process



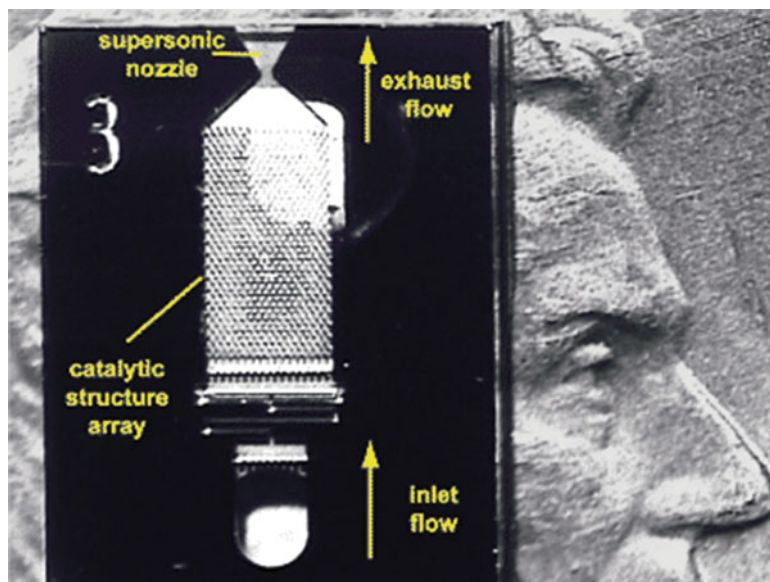
self-assembly. As an example, in Fig. 1 GaSb crystalline droplets are formed on the surface of Si wafer, as a result of surface tensions produced because of lattice constant differences between the two materials. These dot-like structures have been given the name of quantum dots, because the physics which describes electronic behavior in these structures requires a quantum mechanical treatment. Self-assembly is also credited with building more complicated structures such as nanorods and ribbons; again the physics and chemistry of atomic assembly produce these structures governed by minimum energy.

Within the specific context of micro- and nanofluidics, the fabrication of self-assembled nanostructures can represent an enabling technology for novel engineering applications. One such application – and the specific motivation for this entry – lies in the creation of catalytic nanostructures for micro-/nanoscale reacting flow systems. A specific example is the catalyzed chemical decomposition of monopropellant fuels for the purposes of small satellite micropropulsion [1] (Fig. 2). Here, the size and density of nanorod formations naturally provide the high surface area-to-volume ratios desirable for efficient catalysis in microscale geometries. Certainly other important applications exist, including those that leverage nanotechnology to produce *clean* energy and/or reduce emission of greenhouse gases. Some

specific, high-profile applications include fuel cell electrode fabrication, pollution control, hydrogen production, and chemical reagent production. For example, platinum (Pt) nanocrystalline layers are used in proton exchange membrane (PEM) fuel cells to catalyze the reduction of oxygen and oxidation of hydrogen on the cathodes and anodes, respectively. The current challenge is that the Pt nanostructured layer has been found to degrade through normal use owing to a number of factors such as fouling by fuel impurities, Pt dissolution, and nanoparticle coalescence and agglomeration [2]. Research efforts are targeted at identifying new alloy combinations with Pt that might overcome or mitigate these issues.

### Basic Methodology

Scientists are developing an ability to use nanofabrication techniques to make artificially structured catalyst arrays that can drive a chemical reaction to products with dramatically improved energy efficiency and chemical specificity. In general, nanorod structures have been demonstrated in a growing number of solid-state materials; a non-exhaustive, but illustrative, list includes the following: Si, InP, SiC, ZnO, CdS, GaN, and RuO<sub>2</sub> [3–8]. Currently it is not possible to predict with certainty what will be the best



**Fabrication of Self-Assembled Catalytic Nanostructures, Fig. 2** A photograph of a prototype monopropellant-based microthruster developed for miniaturized satellite applications (*nanosats*) by NASA/Goddard Space Flight Center in collaboration with the University of Vermont [1]. This device utilizes the catalyzed decomposition of hydrogen peroxide as the energy

source for propulsion. The catalytic structures in this device are not self-assembled but rather consist of a three-dimensional array of MEMS-fabricated pillar-type structures coated with a silver catalyst. For reference of scale, the entire catalytic array is  $\sim 1$  mm wide and 2 mm long

catalyst material for a specific chemical reaction. Research is proceeding both experimentally and theoretically to develop a deeper understanding of these materials and processes that one day will make this possible.

Much of the initial work in the overall area of nanotechnology involved ZnO; this is a result of the fact that this material has a combination of physical and chemical properties which makes it ideal for the fabrication of complex nanostructures [4–9]. These properties have given ZnO a ubiquitous role in the nanotechnology world. Once nucleated, the growth of single-crystal ZnO nanostructures (nanorods) is possible. The epitaxial growth of single-crystal ZnO as a thin film is preferred in its  $c$ -axis along the (0001) direction. Further, from energetic considerations, crystal growth proceeds by maximizing the areas of its sidewall facets, oriented in the (2110) and (0110) directions. These growth mode constraints result in the formation of tall hexagonally shaped nanorod structures.

It has been shown by Wang et al. [7] that the addition of elemental impurities can affect the final nanostructure of the grown material. Another interesting concept for the purposes of this application and nanotechnology in general is the continued growth of additional materials onto the sidewalls of existing ZnO or other nanorods. Norton et al. [4] reported on the epitaxial growth of a Mg-doped ZnO layer on the sidewall of an existing ZnO nanorod. The process used to grow the additional layer on the ZnO nanorod structure in that study was molecular beam epitaxy (MBE).

There are a number of experimental techniques used to fabricate self-assembled nanostructures from ZnO and other materials. These techniques include the following: vapor-liquid-solid, metalorganic chemical vapor deposition, template-assisted, chemical reaction, molecular beam epitaxy, and reactive sputtering. In this section we provide a brief overview of these techniques.

### Vapor-liquid-Solid (VLS) Technique

In the VLS method, a thin layer (70 Å) of metal such as Au, Ag, Pt, Pd, Cu, or Ni is deposited on the substrate surface. The substrate is then annealed at high temperature (500 °C for Au) to form nanodots of the metal catalyst, which provide the preferential site for the adsorption of gas-phase reactants. For the case of ZnO nanorods, the substrate is placed in a furnace containing ZnO powder and a source of carbon. When heated to 700 °C, the ZnO and carbon react to produce CO<sub>2</sub> and Zn. The gaseous Zn is dissolved to supersaturation in the metal dot, and crystal growth occurs from the substrate side of the metal dot. The growth continues as long as the conditions for growth remain sufficient, such as reactant concentration and the proper temperature for growth. The method has been used to form a variety of nanowires such as InP, GaN, CdS, and Si [6]. Several groups have repeated the process with variations such as the substrate used for growth and the reactor design.

### Metalorganic Chemical Vapor Deposition (MOCVD)

To date the greatest success in growing straight, tall, and well-aligned rod-shaped structures has been with an MOCVD growth process. This approach relies typically on the use of chemical precursors (e.g., diethylzinc and oxygen in the case of ZnO growth). It appears that the chemical nature of this process technique encourages the growth of exceptionally straight nanorods. Different metalorganic precursors are used as the starting materials for different inorganic nanorod materials [8].

### Template-Assisted Growth

This technique can use several different variations to achieve the growth of nanostructured materials. In one version, a metal catalyst is deposited and/or patterned into a desired layout. From these metal catalyst locations, the nanorod materials are assembled to the finished length or size. Another approach can involve the actual growth of a different material inside or on an existing nanostructured material such a carbon nanotube. This technique can be used to grow

nanostructured materials with chemical compositions that have not been fabricated into nanostructures [10].

### Solution-Based Approaches

These methods are, in theory, the least technically challenging procedures for the fabrication of nanometer-sized structures of a given composition. The techniques of hydrothermal and solvothermal production are included under this general heading of solution-based approaches. These methods all involve the dissolution of a targeted nanorod material (e.g., TiO<sub>2</sub>) in a basic solution (e.g., NaOH in water). This solution is raised to a temperature and pressure above standard temperature and pressure and held for several hours. The resulting nanostructure precipitates are freestanding and need to be collected from a liquid solution by filtration. The precipitate in this example would be Ti(OH)<sub>x</sub> and would require further processing called calcination. Calcination is performed at a temperature of about 700 °C removing the H species from the nanorod material.

Modifications of this process have resulted from the use of different basic solutions that have reduced the required process temperatures or pressures. An example would be the formation of Eu<sub>2</sub>O<sub>3</sub> nanorods [11]. These are formed by dissolving Eu(NO<sub>3</sub>)<sub>3</sub> in a cyclohexamine base solution. The resulting precipitate is calcinated at 700 °C for 1 h, and nanorods with a length of 300 nm and diameter of 20–30 nm are obtained.

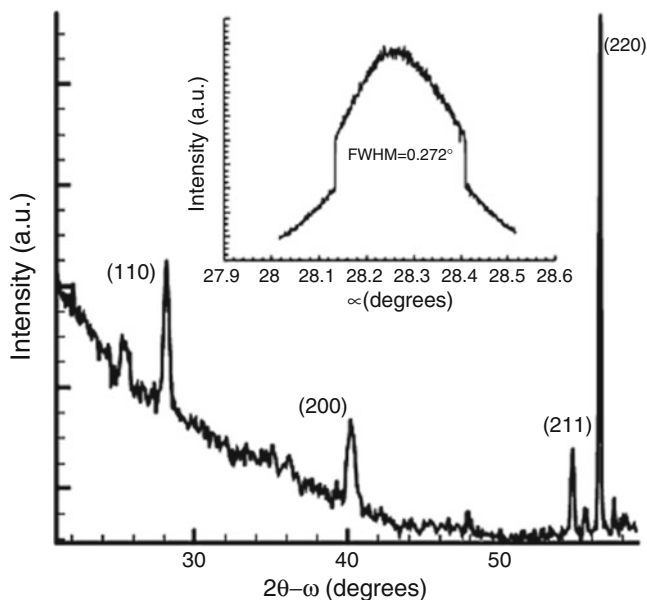
These solution-based approaches have the benefit of producing a large volume of material with an inexpensive process. A downside is that the catalyst material is freestanding and to be used in a heterogeneous reactor will require additional process complications.

### Molecular Beam Epitaxy (MBE)

This technique is prized for the high level of control that is possible, in terms of the control of both desired (the materials which constitute the nanorods) and undesired species fluxes (contaminants, e.g., water and oxygen) at the growth surface. This technique has been successfully used to grow a wide variety of

### Fabrication of Self-Assembled Catalytic Nanostructures,

**Fig. 3** The X-ray diffraction pattern of RuO<sub>2</sub> nanorods grown on a Si substrate for 10 min at 600 °C. The inset is an omega scan of (220) peak. Major peaks indicate particular crystal orientation of the atoms in the nanorods



semiconductor nanostructures. Due to high capital cost and cost of operation, it is not expected that this technique will prove capable of producing catalyst materials on a large scale.

### Reactive Sputtering

Deposition of metal oxide nanorods has been achieved by reactive sputtering. As an example of this deposition approach, RuO<sub>2</sub> nanorods have been obtained by sputtering on a Si/SiO<sub>2</sub> surface [12]. In this particular case, these structures were used as the starting substrate for the further growth of TiO<sub>2</sub>. Sputtering is a process that has been used in large-volume manufacturing such as the automotive industry; therefore, it is possible to envision its use in the manufacture of heterogeneous catalyst layers.

### Key Research Findings

The scientific literature has shown that self-assembled nanorod structures have been grown from a large number of materials and for a wide variety of engineering applications. For illustrative purposes, in this entry we focus on the fabrication and growth characteristics of ruthenium oxide nanorods; the target application lies in the catalyzed decomposition of hydrogen peroxide

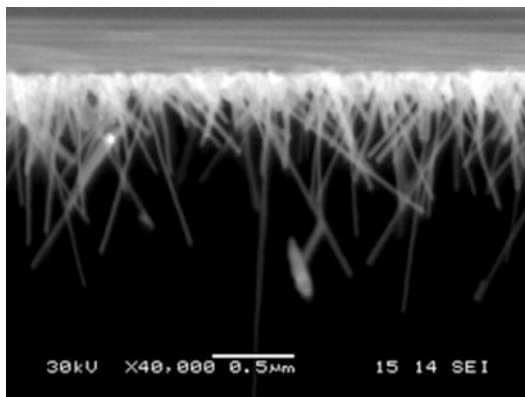
for small satellite micropropulsion (e.g., Fig. 2). The findings reported here, while case specific, are nonetheless reflective of broader phenomena and considerations associated with the growth of self-assembled nanostructures.

Our laboratory at the University of Vermont has successfully grown RuO<sub>2</sub> nanorods by reactive sputtering on Si wafer substrates with a variety of preexisting surface conditions. Proof of a crystalline structure has been obtained by X-ray diffraction. A sample X-ray diffraction spectrum of the deposited nanorods is shown in Fig. 3. Each of the major peaks in Fig. 3 corresponds to a single-crystal orientation of the nanorods. Although each nanorod is single crystal, each nanorod is randomly oriented relative to another, thus displaying the random pattern observed under scanning electron microscopy (SEM) imaging (Fig. 4).

### Experimental Apparatus

The reactor used in this investigation is shown in Fig. 5. The samples were prepared by sputtering from a 1.5 in. diameter Ru metal target, operated at 13.56 MHz and a power level of 50 W. The reactor ambient was obtained by flowing 100 sccm of a 5/95 % O<sub>2</sub>/Ar gas mixture, throttled to a pressure of 15 mtorr. The samples were heated radiatively from behind with a resistive

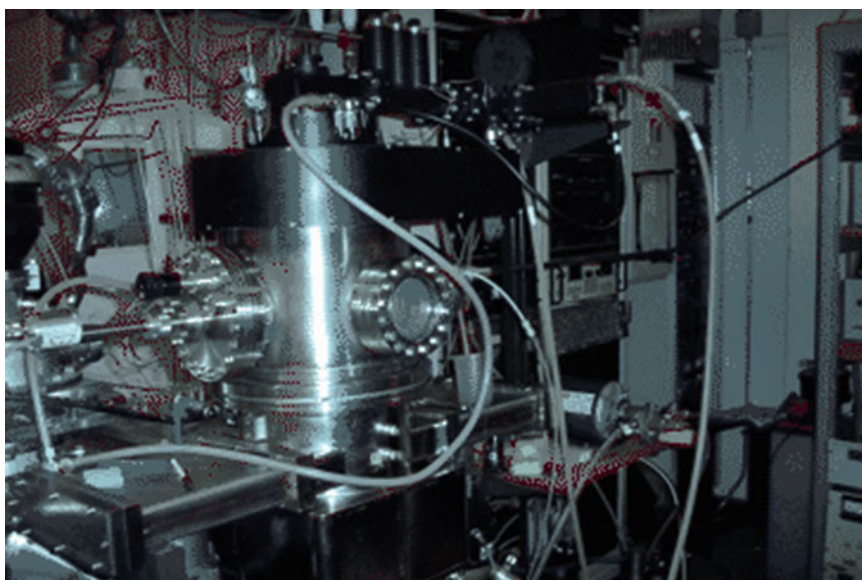
boron nitride-coated pyrolytic graphite heater. Silicon wafer substrates with three different surface preparations were used: Si with a native oxide layer, Si with the oxide layer removed by hydrofluoric acid (HF) treatment leaving a hydrogen passivated surface, and Si with Au dots nucleated on the surface. Nanorod growth was obtained to varying degrees on all surface preparations, as can be observed in Fig. 6.



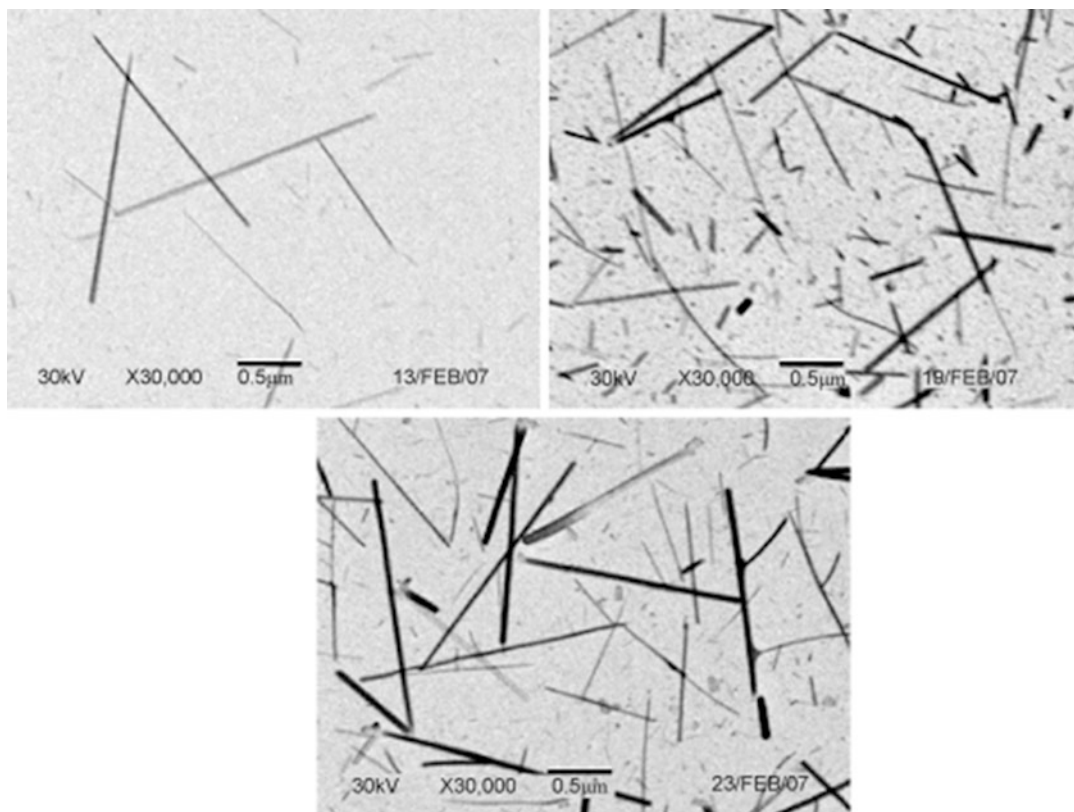
**Fabrication of Self-Assembled Catalytic Nanostructures, Fig. 4** Scanning electron microscope image of RuO<sub>2</sub> nanorods grown on (100) Si at 600 °C for 10 min

### Temperature Dependence of Growth

Ruthenium oxide nanorods were found to form on all samples independent of preexisting surface preparation, yet not at all substrate temperatures. Initially the effect of substrate temperature on the growth of RuO<sub>2</sub> nanorods was investigated. SEM images of samples prepared at varying substrate temperatures are shown in Fig. 7 for the case of RuO<sub>2</sub> grown on Si covered with Au nucleation sites. The RuO<sub>2</sub> layer was prepared by exposing the Si surface to the sputtered Ru flux at substrate temperatures of 400 °C, 500 °C, 600 °C, and 700 °C for a period of 5 min. At a substrate temperature of 400 °C, short, sparse RuO<sub>2</sub> nanorods formed. There is also the appearance of randomly scattered dots on the surface, assumed to be composed of RuO<sub>2</sub> deposited on a continuous island-like thin-film structure. Increasing the substrate temperature to 500 °C resulted in conditions that caused these nucleation sites to develop into nanorods again rising above a continuous cauliflower-like film. From a plan view SEM image such as seen in Fig. 7, the nanorods appear to be randomly oriented. Measuring the average length of the nanorods from this vantage point is not possible because of the



**Fabrication of Self-Assembled Catalytic Nanostructures, Fig. 5** Sputtering system used in the growth of RuO<sub>2</sub> nanorods in our laboratory



**Fabrication of Self-Assembled Catalytic Nanostructures, Fig. 6** SEM images (shown in *negative tone*) of RuO<sub>2</sub> nanorods grown at 600 °C. Shown

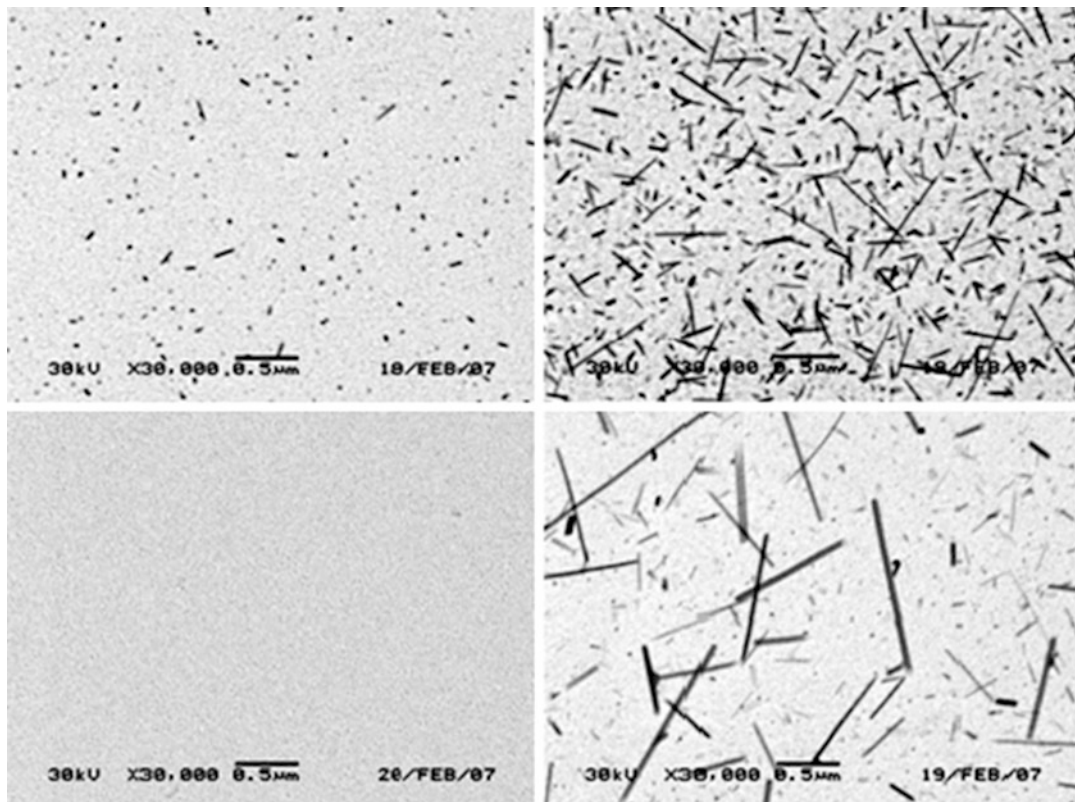
clockwise from top left are nanorods deposited on HF-dipped Si, Au dots, and native oxide

nanorod's angular projection from the Si surface. It is more significant to simply measure the length of the longest nanorods for a given set of process conditions and compare these to those obtained for different growth conditions. Considering that the number of rods sampled in a field of view is large (approximately  $6 \mu\text{m}^{-2}$ ), the measured rod length is an accurate representation of the maximum rod length. At a substrate temperature of 400 °C, 0.18  $\mu\text{m}$  tall nanorods were observed. The conditions of a 500 °C substrate temperature produced nanorods with a maximum length of 0.6  $\mu\text{m}$ . When the temperature was increased further to 600 °C, the maximum length of the nanorods has grown to 1.3  $\mu\text{m}$ . Finally, when a substrate temperature of 700 °C is used, growth of the nanorods is not obtained past the formation of RuO<sub>2</sub> dots.

### Axial Growth Rate

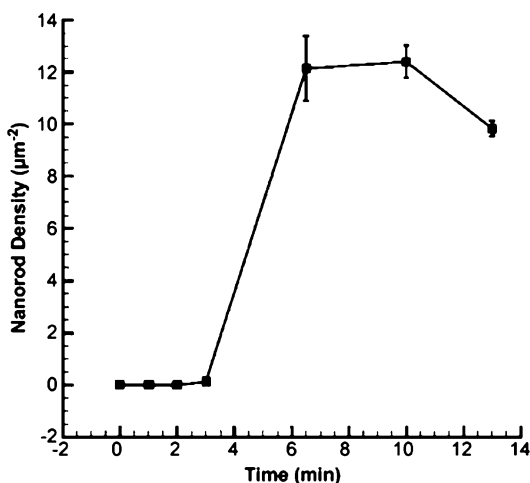
To further understand the mechanism which governs the growth of RuO<sub>2</sub> nanorods in a radio-frequency sputtering process, a series of runs were made under identical process conditions and were terminated after increasingly longer periods of time, following which characterization was carried out. The process conditions used in this sequence of runs were similar to those in the temperature investigation, but in this case a substrate temperature of 600 °C was used. The periods of growth were 2, 3, 6.5, 10, and 13 min. From the plot in Fig. 8, one can observe that the density of nanorods increases with time. The maximum nanorod length for these depositions is approximately 1.3  $\mu\text{m}$ , and this value does not change with time.

Relative to the growth rate of nanorods presented in the literature, using different



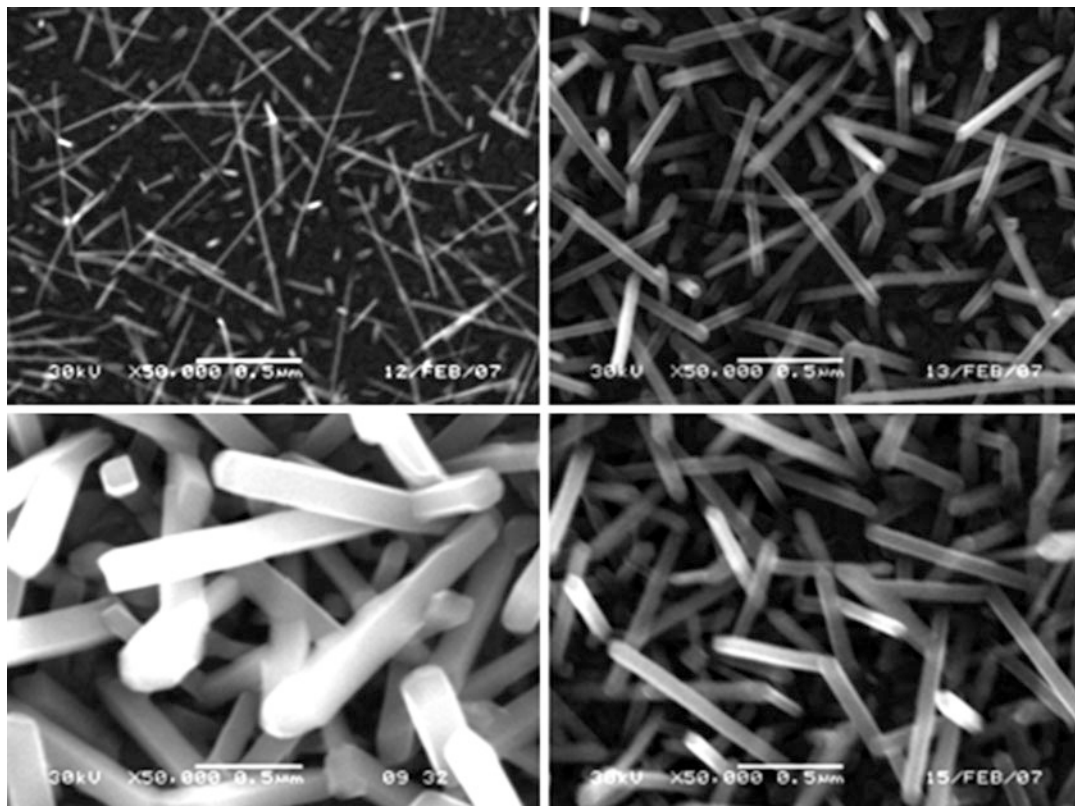
**Fabrication of Self-Assembled Catalytic Nanostructures, Fig. 7** SEM images (shown in *negative tone*) of RuO<sub>2</sub> nanorods. Nanorods were deposited on

Au dots for 5 min. Shown clockwise from top left are substrate temperatures of 400 °C, 500 °C, 600 °C, and 700 °C



**Fabrication of Self-Assembled Catalytic Nanostructures, Fig. 8** Plot of a RuO<sub>2</sub> nanorod density at varying deposition times. Nanorods were deposited at 600 °C

processing techniques, the rate of growth observed herein is relatively fast. In the time evolution study described above, the nucleation of nanorods is very fast and short relative to the time increments investigated. In the time period from 3 to 6.5 min, the density of nanorods increases at a rate of  $5.41 \cdot 10^6 \text{ cm}^{-2} \text{ s}^{-1}$ . The Rutherford backscattering spectrometry (RBS) analysis of a film deposited at room temperature can be used to calculate a measured flux of Ru atoms to be  $7.08 \cdot 10^{-10} \text{ mol cm}^{-2} \text{ s}^{-1}$ . The diameter of the nanorods grown after a time of 10 min was observed by SEM to be approximately 100 nm. Assuming a final rod diameter of 100 nm and that all of the sputtered flux of Ru adatoms are successfully incorporated into the nanorods structure, a simple mass balance can be performed to estimate the average length of the nanorods. Using



**Fabrication of Self-Assembled Catalytic Nanostructures, Fig. 9** SEM images of RuO<sub>2</sub> nanorods. Nanorods were deposited on HF-dipped Si at 460 °C. Shown clockwise from top left are deposition times of 5, 15, 25, and 60 min

this assumption and the measured Ru flux and density of nanorods formed, a nanorod length of 0.32  $\mu\text{m}$  is estimated. This value is comparable with the values obtained from the cross-sectional SEM view shown in Fig. 4.

#### Radial Growth Rate

The growth of nanorods in the vertical direction is very fast once nucleated. After viewing all SEM images, it is interesting to note that for varying periods of growth, the nanorods grew to a maximum length and then virtually stopped. There seems to be no apparent explanation for the cessation of vertical growth. Under closer examination, the SEM images of RuO<sub>2</sub> nanorods grown under identical conditions, but after different periods of growth (5, 15, 25, and 60 min),

were examined (Fig. 9). It is first observed that the nanorods actually have a square profile. It is further observed that the square profile of the nanorods is also increasing with time. The nanorod radial growth rate is estimated to be 1.9  $\text{nm min}^{-1}$ . It is proposed that the further axial growth is halted as a result of the consumption of Ru adatoms used in the radial growth process. The axial reaction rate constant is assumed to be large relative to the radial growth constant, and the axial growth dominates initially. As the cross-section of the square rod increases, the density of surface states dominates the consumption of Ru adatoms, and axial growth is halted.

In this entry, a brief overview of fabrication techniques and issues associated with the growth

of nanostructures made of catalytic materials has been given. Illustrative research findings were also presented for the specific case of RuO<sub>2</sub> nanostructures.

## Future Directions for Research

To date, much of the research in this area can best be categorized as phenomenological. As such, there are many important areas for future research. We close this entry by identifying three key areas for immediate research:

- *Growth mechanisms.* Observations on the growth mechanisms of RuO<sub>2</sub> nanorods have been reviewed. In particular, the dependence of the length of nanorods on substrate temperature and the width of nanorods on deposition time has been described. Further studies are required to fully develop a theoretical model for the growth mechanism of these structures and to gain a better understanding of the limiting factors of growth.
- *Mechanical characterization.* For the application of catalytic nanostructures, these nanorods may experience significant forces due to the flow of liquid and gas around them. The mechanical robustness of the nanorod structures as well as the connection to the substrate must be evaluated. Techniques such as manipulation via an atomic force microscope may be used to determine the strength of these structures. Theoretical modeling will also contribute to this effort.
- *Device application and integration.* It is clear that self-assembled nanostructures hold great promise for future applications. Nanorod structures have been studied for nearly a decade now; however, very little progress has been made in the implementation of these structures into/as devices. Further work is required in order to integrate these structures into devices. Future work in our laboratory will study the catalytic efficiency of RuO<sub>2</sub> nanorods in a microthruster device.

**Acknowledgments** This work was supported, in part, by the US Air Force Office of Sponsored Research (AFOSR) under Grant #FA9550-06-1-0364.

## Cross-References

- ▶ [Chemical Vapor Deposition for Film Deposition](#)
- ▶ [Droplet Dynamics in Microchannels](#)
- ▶ [Fabrication of 3D Microfluidic Structures](#)
- ▶ [Flow in Channels with 3D Elements](#)
- ▶ [Micro Energy Conversion Devices](#)
- ▶ [Microfluidic Systems in Space Science](#)
- ▶ [Microrockets](#)
- ▶ [Quantum Dot](#)
- ▶ [Self-Assembly](#)
- ▶ [Self-Assembly Fabrication](#)
- ▶ [Sputtering for Film Deposition](#)
- ▶ [Supersonic Micro-Nozzles](#)

## References

1. Hitt DL, Zakrzewski CM, Thomas MK (2001) MEMS-based satellite micropropulsion via catalyzed hydrogen peroxide decomposition. *Smart Mater Struct* 10:1163–1175
2. Ferreira PJ, la O' GJ, Shao-Horn Y, Morgan D, Makharia R, Kocha S, Gasteiger HA (2005) Instability of Pt/C electrocatalysts in proton exchange membrane fuel cells. *J Electrochem Soc* 152(11):A2256–A2271
3. Duan X, Huang Y, Agarwal R, Lieber C (2003) Single-nanowire electrically driven lasers. *Nature* 421:241–245
4. Norton DP, Heo YW, Ivill MP, Ip K, Pearton SJ, Chisholm MF, Steiner T (2004) ZnO: growth, doping and processing. *Mater Today* 7(6):34–40
5. Han W, Fan S, Li Q, Hu Y (1997) Synthesis of GaN nanorods through a carbon nanotube confined reaction. *Science* 277(5330):1287
6. Gudiksen MS, Lieber CM (2000) Diameter-selective synthesis of semiconductor nanowires. *J Am Chem Soc* 122:188
7. Wang G, Hisieh CS, Tsai DS, Chen RS, Huang YS (2004) Area-selective growth of ruthenium dioxide nanorods on LiNbO<sub>3</sub> (100) and Zn/Si substrates. *J Mater Chem* 14:3503–3508
8. Si J, Desu B (1996) RuO<sub>2</sub> films by metal-organic chemical vapor deposition. *J Mater Res* 8(10):2644
9. Wang ZL (2004) Nanostructures of ZnO. *Mater Today* 7(6):26–34

10. Quinn BM, Lemay SG (2006) Single-walled carbon nanotubes as templates and interconnects for nanoelectrodes. *Adv Mater* 18:855–859
11. Du N, Zhang H, Chen B, Wu J, Li D, Yang D (2007) Low temperature chemical reaction synthesis of single-crystalline  $\text{Eu}(\text{OH})_3$  nanorods and their thermal conversion to  $\text{Eu}_2\text{O}_3$ . *Nanotechnology* 18:065605
12. Cheng KW, Lin YT, Chen CY, Hsiung CO, Gan JY, Yeh JW, Hsieh CH, Chou LJ (2006) In situ epitaxial growth of  $\text{TiO}_2$  on  $\text{RuO}_2$  nanorods with reactive sputtering. *Appl Phys Lett* 88:43115

---

## Fabry-Perot Optical Filter

### Synonyms

Optical narrow-passband filter

### Definition

A Fabry-Perot optical filter consists of two flat highly reflective parallel mirrors spaced a well-defined distance apart with the reflecting parts facing each other. The space between the mirror surfaces is essentially a resonance cavity. The incident light suffers multiple reflections between the coated surfaces that define the cavity. When the cavity width is equal to an odd multiple of a half wavelength of the incident light, the reflected beams interfere constructively, and the optical transmission is maximum. At other cavity widths, the reflected beams interfere destructively, and the optical transmission can be reduced toward zero. Therefore, this device acts as a passband filter that transmits certain wavelengths. To perform high reflectivity and high transmittance, dielectric mirrors are used instead of metallic mirrors.

### Cross-References

- ▶ [Lab-on-a-Chip Devices for Chemical Analysis](#)
- ▶ [Optofluidics: Optics Enabling Fluidics](#)
- ▶ [Sputtering for Film Deposition](#)

---

## Far-Field Nanoscopic Measuring Technique

Hong Jiang<sup>1</sup> and Guiren Wang<sup>2</sup>

<sup>1</sup>Graceflow Technology LLC, Irmo, SC, USA

<sup>2</sup>Department of Mechanical Engineering and Biomedical Engineering Program, University of South Carolina, Columbia, SC, USA

### Synonyms

Far-field nanoscopic measuring technique; Far-field optical nanoscopic measuring technique; Laser-induced fluorescence photobleaching anemometer; Nanoscopy; Stimulated emission depletion

### Definition

In this entity, far-field optical nanoscopic measuring technique means the measuring techniques that use optical lens to focus light but can overcome conventional well-known Abbe's diffraction limit to achieve nanoscale spatial resolution. The "far-field" means the distances between the investigated object, and the lens are at least several thousands of wavelengths of the light. In addition, the measuring technique means measuring physical parameters, such as flow velocity and scalar, such as fluid concentration.

### Overview

With recent progress in nanofabrication, nanotechnology, and microfluidics [1–4], the field of nanofluidics is rapidly gaining importance. To meet the need of basic research in nanofluidics, e.g., measuring the profile of flow velocity and analyte in a nanochannel, experimental measuring techniques with nanoscale spatial resolution are required. Optical microscopic measuring techniques play a key role in microfluidics and nanofluidics and lab-on-a-chip. Unfortunately

almost all optical measuring techniques suffer from the well-known Abbe diffraction limit: their spatial resolution is limited to roughly half of the light wavelength, i.e., about 200–300 nm [5] for visible light. With confocal microscopy the resolution is  $\sim 150$ –200 nm for visible light, [6, 7] still much larger than many interested structures in nanofluidics.

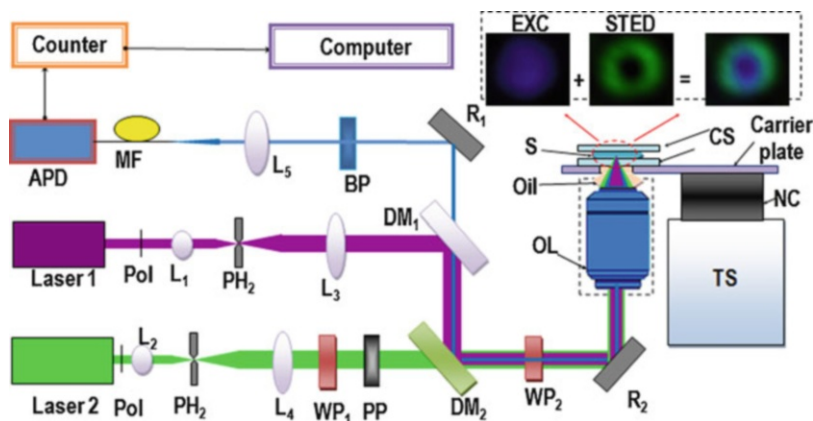
While some breakthrough technologies of scanning near-field optical microscope have been developed to overcome the diffraction limit to increase resolution, these near-field techniques require the distance between the tip and the specimen surface to be in the order of one to several percents of a wavelength, normally less than 1  $\mu\text{m}$ . However, in nanofluidics and lab-on-a-chip, the channels are mostly enclosed ones and the solid walls are more than 100  $\mu\text{m}$  thick, and hence, the near-field scanning microscopes cannot be applied to nanofluidics. For lab-on-a-chip application, far-field nanoscopy, where the working distance is similar to that of conventional confocal microscope, is required for nanofluidics applications.

To overcome the issue of near-field scanning optical microscopes because of short working distance, revolutionary far-field nanoscopic technologies that can break the barrier of diffraction limit have recently been developed in order to carry our 3-D cellular imaging. These include stimulated emission depletion (STED) [8–10], photoactivated localization microscopy (PALM), and stochastic optical reconstruction microscopy (STORM) [7, 11]. In contrast to the near-field nanoscopy, the far-field is the lens-based focusing light microscope, where the working distance is at least several thousands of wavelengths, i.e., can be more than 200  $\mu\text{m}$ , making them applicable to nanofluidics applications. Among these far-field nanoscopic technologies, only STED has a defined spatial position and can be applied for velocity and scalar measurement in nanofluidics and lab-on-a-chip. Therefore, STED and its applications in nanofluidics will be discussed here. Since this is a quite new area, few works have been available; we will mainly focus on velocity and proton concentration measurement in nanofluidics application.

## Flow Velocity Measurement

There are many excellent velocimetrys in fluid mechanics. The most successful and widely used velocimetrys that have been applied in microfluidics are Micro-Particle Imaging Velocimetry ( $\mu\text{PIV}$ ) pioneered by Arian's group [12–16] and Molecular Tagging Velocimetry (MTV) [17–27], respectively. Evanescent wave total internal reflection based nano-PIV (nPIV), pioneered by Yoda group, enables measurement of velocity distribution within  $\sim 400$  nm from the solid wall of a microchannel [28–32]. This method can even measure the flow velocity at a distance of 150 nm from the solid wall in microchannel [33]. A quantum dot of 6 nm in diameter has also been developed for nPIV [34] in microchannel. The MTV method uses a molecular tracer and avoids the issues related to nanoparticle tracers. There are several methods employed by MTVs [25], including caged-fluorescence visualization [35, 36], fluorescence recovery after photobleaching (FRAP) [26, 37], photobleached fluorescence visualization [20], line writing technique with photobleaching [19], and laser-induced fluorescence photobleaching anemometer (LIFPA) [38–43]. Unfortunately all these optical methods suffer from diffraction limit for nanofluidics application. Although evanescent wave total internal reflection can overcome the diffraction in axial direction, but not in the lateral plane. In addition, to the best of our knowledge, so far no nPIV technique has been applied to submicro- and nanochannels, which is the major focus of the work here.

In order to overcome diffraction limit for velocity measurement in nanofluidics, Piorek et al. developed a prominent velocimeter based on force microscope (AFM) in a open nanochannel [44] and achieved a high spatial resolution of about 50 nm. Unfortunately this is an intrusive method, and the tip has to be in contact with fluid. In most nanofluidics application, the channel is enclosed and there is no access window for the tip of the AFM; thus it could be very difficult to use this technique in nanochannel that does not have an opened



### Far-Field Nanoscopic Measuring Technique,

**Fig. 1** Schematic of a typical STED system setup.  $L_1$ ,  $L_2$ ,  $L_3$ ,  $L_4$ , and  $L_5$  optical lenses,  $PH_1$  and  $PH_2$  pinholes,  $WP_1$  and  $WP_2$  wave plate ( $WP_1$  half wave plate,  $WP_2$  quarter wave plate),  $Pol$  light polarization direction,  $DM_1$  and  $DM_2$  dichroic mirrors,  $PP$  phase plate (vortex mode),  $APD$  avalanche photon detector,  $MF$  multimode

optical fiber,  $R_1$  and  $R_2$  reflector mirrors,  $BP$  band-pass filter,  $OL$  objective lens (Plan Apo, 100X; NA = 1.4 oil immersion),  $CS$  coverslip (about 170  $\mu\text{m}$  thickness),  $S$  sample,  $NC$  nano-cube piezo stage (3-axis),  $TS$  translation stage (3-axis). The zoom-in part on the top-right corner is the focused beam to illustrate STED principle

sidewall. Fortunately, recent development of LIFPA in combination with STED in Wang's group could provide a new opportunity for velocity measurement in nanofluidics [45].

### Concentration Measurement

Laser-induced fluorescence (LIF) is mostly used for the measurement of analyte concentration in liquid. Again, this method generally has limited spatial resolution because of the diffraction limit. With STED, the spatial resolution can be increased for nanofluidics application. Recently Kitamori's group applied STED to measure proton concentration distribution within an extended nanochannel to evaluate theoretical prediction of ion distribution and influence of electrical double layer on the proton concentration distribution [46].

### Basic Methodology

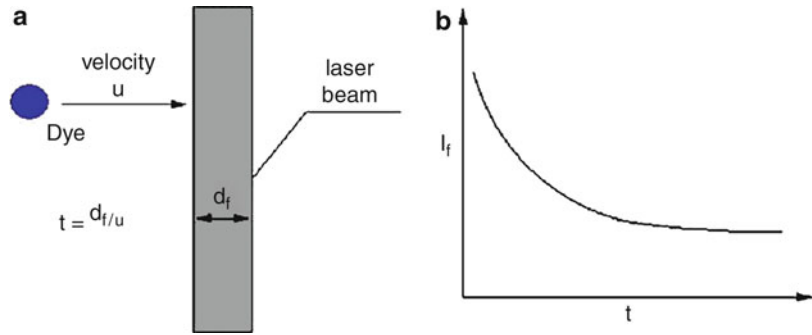
#### STED

Motivated by breaking diffraction barrier to achieve high resolution for developing 3-D

cellular imaging, Hell pioneered STED technology [10, 47]. STED has revolutionarily broken the barrier of diffraction limit to increase spatial resolution for far-field, noninvasive nanoscale imaging of fluorescently labeled structures. Here we use a typical schematic of optical setup for a STED system shown in Fig. 1 to illuminate its basic principles. While in a conventional fluorescence microscopy, there is only one laser, in a STED microscopy, there are two lasers: one is excitation laser and the other is STED laser. The excitation laser beam (violet light) is reflected by a dichroic mirror through an objective lens and is focused to a spot in detection point. The smaller the excitation spot, the better the resolution. However, because of diffraction limit, the laser beam cannot be focused by an objective to smaller than  $\sim 200$  nm at the detecting zone. In the STED nanoscopy, there is a second laser beam (green light), which is doughnut shaped generated by a phase plate modulation as shown in Fig. 1 on the top-tight corner. The second laser beam is focused concentrically with the excitation beam at the focus spot by the same objective to preferentially quench the fluorescent dye at the outer edge of the excitation spot before it emits fluorescence. In this case, only the middle part of

### Far-Field Nanoscopic Measuring Technique,

**Fig. 2** Schematic of a simplified model for LIFPA. (a) Dye passes through laser beam. (b) Fluorescence intensity decay with time because of photobleaching



the excitation spot, where the STED beam has not covered, will emit fluorescence.

This smaller effective fluorescence spot determines the new spatial resolution of STED nanoscope. If  $I_{\text{sat}}$  denotes the saturation laser intensity, at which half of the excited molecules are stimulated to the ground state, the lateral resolution of a STED system ( $\Delta x$ ) can be theoretically described by [48]

$$\Delta x = \frac{\lambda}{2n \sin \theta \sqrt{1 + I/I_{\text{sat}}}} \quad (1)$$

where  $\lambda$ ,  $n$ , and  $\theta$  are beam wavelength, refractive index, and half aperture angle of the lens, respectively. This shows that by increasing the intensity ( $I$ ) of the STED laser beam, the more fluorescence signal will be depleted at the focused spot's periphery and  $\Delta x$  will decrease towards the middle. However, in the region of the doughnut hole, the fluorescence is not affected at all. Therefore, by increasing the intensity of the doughnut-shaped second STED beam, the spatial resolution  $\Delta x$  of the measurement point can be progressively narrowed to increase spatial resolution [8, 48–51]. So far spatial resolution down to 5.8 nm has been achieved. This is about two orders smaller than the diffraction limit value for visible light.

### LIFPA Measurement Mechanism and STED-Based LIFPA

Measurement of flow velocity based on fluorescence dye is normally much more complicated and difficult than measurement of concentration. In LIFPA, a molecular tracer of fluorescence dye

and the photobleaching effect are applied as a transducer to measure the flow velocity. The relation between fluid velocity  $V$  and fluorescence intensity  $I_f$  can be expressed by a simplified model [40] as shown in Fig. 2:

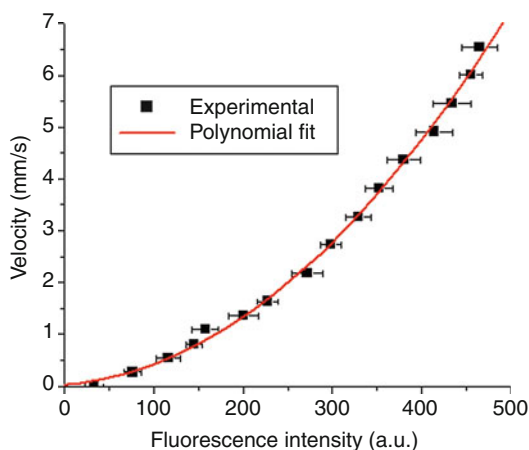
$$C = C_0 \times e^{-t/\tau} \quad (2)$$

$$I_f = kI_L C \quad (3)$$

$$t = d/V \quad (4)$$

$$I_f = kI_L C_0 \times e^{-t/\tau} = I_{f0} \times e^{-d/(V\tau)} \quad (5)$$

where  $C$  is the dye concentration and  $C_0$  is the initial concentration; Constant  $\tau$  denotes the photobleaching time constant and  $t$  represents the dye residence time, i.e., photobleaching time within the laser beam at the detection spot;  $I_L$  is the laser intensity at the detection spot and  $k$  is a constant;  $d$  denotes the width of the focused laser beam spot;  $V$  is the flow velocity at the focused spot; and  $I_{f0}$  represents fluorescence intensity at  $t = 0$ . In reality,  $\tau$  as a system parameter depends on laser wavelength and intensity at the detection point, type of dye and buffer, etc. For a given bleaching time  $t$ , the smaller the  $\tau$ , the lower the  $I_f$ . Thus, lower  $\tau$  causes faster photobleaching and higher  $dI_f/dt$ , i.e., higher temporal resolution. So far a temporal resolution of  $\sim 5 \mu\text{s}$  has been achieved [52].  $\tau$  decreases with reduced laser wavelength and increased laser intensity. The parameter  $\tau$  can be determined through experiment. Based on Eq. 5, the higher the velocity  $V$ , the larger the fluorescence intensity  $I_f$ . If  $I_f$  is known, the velocity  $V$  can be



### Far-Field Nanoscopic Measuring Technique,

**Fig. 3** Typical calibration curve between fluorescence intensity and flow velocity in LIFPA measured in a submicrocapillary (Reproduced from Lab-on-a-Chip with permission of RSC)

calculated using Eq. 1. For practice, since  $\tau$  is not easy to be calculated, a calibration relation is measured first between  $V$  and  $I_f$ . Then  $V$  can be determined by simply measuring  $I_f$ . Figure 3 shows a typical calibration curve in a subnanocapillary.

It is important to note that at the detection point, molecular diffusion will cause fluorescence recovery of the bleached dye molecules. However, unlike some of other photobleaching-based velocimeters, LIFPA here does not measure the recovery. In LIFPA, a calibration curve between  $V$  and  $I_f$  is measured first to determine  $V$  from measured  $I_f$ . In this case, the recovery effect has already been included in the calibration relation. This is the main reason why LIFPA has high temporal resolution.

Since  $I_f$  is proportional to dye concentration, for a given laser power, the changing  $V$  will cause alteration in bleaching time, which in turn results in change in real dye concentration that can emit fluorescence, i.e., whose dye molecules, whose electrons can return to the ground state, not those that are in the triplet state and cannot emit fluorescence. Therefore, in reality LIFPA measures the  $V$  through measuring the real concentration of

the dye, whose change is caused by the bleaching time or the dye residence time within the focused laser spot and thus flow velocity  $V$  within it.

In order to measure the velocity profile in a nanochannel, a measurement system having nanoscale spatial resolution is required. LIFPA itself also suffers from diffraction limit. Fortunately, LIFPA is compatible with STED. By selecting a fluorescent dye that has both fast bleaching and STED effect, one can combine STED and LIFPA to overcome the Abbe diffraction limit to measure flow velocity profile within a nanochannel with nanoscale resolution [45].

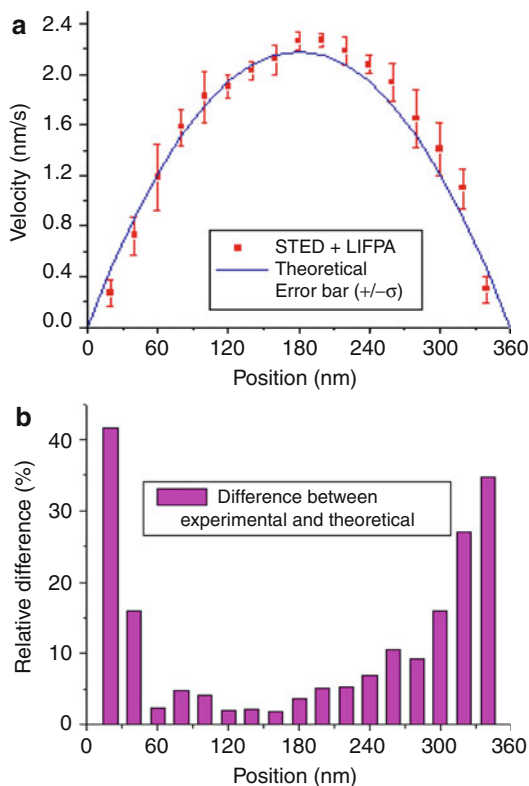
### Principle of Concentration Measurement

LIF is a well-established method for concentration measurement. In fact, STED is also a LIF-based method. Therefore, it is straightforward to utilize STED to measure concentration profile in nanochannels. As aforementioned, LIFPA itself measures the real concentration of fluorescent dye. The principle of measuring proton concentration in a nanochannel is that the fluorescence intensity increases with the increase of pH, which is related to  $H^+$  [46]. Through measurement of the calibration relationship between fluorescence intensity and pH, one can measure  $H^+$  by simply measuring fluorescence intensity, similar to LIFPA.

## Key Research Findings

### Velocity Profile Measurement in a Submicrocapillary

Using STED to break diffraction barrier, LIFPA can measure flow velocity with nanoscopic resolution. To the best of our knowledge, Kuang and Wang [45] for the first time, probably still the only one [53], developed a continuous wave (cw) laser-based STED and LIFPA system and measured the average flow velocity profile in a pressure-driven flow in a submicrocapillary with inner diameter (ID) of 360 nm. A violet laser 405 nm and a green laser 530 nm were used as the excitation and STED beam, respectively. The spatial resolution was measured to be about



**Far-Field Nanoscopic Measuring Technique, Fig. 4** Velocity profile. (a) Velocity profile in a submicrocapillary of 360 nm ID; (b) relative difference between the experimental results and theoretical prediction (*parabolic*) (Reproduced from *Lab-on-a-Chip* with permission of RSC)

70 nm. The measuring point was controlled through a piezoelectric stage with nanoscale resolution, and the closest measuring point to the wall was about 35 nm. The submicrocapillary was mounted on the stage.

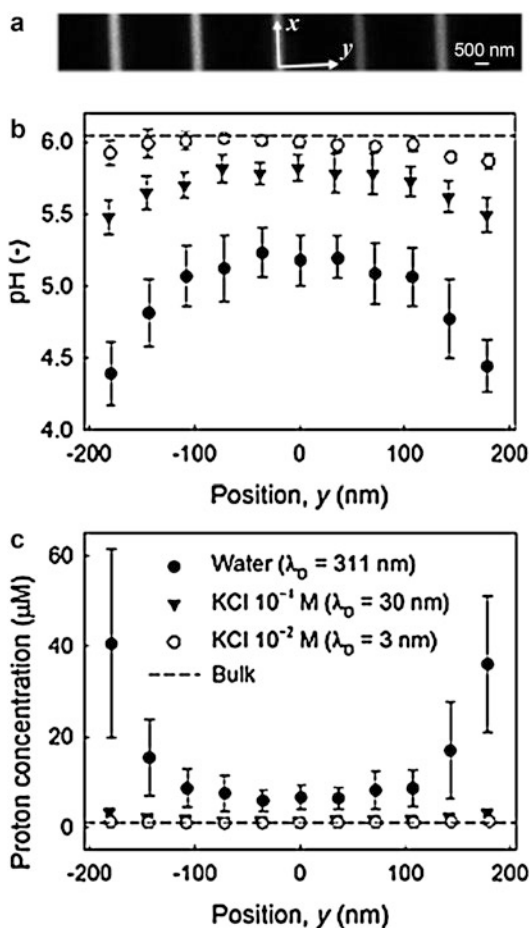
After calibration was measured between the flow velocity and fluorescence intensity, flow velocity profile in a pressure-driven flow was measured. The measured flow velocity profile within the submicrocapillary and comparison with theoretical prediction based on the Hagen-Poiseuille equation is shown in Fig. 4a, where rectangular dots represent the average velocity of the measurement point. The standard deviation error bars are also shown in Fig. 4a. The difference between the experimental data and

theoretical prediction is given in Fig. 4b. The measurement result is an approximation to the parabolic Poiseuille flow profile, which is basically similar to the theoretical prediction. The measured velocity profile in Fig. 4a could indicate that at least the classical Hagen-Poiseuille equation could still be valid when the capillary ID is 360 nm. The velocity can clearly be differentiated within just a 20 nm step, even near the axial region of the subnanocapillary.

Note that the difference between the experimental result and theoretical prediction increases as the measuring points are approaching to the wall of the nanocapillary. This phenomenon could be explained as follows: (1) The total internal reflection phenomenon is partially generated on the nanocapillary because of the mismatch of the refraction index between the fluid and the solid wall. Evanescent wave has an intensity that decays exponentially along the distance normal to the interface [33], causing change in laser intensity at different measuring points. This error could be decreased if the nanochannel is rectangular and if the refraction index of the capillary wall and the fluid is the same. (2) The calibration could also cause error, since the calibration is conducted only on the axis. Such an error could be reduced if time flight [17, 18] is also used for the calibration. (3) In addition, in a nanoscale capillary, the real velocity profile might be different from the prediction of classical theory [54–56].

### Concentration Profile Measurement in a Subnanochannel

Kazoe et al. recently measured the proton concentration profile in a 2-D rectangular subnanochannel, 410 nm in width and 405 nm in depth, using STED fluorescein [46]. Since the detection volume is small, the signal to noise ratio (S/N) is relatively low. In order to increase S/N, two methods have been used. First, since the fluorescent intensity is also affected by the excitation intensity of laser beam and concentration of fluorescent dye and there can be a nonuniform distribution of fluorescein ions within the EDL near the wall because of electrostatic potential in



**Far-Field Nanoscopic Measuring Technique, Fig. 5** (a) Fluorescence image of the 400 nm 2-D nanochannels. Image was obtained from 320 frame averaging. (b) Profiles of the pH and (c) the proton concentration in the 400 nm 2D nanochannel for water, KCl 10<sub>-4</sub>, and 10<sub>-2</sub> mol/L compared to the bulk pH measured in the microchannel (Reproduced from *Analytical Chemistry* with permission of ACS)

the nanochannel, and these two factors can cause significant errors, ratiometric imaging using two excitation wavelengths can be used to reduce the noise to ensure the signal depends only on pH in nanochannels. The ratiometric method takes advantage of the different behaviors of the molar absorption coefficient of a fluorescent dye: its fluorescence is strongly dependent on the pH at excitation of one wavelength, but almost independent at another wavelength of the

excitation light. Hence, two lasers with different wavelengths can be used to excite two different fluorescence signals and their ratio (one is sensitive to pH and the other not) can have higher S/N. (2) Second, averaging multiple images can also reduce random noise to increase S/N. The STED resolution for a cover glass and fused silica plate was claimed to be 66 and 87 nm, respectively.

The concentration was measured by scanning the flow field with the two lasers. Figure 5 is the results of proton concentration profile averaged from five subnanochannel with 320 frames for three different solutions, water, and KCl solution with concentration of 10<sup>-4</sup> and 10<sup>-2</sup> mol/L, respectively. The result shows that the proton concentration is higher near the wall for pure water, but becomes more uniformly distributed with the increase of electrolyte concentration. These results for the proton distribution in the nanochannel suggest that the ions distribute in the channel to cancel the wall charge strongly depending on the Debye length, as expected in the classical theory.

## Future Directions for Research

Far-field optical measuring technique is in its burgeoning stage and could provide new opportunity for nanofluidics in lab-on-a-chip research.

## Cross-References

- ▶ [Fluorescence Measurements](#)
- ▶ [Velocimetry](#)

## References

1. Whitesides GM (2006) The origins and the future of microfluidics. *Nature* 442(7101):368–373
2. Beebe DJ, Mensing GA, Walker GM (2002) Physics and applications of microfluidics in biology. *Annu Rev Biomed Eng* 4(1):261–286
3. Darhuber AA, Troian SM (2005) Principles of microfluidic actuation by modulation of surface stresses. *Annu Rev Fluid Mech* 37(1):425–455

4. Stone HA, Stroock AD, Ajdari A (2004) Engineering flows in small devices. *Annu Rev Fluid Mech* 36(1):381–411
5. Weiss S (2000) Shattering the diffraction limit of light: a revolution in fluorescence microscopy? *Proc Natl Acad Sci* 97:8747–8749
6. Gryczynski Z (2008) FCS imaging—a way to look at cellular processes. *Biophys J* 94:1943–1944
7. Huang B, Bates M, Zhuang X (2009) Super resolution fluorescence microscopy. *Ann Rev Biochem* 78:993–1016
8. Hell SW (2003) Toward fluorescence nanoscopy. *Nat Biotechnol* 21(11):1347–1355
9. Hell SW, Schönle A, Bos A (2007) Nanoscale resolution in far-field fluorescence microscopy. In: *Science of microscopy*. pp 790–834
10. Hell SW (2007) Far-field optical nanoscopy. *Science* 316(5828):1153–1158
11. Gitai Z (2009) New fluorescence microscopy methods for microbiology: sharper, faster, and quantitative. *Curr Opin Microbiol* 12:341–346
12. Santiago JG, Wereley ST, Meinhart CD, Beebe DJ, Adrian RJ (1998) A particle image velocimetry system for microfluidics. *Exp Fluid* 25(4):316–319
13. Hagsater SM, Lenshof A, Skafte-Pedersen P, Kutter JP, Laurell T, Bruus H (2008) Acoustic resonances in straight micro channels: beyond the 1D-approximation. *Lab Chip* 8(7):1178–1184
14. Liu Y, Olsen MG, Fox RO (2009) Turbulence in a microscale planar confined impinging-jets reactor. *Lab Chip* 9(8):1110–1118
15. Lu H-W, Bottausci F, Fowler JD, Bertozzi AL, Meinhart C, Kim C-JC (2008) A study of EWOD-driven droplets by PIV investigation. *Lab Chip* 8(3):456–461
16. Kinoshita H, Kaneda S, Fujii T, Oshima M (2007) Three-dimensional measurement and visualization of internal flow of a moving droplet using confocal micro-PIV. *Lab Chip* 7(3):338–346
17. Pittman JL, Henry CS, Gilman SD (2003) Experimental studies of electroosmotic flow dynamics in microfabricated devices during current monitoring experiments. *Anal Chem* 75(3):361–370
18. Pittman JL, Gilman SD, Schrum KF (2001) On-line monitoring of electroosmotic flow for capillary electrophoretic separations. *Analyst* 126(8):1240–1247
19. Schrum KF, Lancaster JM, Johnston SE, Gilman SD (2000) Monitoring electroosmotic flow by periodic photobleaching of a dilute, neutral fluorophore. *Anal Chem* 72(18):4317–4321
20. Mosier B, Molho J, Santiago J (2002) Photobleached-fluorescence imaging of microflows. *Exp Fluid* 33(4):545–554
21. Moore AW, Jorgenson JW (1993) Study of zone broadening in optically gated high-speed capillary electrophoresis. *Anal Chem* 65(24):3550–3560
22. Flamion B, Bungay PM, Gibson CC, Spring KR (1991) Flow rate measurements in isolated perfused kidney tubules by fluorescence photobleaching recovery. *Biophys J* 60(5):1229–1242
23. Hu H, Koochesfahani MM (2006) Molecular tagging velocimetry and thermometry and its application to the wake of a heated circular cylinder. *Meas Sci Technol* 6:1269
24. Falco RE, Nocera DG (1993) Quantitative multipoint measurements and visualization of dense solid–liquid flows using laser induced photochemical anemometry (LIPA). In: Rocco MC (ed) *Particulate two-phase flow*. Butterworth-Heinemann, London
25. Koochesfahani MM, Nocera DG (2007) Molecular tagging velocimetry. In: Foss J, Tropea C, Yarin A (eds) *Handbook of experimental fluid dynamics*. Springer, Berlin, Chapter 5.4
26. Paul PH, Garguilo MG, Rakestraw DJ (1998) Imaging of pressure- and electrokinetically driven flows through open capillaries. *Anal Chem* 70(13):2459–2467
27. Herr AE, Molho JI, Santiago JG, Mungal MG, Kenny TW, Garguilo MG (2000) Electroosmotic capillary flow with nonuniform zeta potential. *Anal Chem* 72(5):1053–1057
28. Gai H, Li Y, Silber-Li Z, Ma Y, Lin B (2005) Simultaneous measurements of the flow velocities in a microchannel by wide/evanescent field illuminations with particle/single molecules. *Lab Chip* 5(4):443–449
29. Zettner C, Yoda M (2003) Particle velocity field measurements in a near-wall flow using evanescent wave illumination. *Exp Fluid* 34(1):115–121
30. Kihm KD, Banerjee A, Choi CK, Takagi T (2004) Near-wall hindered Brownian diffusion of nanoparticles examined by three-dimensional ratiometric total internal reflection fluorescence microscopy (3-D R-TIRFM). *Exp Fluid* 37(6):811–824
31. Jin S, Huang P, Park J, Yoo JY, Breuer KS (2004) Near-surface velocimetry using evanescent wave illumination. *Exp Fluid* 37(6):825–833
32. Li H, Sadr R, Yoda M (2006) Multilayer nano-particle image velocimetry. *Exp Fluid* 41(2):185–194
33. Duong-Hong D, Wang J-S, Liu G, Chen Y, Han J, Hadjiconstantinou N (2008) Dissipative particle dynamics simulations of electroosmotic flow in nano-fluidic devices. *Microfluid Nanofluid* 4(3):219–225
34. Pouya S, Koochesfahani M, Greytak A, Bawendi M, Nocera D (2008) Experimental evidence of diffusion-induced bias in near-wall velocimetry using quantum dot measurements. *Exp Fluid* 44(6):1035–1038
35. Ross D, Johnson TJ, Locascio LE (2001) Imaging of electroosmotic flow in plastic microchannels. *Anal Chem* 73(11):2509–2515
36. Molho JI, Herr AE, Mosier BP, Santiago JG, Kenny TW, Brennen RA, Gordon GB, Mohammadi B (2001) Optimization of turn geometries for microchip electrophoresis. *Anal Chem* 73(6):1350–1360

37. White J, Stelzer E (1999) Photobleaching GFP reveals protein dynamics inside live cells. *Trends Cell Biol* 9(2):61–65
38. Sugarman J, Prud'homme R (1987) Effect of photobleaching on the output of an on-column laser fluorescence detector. *Ind Eng Chem Res* 26:1449–1454
39. Rička J (1987) Photobleaching velocimetry. *Exp Fluid* 5(6):381–384
40. Wang GR (2005) Laser induced fluorescence photobleaching anemometer for microfluidic devices. *Lab Chip* 5(4):450–456
41. Wang GR, Jiang H (2007) Method and apparatus for fluid velocity measurement based on photobleaching. US patent 7,283,215 B2
42. Wang GR, Sas I, Jiang H, Janzen WP, Hodge CN (2008) Photobleaching-based flow measurement in a commercial capillary electrophoresis chip instrument. *Electrophoresis* 29(6):1253–1263
43. Kuang C, Zhao W, Yang F, Wang G (2009) Measuring flow velocity distribution in microchannels using molecular tracers. *Microfluid Nanofluid* 7(4):509–517
44. Piorek B, Mechler A, Lal R, Freudenthal P, Meinhard C, Banerjee S (2006) Nanoscale resolution microchannel flow velocimetry by atomic force microscopy. *Appl Phys Lett* 89(15):153123
45. Kuang C, Wang G (2010) A far-field nanoscopic velocimeter for nanofluidics. *Lab Chip* 10:240–245
46. Kazoe Y, Mawatari K, Sugii Y, Kitamori T (2011) Development of a measurement technique for ion distribution in an extended nanochannel by super-resolution-laser-induced fluorescence. *Anal Chem* 83(21):8152–8157
47. Hell S, Wichmann J (1994) Breaking the diffraction resolution limit by stimulated emission: stimulated-emission-depletion fluorescence microscopy. *Opt Lett* 19(11):780
48. Donnert G, Keller J, Medda R, Andrei MA, Rizzoli SO, Lüthmann R, Jahn R, Eggeling C, Hell SW (2006) Macromolecular-scale resolution in biological fluorescence microscopy. *Proc Natl Acad Sci* 103(31):11440–11445
49. Han KY, Willig KI, Rittweger E, Jelezko F, Eggeling C, Hell SW (2009) Three-dimensional stimulated emission depletion microscopy of nitrogen-vacancy centers in diamond using continuous-wave light. *Nano Lett* 9(9):3323–3329
50. Rittweger E, Rankin BR, Westphal V, Hell SW (2007) Fluorescence depletion mechanisms in super-resolving STED microscopy. *Chem Phys Lett* 442(4–6):483–487
51. Rittweger E, Han KY, Irvine SE, Eggeling C, Hell SW (2009) STED microscopy reveals crystal colour centres with nanometric resolution. *Nat Photon* 3(3):144–147
52. Kuang C, Wang GR (2009) Ultrafast measurement of transient electrokinetic flow in microfluidics. Ultrafast Measurement of Transient Electrokinetic Flow in Microfluidics (In preparation)
53. Cuenca A, Bodiguel H (2012) Fluorescence photobleaching to evaluate flow velocity and hydrodynamic dispersion in nanoslits. *Lab Chip* 12(9):1672–1679
54. Tamaki E, Hibara A, Kim H-B, Tokeshi M, Kitamori T (2006) Pressure-driven flow control system for nanofluidic chemical process. *J Chromatogr A* 1137(2):256–262
55. Tas NR, Haneveld J, Jansen HV, Elwenspoek M, van den Berg A (2004) Capillary filling speed of water in nanochannels. *Appl Phys Lett* 85(15):3274–3276
56. Ralston J, Popescu M, Sedev R (2008) Dynamics of wetting from an experimental point of view. *Annu Rev Mater Res* 38(1):23–43

---

## Feedback

### Definition

The cycle of observing a dynamic system (sensing), making a decision (control computation), implementing that decision by actuators (actuation), and then observing the new dynamics at the next time instant. This cycle of sensing → computation → actuation is what is meant by the term feedback. Feedback is routinely used in complex systems ranging from electronic systems to airplanes, cars, and chemical plants and is ubiquitous in biological systems (living cells use feedback to control all aspects of their operation).

### Cross-References

- [Control of Micro-fluidics](#)

---

## Ferroelectric

### Definition

The characteristic of an insulating material that exhibits noncentrosymmetric crystal organization. In the strictest sense, a distinct characteristic of ferroelectric materials is the presence of hysteresis. All ferroelectric materials are both piezoelectric and pyroelectric. PZT is a common ferroelectric material.

## Cross-References

- ▶ [Electrostrictive](#)
- ▶ [Hysteresis](#)
- ▶ [Pyroelectric Flow Sensors](#)
- ▶ [Pyroelectricity](#)
- ▶ [Spontaneous Polarization](#)

## Ferrofluids in Microchannels

Nam-Trung Nguyen

Queensland Micro- and Nanotechnology Centre,  
Griffith University, Brisbane, QLD, Australia

### Synonyms

Dispersed magnetic nanoparticles; Liquid magnet; Magnetic fluid

### Definition

A ferrofluid is a liquid consisting of ferromagnetic nanoparticles suspended in a nonmagnetic carrier fluid, typically water or oil. The ferromagnetic nanoparticles are coated with a surfactant such as oleic acid to prevent their agglomeration. The magnetic particles have typical diameters on the order of 5–15 nm and a volume fraction of about 5–10 %.

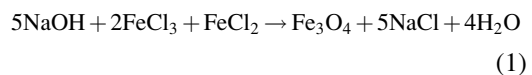
### Chemical and Physical Principles

Although certain pure substances such as liquid oxygen also behave as magnetic liquids, ferrofluids are commonly understood as colloidal ferrofluids (Fig. 1). The fluid is composed of a carrier fluid and ferromagnetic nanoparticles, usually magnetite, hematite, or some other compound containing iron in the 2+ or 3+ state. These nanoparticles are solid, single-domain magnetic particles. The particles are coated with a monolayer of surfactant molecules to prevent them sticking to each other.

Because these particles are so small, Brownian motion is able to disperse them homogeneously in the carrier fluid. The dispersion is sufficiently strong that the solid particles do not agglomerate or separate even under strong magnetic fields. A typical ferrofluid is opaque to visible light. It should be noted that the term *magnetorheological fluid* (MRF) refers to liquids similar in structure to ferrofluids but different in behavior. The particle sizes of MRFs are on the order of micrometers and are one to three orders of magnitude larger than those of ferrofluids. MRFs also have a higher volume fraction of particles, on the order of 20–40 %. Exposing an MRF to a magnetic field can transform it from a light viscous fluid into a thick solid-like material.

The ferromagnetic nanoparticles can be fabricated using size reduction through ball milling, chemical precipitation, or thermophilic iron-reducing bacteria. In ball milling, a magnetic material with a particle size of several micrometers such as magnetite powder is mixed with the carrier liquid and the surfactant. The ball-milling process takes approximately 1,000 h. Subsequently, the product mixture undergoes centrifuge separation to filter out oversized particles. The purified mixture can be concentrated or diluted to obtain the final ferrofluid.

Synthesis by chemical precipitation is a more common approach, in which the particles precipitate out of solution during chemical processes. A typical reaction for magnetite precipitation is

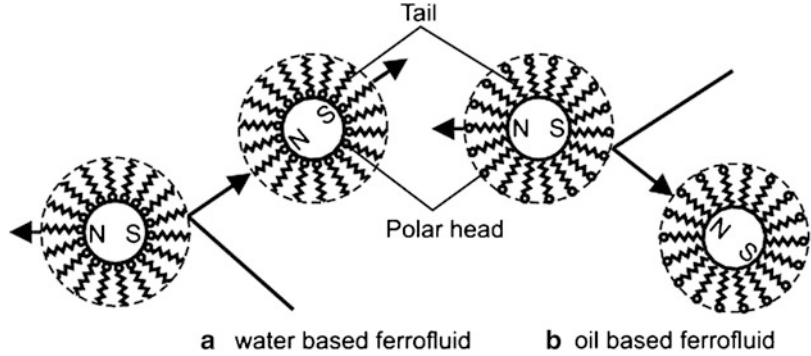


The reaction product is subsequently coprecipitated with concentrated ammonium hydroxide. Next, a peptization process transfers the particles from the water-based phase to an organic phase such as kerosene with a surfactant such as oleic acid. The oil-based ferrofluid can then be separated by use of a magnetic field.

Another approach to the fabrication of ferrofluids is based upon thermophilic bacteria

**Ferrofluids in Microchannels,**

**Fig. 1** Colloidal model of magnetic nanoparticles and schematic representation of an elastic collision between particles: (a) water-based ferrofluid, (b) oil-based ferrofluid



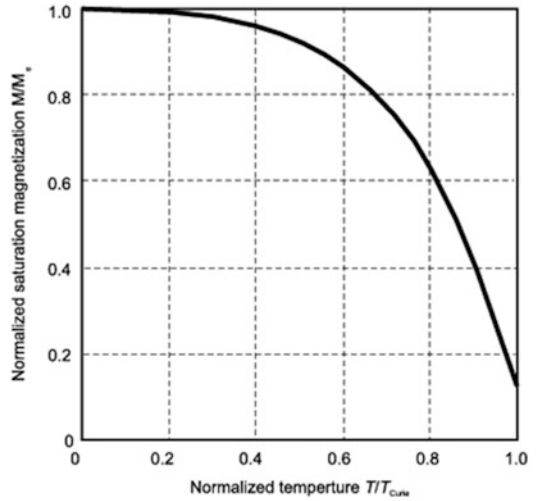
that reduce amorphous iron oxyhydroxides to nanometer-sized iron oxide particles. Thermophilic bacteria are able to reduce a number of different metal ions. Thus, this approach allows other compounds, such as Mn(II), Co(II), Ni(III), and Cr(III) compounds, to be incorporated into magnetite. Varying the composition of the nanoparticles can adjust the magnetic, electrical, and physical properties of the substituted magnetite and, consequently, of the ferrofluid. Ferromagnetic particles with an extremely low Curie temperature can be designed with this method. For instance,  $Mn_xFe_{1-x}Fe_2O_4$  nanoparticles may have Curie temperatures between 75 °C and 325 °C. Most of the particle materials commonly used in ferrofluids have much higher Curie temperatures. The temperature dependence of the magnetic properties depicted in Fig. 2 can be used in microfluidic applications.

**Key Research Findings**

At the typical channel size of microfluidics (about 100 μm), ferrofluid flow in a microchannel can be described as a continuum flow. The governing equations are based on conservation of mass and conservation of momentum. In case of temperature-dependent magnetic properties, conservation of energy may be needed for calculating the temperature field.

The continuity equation has the general form

$$\frac{D\rho}{Dt} + \delta \text{div} \nabla = 0, \tag{2}$$



**Ferrofluids in Microchannels, Fig. 2** Temperature dependence of magnetization

where  $\nabla$  is the nabla operator and  $D\rho/Dt$  is the substantial (or total) derivative operator:

$$\begin{aligned} \frac{D}{Dt} &= \frac{\partial}{\partial t} + u \frac{\partial}{\partial x} + v \frac{\partial}{\partial y} + w \frac{\partial}{\partial z} \\ &= \frac{\partial}{\partial t} + (\mathbf{v} \cdot \nabla). \end{aligned} \tag{3}$$

Newton’s second law formulates the conservation of momentum:

$$\begin{aligned} \rho \frac{D\mathbf{v}}{Dt} &= \sum \mathbf{f}_i = \mathbf{f}_{\text{pressure}} + \mathbf{f}_{\text{viscous}} + \mathbf{f}_{\text{gravity}} + \mathbf{f}_{\text{magnetic}} \\ \rho \frac{D\mathbf{v}}{Dt} &= -\nabla p + \eta \nabla^2 \mathbf{v} + \rho \mathbf{g} + \mathbf{f}_{\text{magnetic}}. \end{aligned} \tag{4}$$

Compared with a nonmagnetic fluid, the Navier–Stokes equation (4) for ferrofluid flow in a microchannel has an additional term for the magnetic force [1]:

$$\mathbf{f}_{\text{magnetic}} = -\nabla \left[ \mu_0 \int_0^H \left( \frac{\partial Mv}{\partial v} \right)_{H,T} dH \right] + \mu_0 M \nabla H \quad (5)$$

where  $\mu_0 = 4\pi \times 10^{-7} \text{ H m}^{-1}$  is the permeability of free space,  $M$  is the intensity of magnetization,  $v$  is the specific volume, and  $H$  is the magnetic field strength in A/m. The magnetic pressure can be grouped together with the static pressure to form an apparent pressure. Thus, the conservation of momentum can be reduced to the conventional Navier–Stokes equation. Since the magnetic force is a body force, the flow of a ferrofluid in a microchannel should have the same velocity distribution as a pressure-driven flow. The first term in Eq. 5 shows that the magnetic force is a body force, which is proportional to the volume. According to the scaling law, or the so-called cube-square law, the magnetic force will be dominated by the viscous force on the microscale. However, the second term in Eq. 5 may have advantages on the microscale owing to the high magnetic-field gradient  $\nabla H$  that is achievable with integrated microcoils. As mentioned above, ferrofluids with a low Curie temperature are readily available. Using the temperature dependence of the magnetization shown in Fig. 2, the magnetization can be adjusted by varying the temperature from room temperature to an acceptably low Curie temperature. The temperature dependence of the magnetization can be implemented in the first term of Eq. 5; the magnetic force then has the form [2]

$$\mathbf{f}_{\text{magnetic}} = \frac{1}{2} \mu_0 \left( H \frac{\partial M}{\partial T} \right) \nabla T + \mu_0 M \nabla H. \quad (6)$$

It is clear from Eq. 6 that the high temperature gradient  $\nabla T$  that can be achieved on the microscale can be another advantage when one wishes to drive a ferrofluid in a microchannel.

## Examples of Applications

The following examples present the utilization of the high magnetic gradient and temperature gradient on the microscale for pumping ferrofluids.

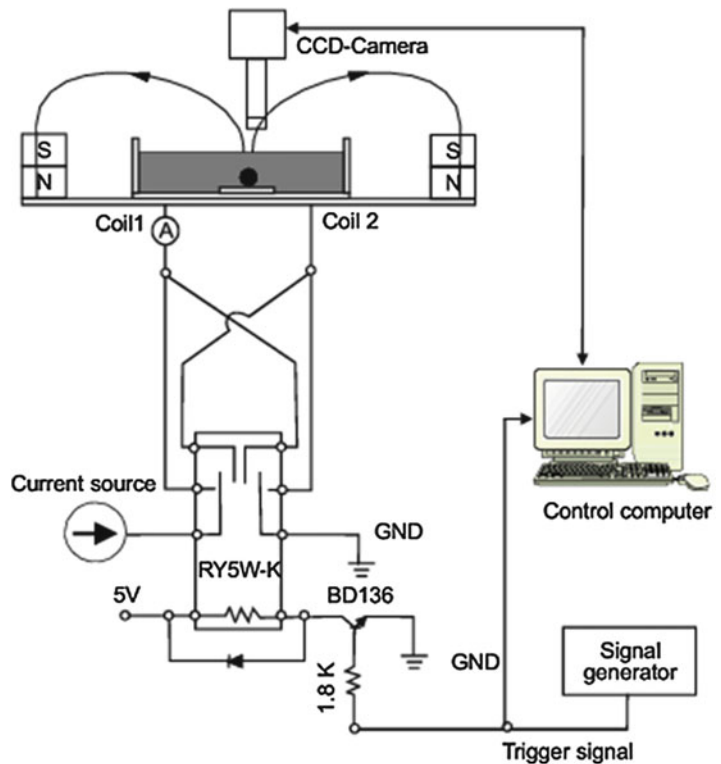
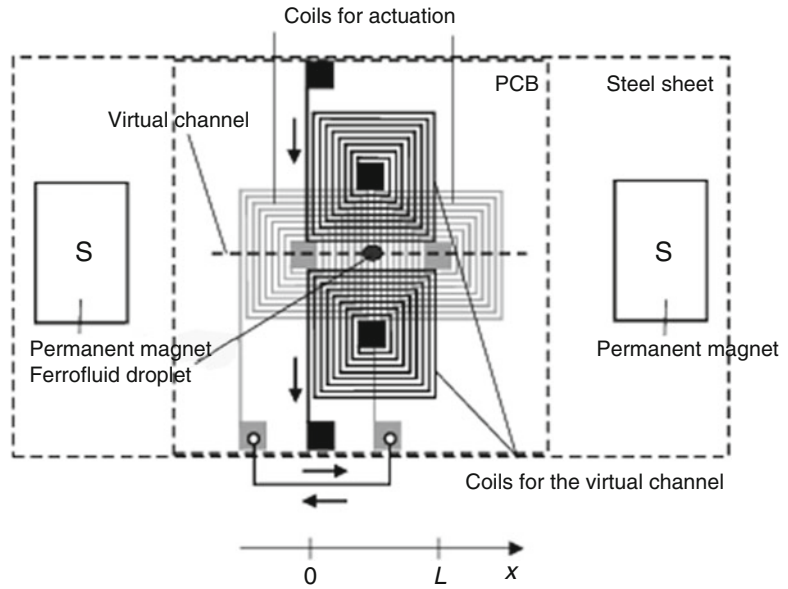
### Manipulation of Ferrofluid Microdroplets

The magnetic force is proportional to both the magnetic moment and the gradient of the magnetic field. At a constant temperature below the Curie point, the magnetic moment is proportional to the volume. The disadvantage of volume-based actuation on the microscale can be compensated by the high magnetic-field gradient achievable with microcoils. Since the magnetic nanoparticles in a ferrofluid have a diameter on the order of a few nanometers, the random movement of the particles is larger than the effects of magnetic and gravitational forces. Thus, the dispersion of these particles is stable even under a strong magnetic field. Nanoparticles polarized by an external magnetic field cause a ferrofluid droplet to act as a liquid magnet. This unique feature allows a ferrofluid droplet to be controlled by an external magnetic field. A controlled ferrofluid microdroplet can potentially be used as a reaction platform for handling samples in Lab-on-a-Chip applications.

Figure 3 shows the basic setup for controlling a ferrofluid microdroplet [3]. The main part of the setup is a double-sided printed circuit board (PCB). Two planar coils are etched on each side of the PCB, as depicted. The black and gray lines represent coils on the front and the back, respectively, of the PCB. Two permanent magnets (NdFeB) are placed on a soft magnetic steel sheet, which carries the PCB device. The permanent magnets induce a large uniform magnetic field perpendicular to the direction of motion  $x$  of the ferrofluid droplet and consequently polarize the magnetic particles in the ferrofluid. The fields generated by the two front coils (black in Fig. 3) are permanent and have the same sign. These fields form a potential valley between the coils, where the gradient in the  $y$ -direction is zero. Thus, these fields work as a *virtual channel* for the ferrofluid droplet. The ferrofluid droplet is

### Ferrofluids in Microchannels,

**Fig. 3** Experimental setup for controlling ferrofluid droplets. The coils are etched on a double-sided printed circuit board. The gray coils are on the back of the PCB. The PCB is placed on a soft magnetic steel sheet with two permanent magnets at either side. The magnetic field of the two permanent magnets polarizes the magnetic particles in the ferrofluid droplet



### Ferrofluids in Microchannels,

**Fig. 4** Switching circuit and optical setup

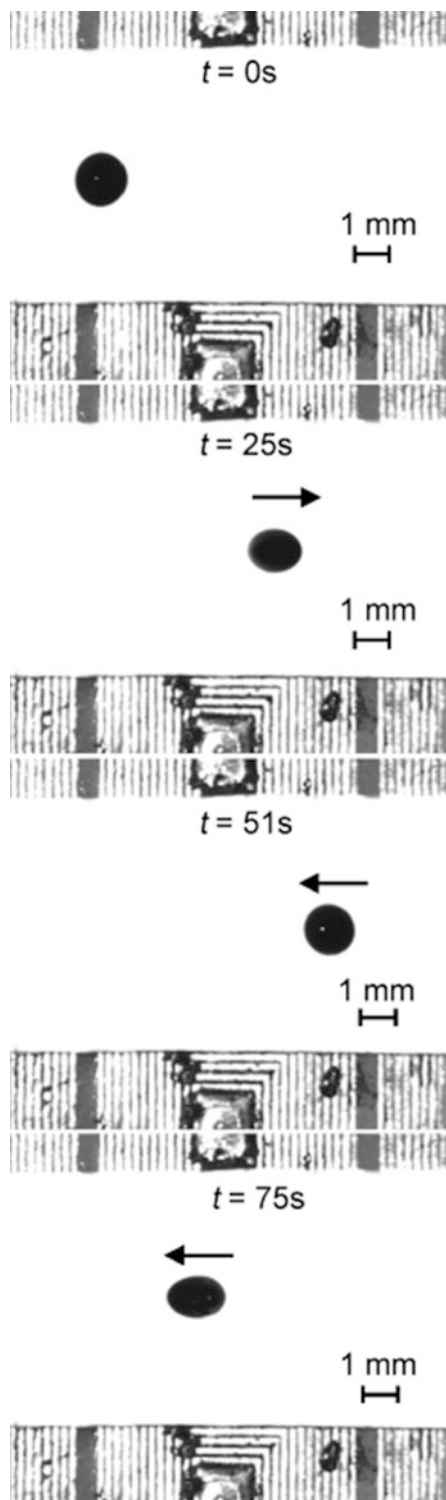
confined in this *virtual channel* and can move only in the  $x$ -direction. This *virtual channel* can be replaced by a real microchannel in the  $x$ -direction. In this case, only two driving coils

are needed. The two coils on the back of the PCB are connected in series, so that their fields always have opposite signs. The field gradients between the two coils have the same sign, allowing the

droplet to move in a prescribed direction. The direction of motion can be changed if the current in the coils is reversed. The switching circuit for changing the current direction is shown in Fig. 4.

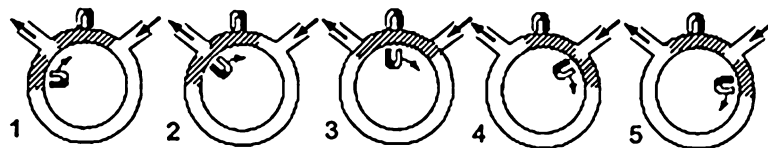
The carrier liquid of the ferrofluid used in the experiment (APG S10n, Ferrotec) was a synthetic ester oil which was immiscible in silicone oil. The viscosity  $\eta$ , density  $\rho$ , and surface tension  $\sigma$  of the ferrofluid at 25 °C were 0.406 kg/ms, 1,330 kg/s, and  $32 \times 10^{-3}$  N/m, respectively. The saturation magnetization and the initial susceptibility  $\chi$  of this ferrofluid were 44 mT and 1.6, respectively. Two silicone oils with different viscosities were used to investigate the effect of viscous friction:  $[-\text{Si}(\text{CH}_3)_2\text{O}-]_n$ , with a kinematic viscosity of  $\nu = 50$  cSt, and  $[-\text{C}_7\text{H}_8\text{OSi}-]$ , with a kinematic viscosity of 100 cSt. Both oils had approximately the same surface tension of  $2.03 \times 10^{-7}$  N/m and a density of  $960 \text{ kg/m}^3$ . In the experiments, the ferrofluid droplet was surrounded by the silicone oil. The higher density of the ferrofluid ensured that the droplet remained on the bottom surface of a 0.5 mm-thick Teflon sheet. The hydrophobic surface of the Teflon sheet allowed the droplet to keep its spherical shape. The two virtual-channel coils were supplied with a constant current of 750 mA. The direction of the current in the driving coils was switched using the control circuit shown in Fig. 4. The periodic motion of the ferrofluid droplet was captured with a CCD camera. The camera was synchronized with the switching signal to record the position of the droplet at given time instants. Figure 5 shows an example of a recorded image sequence from this experiment. It is apparent that the droplet elongates under the induced magnetic force. Since the driving magnetic force is a body force, a larger droplet will have a better volume-to-surface ratio or a larger ratio between the magnetic force and the drag force. A larger droplet can accelerate faster and reach its final position in a shorter time.

This actuation concept can be used for transport and sorting applications in droplet-based microfluidics. The results show the potential use of ferrofluid droplets as both a vehicle and a microreaction platform for droplet-based Lab-on-a-Chip applications.

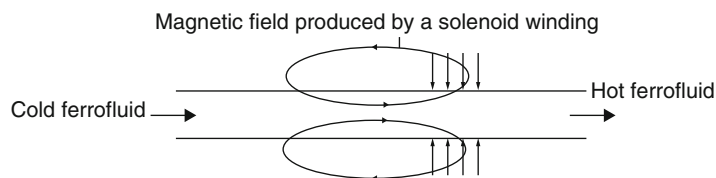


**Ferrofluids in Microchannels, Fig. 5** Recorded motion of a ferrofluid microdroplet

**Ferrofluids in Microchannels,**  
**Fig. 6** Concept of a ferrofluidic micropump



**Ferrofluids in Microchannels,**  
**Fig. 7** Concept of magnetocaloric pumping



### Ferrofluid as an Actuator

The above example shows that a ferrofluid droplet or plug in a microchannel can function as an actuator. The actuating force is induced by an external magnetic field. The external magnetic field can be generated either by a microcoil, as demonstrated in the previous example, or by a moving magnet. In this concept, a ferrofluid plug is suspended in the channel. An external permanent magnet controls the position of the ferrofluid plug. Moving the permanent magnet pushes the ferrofluid plug in the desired direction. While moving in the microchannel, the ferrofluid plug pushes the surrounding liquid on one side and pulls it on the other side. The effect causes a pumping effect. If the magnet stops, the magnetic field holds the plug at its current location and prevents the pumped liquid from moving back. This sealing property means that a ferrofluid plug can also work as an active valve. The pumping power depends on the gradient of the external magnetic field and the magnetization of the ferrofluid. The field strength can be adjusted by the external permanent magnet, and so the pump design becomes independent of the type of liquid pumped.

Magnetic pumping using a ferrofluid has been implemented on a microscale by Hatch et al. [4]. The pump was fabricated in silicon and glass. The channel structure was etched in silicon and bonded anodically to a borosilicate glass plate. Two permanent magnets were used, as a valve actuator and a plug actuator. The working principle of this rotary concept is explained in Fig. 6. A fixed permanent magnet creates a stationary ferrofluid plug between the inlet and the outlet (1).

First, a moving permanent magnet merges a second plug with the stationary plug (2). After complete merging has occurred, the large plug blocks both the inlet and the outlet (3). When the large plug is separated into one stationary and one moving plug, the fluid is sucked into the inlet and pushed out of the outlet (4). The design of the pump is similar to the concepts of a rotary pump and a check valve pump. However, this design is a pure magnetic micropump because no mechanical moving parts are involved. This micropump is able to deliver a maximum flow rate of 70 mL/min and a maximum back pressure of 1.3 kPa.

### Continuous Pumping of Ferrofluid in a Microchannel Using a Temperature Gradient

According to Eq. 6, a temperature gradient can cause a magnetic force. This actuation concept has been termed magnetocaloric pumping by Love et al. [2]. Figure 7 shows a simple configuration for this. A magnetic field is induced by a coil or a permanent magnet. A temperature gradient along the flow direction causes a gradient in the magnetization, which in turn results in a net force that pumps the ferrofluid. The relationship between magnetization and temperature shown in Fig. 2 indicates that the closer the heating temperature is to the Curie temperature of the magnetic nanoparticles, the larger the force and the higher the flow rate. The ideal particle would have a Curie temperature close to the maximum expected thermal-cycling temperature. Table 1 lists the Curie temperatures of a number of ferrous materials. Most commercial-grade ferrofluids are based

**Ferrofluids in Microchannels, Table 1** Curie temperature and saturation magnetization of various ferromagnetic solids

Substance	Curie temperature (°C)	$\mu_0 M_s$ (T)
Cobalt	1,120	1.82
Dysprosium	-185	3.67
Gadolinium	19	2.59
Iron	770	2.18
Magnetite	585	0.56
Nickel	358	0.64

on magnetite particles and have a relatively high Curie temperature of 585 °C. Thus, almost all liquids will evaporate before this pumping concept works. The solution to this problem is the use of magnetic materials with Curie temperatures below the boiling point or any other critical temperature of the liquids used in the microfluidic system.

## Cross-References

- ▶ [Digital Microfluidics](#)
- ▶ [Magnetic Pumps](#)
- ▶ [Temperature Gradient Generation and Control](#)

## References

1. Rosenzweig RE (1985) Ferrohydrodynamics. Cambridge University Press, Cambridge
2. Love LJ, Jansen JF, McKnight TE, Roh Y, Phelps TJ (2004) A magnetocaloric pump for microfluidic applications. *IEEE Trans Nanobiosci* 3:101–110
3. Nguyen NT, Ng KM, Huang XY (2006) Manipulation of ferrofluid droplets using planar coils. *Appl Phys Lett* 89:052509
4. Hatch A, Kamholz AE, Holman G, Yager P, Böhringer KF (2001) A ferrofluidic magnetic micropump. *J Microelectromech Syst* 10:215–221

## Fiber-Optic Cables

### Definition

Fiber-optic cables are flexible tubes that allow user-friendly transportation of light; thus, positioning and handling of a light beam or spot is

possible without using a complex system of mirrors and lenses. Fiber-optic cables consist of a bundle of tiny glass fibers or they are filled with a transparent liquid. A clever exploitation of total reflectance and interference at the inner surface of the fiber leads to lossless channeling of the light.

## Field of View (FOV)

### Definition

FOV describes the extent of an image which is captured with the camera. The bigger the magnification of the optics, the smaller is the field of view.

## Finite Volume and Finite Difference Methods for Modeling and Simulation

Suman Chakraborty

Department of Mechanical Engineering, Indian Institute of Technology Kharagpur, Kharagpur, India

### Synonyms

Computational fluid dynamics (CFD); Control volume method; Control volume-based finite difference method

### Definition

The present entry briefly discusses two of the basic discretization techniques commonly used for computational fluid dynamics (CFD) analysis of systems involving fluid flow, heat transfer, and associated phenomena such as chemical reactions. These mathematical tools, however, are generalized enough to address other transport processes occurring in electrical, magnetic, or electromagnetic systems as well.

## Overview

In order to simulate fluid flow, heat transfer, and other related physical phenomena over various length scales, it is necessary to describe the associated physics in mathematical terms. Nearly all the physical phenomena of interest to the fluid dynamics research community are governed by the principles of continuum conservation and are expressed in terms of first- or second-order partial differential equations that mathematically represent these principles (within the restrictions of a continuum-based framework). However, in case the requirements of continuum hypothesis are violated altogether for certain physical problems (for instance, in case of high Knudsen number rarefied gas flows), alternative formulations in terms of the particle-based statistical tools or the atomistic simulation techniques need to be resorted to. In this entry, we shall only focus our attention to situations in which the governing differential equations physically originate out of continuum conservation requirements and can be expressed in the form of a general differential equation that incorporates the unsteady term, the advection term, the diffusion term, and the source term to be elucidated as follows.

A generic form of the general conservation principle for any dependent variable,  $\phi$ , can be expressed as

$$\underbrace{\frac{\partial}{\partial t}(\rho\phi)}_{\text{transient term}} + \underbrace{\nabla \cdot (\rho\mathbf{V}\phi)}_{\text{advection term}} = \underbrace{\nabla \cdot (\Gamma\nabla\phi)}_{\text{diffusion term}} + \underbrace{S}_{\text{source term}}. \quad (1)$$

The well-known equations of mass, momentum, and energy conservation can all be cast in the above general form, with the expressions for  $\phi$ ,  $\Gamma$  (general diffusion coefficient), and  $S$  (general source term) being the sole distinctive features of one equation from another. This issue is summarized in Table 1, for convenience. In Table 1,  $\mu$  denotes the viscosity,  $p$  denotes the pressure,  $\mathbf{F}$  denotes the body force per unit volume,  $T$  denotes the temperature,  $k$  denotes the

**Finite Volume and Finite Difference Methods for Modeling and Simulation, Table 1** Conservation equations in the general form

Equation	$\Phi$	$\Gamma$	$S$
Continuity	1	0	0
Momentum	$\mathbf{V}$	$\mu$	$-\nabla p + \mathbf{F}$
Energy	$T$	$k/c_p$	$\dot{Q}/C_p$

thermal conductivity,  $c_p$  denotes the specific heat, and  $\dot{Q}$  denotes the rate of heat generation per unit volume.

In many situations, the complicated and/or coupled nature of the governing differential equations makes it difficult, if not impossible, to solve them analytically. Keeping that in view, it has always been a challenging task to the research community to develop efficient numerical techniques for solving the general transport equations. Fundamental to the development of a numerical method for solving these differential equations is the idea of discretization. Although an analytical solution to a partial differential equation gives us the value of the variable  $\phi$  as a continuous function (in the absence of any continuum-level discontinuities in the problem domain) of the independent variables (viz., the spatial and temporal variables), the numerical solution aims to provide us with values of  $\phi$  at a *discrete* number of points in the domain. These points are typically called as *grid points* or, equivalently, as the *nodes* or the *cell centroids*, depending on the specific numerical method being employed. The process of converting the governing transport equation into a set of equations for the discrete values of  $\phi$  is called the *discretization process* and happens to be one of the key aspects of the numerical solution strategy. The specific methods employed to bring about this conversion are called as the *discretization methods*. The finite difference and the finite volume methods are two of the common discretization methods often employed for fluid flow analysis and will be briefly discussed here. The other commonly used methods, such as the finite element method, the boundary element method, the meshless method, etc., fall beyond the scope of this article and will not be discussed here. It, however, needs to be kept in mind that all

these discretization methods share one common philosophy: their only goal is to convert the governing differential equation into a system of discretized algebraic equations (the number of algebraic equations being same as the number of scalar unknowns considering the discrete grid points (or the nodal points) at which these variables are to be solved). It is the methodology and philosophy of this discretization technique in which one numerical method differs from the other.

### Basic Methodology

#### Finite Difference Method

The finite difference methods approximate the derivatives in the governing differential equation using the truncated Taylor series expansions, for the purpose of discretization [1]. The starting point of formulating a finite difference scheme is to discretize the domain into a number of grid points and to express the derivatives at those grid points in terms of the nodal values of the function itself. The grid points can be numbered by a number of free indices (depending on the dimensionality of the problem), provided that the grid system is a structured one. For illustration, let us express the value of a variable in the vicinity of the grid point  $i$ , in the form of Taylor series, as

$$\begin{aligned} \phi(x) = & \phi(x_i) + (x - x_i) \left( \frac{\partial \phi}{\partial x} \right)_i \\ & + \frac{(x - x_i)^2}{2!} \left( \frac{\partial^2 \phi}{\partial x^2} \right)_i \\ & + \frac{(x - x_i)^3}{3!} \left( \frac{\partial^3 \phi}{\partial x^3} \right)_i \\ & + \dots \\ & + \frac{(x - x_i)^n}{n!} \left( \frac{\partial^n \phi}{\partial x^n} \right)_i + H \end{aligned} \tag{2}$$

where  $H$  means the *higher-order terms*. By replacing  $x$  by  $x_{i+1}$  or  $x_{i-1}$  in Eq. 1, one may obtain the expressions for the values of the variable  $\phi$  at these points, in terms of the values and derivatives at the point  $x_i$ . Executing this exercise, the first-order derivative at the point  $x_i$  can

be written in any of the following ways (Eqs. 3a, 3b, or 3c):

$$\begin{aligned} \left( \frac{\partial \phi}{\partial x} \right)_i = & \frac{\phi_{i+1} - \phi_i}{x_{i+1} - x_i} - \frac{x_{i+1} - x_i}{2} \left( \frac{\partial^2 \phi}{\partial x^2} \right)_i \\ & - \frac{(x_{i+1} - x_i)^2}{6} \left( \frac{\partial^3 \phi}{\partial x^3} \right)_i + H \end{aligned} \tag{3a}$$

where  $\phi_i \equiv \phi(x - x_i)$ .

$$\begin{aligned} \left( \frac{\partial \phi}{\partial x} \right)_i = & \frac{\phi_i - \phi_{i-1}}{x_i - x_{i-1}} - \frac{x_i - x_{i-1}}{2} \left( \frac{\partial^2 \phi}{\partial x^2} \right)_i \\ & - \frac{(x_i - x_{i-1})^2}{6} \left( \frac{\partial^3 \phi}{\partial x^3} \right)_i + H \end{aligned} \tag{3b}$$

$$\begin{aligned} \left( \frac{\partial \phi}{\partial x} \right)_i = & \frac{\phi_{i+1} - \phi_{i-1}}{x_{i+1} - x_{i-1}} \\ & - \frac{(x_{i+1} - x_i)^2 - (x_i - x_{i-1})^2}{2(x_{i+1} - x_{i-1})} \left( \frac{\partial^2 \phi}{\partial x^2} \right)_i \\ & - \frac{(x_{i+1} - x_i)^3 + (x_i - x_{i-1})^3}{6(x_{i+1} - x_{i-1})} \left( \frac{\partial^3 \phi}{\partial x^3} \right)_i + H \end{aligned} \tag{3c}$$

All three of the above expressions are exact if all terms in the right-hand side are retained. However, the terms involving the higher derivatives can be neglected in case the distance between the successive grid points is small enough, except for the typical situations in which the magnitudes of the higher-order derivatives are locally very large. The truncation of the Taylor series up to the first term in the right-hand side of Eqs. 3a, 3b, and 3c leads to the following approximations of the first-order derivative:

$$\left( \frac{\partial \phi}{\partial x} \right)_i \approx \frac{\phi_{i+1} - \phi_i}{x_{i+1} - x_i} \tag{4a}$$

$$\left( \frac{\partial \phi}{\partial x} \right)_i \approx \frac{\phi_i - \phi_{i-1}}{x_i - x_{i-1}} \tag{4b}$$

$$\left( \frac{\partial \phi}{\partial x} \right)_i \approx \frac{\phi_{i+1} - \phi_{i-1}}{x_{i+1} - x_{i-1}} \tag{4c}$$

Expressions 4a, 4b, and 4c correspond to the so-called forward difference scheme, backward

difference scheme, and central difference scheme, respectively. The error incurred in truncating the infinite Taylor series up to a finite number of terms for the calculation of the derivatives is known as the *truncation error*. Since the higher-order terms are expected to be smaller (as they vary with higher powers of the small grid spacing), the first truncated term is usually the principal source of truncation error. The order of the truncation error, therefore, is usually estimated by the order of this term. For an equally spaced grid arrangement (such that  $x_{i+1} - x_i = x_i - x_{i-1} = \Delta x$  (say)), the forward difference and the backward difference schemes for evaluating the first-order derivatives are  $O(\Delta x)$ , whereas the central difference scheme for the same is  $O(\Delta x^2)$ . It is, however, possible to derive higher-order versions of these schemes, by using higher-order polynomial interpolations as approximations for evaluating the functional derivatives, instead of going through the direct route of Taylor series approximations.

Analogous to the first derivative, the second-order derivatives can also be approximated by going through the route of Taylor series expansions. For example, one can approximate the second-order derivative in terms of a central difference of the first-order derivatives as

$$\left(\frac{\partial^2 \phi}{\partial x^2}\right)_i \approx \frac{\left(\frac{\partial \phi}{\partial x}\right)_{i+1} - \left(\frac{\partial \phi}{\partial x}\right)_i}{x_{i+1} - x_i} \tag{5}$$

Good choices of points for evaluation of the first-order derivatives appearing in the above expression may be the points that are located midway between  $x_i$  and  $x_{i+1}$  and  $x_{i-1}$  and  $x_i$ . Central difference approximations for these derivatives are as follows:

$$\begin{aligned} \left(\frac{\partial \phi}{\partial x}\right)_{i+\frac{1}{2}} &\approx \frac{\phi_{i+1} - \phi_i}{x_{i+1} - x_i}, & \left(\frac{\partial \phi}{\partial x}\right)_{i-\frac{1}{2}} \\ &\approx \frac{\phi_i - \phi_{i-1}}{x_i - x_{i-1}} \end{aligned} \tag{6}$$

The above leads to a simplified expression of Eq. 5, for equidistant grid spacings, as

$$\left(\frac{\partial^2 \phi}{\partial x^2}\right)_i \approx \frac{\phi_{i+1} - 2\phi_i + \phi_{i-1}}{(\Delta x)^2} \tag{7}$$

Equation 7 is a well-known expression for a second-order accurate estimation of the second-order derivatives using the central difference scheme.

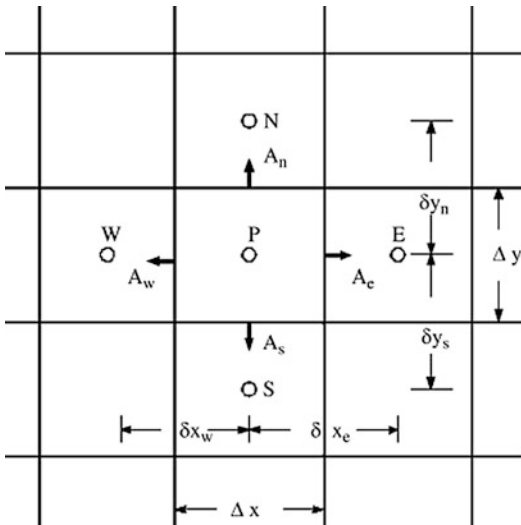
One of the disadvantages associated with the finite difference method is that the physical principle of conservation is not automatically enforced in the scheme, unless special care is taken. Moreover, the implementation of this method is often restricted to simple geometries, since this method cannot be implemented with convenience on unstructured grids.

### Finite Volume Method

The starting point of the finite volume method is the integral form of the governing conservation equations [2]. This is achieved by first subdividing the problem domain into a number of contiguous control volumes of finite dimensions and then integrating the governing differential equation over each of these elemental control volumes. The representative value of the variable to be solved for each control volume may be taken as the value of the variable at the geometric center of the control volume. For evaluating the integrals, suitable profile assumptions for the dependent variable can be taken (giving rise to approximating quadrature formulae for the surface and the volume integrals), without violating the constraints of physical consistency and overall balance. However, once the integrals have been evaluated, the history of the profile assumption is essentially lost. This gives the analyst a freedom to adopt different profile assumptions for the same variables appearing in different terms of a governing equation. Integrations with respect to time can be carried out with the following linear interpolation formula:

$$\int_t^{t+\Delta t} \phi dt = [f\phi^{t+\Delta t} + (1-f)\phi^t] \Delta t, \quad 0 \leq f \leq 1 \tag{8}$$

The special cases of  $f = 0$ ,  $f = 0.5$ , and  $f = 1$  give rise to the *explicit scheme*, the



**Finite Volume and Finite Difference Methods for Modeling and Simulation, Fig. 1** A generic finite volume discretization stencil in two dimensions

*Crank-Nicolson scheme*, and the *implicit scheme*, respectively. The integration with respect to the temporal and the spatial variables eventually results in a system of algebraic equations (one for each control volume), which can be solved by standard numerical techniques.

For a simple illustration of the finite volume discretization methodology, one may consider a two-dimensional rectangular control volume with the grid point P at its geometric center, as depicted in Fig. 1. The neighboring grid points for the point P are the points E, W, N, and S (symbolizing the “east,” “west,” “north,” and “south” neighbors). The locations of the four faces of the control volume containing the point P are denoted by the corresponding lowercase alphabets. If we take the two-dimensional transient heat conduction equation as a prototype example, in the form

$$\rho c_p \frac{\partial T}{\partial t} = \frac{\partial}{\partial x} \left( k \frac{\partial T}{\partial x} \right) + \frac{\partial}{\partial y} \left( k \frac{\partial T}{\partial y} \right) + S \quad (9)$$

then an implicit time discretization, a piecewise linear temperature profile assumption between consecutive grid points for the diffusion terms, and a piecewise constant temperature profile within each control volume

for the source term give rise to a discretized version of the control volume integral of Eq. 9 in the following form:

$$a_P T_P = a_E T_E + a_W T_W + a_N T_N + a_S T_S + a_P^0 T_P^0 + b \quad (10)$$

where  $a_E = k_E \Delta y / \delta x_e$ ,  $a_W = k_W \Delta y / \delta x_w$ ,  $a_N = k_N \Delta x / \delta y_n$ ,  $a_S = k_S \Delta x / \delta y_s$ ,  $a_P^0 = \rho c_p \Delta x \Delta y / \Delta t$ ,  $b = S_c \Delta x \Delta y + a_P^0 T_P^0$ , and  $a_P = a_E + a_W + a_N + a_S + a_P^0 - S_P \Delta x \Delta y$ . Here the superscript “0” symbolizes the value at a time instant of  $t$ , and the superscript is omitted to symbolize the value at a time instant of  $t + \Delta t$ . Further, the source term is linearized in the form  $S = S_c + S_P T_P$ , to arrive at the above discretization. In general, for executing the finite volume discretization of heat conduction problems, the following important points may be taken into account [2]:

- The profile assumption should be consistent with the requirements of the continuity of fluxes at the control volume faces.
- All coefficients in the discretized algebraic equation should be of the same sign.
- The interfacial value of thermal conductivity can be best interpolated by invoking a harmonic mean approximation, based on values of the same at the adjacent grid points.
- The explicit scheme gives rise to a system of discretized algebraic equations that are not mathematically coupled. However, the cost that one might have to pay against this simplification is that the scheme is conditionally stable. On the other hand, the implicit scheme requires a coupled system of linear algebraic equations to be solved but is unconditionally stable (the issues of “stability” in the context of discretized equations will be elaborated later).

## Key Research Findings

### Convection-Diffusion Problems

The finite volume formulation for diffusion-type problems can be extended for solving the

convection-diffusion types of problems, in which additional advection terms appear in the governing differential equations. Assuming that the velocity field is already obtained from a separate solution module, various discretization strategies can be formulated for solving the convection-diffusion problem, based on the “cell Peclet number” ( $P$ ), which is nothing but the ratio of the advection to diffusion strengths, based on control volume-specific length scales. Considering the following generic form of a two-dimensional unsteady-state convection-diffusion equation as an illustrative example

$$\begin{aligned} \frac{\partial}{\partial t}(\rho\phi) + \frac{\partial}{\partial x}(\rho u\phi) + \frac{\partial}{\partial y}(\rho v\phi) \\ = \frac{\partial}{\partial x}\left(\Gamma\frac{\partial\phi}{\partial x}\right) + \frac{\partial}{\partial y}\left(\Gamma\frac{\partial\phi}{\partial y}\right) + S \end{aligned} \quad (11)$$

one can arrive at a discretization equation as

$$\begin{aligned} a_P\phi_P = a_E\phi_E + a_W\phi_W + a_N\phi_N + a_S\phi_S \\ + a_P^0\phi_P^0 + b \end{aligned} \quad (12)$$

where  $a_E = D_e A(|P_e|) + \max(-F_e, 0)$ ,  $a_W = D_w A(|P_w|) + \max(F_w, 0)$ ,  $a_N = D_n A(|P_n|) + \max(-F_n, 0)$ ,  $a_S = D_s A(|P_s|) + \max(F_s, 0)$ ,  $a_P^0 = \rho_P^0 \Delta x \Delta y / \Delta t$ ,  $b = S_c \Delta x \Delta y + a_P^0 \phi_P^0$ , and  $a_P = a_E + a_W + a_N + a_S + a_P^0 - S_P \Delta x \Delta y$ . Here,  $D_e = \Gamma_e \Delta y / \delta x_e$ ,  $D_w = \Gamma_w \Delta y / \delta x_w$ ,  $D_n = \Gamma_n \Delta x / \delta y_n$ ,  $D_s = \Gamma_s \Delta x / \delta y_s$ ,  $F_e = (\rho u)_e \Delta y$ ,  $F_w = (\rho u)_w \Delta y$ ,  $F_n = (\rho v)_n \Delta x$ ,  $F_s = (\rho v)_s \Delta x$ ,  $P_e = F_e / D_e$ ,  $P_w = F_w / D_w$ ,  $P_n = F_n / D_n$ , and  $P_s = F_s / D_s$ .

The function  $A(|P|)$ , as appearing in the above equation, depends on the specific interpolation scheme chosen to discretize the convection-diffusion terms. Appropriate expressions of the same, for different schemes, are given in Table 2. Regarding the choice of a suitable scheme, certain important considerations can be noted [2]:

- The central difference scheme can give rise to physically inconsistent solutions, in case  $|P| > 2$ .
- The upwind scheme does not suffer from the above limitation, but tends to overpredict diffusion.

- Although the exponential scheme gives a reasonably accurate estimation of the profile variation of  $\phi$ , it involves costly computation of exponential terms.
- The hybrid scheme is a piecewise linearization of the exponential scheme and therefore retains a correct physical behavior. However, it tends to set the diffusion effects to zero as soon as  $|P| > 2$ .
- The power law scheme is essentially a curve fitting of the exponential scheme that attempts to eliminate the abovementioned discrepancy.
- The upwind scheme had been identified by many researchers as a common source of “numerical diffusion” or “false diffusion,” which means an “overprediction” of the diffusion strength as a numerical artifact. However, a different (and, possibly, more logical) viewpoint is that the false diffusion is not so much attributable to the specific convection-diffusion scheme chosen (since the best portrayed scheme for overcoming false diffusion, viz., the central difference scheme, itself ceases to work at high values of cell Peclet number), but can be associated with the obliquity of the flow directions with respect to the grid lines that form the discretized space. Higher-order upwind schemes, for example, the QUICK (quadratic upstream interpolation for convective kinetics) differencing scheme [3], have been suggested as alternative remedies to overcome false diffusion effects. Such alternative schemes, however, also suffer from certain shortcomings in the sense that these are conditionally stable.

### Discretization of Fluid Flow Equations

So far, we have discussed the solution of general transport equations, by assuming the velocity field to be known. In principle, the equations governing the velocity field (viz., the continuity and the momentum conservation equations) are also of a general conservative nature (see Table 1) and ideally should have been solvable by the standard convection-diffusion discretization methodologies discussed earlier. In reality, however, the strategy does not work in that way, and additional considerations need to be invoked.

**Finite Volume and Finite Difference Methods for Modeling and Simulation, Table 2** Convection-diffusion discretization schemes

Scheme	$A( P )$
Central difference	$1 - 0.5  P $
Upwind	1
Exponential	$ P /(\exp P  - 1)$
Hybrid	$\max(0, 1 - 0.5 P )$
Power law	$\max(0, (1 - 0.5 P )^5)$

This is because of the fact that the momentum equation source terms contain pressure as an additional scalar variable, although there is no separate explicit governing differential equation for pressure. Early efforts in solving the fluid flow equations were mainly based on the stream function-vorticity approach, in which the pressure gradient terms from the momentum conservation equations are eliminated by cross-differentiating the two components of the momentum conservation equation (in case of a two-dimensional flow field) and subtracting one from the other, giving rise to the following two coupled equations:

$$\frac{\partial \zeta}{\partial t} + u \frac{\partial \zeta}{\partial x} + v \frac{\partial \zeta}{\partial y} = \frac{\mu}{\rho} \left( \frac{\partial^2 \zeta}{\partial x^2} + \frac{\partial^2 \zeta}{\partial y^2} \right) \quad (13)$$

$$\frac{\partial^2 \psi}{\partial x^2} + \frac{\partial^2 \psi}{\partial y^2} = -\zeta \quad (14)$$

where  $\zeta$  is the vorticity vector ( $\zeta = \nabla \times \nabla$ ) and  $\psi$  is the stream function ( $u = \partial\psi/\partial y, v = -\partial\psi/\partial x$ ). These two coupled equations can be discretized in the same manner outlined above, and the pressure field can subsequently be computed by solving for the following Poisson equation:

$$\frac{\partial^2 p}{\partial x^2} + \frac{\partial^2 p}{\partial y^2} = 2\rho \left[ \frac{\partial^2 \psi}{\partial x^2} \frac{\partial^2 \psi}{\partial y^2} - \left( \frac{\partial^2 \psi}{\partial x \partial y} \right)^2 \right] \quad (15)$$

The apparently elegant stream function-vorticity approach, however, suffers from certain shortcomings, as follows [2]:

- The vorticity at the wall may be difficult to specify for many practical problems.
- The pressure can be required as an intermediate outcome for updating the density values

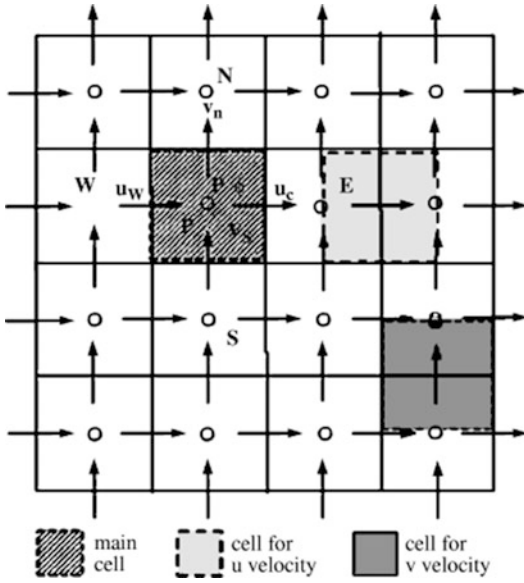
through the equation of state, so that a complete elimination of pressure might not always be desirable.

- Most importantly, the method cannot be extended to three dimensions in which the stream function is not defined.

In order to overcome such shortcomings, the primitive variable-based methods have been suggested as better alternatives in the literature. The challenges associated with the primitive variable methods are not to eliminate the pressure, but to convert the indirect information in the continuity equation into a direct algorithm for the calculation of pressure. However, a straightforward discretization of the pressure gradient terms in the momentum conservation equation, based on the linearly interpolated values of pressure from the adjacent grid points, may give rise to certain anomalies, leading to a condition in which a zigzag pressure field could be numerically interpreted as a uniform one. As a remedy, the concept of “staggered” (displaced) grids has been introduced, according to which the velocity components are calculated for the points that lie on the faces of the control volumes (see Fig. 2). Advantages of such kinds of grid arrangement are mainly twofold [2]:

- The discretized continuity equation would contain the differences of the adjacent velocity components, so that wavy velocity fields are not wrongly predicted as outcomes of the continuity equation for cases in which a uniform velocity field is expected to physically exist.
- The pressure difference between two adjacent grid points becomes the natural driving force for the velocity variations between these grid points, so that unrealistic predictions of the pressure field are ruled out.

It is important to mention here that the use of staggered grids is not always a compulsion. In case special pressure interpolation schemes are employed to overcome the difficulties associated with the non-staggered grids mentioned earlier, the staggered grid arrangement might not be necessary. In such cases, the same grid arrangement can be employed for solution of the velocity field and the other scalar variables, which is commonly referred to as a “colocated grid.”



**Finite Volume and Finite Difference Methods for Modeling and Simulation, Fig. 2** Staggered grid arrangement for the solution of momentum equations

Several algorithms do exist in the literature for numerical computation of fluid flow problems on the basis of primitive variables, in a finite volume framework. One of the most commonly used algorithms of this kind is the SIMPLE (semi-implicit method for pressure-linked equations) algorithm [2]. With reference to a generic staggered control volume for solution of the momentum equation for  $u$  (see Fig. 3) and with similar considerations for the other velocity components, major steps of the SIMPLE algorithm can be summarized as follows:

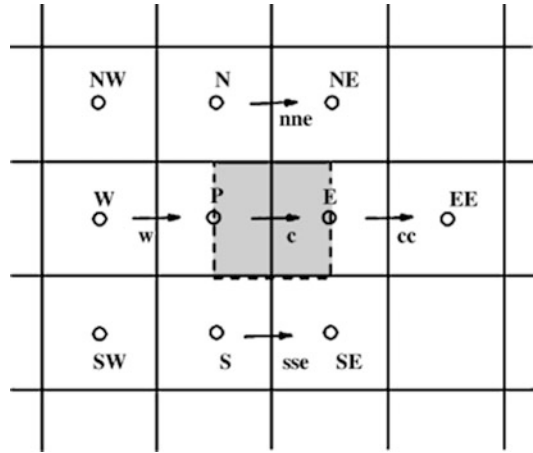
1. Guess the pressure field,  $p^*$ .
2. Solve the discretized momentum conservation equations, to be cast in the following forms:

$$a_c u_c^* = \sum a_{nb} u_{nb}^* + b + (p_P^* - p_E^*) A_c;$$

$$a_n v_n^* = \sum a_{nb} v_{nb}^* + b + (p_P^* - p_N^*) A_n;$$

$$a_t u_t^* = \sum a_{nb} u_{nb}^* + b + (p_P^* - p_T^*) A_t,$$

where the subscript “nb” refers to the neighboring grid points.



**Finite Volume and Finite Difference Methods for Modeling and Simulation, Fig. 3** A generic staggered control volume for discretization of the x-momentum equation

3. Substitute a “velocity correction” formula, expressed in terms of “pressure corrections” at the main grid points in the discretized continuity equation (discretized over the main control volume, not the staggered one), to get the pressure correction equation in the following form (with “T” and “B” denoting the “top” and “bottom” grid points relative to the point P in a three-dimensional space):

$$a_P p'_P = a_E p'_E + a_W p'_W + a_N p'_N + a_S p'_S + a_T p'_T + a_B p'_B + b \tag{16}$$

where  $a_E = \rho_c d_c \Delta y \Delta z$  (where  $a_E = A_c / a_c$ ),  $a_W = \rho_w d_w \Delta y \Delta z$ ,  $a_N = \rho_n d_n \Delta x \Delta z$ ,  $a_S = \rho_s d_s \Delta x \Delta z$ ,  $a_T = \rho_t d_t \Delta x \Delta y$ ,  $a_B = \rho_b d_b \Delta x \Delta y$ ,  $a_P = a_E + a_W + a_N + a_S + a_T + a_B$ , and

$$b = \frac{(\rho_P^0 - \rho_P) \Delta x \Delta y \Delta z}{\Delta t} + [(\rho u^*)_w - (\rho u^*)_e] \Delta y \Delta z + [(\rho v^*)_s - (\rho v^*)_n] \Delta x \Delta z + [(\rho w^*)_b - (\rho w^*)_t] \Delta x \Delta y$$

4. Correct the pressure field as  $p = p^* + p'$ .
5. Correct the velocity field as  $u_c = u_c^* + d_c (p'_P - p'_E)$  and similarly for the other velocity components.

6. Go to step 2 with the corrected value of  $p$  obtained from step 4 and the new  $p^*$ .
7. Repeat the loop until convergence.

With regard to the SIMPLE algorithm outlined above, certain important points can be carefully noted:

- No attempt is made for the direct solution of momentum equations. In the velocity correction expression, i.e.,  $u'_e = \sum a'_{nb}u'_{nb} + b + (p'_p - p'_e)A_e$ , the first term in the right-hand side is essentially dropped, which enables one to cast the pressure correction equation in a general conservative form.
- The algorithm is called as *semi-implicit* to acknowledge the dropping of the term  $\sum a'_{nb}u'_{nb}$ . This term essentially represents an indirect or implicit influence of the pressure correction on velocity. Although pressure corrections at nearby locations can alter the neighboring velocities and thus can cause a velocity correction at the point under consideration, this influence is not considered in the SIMPLE algorithm. However, it needs to be noted here that this semi-implicit nature has nothing to do with any possible implicit or explicit nature of the time-discretization scheme.
- On convergence, all the velocity and pressure corrections tend to zero. This implies that no error is incurred on dropping the  $\sum a'_{nb}u'_{nb}$  term, once the convergent solution has been obtained, with an understanding that the term “ $b$ ” in Eq. 15, which is essentially a mass source term for the discretized continuity equation, should tend to zero once the mass conservation is satisfied. The sole emphasis here is to obtain a pressure field that satisfies the continuity equation. The dropping of the  $\sum a'_{nb}u'_{nb}$  term, however, is related to the rate at which the convergence is obtained.
- For highly compressible flows, the pressure correction formula should also accommodate the provision of a density correction term.
- The pressure is a relative variable, as an outcome of this algorithm, and not an absolute quantity.
- The approximation introduced in the derivation of the pressure correction equation by

dropping the term  $\sum a'_{nb}u'_{nb}$  leads to a rather exaggerated pressure correction. Because of the omission of the neighboring velocity corrections, the pressure correction carries the entire burden of correcting the velocities, which results in a rather severe pressure correction field. Thus, although the pressure correction equation does a fairly good job in correcting the velocities, it does a poorer job in correcting the pressure. Taking this into consideration, a revised version of the SIMPLE algorithm, namely, the SIMPLER algorithm [2], has later been proposed, in which a separate pressure equation is formulated (by discretizing the continuity equation) to solve for the pressure field, and the pressure correction is solely employed to correct the velocity field but not the pressure field. This leads to a faster convergence, although a slightly increased overhead of solving another scalar equation (viz., the pressure equation).

- Other variants of the SIMPLE algorithm have also been proposed in the literature. For example, Van Doormal and Raithby [4] developed the SIMPLEC (SIMPLE-Consistent) algorithm, which follows similar steps as that of the SIMPLE algorithm, with the sole difference that the momentum equations are manipulated so that the modified velocity correction formulae omit terms that are less significant than those omitted in the SIMPLE algorithm. Issa [5] introduced the PISO (Pressure Implicit with Splitting of Operators) algorithm for the non-iterative computation of unsteady compressible flows. This algorithm involves one predictor step and two corrector steps, as an extension of the SIMPLE algorithm. The SIMPLEC and the PISO algorithms have been found to work as efficiently as the SIMPLER algorithm in many cases, although it cannot be convincingly concluded their relative superiorities, which strongly depend on the extent of coupling between the velocity field and the other scalar fields and often on the strategy of solving the system of discretized algebraic equations.

**Issues of Consistency, Stability, and Convergence**

Irrespective of the discretization method chosen, the success of the numerical scheme depends heavily on certain factors, associated with the terminologies such as consistency, stability, and convergence. A numerical scheme is said to be consistent if it produces systems of algebraic equations that can be demonstrated as equivalent to the original governing differential equation, in the limit as the grid spacings tend to zero. In more technical terms, the truncation error must tend to zero with limitingly thin grid spacings. In general, the truncation error can be numerically assessed by obtaining the numerical solutions over two different grid spacings ( $h$  and  $2h$ , say). Let the corresponding numerical solutions be  $\phi_h$  and  $\phi_{2h}$ , respectively. It can also be noted that for sufficiently fine grids, the truncation error is proportional to the leading-order term in the Taylor series, i.e.,  $T.E \approx \alpha h^p + H$ , where  $\alpha$  depends on the derivatives at a given point but is independent of  $h$  and  $H$  stands for the higher-order terms. Thus, one can write

$$\begin{aligned} \phi_{\text{exact}} &= \phi_h + \alpha h^p + H \\ &= \phi_{2h} + \alpha(2h)^p + H \end{aligned} \tag{17}$$

so that the truncation error for the grid size of  $h$  can be estimated as

$$(T.E)_h \approx \frac{\phi_h - \phi_{2h}}{2^p - 1} \tag{18}$$

Equation 16 forms the basis of the Richardson extrapolation formula [6] commonly used in numerical analysis, for improving the accuracy of the numerical solutions by accommodating for the truncation error estimates.

Another important factor for the successful performance of a discretization scheme is its stability. In simple terms, a numerical solution method is said to be stable if it does not magnify the errors that appear in the course of a numerical solution process. For unsteady problems, stability guarantees that the numerical method yields a bounded solution, provided that the solution of

the original governing differential equation is also bounded. For iterative methods, the iterations act as *virtual* time steps, and the meaning of stability has analogous physical implications. Classically, the stability of a discretization scheme is assessed by employing the von Neumann analysis. For nonlinear problems, stability might be rather difficult to investigate by adopting this method. Here, we outline the stability analysis of a linear problem in which explicit method of time discretization is used, for the sake of illustration. For simplicity, let us consider a one-dimensional diffusion problem with constant thermophysical properties and no source terms, numerically solved by employing uniform grids and an explicit time-discretization scheme. In this special case, the discretization equation takes the form of

$$\begin{aligned} a_P \phi_P &= a_E \phi_E^0 + a_W \phi_W^0 \\ &+ (a_P^0 - a_E - a_W) x \phi_P^0 \end{aligned} \tag{19}$$

where  $a_E = \Gamma_e / \delta x_e$ ,  $a_W = \Gamma_w / \delta x_w$ ,  $a_P^0 = \rho \Delta x / \Delta t$ , and  $a_P = a_P^0$ . Let  $\Phi$  represent a solution of the discretized equations (not the original governing differential equation) using infinite computational precision. With practical computing systems, however, there would definitely be some roundoff error, given as  $\varepsilon = \phi - \Phi$ . Using this definition in Eq. 19 and noting that  $\Phi$  satisfies this equation exactly, one obtains

$$a_P \varepsilon_P = a_E \varepsilon_E^0 + a_W \varepsilon_W^0 + (a_P^0 - a_E - a_W) \varepsilon_P^0 \tag{20}$$

In order to assess whether the round-off error gets amplified with time, one may expand the error in an infinite series as

$$\varepsilon(x, t) = \sum_m e^{\sigma_m t} e^{i \lambda_m x}, \quad m = 0, 1, 2, \dots, M \tag{21}$$

where  $\sigma_m$  is either real or complex and  $\lambda_m = m\pi/L$  and  $m = 0, 1, 2, \dots, M$ , with  $L$  being the width of the problem domain. If  $\sigma_m$  is real and greater than zero, then the error grows with time,

whereas if  $\sigma_m$  is real and less than zero, then the error is damped out with time. If  $\sigma_m$  is complex, the solution is oscillatory. In particular, the nature of evolution of the error can be estimated from the amplification factor,  $a = \varepsilon(x, t + \Delta t)/\varepsilon(x, t)$ . If the magnitude of  $a$  is greater than unity, then the error grows with the time step, whereas if  $a$  is less than unity, then the error is damped out with the time step so that the scheme can be predicted as stable. In order to assess this factor for the special case under consideration, one may exploit the linearity of the equation and just examine the stability consequences of a single error term in Eq. 21, rather than the summation. Substituting a single term from Eq. 21 to 20, one can obtain an expression for  $a$  as

$$a = e^{\sigma_m \Delta t} = 1 - \frac{4\Gamma \Delta t}{\rho(\Delta x)^2} \quad (22)$$

The above gives rise to the conditional stability criterion of the explicit scheme as

$$\Delta t \leq \frac{\rho(\Delta x)^2}{2\Gamma} \quad (23)$$

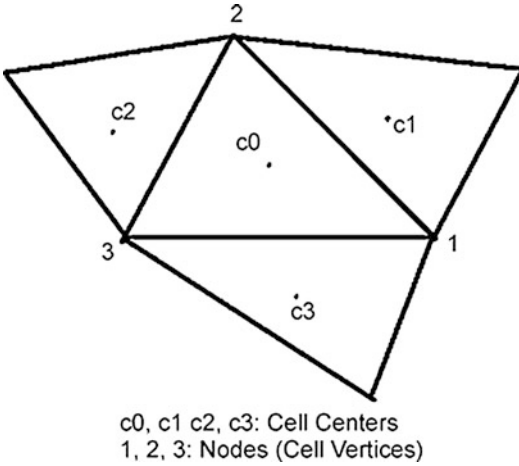
Analogous stability analyses can be executed for the other time-discretization schemes as well. It is important to note here that although the von Neumann stability analysis yields a limiting time-step estimate to keep the roundoff errors bounded, it does not preclude the occurrence of *bounded* but *unphysical* solutions. A classical example is the Crank-Nicolson scheme, which from the von Neumann viewpoint is unconditionally stable but can give rise to bounded unphysical solutions in case all the coefficients of the discretization equation do not happen to be of the same sign [2].

Closely associated with the concepts of consistency and stability is the idea of convergence. A numerical scheme is said to be convergent if the solution of the discretized equations tends to the exact solution of the governing differential equation as the grid spacing tends to zero. For linear initial value problems, both consistency

and stability are the necessary and sufficient conditions of convergence as per the Lax equivalence theorem [6], which states that “given a properly posed linear initial value problem and a finite difference approximation to it that satisfies the consistency condition, stability is the necessary and sufficient condition for convergence.” For nonlinear problems, however, consistency and stability are only the necessary conditions for convergence but not sufficient.

### Concepts of Discretization in Unstructured Meshes

The use of unstructured meshes [7] for solving fluid flow and other transport problems has become increasingly popular over the past few decades, because of its elegant capability of discretizing complicated and irregular-shaped geometries. Although the finite volume method was originally developed for structured grids (as outlined in the preceding discussions), it has been subsequently adapted to accommodate the features of unstructured meshes. A conceptual distinguishing feature between the structured and the unstructured meshes is that an unstructured mesh has the provision of having a variable number of neighboring cell vertices (although it might not exploit this feature always), whereas in a structured mesh, each cell vertex has a fixed number of neighboring cell vertices (except for the boundary cells). Since the fluxes calculated at the cell faces in unstructured meshes need not necessarily be aligned with the direction joining the neighboring grid points, special considerations are necessary to formulate the discretization equations. In this context, it needs to be recognized that in case of unstructured grids, it is possible to have a hybrid mesh composed of polygons with different shapes. Although the discretization policy, in principle, is similar for all polygonal shapes, precise forms of the discretization equations strongly depend on the specific shape of the control volume under consideration. Here, for the sake of illustration, we only outline the discretization methodology for unstructured triangular meshes. A typical triangular control volume with three neighboring



**Finite Volume and Finite Difference Methods for Modeling and Simulation, Fig. 4** A triangular-shaped control volume (with cell center at c0) and three of its neighboring control volumes

triangular cells is depicted in Fig. 4. Here, we illustrate a prototype discretization of the steady version of the x-momentum equation. The first step is to integrate the governing differential equation over the triangular control volume, to yield

$$\underbrace{\int_{CV} \nabla \cdot (\rho \mathbf{V}u) dV}_{\text{term 1}} = - \underbrace{\int_{CV} \frac{\partial p}{\partial x} dV}_{\text{term 2}} + \underbrace{\int_{CV} \nabla \cdot (\mu \nabla u) dV}_{\text{term 3}} \tag{24}$$

The various terms appearing in Eq. 24 can be simplified by applying the divergence theorem, so as to convert the volume integrals into equivalent surface integrals, to obtain

$$\begin{aligned} \text{term 1} &= \int_{CV} \nabla \cdot (\rho \mathbf{V}u) dV = \int_{CS} (\rho \mathbf{V}u) \cdot d\mathbf{A} \\ &= \sum_{i=1}^{\text{number of edges (3)}} (\rho u)_i (\mathbf{V} \cdot d\mathbf{A})_i, \end{aligned}$$

or equivalently

$$\text{term 1} = \sum_{i=1}^3 (\rho u)_i U_{f,i} = \sum_{i=1}^3 F_i U_{f,i},$$

say, where

$$\mathbf{U} = \mathbf{V} \cdot d\mathbf{A} = u dA_x + v dA_y$$

is the contravariant velocity vector, the subscript ‘‘F’’ refers to a cell face, and  $F$  symbolizes the advection strength

$$\begin{aligned} \text{term 2} &= \int_{CV} -\frac{\partial p}{\partial x} dV = \int_{CS} -(p\hat{i}) \cdot d\mathbf{A} \\ &= -\sum_{i=1}^3 (p dA_x)_i, \end{aligned}$$

or equivalently

$$\begin{aligned} \text{term 2} &= -\sum_{i=1}^3 p_i \Delta y_i \\ &= -[(p_{c1} - p_{c0})\Delta y_1 + (p_{c2} - p_{c0})\Delta y_2 \\ &\quad + (p_{c3} - p_{c0})\Delta y_3]. \end{aligned}$$

Here,  $\Delta y_i$  represents the difference of the y-coordinates of the two vertices of the edge ‘‘i,’’ the vertices being taken in a specific (positive oriented, as a convention) order for the evaluation of this parameter, for all edges.

$$\begin{aligned} \text{term 3} &= \int_{CV} \nabla \cdot (\mu \nabla u) dV = \int_{CS} (\mu \nabla u) \cdot d\mathbf{A} \\ &= \sum_{i=1}^3 \mu_i \left[ \frac{\partial u}{\partial x} \Delta y - \frac{\partial u}{\partial y} \Delta x \right]_i. \end{aligned}$$

The partial derivatives appearing in this expression can be evaluated by choosing auxiliary control volumes surrounding an edge ‘‘i,’’ for the evaluation of integrals associated with that edge. For example, for evaluation of the integrals over the edge 1–2, one can construct an auxiliary control volume with the bounding edges as 1 – c1 – 2 – c0 – 1. As an illustration, the term  $(\partial u/\partial x)_i$  can be evaluated as follows:

$$\left(\frac{\partial u}{\partial x}\right)_i = \frac{\int_{A_i} \frac{\partial u}{\partial x} dA}{A_i} = \frac{\int_C u dy}{A_i},$$

where  $C$  is a closed contour that forms the surface of the auxiliary control volume. This contour integral

can be numerically approximated by employing the trapezoidal rule, so that one can write

$$\left(\frac{\partial u}{\partial x}\right)_1 = \frac{[(u_{c1} - u_{c0})\Delta y_1 + (u_1 - u_2)\Delta y_{c1-c0}]}{A_1},$$

where  $\Delta y_1 = y_2 - y_1$  and  $\Delta y_{c1-c0} = y_{c1} - y_{c0}$ . Analogous considerations can be made for the other integrals to be evaluated for term 3 as well. The discretized form of term 3, therefore, becomes

$$\text{term 3} = \underbrace{\sum_{i=1}^3 D_i(u_{ci} - u_{c0})}_{\text{orthogonal diffusion flux}} + \underbrace{D_{n1}(u_1 - u_2) + D_{n2}(u_2 - u_3) + D_{n3}(u_3 - u_1)}_{\text{non-orthogonal diffusion flux}},$$

where

$$D_i = \frac{\mu_i}{2A_i} [(\Delta x)^2 + (\Delta y)^2]_i,$$

$$D_{ni} = \frac{\mu_i}{2A_i} [(\Delta x)_i(\Delta x)_{ci-c0} + (\Delta y)_i(\Delta y)_{ci-c0}].$$

For numerical implementation, the orthogonal diffusion flux may be treated implicitly, whereas the non-orthogonal diffusion flux may be treated explicitly by clubbing the same together with the source term. The discretized forms of the three terms can finally be assembled together to obtain the discretized x-momentum equation for the triangular control volume in the following form:

$$a_P u_{c0} = A_1 u_{c1} + A_2 u_{c2} + A_3 u_{c3} + S \quad (25)$$

where  $A_i = [D_i A(|Pe|_i) + \max(\pm F_i, 0)]$  ( $F_i$  is taken to be positive if the cell is to the left of edge  $i$ ; otherwise, it is taken as negative),  $A_P = A_1 + A_2 + A_3$ , and  $A(|Pe|_i)$  depends on the chosen interpolation scheme for representing the convection-diffusion phenomenon (see Table 2). Similar considerations can be made for discretization of other equations as well.

### Future Directions of Research

CFD has now become a somewhat mature field, in which the basics of algorithm development associated with the finite difference and finite volume methodologies have been relatively well

established. However, there are certain issues yet to be well resolved, on which future directions of research related to these topics can be based:

- Efficient parallelization of the solution strategies
- Embedding the aspects of multi-scale physics in the discretization techniques
- Establishing hybrid simulation strategies with coupled molecular- and continuum-based discretizations

### Cross-References

- ▶ [Boundary Element Method and Its Applications to the Modeling of MEMS Devices](#)
- ▶ [Finite Volume and Finite Difference Methods for Modeling and Simulation](#)
- ▶ [Lattice Boltzmann Method \(LBM\)](#)
- ▶ [Molecular Dynamics Simulation Method](#)
- ▶ [Monte Carlo Method](#)
- ▶ [Multiscale Modeling and Numerical Simulations](#)
- ▶ [Meshless Methods](#)

### References

1. Anderson DA, Tannehill JC, Pletcher RH (1984) Computational fluid mechanics and heat transfer. Hemisphere, New York
2. Patankar SV (1980) Numerical heat transfer and fluid flow. Hemisphere, New York

3. Leonard BP (1979) A stable and accurate convective modeling procedure based on quadratic upstream interpolation. *Comput Method Appl Mech Eng* 19:59–98
4. Van Doormal JP, Raithby GD (1984) Enhancements of the SIMPLE method for predicting incompressible fluid flows. *Numer Heat Trans* 7:147–163
5. Issa RI (1986) Solution of the implicitly discretized fluid flow equations by operator splitting. *J Comput Phys* 62:40–65
6. Ferziger JH, Peric M (1996) *Computational methods for fluid dynamics*. Springer, New York
7. Mathur SR, Murthy JY (1997) A pressure-based method for unstructured meshes. *Numer Heat Trans Part B* 31:195–215

---

## Flexible Shear Stress Sensor

### Synonyms

Smart skin

### Definition

Fluid shear stress information is of great interest for many fluidic dynamic monitoring/diagnostics applications. For example, oscillatory shear stress plays an important role in the biological activities of vascular endothelial cells, which may lead to atherosclerosis. The emergence of the microelectromechanical systems (MEMS) technology provides us with the miniaturization of ► [shear stress sensors](#) with perfect spatial and temporal resolutions. The conventional MEMS sensors are based on the fabrication with the rigid silicon substrate, which limits the application to only the flat surface. In vivo biomedical applications demand the deployment of the sensors on the curved and nonplanar surface, which will maximize the measurement precision and minimize the disturbance due to the intruding sensor. Scientists have combined the silicon technology with the polymer process to fabricate the sensor skin, which can conformally coat the nonflat surface and precisely measure the microfluidic parameters such as shear stress, temperature, and pressure.

### Cross-References

- [Micro- and Nanoscale Anemometry: Implication for Biomedical Applications](#)

---

## Flow Bifurcation in Microchannel

Y. F. Yap<sup>1</sup>, Yali Zhang<sup>2</sup>, Teck Neng Wong<sup>2</sup>, Nam-Trung Nguyen<sup>3</sup> and John C. Chai<sup>1</sup>

<sup>1</sup>Department of Mechanical Engineering, The Petroleum Institute, Abu Dhabi, UAE

<sup>2</sup>School of Mechanical and Aerospace Engineering, Nanyang Technological University, Singapore

<sup>3</sup>Queensland Micro- and Nanotechnology Centre, Griffith University, Brisbane, QLD, Australia

### Synonyms

Bifurcating microchannel; T-junction

### Definition

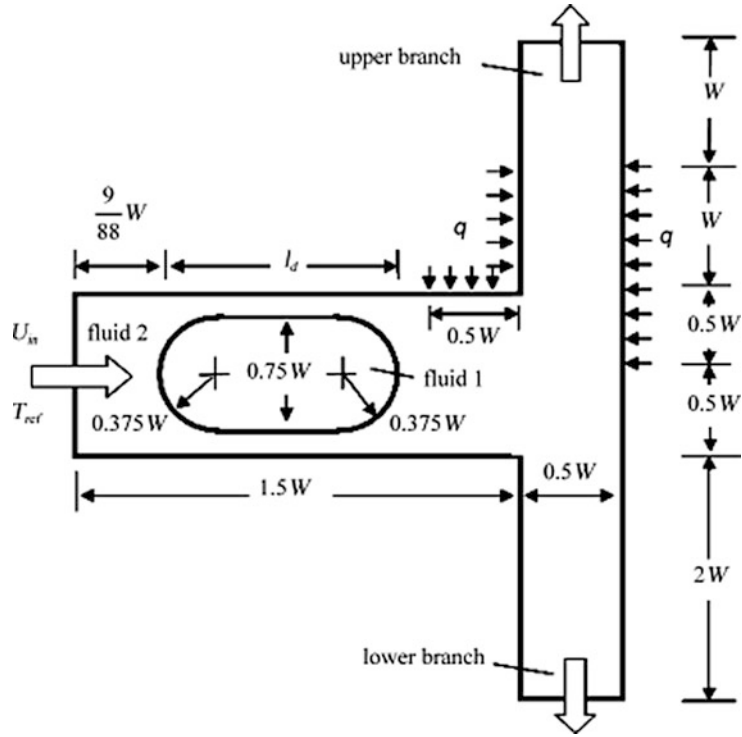
Flow bifurcation in microchannels is discussed in this entry. In this entry, flow bifurcation refers to geometrical bifurcation. Specifically, the transport of droplets in microchannel where a mother branch bifurcates into two daughter branches with thermocapillary effects is examined.

### Overview

Microchannel bifurcations have been employed in manipulating droplets. These manipulations include but are not limited to droplet fusion and splitting. Fusing of droplets has been demonstrated using a microchannel with three bifurcating branches [1]. A bifurcating T-junction can be employed to split a droplet into two daughter droplets of smaller size [2]. The relative size of the two daughter droplets is determined by the length of the branches. A longer branch creates larger resistance to flow, therefore creating smaller daughter droplet. In the extreme case

**Flow Bifurcation in Microchannel,**

**Fig. 1** Schematic of a droplet in a micro T-junction



where one of the branches is sufficiently long, the droplet does not break but is switched into the other branch. Such a passive geometrical control is limited in terms of its versatility. A more versatile active control utilizing thermocapillary effects [3] is presented in this study. The focus is on unequal splitting and switching the droplet into a desired branch at a T-junction.

**Basic Methodology**

**Problem Description**

Figure 1 shows a fluid 1 droplet of length in a micro T-junction. Fluid 2 at temperature  $T_{ref}$  flows into the micro T-junction with a fully developed velocity profile of  $u_{in}$  at the inlet. This corresponds to a mean velocity of  $u_m$ . As fluid 2 flows, it carries the droplet.

An asymmetric temperature field is induced in the T-junction by applying a heat flux  $q$  at the selected locations. The remaining walls of the channel are properly insulated. As a result, the temperature-dependent surface tension  $\sigma(T)$

varies along the droplet interface.  $\sigma$  is assumed to vary linearly with temperature, i.e.,

$$\sigma = \sigma_o + \frac{d\sigma}{dT}(T - T_{ref}) \tag{1}$$

where  $\sigma_o$  is the surface tension at temperature  $T_{ref}$ . The variation of  $\sigma$  induces an additional interfacial (thermocapillary) force on the droplet at the interface. This suggests that the net force on the droplet, and thus its motion, can be controlled by adjusting the heater power.

Driven by the pressure gradient and the thermocapillary force, fluid 2 together with the droplet flows out of the domain via either the upper or the lower branch. It is possible that the droplet splits at the T-junction. The two outlets are maintained at the same pressure with a fully developed temperature profile.

**Governing Equations**

The level-set method [4] is used to capture the droplet interface. The level-set function  $\zeta$  is defined as the signed distance function from the



interface. Obviously, the value of  $\xi$  at the interface is zero. In the present study, the value of  $\xi$  for fluid 2 (the carrier fluid) is assigned negative. The distance function  $\xi$  for fluid 1 (the droplet) is positive. As a result,  $\xi$  can be expressed as

$$\xi(\mathbf{x}, t) = \begin{cases} < 0, & \text{if } \mathbf{x} \in \text{fluid2} \\ = 0, & \text{if } \mathbf{x} \in \text{interface} \\ > 0, & \text{if } \mathbf{x} \in \text{fluid1} \end{cases} \quad (2)$$

With the knowledge of  $\xi$ , any property of the fluid  $\alpha$  (e.g., the density, viscosity, thermal conductivity, or other properties of interest) in the domain at any given time  $t$  can be calculated conveniently as

$$\alpha = (1 - H)\alpha_1 + H\alpha_2 \quad (3a)$$

where subscripts 1 and 2 refer to fluid 1 and 2, respectively. The smoothed Heaviside function  $H$  is given by

$$H(\xi) = \begin{cases} 0, & \xi < -\varepsilon \\ \frac{\xi + \varepsilon}{2\varepsilon} + \frac{1}{2\pi} \sin\left(\frac{\pi\xi}{\varepsilon}\right), & |\xi| \leq \varepsilon \\ 1, & \xi > \varepsilon \end{cases} \quad (3b)$$

The Heaviside function is smoothed over a finite thickness of  $2\varepsilon$ . The parameter  $\varepsilon$  is related to the grid size and is usually taken as a factor of the grid spacing. In this entry,  $\varepsilon$  is set to one control volume thickness.

The conservation equations, i.e., continuity, incompressible Navier-Stokes, and energy equations, can now be written for the whole domain. These are expressed as

$$\nabla \cdot \mathbf{u} = 0 \quad (4)$$

$$\frac{\partial(\rho\mathbf{u})}{\partial t} + \nabla \cdot (\rho\mathbf{u}\mathbf{u}) = -\nabla p + \nabla \cdot [\mu(\nabla\mathbf{u} + \nabla\mathbf{u}^T)] + \mathbf{f}_F \quad (5)$$

$$\frac{\partial(\rho c T)}{\partial t} + \nabla \cdot (\rho c \mathbf{u} T) = \nabla \cdot (k \nabla T) \quad (6)$$

where  $\mathbf{u}$ ,  $p$ ,  $\rho$ ,  $\mu$ ,  $T$ ,  $c$ , and  $k$  are the velocity vector, pressure, density, viscosity, temperature, specific heat, and thermal conductivity, respectively. Viscous dissipation is neglected in the energy equation.

In Eq. 5, the surface tension force  $\mathbf{f}_F$  is modeled using the continuum surface force model [5]. It is reformulated as an equivalent body force acting within a band of  $2\varepsilon$  at the interface using a smeared-out Dirac delta function  $D(\xi)$ . The surface tension force can be expressed as

$$\mathbf{f}_F = -\kappa\sigma\mathbf{N}_F D(\xi) + (\mathbf{N}_F \times \nabla\sigma) \times \mathbf{N}_F D(\xi) \quad (7a)$$

where  $D(\xi)$ ,  $\mathbf{N}_F$ , and  $\kappa$  are defined respectively as

$$D(\xi) \equiv \begin{cases} \frac{1 + \cos(\pi\xi/\varepsilon)}{2\varepsilon} & |\xi| < \varepsilon \\ 0 & \text{otherwise} \end{cases} \quad (7b)$$

$$\mathbf{N}_F \equiv \frac{\nabla\xi}{|\nabla\xi|} \quad (7c)$$

$$\kappa \equiv \nabla \cdot \mathbf{N}_F \quad (7d)$$

The first and the second terms on the right side of Eq. 7a represent the capillary and the Marangoni effects respectively. The capillary force is induced by the curvature of the interface and acts perpendicular to the interface. However, the Marangoni force is generated by a variation of surface tension along the interface and acts tangentially along the interface. For the present situation, since the variation of surface tension is caused by temperature gradient, the Marangoni force is referred to as thermocapillary force.

The interface is convected by the velocity field. The evolution of the interface is governed by

$$\frac{\partial\xi}{\partial t} + \mathbf{u} \cdot \nabla\xi = 0 \quad (8)$$

To ensure that  $\xi$  remains a distance function, i.e., satisfying  $|\nabla\xi| = 1$ , redistancing is performed. This is achieved by solving for the

“steady-state” solution of a second distance function  $\psi$  given by

$$\frac{\partial \psi}{\partial \bar{t}} = \text{sign}(\xi)(1 - |\nabla \psi|) \quad (9)$$

where  $\bar{t}$  is a pseudo time for the variable  $\psi$ . The “initial” condition for Eq. 13 is  $\psi(\mathbf{x}, 0) = \xi(\mathbf{x})$ . Even with proper redistancing, mass might not be conserved. To overcome this, a global mass correction [6] is employed. The “steady-state” solution to a third distance function  $\psi'$  that ensures proper mass conservation is solved. This is written as

$$\frac{\partial \psi'}{\partial t'} = \text{sign}_{(\text{ref})} \frac{M_d M_c}{M_d} \quad (10a)$$

where  $M_d$  and  $M_c$  are the desired mass and the most current mass of the reference phase respectively. The mass of the reference phase can be calculated as

$$M = \begin{cases} \sum \rho_{\text{ref}} H \Delta - V & H_{\text{ref}} = 1 \\ \sum \rho_{\text{ref}} (1 - H) \Delta - V & H_{\text{ref}} = 0 \end{cases} \quad (10b)$$

The summation is performed over the whole solution domain. The desired mass of the reference phase is calculated as the initial mass of the reference phase. In Eq. 10a,  $t'$  is a pseudo time. The term  $\text{sign}(\xi_{\text{ref}})$  refers to the sign of  $\xi$  for the reference phase. The droplet is chosen as the reference phase in this entry. The “steady-state” values of  $\psi$  are used as the “initial” condition for Eq. 10a.

### Boundary Conditions

In this entry, the normal and tangential velocities at the inlet are specified as  $u_{\text{in}}$  and zero, respectively. No slip condition is used at all walls. The two outlets are set to the same pressure. For the energy equation, the temperature at the inlet is specified and zero gradient is applied at both outlets. All walls are insulated except the locations where the heat fluxes are applied. For the level-set functions,  $|\nabla \xi| = 1$  is imposed at all boundaries.

### Solution Procedure

The solution procedure can be summarized as:

1. Specify the locations of the interface at time  $t = 0$  and construct  $\xi$  for all nodes.
2. Set  $t = t + \Delta t$ .
3. Specify the properties for all nodes using Eq. 3a.
4. Solve the continuity and momentum equations (Eqs. 4 and 5) for  $\mathbf{u}$  and  $p$  at  $t + \Delta t$ .
5. Solve the energy equation (Eq. 6) for  $T$  at  $t + \Delta t$ .
6. Solve for  $\xi$  (Eq. 8), and perform redistancing (Eq. 9) and mass correction (Eq. 10a).
7. Repeat steps 3–6 until the solution converges.
8. Repeat steps 2–7 for all time steps.

### Numerical Method

The continuity (Eq. 4), Navier-Stokes (Eq. 5), energy (Eq. 6), and level-set (Eqs. 8, 9, and 10a) equations are special cases of a general transport equation

$$\rho \frac{\partial \phi}{\partial t} + \rho u_j \frac{\partial \phi}{\partial x_j} = \frac{\partial}{\partial x_j} \left( \Gamma \frac{\partial \phi}{\partial x_j} \right) + S \quad (11)$$

where  $\phi$ ,  $\rho$ ,  $\Gamma$ , and  $S$  are the dependent variable, density, diffusion coefficient, and source term, respectively. The finite-volume method of Patankar [7] is used to solve the transport equation given in Eq. 11. A staggered grid with the scalar variables stored at the centers of the control volumes (CVs) and the velocities located at the CVs is employed. In this entry, the power law of Patankar [7] is used to model the combined convection-diffusion effect in the momentum equations. The CLAM scheme [8] is used to model the convection of the level-set equations. The SIMPLER algorithm is used to resolve the velocity-pressure coupling. The fully implicit scheme is used to discretize the transient term. The resulting algebraic equations are solved using the tridiagonal matrix algorithm.

### Key Research Findings

The present problem is governed by a total of 8 dimensionless numbers: droplet length to

channel width ratio ( $l_d/W$ ), density ratio ( $\rho_1/\rho_2$ ), viscosity ratio ( $\mu_1/\mu_2$ ), thermal diffusivity ratio ( $\alpha_1/\alpha_2$ ), Prandtl number (Pr), Reynolds number (Re), capillary number (Ca), and Marangoni number (Ma). Pr, Re, Ca, and Ma are defined respectively as

$$\text{Pr} = \frac{\mu_2}{\rho_2 \alpha_2} \quad (12)$$

$$\text{Re} = \frac{\rho_2 u_m W}{\mu_2} \quad (13)$$

$$\text{Ca} = \frac{u_m \mu_2}{\sigma_o} \quad (14)$$

$$\text{Ma} = \frac{|d\sigma/dT| \Delta T}{\mu_2 u_m} \quad (15a)$$

The Marangoni number represents the ratio of the thermocapillary force to the viscous force. The driving temperature difference  $\Delta T$  is created by the applied heat flux  $q$ . For the purpose of nondimensionalization, the applied heat flux  $q$  is assumed to increase the fluid 2 temperature flowing out at the upper outlet by  $\Delta T$ . With this,  $\Delta T$  can be expressed in terms of  $q$  as

$$\Delta T = \frac{6q}{\rho_2 u_m c_{p2}} \quad (15b)$$

The dimensionless time  $t^*$  and temperature  $T^*$  are given by

$$t^* = \frac{t u_m}{W} \quad (16)$$

$$T^* = \frac{T - T_{\text{ref}}}{\Delta T} \quad (17)$$

Computations were made for a micro T-junction of  $W = 400 \mu\text{m}$ . The dimensionless numbers are set to  $l_d/W = 1.1$ ,  $\rho_1/\rho_2 = 1.0961$ ,  $\mu_1/\mu_2 = 0.0192$ ,  $\alpha_1/\alpha_2 = 1.1078$ ,  $\text{Pr} = 441.9882$ ,  $\text{Re} = 0.0175$ , and  $\text{Ca} = 0.00625$ . Of the 8 dimensionless numbers, only variation of Ma is considered as the effect of the thermocapillary force on the droplet motion is of interest. Results for the

case of  $\text{Ma} = 0, 40$ , and  $80$  are presented. Validations of the solution procedure were presented in [6] and will not be repeated here.

### The Case of $\text{Ma} = 0$

Figure 2 shows the evolution of a droplet in the T-junction for the case where the heater is switched off, i.e.,  $\text{Ma} = 0$ . Only the portion of the T-junction containing the droplet is depicted. To avoid overcrowding the figure, only one in every two velocity vectors is shown. Although not shown, a mesh of  $63 \times 150$  CVs with a time step of  $\Delta t^* = 1.5625 \cdot 10^{-4}$  is sufficient to achieve grid independent solution. Therefore, all subsequent computations were made with this mesh and time step size.

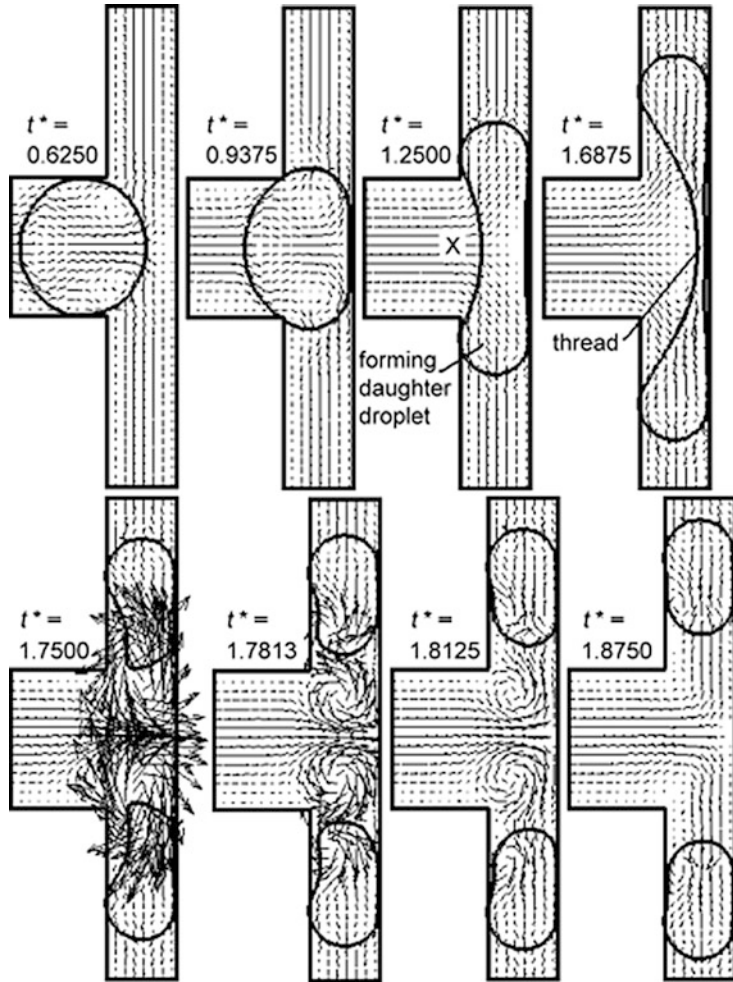
The droplet is much larger than either of the branches. When it arrives at the T-junction ( $t^* = 0.9375$ ), it blocks the T-junction and consequently creates an upstream pressure buildup. The pressure buildup squeezes the droplet into the shape of a dumbbell. The two forming daughter droplets at the two ends of the mother droplet are joined by a fluid 1 thread ( $t^* = 1.2500$ ). These two forming daughter droplets further block the flow of carrier fluid into the branches. With the increase in the pressure buildup, the forming daughter droplets are pushed further into the branches and result in a thinning of the thread ( $t^* = 1.6875$ ). The fluid 1 thread breaks eventually. The two forming daughter droplets detach from each other and become two smaller daughter droplets.

The velocity field just after the breaking off of the fluid 1 thread is highly complicated with vortices forming adjacent of the daughter droplets. For the ease of explanation, a schematic of the two daughter droplets just after the thread breaks is shown in Fig. 3.

Upon detachment, a pointed tail forms at the rear of each daughter droplet from the broken fluid 1 thread. Such a sudden creation of pointed interfaces with large curvature generates strong capillary forces instantly. The sudden availability of these strong capillary forces has a profound effect on the flow field. Given the symmetry of the flow field, the effect of the capillary forces on the lower forming daughter droplet only is discussed.  $\tau_1$  is the capillary force acting on

**Flow Bifurcation in Microchannel,**

**Fig. 2** Evolution of a droplet in a T-junction for  $Ma = 0$



lower daughter droplet at the pointed tail. It acts to pull the pointed tail towards the center of lower daughter droplet, effectively shortening the tail in the process.  $\tau_1$  is so large that the tail is able to drag along the particles of the carrier fluid adjacent to it and simultaneously increases the carrier fluid velocity dramatically. This can be seen from the suddenly increase in the carrier fluid velocity around the detached daughter droplets. However, the lower daughter droplet is still blocking branch B. This drives the fluid particles of the carrier fluid to circulate at the T-junction, generating the lower circulation. As the tail of the droplet is shortened, it becomes more rounded off, thus possesses a smaller curvature. The decrease in curvature is accompanied by decreasing capillary force. It follows that the circulation dies down as

the capillary force at the tail is no longer strong enough to sustain it. Similar phenomenon occurs to the upper daughter droplet resulting in the formation and decay of the upper circulation.

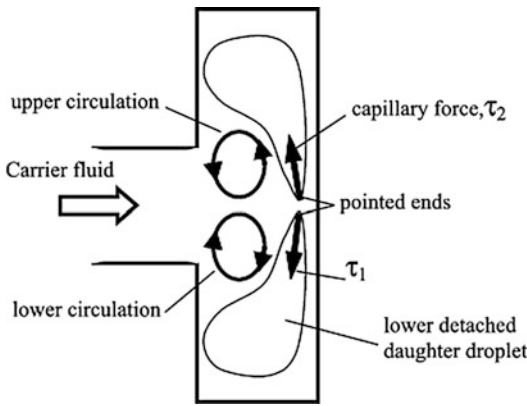
The daughter droplets become more and more circular as they travel downstream under the influence of surface tension ( $t^* = 1.8750$ ). The two daughter droplets are of equal size. This is expected given the symmetry of the flow field. Each of these daughter droplets leaves the T-junction via one of the branches.

From the above observation, a mother droplet of size smaller than the branch does not break for it fails to create the required pressure buildup for splitting. It can only flow into one of the channels at the T-junction that depends on the flow conditions in these branches.

**The Case of  $Ma = 40$**

The heater is now switched on. A nonzero heat flux  $q$ , corresponding to  $Ma = 40$ , is generated. The induced asymmetric dimensionless temperature field is shown in Fig. 4.

A strong temperature gradient is induced in the upper branch. This gives a larger variation of surface tension and results in a larger thermocapillary force. However, given the location of the applied heat flux, the temperature gradient along branch B is minimal. As a result, the variation of surface tension and the

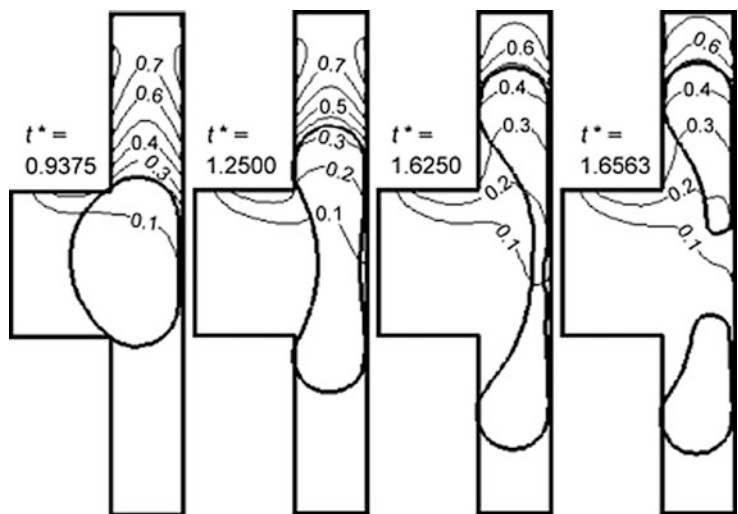


**Flow Bifurcation in Microchannel, Fig. 3** Formation of vortices as the two daughter droplets detach

thermocapillary force are both smaller. The evolution of the droplet is shown in Fig. 5.

The droplet is asymmetrically split with a larger daughter droplet formed in the upper branch. The detachment of the daughter droplets occurs earlier ( $t^* = 1.6563$ ) than that in the case of  $Ma = 0$  ( $t^* = 1.7500$ ). To explain these, Fig. 6, illustrating the flow induced by the thermocapillary forces, is constructed.

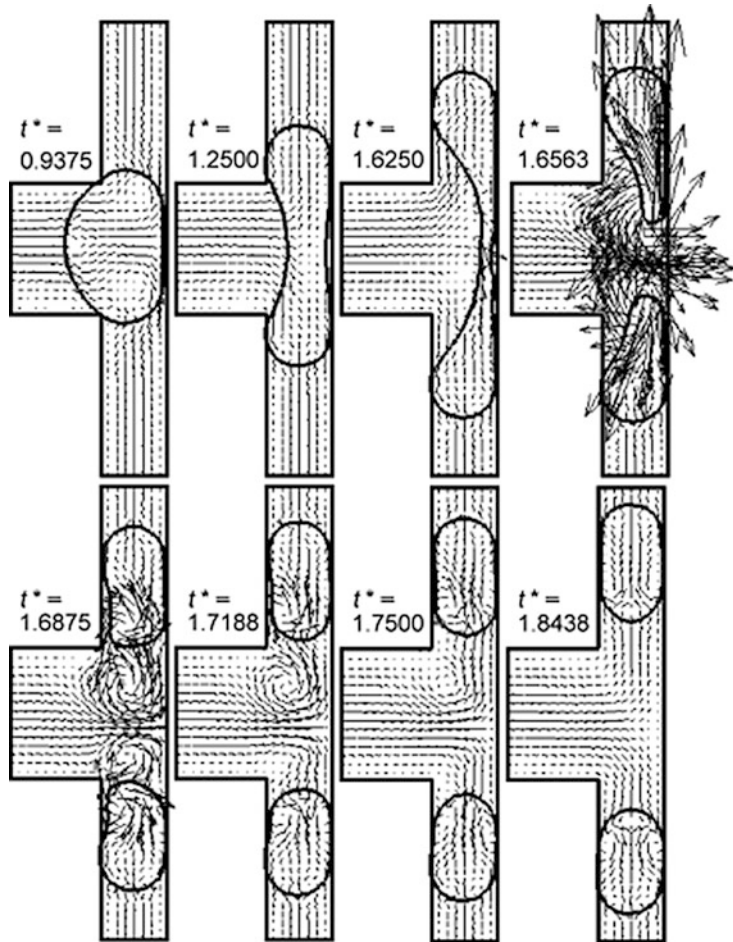
Figure 6 shows the thermocapillary forces,  $\tau_1$ ,  $\tau_2$ ,  $\tau_3$ , and  $\tau_4$ , acting at different locations of the droplet interface. These forces, downwardly directed, induce a secondary flow within the droplet of the following nature. The thermocapillary forces drive the fluid 1 particles adjacent to the interface downwards into the lower forming daughter droplet. This has the effect of depleting the fluid 1 thread and accelerates its thinning. The accumulation of the fluid 1 particles in the lower forming daughter droplet tends to inflate it. It should be noted that the magnitude of the surface tension in lower branch is larger than that of the upper branch given the lower temperature in the lower branch. Creating larger interfacial area at the tip of the lower forming daughter droplet to accommodate additional fluid 1 is not favorable as more energy is required. The fluid 1 particles then turn and flow upwards into the upper forming daughter droplet via the center of the



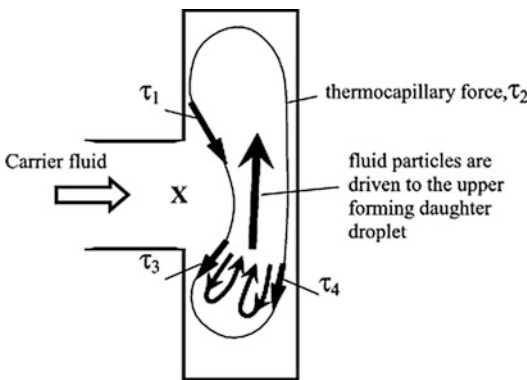
**Flow Bifurcation in Microchannel, Fig. 4** Dimensionless temperature field in a T-junction for  $Ma = 40$

**Flow Bifurcation in Microchannel,**

**Fig. 5** Unequal splitting of a droplet in a T-junction for  $Ma = 40$



F



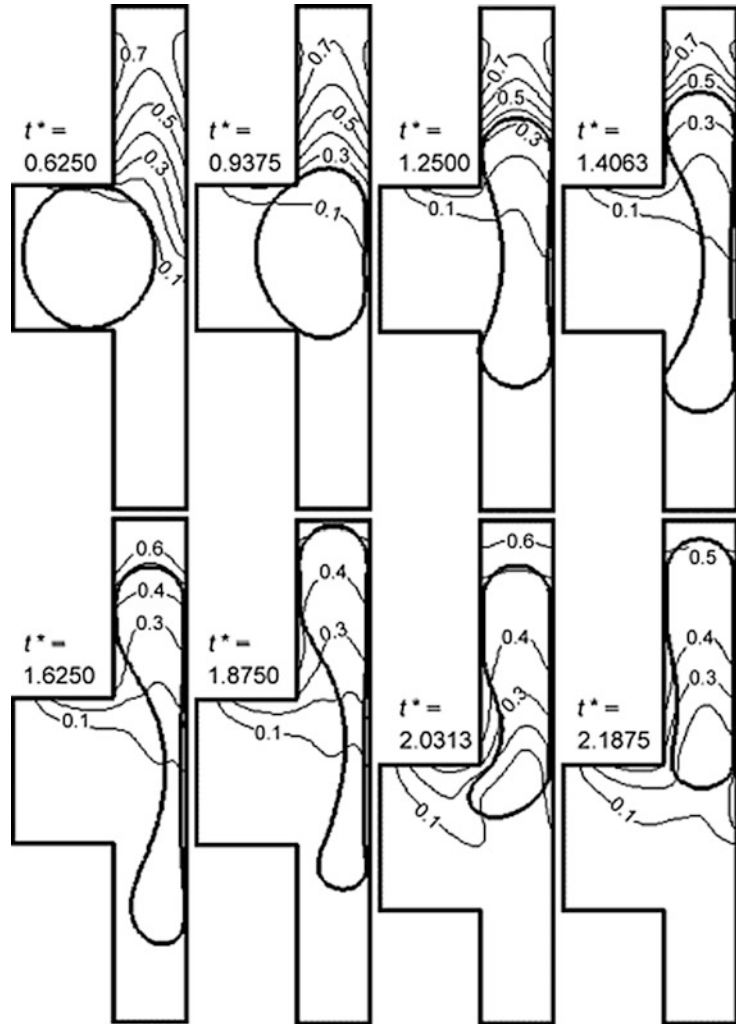
**Flow Bifurcation in Microchannel,**  
**Fig. 6** Thermocapillary forces acting on a droplet at a T-junction

fluid 1 thread. When these particles reach the tip of the upper forming daughter droplet, larger interface can be favorably created as the surface tension is smaller and thus less energy is required. As a result, more fluid 1 particles accumulate in the upper forming droplet. Upon the detachment of the two daughter droplets, the upper daughter droplet is naturally larger.

The mechanism in generating the circulations is similar to the case of  $Ma = 0$ . However, since now the interfacial forces (the resultant of capillary and thermocapillary forces) at the pointed tails of the detached daughter droplets are no longer of the same magnitude, the strength of the induced circulations is different. Although

### Flow Bifurcation in Microchannel,

**Fig. 7** Dimensionless temperature field in a T-junction for  $Ma = 80$



the capillary force at the tip of the upper detached droplet is smaller, it is compensated by a much stronger thermocapillary force. With this, the upper circulation is stronger and dies down slower.

#### The Case of $Ma = 80$

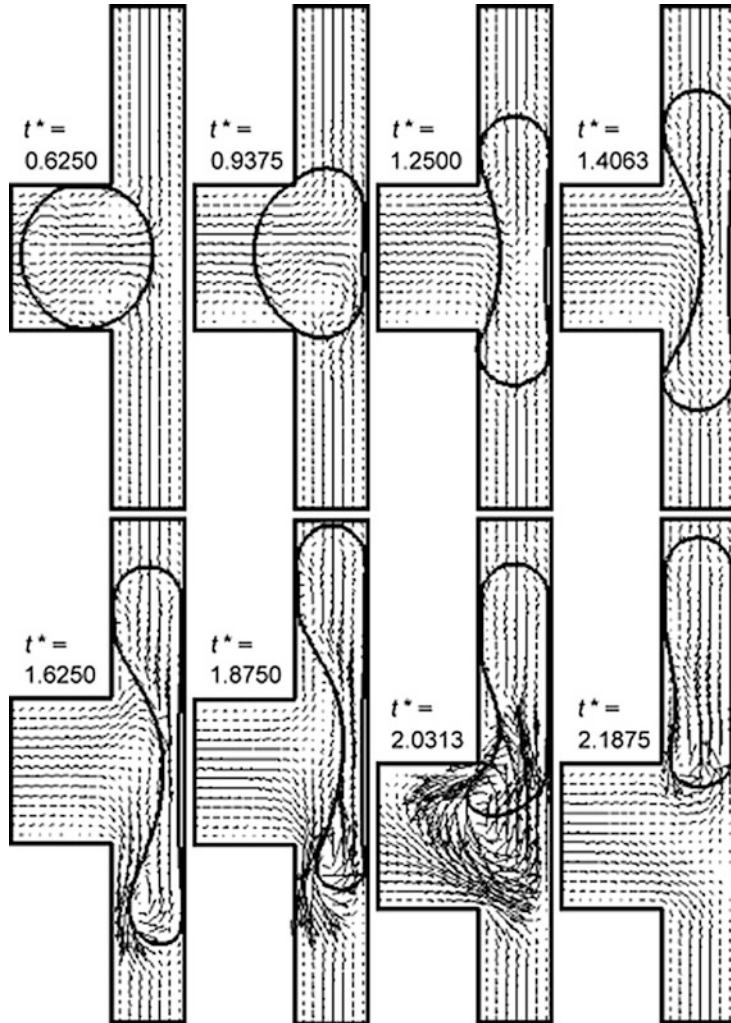
The heat flux is further increased to achieve  $Ma = 80$ . Figure 7 shows the induced dimensionless temperature field. The dimensionless temperature field exhibits a similar trend to that of the case  $Ma = 40$ . It should be noted that the actual temperature and its gradient are twice of the case with  $Ma = 40$  as a larger  $q$  is used in obtaining the dimensionless temperature. The

thermocapillary effect should therefore be twice as strong. The thermocapillary force is so strong that the droplet becomes asymmetric as early as  $t^* = 0.9375$ . The corresponding velocity field during the evolution of the droplet is given in Fig. 8. In this case, the droplet no longer splits but switches entirely into the upper branch.

To obtain a clearer picture of the switching mechanism, a more detailed flow field is required. Figure 9 shows the evolution of the droplet from  $t^* = 1.4063$  to  $t^* = 1.7813$  with all the velocity vectors plotted. For the present case, the secondary flow induced by the thermocapillary forces is much stronger. The induced secondary flow of a circulatory nature (as in the case of  $Ma = 40$ )

### Flow Bifurcation in Microchannel,

**Fig. 8** Switching of a droplet in a T-junction for  $Ma = 80$



F

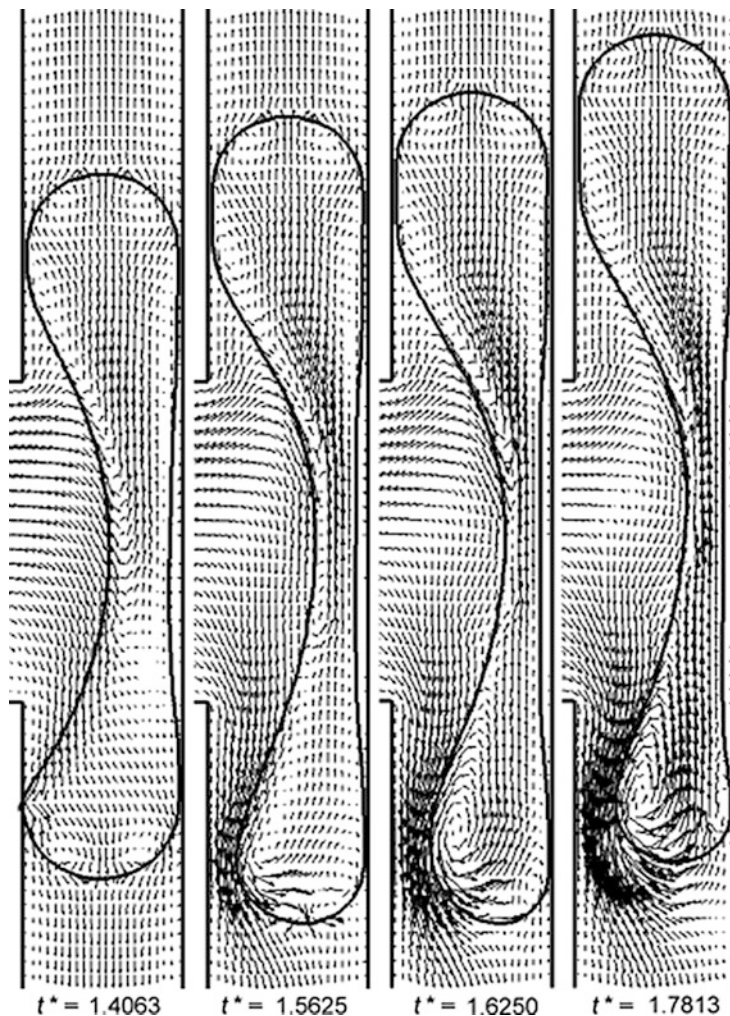
within the upper forming daughter droplet is obvious ( $t^* = 1.4063$ ). It increases significantly the flow of fluid 1 particles into the upper forming daughter droplet. The asymmetric shape of the droplet is obvious with a larger upper forming daughter droplet. Since temperature gradient induced in the lower branch is minimal, no obvious circulatory motion is observed.

Although the lower forming droplet is smaller, it is still sufficient to block the lower branch at  $t^* = 1.4063$ . Pressure does build up. The pressure buildup pushes the two forming daughter droplets into the respective branch. This is accompanied by a thinning of the fluid 1 thread. However, given the different size in the forming

daughter droplet, the ability to withstand the pressure buildup is different. The smaller lower forming droplet fails to withstand further pressure buildup eventually, and the pressure forces the creation of a small gap between the lower forming droplet and the wall ( $t^* = 1.5625$ ). The sudden release of pressure accelerates the carrier fluid into the lower branch via the gap ( $t^* = 1.5625$ ). This generates a large shear stress, downwardly directed, on the interface of the lower forming daughter droplet, creating two circulations within it. The stronger circulation accelerates the fluid particles in the lower forming daughter droplet upwards into the upper forming daughter droplet. The lower

### Flow Bifurcation in Microchannel,

**Fig. 9** Circulations in the lower forming daughter droplet



forming daughter droplet becomes smaller ( $t^* = 1.7813$ ). The fluid 1 thread does not break for (1) there is no further pressure buildup thinning it and (2) the flow of the fluid 1 particles from the lower daughter droplet to the upper daughter droplet replenishes it. As a result, the lower forming daughter droplet does not detach but merges with the upper forming daughter droplet instead. In the process, the whole mother droplet is switched into the branch A.

The two cases of nonzero  $Ma$  suggest that a temperature gradient can be used to (1) split a droplet or droplet into two daughter droplets of controllable sizes and (2) switch a droplet into a desired branch in a bifurcating microchannel.

### Future Directions for Research

Controllable splitting and switching of a droplet into a desired branch at a bifurcating T-junction with thermocapillary effects has been demonstrated numerically. The relative size of the two daughter droplets, strongly dictated by the Marangoni number, is a parameter of interest and requires further investigation. Occasionally, the droplet carries non-fluid particles, e.g., cells or bioparticles, in the form of encapsulation. These particles may break out from the encapsulation during splitting or switching. Therefore, effect of having these encapsulated particles needs to be examined.

## Cross-References

- ▶ [Droplet Dynamics in Microchannels](#)
- ▶ [Surface-Tension-Driven Flow](#)
- ▶ [Thermocapillarity](#)
- ▶ [Two-Phase Flow](#)

## References

1. Tan YC, Fisher JS, Lee AI, Cristini V, Phillip A (2004) Design of microfluidic channel geometries for the control of droplet volume, chemical concentration and sorting. *Lab Chip* 4:292–298
2. Link DR, Anna SL, Weitz DA, Stone HA (2004) Geometrically mediated breakup of drops in microfluidic devices. *Phys Rev Lett* 92(5):054503/1–054503/4
3. Ting TH, Yap YF, Nguyen NT, Wong TN, John JC, Yobas L (2006) Thermally mediated breakup of drops in microchannels. *Appl Phys Lett* 89(23):234101/1–234101/3
4. Osher S, Sethian JA (1988) Fronts propagating with curvature-dependent speed: algorithms based on Hamilton-Jacobi formulations. *J Comput Phys* 79:12–49
5. Brackbill JU, Kothe DB, Zemach C (1992) A continuum method for modelling surface tension. *J Comput Phys* 100:335–354
6. Yap YF, Chai JC, Wong TN, Toh KC, Zhang HY (2006) A global mass correction scheme for the level-set method. *Numer Heat Trans B* 50:455–472
7. Patankar SV (1980) *Numerical heat transfer and fluid flow*. Hemisphere, New York
8. Van Leer B (1974) Towards the ultimate conservative difference scheme. II. Monotonicity and conservation combined in a second-order scheme. *J Comput Phys* 14:361–370

## Flow Boiling Instability

David Brutin  
 Mechanical Engineering Department,  
 Aix-Marseille University, IUSTI UMR 7343  
 CNRS, Marseille, France

## Synonyms

Liquid–vapor instability; Two-phase flow instability

## Definition

When two-phase flow phase change occurs in a channel with a small hydraulic diameter compared with the capillary length, *flow boiling instabilities* may arise. As in classical-sized channels, the instabilities can be static or dynamic; however, their intensity is higher in microchannels due to the higher rate of volumic generation of vapor which induces considerable pressure drops.

## Overview

Between 1985 and 2006, 1,247 papers were published on ScienceDirect® on the subject of boiling, of which only 49, i.e., about 4 %, deal with mini- or microchannels. Four of these 49 papers report flow instabilities. Even if flow boiling is a well-developed research subject, flow boiling in microchannels, not to mention instabilities which occur in these microchannels, have not been discussed or reported to any considerable extent in the literature. In Table 1, a few studies dealing with *flow boiling instabilities* in microchannels are listed. We will discuss some of these studies below.

Wu and Cheng [1] conducted experiments using eight parallel silicon microchannels heated from the bottom. They observed water flows with large-amplitude or long-period oscillating boiling modes as a function of heat flux and mass flux depending on whether the water outlet is at saturation temperature or superheated.

Qu et al. [2] found evidence of two kinds of unsteady flow boiling for 21 parallel microchannels measuring  $231 \times 713 \mu\text{m}$ . They observed in their parallel microchannel array either a global fluctuation of the whole two-phase zone for all the microchannels (Fig. 1) or chaotic fluctuations of the two-phase zone (Fig. 2): overpressure in one microchannel and under-pressure in another. The individual microchannel mass flow rate was not controlled.

Hetsroni et al. [3] created an experimental setup to study liquid–gas and liquid–vapor flow in parallel triangular microchannels with diameters of  $103\text{--}161 \mu\text{m}$ . They used a fast video camera coupled with a microscope through a Pyrex

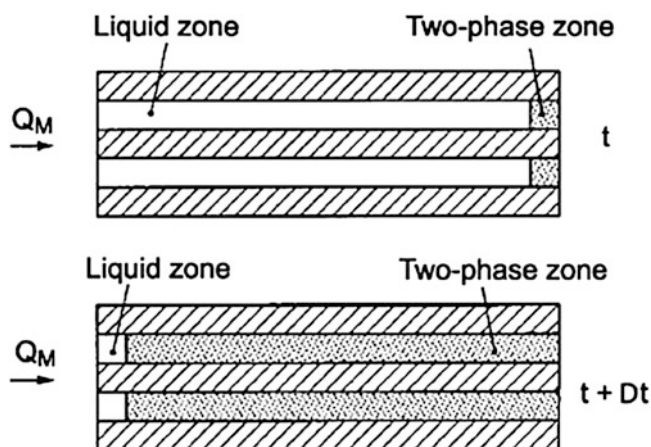
**Flow Boiling Instability, Table 1** Studies on boiling flow instabilities in microchannels

Authors, year [reference]	Size	Shape	Aim of the study
Brutin, 2003 [7]	889 $\mu\text{m}$	Rect.	Evidence of confinement flow instabilities
Wu, 2003 [1]	186 $\mu\text{m}$	Tri.	Surface temperature fluctuations
Peles, 2003 [4]	50–200 $\mu\text{m}$	Tri.	Observation of flow regimes
Bergles, 2003 [10]	–	–	CHF and flow instabilities
Qu, 2003 [2]	349 $\mu\text{m}$	Rect.	Coupling instabilities in parallel microchannels
Li, 2003 [11]	51.7 $\mu\text{m}$	Tri.	Unsteady flows observed in two parallel microchannels

Rect rectangular, Tri triangular

**Flow Boiling Instability,**

**Fig. 1** Top view of a severe pressure drop oscillation [2]

**Flow Boiling Instability,**

**Fig. 2** Top view of a mild parallel channel instability [2]

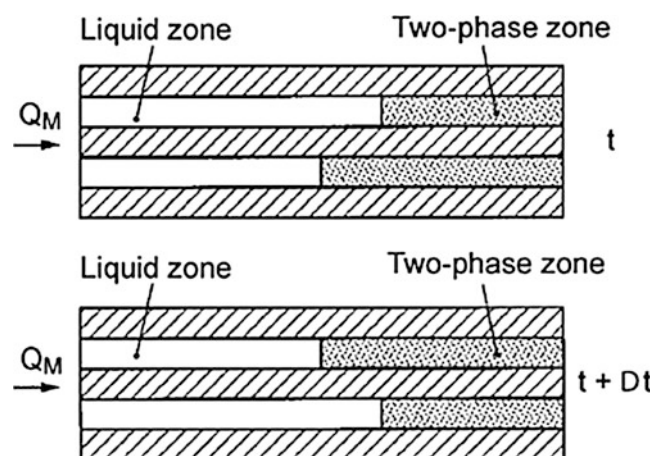


plate to record the flow patterns. They showed the influence of the injection method (plenum shape) and found evidence for the same inlet conditions, i.e., mass flow rate and heat flux and different flow patterns (annular flow, bubbly flow, etc.). The random nature of this flow in the parallel microchannels results from the inlet mass flow

rate, which is not constant but depends on the pressure drop in each microchannel.

Peles [4] made a micro heat exchanger using photolithography processes on a silicon substrate. The micro heat exchanger was based on multiple parallel triangular microchannels. The results obtained using pressure measurements and fast

**Flow Boiling Instability, Table 2** Classification of flow instabilities (based on [5])

Class	Type	Characteristics	Observed by
Static	Ledinegg instability	Flow undergoes sudden, large-amplitude excursion to a new stable operating condition	[3, 7]
Static	Boiling crisis	Wall temperature excursion and flow oscillation	[3, 7]
Static	Flow pattern transition instability	Cyclic flow pattern transition and flow rate variations	[8]
Static	Bumping, geysering, or chugging	Period process of superheat and violent evaporation with possible expulsion and refilling	[7]
Dynamic	Acoustic oscillations	High frequencies related to time required for pressure wave propagation in system	–
Dynamic	Density wave oscillation	Low frequencies related to transmit time of a continuity wave	–
Dynamic	Thermal oscillations	Occur in film boiling	–
Dynamic	Coupling instabilities	Strong only for a small fuel time constant and under low pressures	[3, 7]
Dynamic	Pressure drop oscillations	Very low-frequency periodical process	[2, 7]

video recording of flow boiling evidence various flow regimes such as *rapid bubble growth*, *complete bubble flow*, *bubbly flow*, and *annular flow*. The first two regimes described by the author are presented as specific at the microscale. Flow instabilities are observed such as temperature and pressure fluctuations at a frequency which decreases with increasing mass flow rates (high peristaltic pump frequency).

As for flow boiling instabilities in classical channels, several types of instabilities have been observed and reported by different authors. Table 2 summarizes these instabilities and their physical consequences on the fluid flow. We also show in the following table which publications reported these instabilities in microchannels. This classification is based on the one proposed for channels by Bergles in 1976 [5] and is divided into two categories:

- Static instabilities induce a shift of the equilibrium point to a new steady-state point: Ledinegg instability, boiling crisis, bumping, geysering, or chugging are all static instabilities since they can be analyzed using only stationary models.
- Dynamic instabilities are driven by the inertia of the system; the stationary state is not sufficient to predict the destabilization threshold of these instabilities such as acoustic waves, pressure drop oscillations, or thermal oscillations.

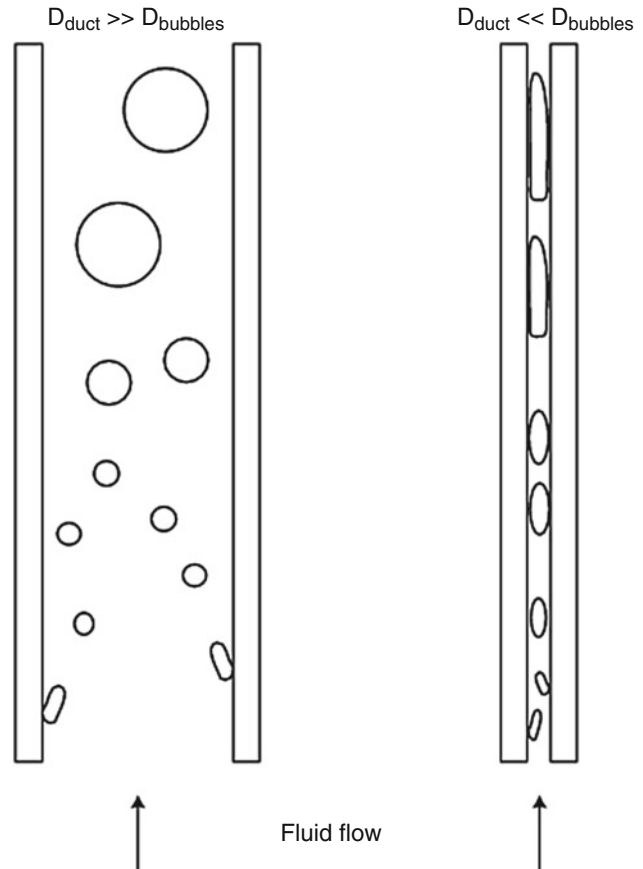
## Basic Methodology

### Influence of Confinement on Flow Boiling

The confinement effect on boiling appears through the influence of the wall on the flow. In a large tube, boiling is not influenced by the wall of the duct, and the flow is free to structure itself and evolve inside. In our minichannel, dimensions are such that the bubble growth from a nucleation site is modified by the proximity of the wall (Fig. 3). One criterion is to verify whether the theoretical diameter of the bubbles is larger than the diameter of the duct. We estimate the bubble detachment diameter using the correlation of Fritz [6] which takes into account nucleation surface orientation for *n*-pentane. Equation 1 is used where  $\theta$  is the wetting angle expressed in degrees. This relation is based on the balance between surface tension and buoyancy forces. We obtain a bubble detachment diameter of 600  $\mu\text{m}$ , which means that inside our minichannel with a thickness of 500  $\mu\text{m}$ , the proximity of the wall influences the evolution of the bubble. Thus, it is reasonable to think that wall confinement influences the vapor bubble behavior and coalescence in the minichannel:

$$D_{\text{bubbles}} = 0.0208 \theta \sqrt{\frac{\sigma}{g(\rho_L - \rho_G)}} \quad (1)$$

**Flow Boiling Instability,**  
**Fig. 3** Wall influence on  
 flow boiling behavior



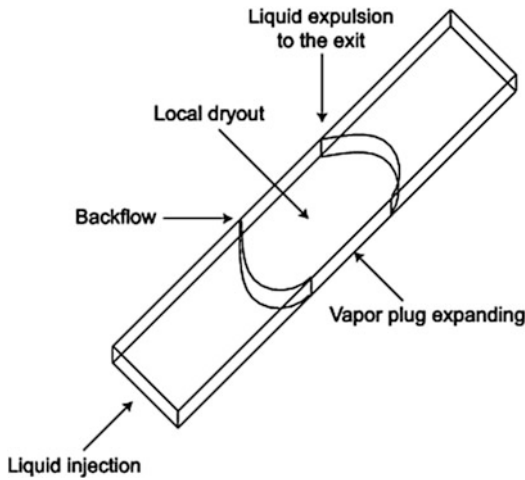
We can consider that one degree of freedom has been removed. The consequence is that bubbles grow along the other two axes (width and length). Whereas bubbles are supposed to be spherical without the influence of any wall, here they are compressed. This modification of shape induces an increase in wall friction. Confinement increases bubble coalescence by reducing the volume of the channel for a given heating surface; the volumic density of the bubbles grows quickly, and thus bubbles group together to form slugs. Due to the proximity of the wall, wall friction for the evolution of bubbles and slugs is increased. When vapor slugs flow through the minichannel, this induces overheating of the wall due the reduction of heat transfer associated with the vapor phase (Figs. 4 and 5). These periodical slugs become more and more numerous as the heat flux increases or the liquid mass flow rate decreases.

### Analysis of Instabilities

**Pressure Drop and Visualization of Flow Patterns**  
 To analyze flow boiling instabilities in a minichannel or a microchannel, pressure measurements recorded at a high frequency (e.g., 200 Hz) are usually performed. The analysis of the microchannel pressure drop is then related to flow patterns to understand destabilization mechanisms.

Brutin et al. [7] recorded the pressure signal of the unsteady flow simultaneously with video recording to compare both frequencies: pressure drop and flow pattern oscillation frequencies. In Fig. 6, they analyze the two-phase flow behavior which is partially presented with pictures in Fig. 7. The different steps observed during one period are the following:

- Liquid flows in the channel (point A). Bubbles are created at the beginning of the two-phase flow zone. Their size and generation rates are

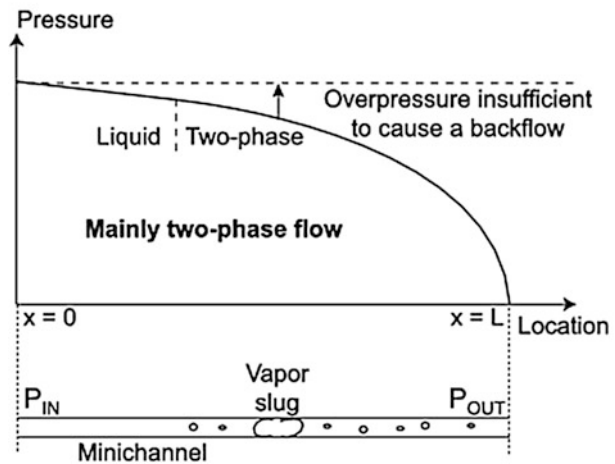
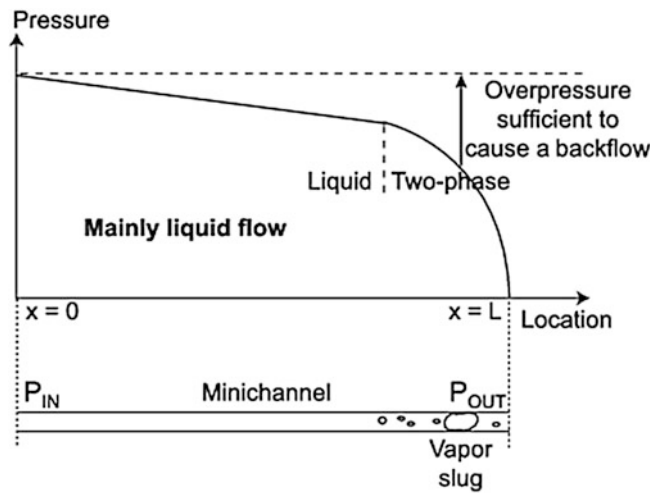


**Flow Boiling Instability, Fig. 4** Local dry out due to a vapor slug

such that bubbles coalesce into vapor slugs which evolve in the channel. Vapor slugs generate overpressure which reduces the upstream boiling flow rate.

- Bubbles growing before the vapor slug slow down, stop (point B), and then quickly reach the entire channel cross section. Vapor created by bubble expansion must be evacuated, but downstream in the channel vapor slugs block the flow.
- Expanding vapor pushes the inflow back to the entrance using the buffer tank as a mass flow storage (point C).
- Eventually, the channel is full of vapor (point D). The surface temperature rises due to the fact that the heat flux is permanently supplied to the fluid and not removed by boiling.

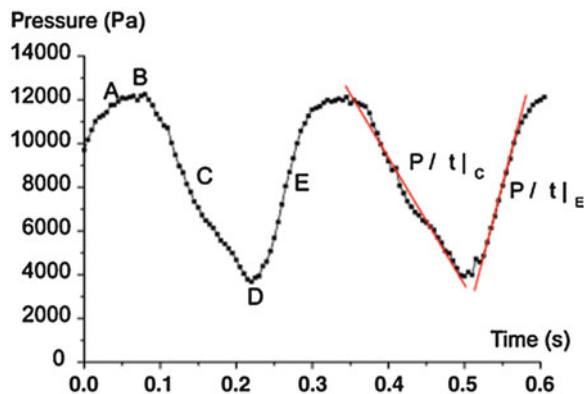
F



**Flow Boiling Instability, Fig. 5** Local pressure in a minichannel for two situations: a mainly liquid flow and a mainly two-phase flow

**Flow Boiling Instability,**

**Fig. 6** Typical outlet pressure signal during unsteady boiling over two periods ( $D_H = 888.9 \mu\text{m}$ ,  $L = 200 \text{ mm}$ ,  $\text{Re}_L = 955$ ,  $Q_W = 9.6 \text{ Wcm}^{-2}$ )



- When the channel is empty and upstream pressure before the channel entrance is sufficient, the entire vapor slug which occupies the channel is expelled. The channel is refilled with liquid (point E).
- Due to the high surface temperature, bubbles are formed rapidly (point A), and the phenomenon is repeated.

If we look at the evolution of pressure in Fig. 6, we observe three distinct parts in one period (about 275 ms). The first consists of the decrease in pressure for approximately 150 ms from B to D. The average pressure decrease in C is 62 kPa/s, whereas in the second part the refilling of the liquid, with a duration of about 65 ms, corresponds to the D to A part on the curve. The average pressure increase in E is about 136 kPa/s. The third part between A and B flowing in the channel and slowing down accounts for only 60 ms of one period.

Qu et al. [2] observed in their experiment that hydrodynamic instabilities influence inlet and outlet pressures and can induce a degree of uncertainty in the measurement of pressure drop. They recorded temporal pressure signals and made the following observations: even with a small heat flux supplied to the parallel channels, the case of pressure drop oscillations presents pressure fluctuations with quite constant frequency, whereas in the case of instability in the parallel channels, the fluctuations are small and random.

Hetsroni et al. [3] also found evidence of a coupling phenomenon for an array of 17 parallel

microchannels. In Fig. 7 from [3], they found evidence of two-phase flow oscillations. Only one channel is followed as a function of time. The water-steam flow is from the left to the right. Steam appears in the fifth picture. The liquid-vapor interface then moves to the exit or to the entrance. This interface movement is representative of a nonconstant mass flow provided to the microchannel. The inlet condition before the plenum is a constant inlet pressure; however, due to the plenum, the flow can come back and induce such coupling. The frequency of the interface oscillation can usually be related to the total pressure drop oscillation frequency.

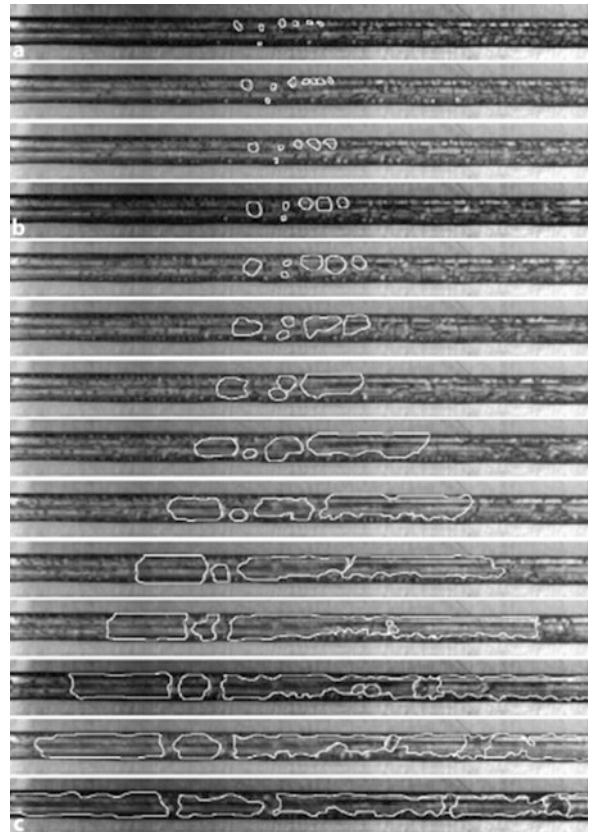
**Scaling Laws Analysis**

Scaling laws help to understand the flow patterns and heat transfer phenomenon without any constraint of geometry, fluid type, or operation conditions. The terms used to determine these scaling laws are dimensionless and usually balance the physical processes involved. In the present case of flow boiling, the pressure drop is considered without dimension usually using the dynamic pressure.

Figure 8 from [8] presents the total minichannel pressure loss as a function of the inlet Reynolds number. The total pressure loss includes liquid, two-phase, and vapor depending on the boiling stage in the minichannel. The curve behavior is a classical N-shape observed for all the heat fluxes studied. The total minichannel pressure loss is the sum of fluid pressure loss for each zone and arises when the friction term in the

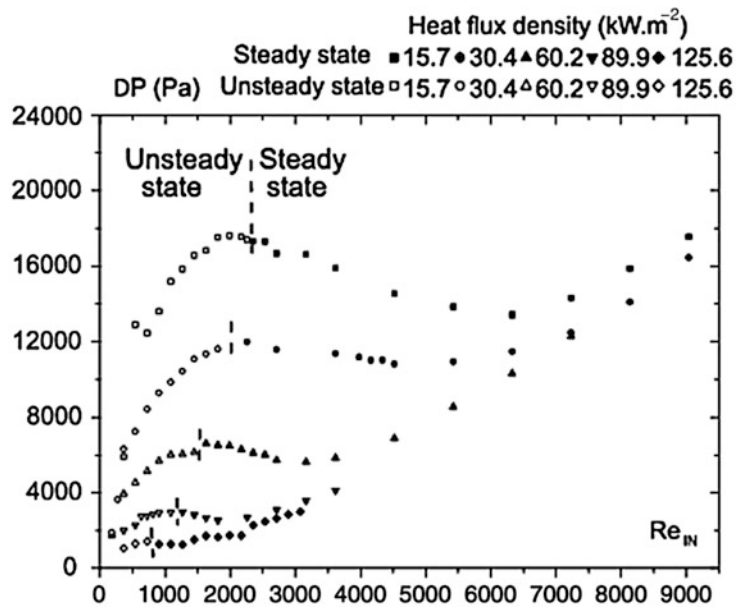
**Flow Boiling Instability,**

**Fig. 7** Vapor slug formation during flow boiling: example of backflow (5 ms between 2 pictures) (some bubble outlines were evidenced in order to follow their evolution)



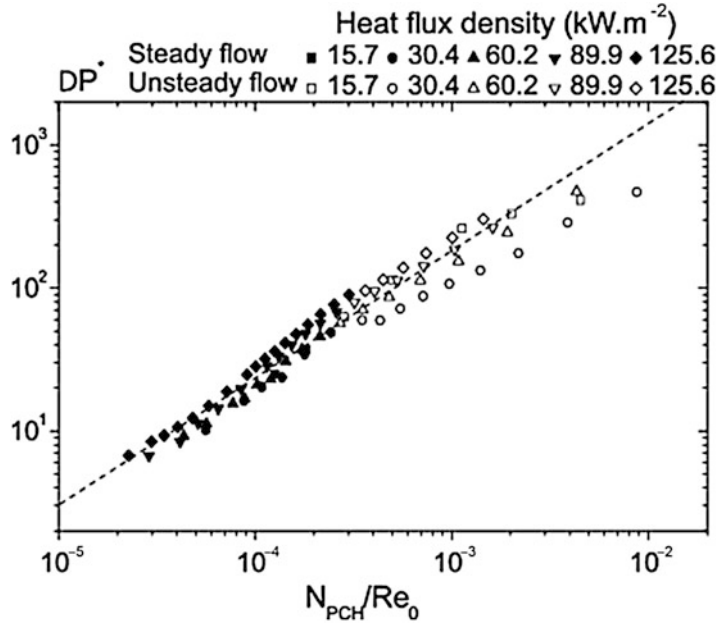
**Flow Boiling Instability,**

**Fig. 8** Average pressure loss versus inlet Reynolds number when the buffer is not connected to the loop for five heat fluxes



**Flow Boiling Instability,**

**Fig. 9** Pressure loss scaling law for all heat flux densities provided: non-dimensioned pressure loss function of the ratio between the phase change number and the Reynolds number for only exit vapor qualities strictly between 0 and 1



two-phase zone reaches a maximum then decreases when the flow is mainly vapor. With increasing heat fluxes, the pressure loss shifts to higher values, and the N-shape is more and more pronounced. Using the experimental results of the visualization, it is possible to propose a global behavior of the fluid flow in the channel with the non-dimensioned pressure loss variation. If we remove all points which present liquid flow operating conditions and those for mainly vapor flow, we obtain in Fig. 9 [9] only the operating conditions which satisfy the exit vapor quality strictly between 0 and 1.

The case studied is characterized by a constant mass flow rate supplied to the channel entrance. All the results concerning pressure loss are on one line, which means the same variation law. Equation 2 gives the pressure loss scaling law numerically. It is also possible from Fig. 9 to extract the criterion for the transition from steady to unsteady. This law provides an equivalent friction factor for the two-phase flow:

$$\Delta P_{comp}^* = 4.46 \cdot 10^4 \left( \frac{N_{pch}}{Re_0} \right)^{0.818} \quad (2)$$

Figure 9 evidences a possible generalization of the steady and unsteady results. The stability

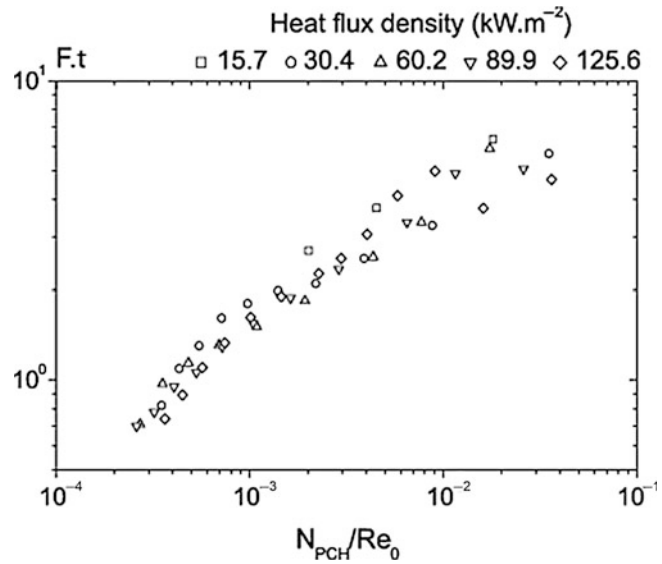
transition appears for a given abscissa and thus a given ordinate. These coordinates are summarized by the ratio  $K_2/K_1$  previously detailed with Eq. 21. The experimental value of  $K_2/K_1$  is  $4.94 \cdot 10^{-6} \pm 30\%$  with a comparison with the theoretical value which is  $3.92 \cdot 10^{-6} \pm 7.5\%$ . We obtain a good agreement between experimental and theoretical thresholds. The gap of 26% for the confinement case should be compared with the total uncertainty of 37.5%. The uncertainty of the experimental and theoretical destabilization thresholds (Eqs. 3 and 4) is four times the liquid inlet velocity uncertainty and four times the hydraulic diameter uncertainty plus the total pressure drop and the heat flux uncertainties:

$$\Delta P^* = \frac{\Delta P}{\frac{1}{2} \rho_0 U_0^2} \quad (3)$$

$$\frac{N_{pch}}{Re_0} = \frac{Q_w}{U_0^2} \frac{4L v_0}{\rho_0 D_H^2} \quad (4)$$

The two-phase flow oscillation frequencies observed can also be analyzed using a nondimensional approach. Their experimental values are obtained on the basis of the fast Fourier

**Flow Boiling Instability,**  
**Fig. 10** Non-dimensioned oscillation frequency as a function of  $N_{pch}/Re_0$



transformation of the pressure drop which evidences frequencies of high energy. The fundamental frequency is the one we deal with here. The oscillation mechanism is based on the two-phase transport along the minichannel; the pressure oscillations are mainly driven by a convective phenomenon. Thus, the convective time ( $\tau$ ) defined in Eq. 5 is used:

$$\tau = \frac{L}{U_0} \tag{5}$$

The nondimensional two-phase flow frequency ( $F.\tau$ ) is plotted as a function of ( $N_{pch}/Re_0$ ). A single curve is found for all the operating conditions. This behavior confirms that the oscillation frequency is mainly driven by the phase change phenomenon and inertia effects (Fig. 10). The dispersion is probably due to the uncertainty associated with the measurement of the frequency.

Scaling laws of flow boiling instabilities can also be applied to heat transfer. In Brutin et al. [9], the heat transfer coefficient calculated is based on the average surface and fluid temperature. A total heat flux is provided ( $\overline{Q}_w$ ), whereas locally the heat flux is redistributed inside the aluminum rod. Thus, the local surface and fluid

temperatures cannot be used to calculate a local heat transfer coefficient but can only provide a global heat transfer coefficient. Using the average temperature difference between surface and fluid ( $\overline{T}_s - \overline{T}_f$ ) and the total heat flux transferred to the fluid, we calculate a global heat transfer coefficient (Eq. 6). Figure 12 of [8] presents only operating conditions which correspond to a two-phase zone in the minichannel. The objective is to analyze how the two-phase flow contributes to heat transfer.

For increasing heat fluxes, the N-shape is more and more pronounced. Dark points in Fig. 12 of [8] represent a steady flow, whereas the white points are for an unsteady flow. A mean heat transfer coefficient is deduced. Introducing the Stanton number, we compare the heat flux transferred to the fluid with the heat transported with the fluid. If we only consider the operating conditions which satisfy a two-phase zone mainly in the minichannel (Fig. 8 of [9]), a heat transfer scaling law appears (Eq. 8). Thus it is possible to predict a mean heat transfer coefficient when a two-phase zone is mainly inside the minichannel:

$$\overline{h} = \frac{\overline{Q}_w}{\overline{T}_s - \overline{T}_f} \tag{6}$$

$$St = \frac{\bar{h}}{\rho_0 C_{p0} U_0} \quad (7)$$

$$St = 0.776 \left( \frac{N_{pch}}{Re_0} \right)^{0.589} \quad (8)$$

### Destabilization Mechanism

To use or predict flow boiling instabilities, it is essential to understand the mechanisms which lead to the instabilities. These mechanisms can usually be found by analyzing the flow patterns. For flow boiling in a microchannel, the previous section evidenced that flow boiling instabilities appear and lead to periodical pressure oscillations. The flow even returns to the entrance (Fig. 7). To determine the destabilization mechanism which occurs in such a situation, we quantified the phenomena involved in the instability, such as vapor generation rate, total channel pressure drop, etc.

Brutin et al. [9] studied the transition from steady to unsteady flow boiling and developed a transition criterion. This study was performed experimentally in minichannels but the theory also applies to confined geometries such as microchannels. This criterion is based on observations of the unsteady two-phase flow: the two-phase flow stops at a location in the microchannel, then all the fluid after this location is expelled toward the exit, whereas all the fluid before this location is sent back to the entrance. This two-phase backflow has been evidenced previously [7]; however, the location of this split remained unexplained.

On the basis of Fig. 5 from [9],  $L_c$  was defined as the location in the channel where the flow stops and the slug expands and then purges all the fluid out of the minichannel.  $U_0$  is the injection liquid velocity at the bottom of the minichannel and  $\bar{U}$  the average two-phase flow evacuation velocity. Two terms were quantified: the overpressure induced by the expansion of the vapor slug and the injection pressure minus the minichannel outlet pressure.

The pressure necessary to evacuate all the fluid from the minichannel is the minichannel pressure loss because the outlet pressure is higher

than atmospheric pressure. To estimate the friction pressure loss in the minichannel, acceleration and gravity terms were ignored. The physical properties of two-phase flow were considered to be the average between the inlet and the outlet. When unsteady states appear, the fluid was considered as entering in a saturated condition. Thus the expression was established of the overpressure ( $\Delta P_{slug}$ ) required to evacuate the entire two-phase flow from the minichannel (Eq. 9). The flow regime considered just after the flow stops is laminar as this minimizes the energy used for the evacuation; a turbulent regime would necessitate much more enthalpy, and thus the overpressure would be much higher. In the expression  $\bar{\lambda} = \alpha/\bar{Re}$ ,  $\alpha = 82.36$  was taken for their geometry aspect ratio. The minichannel pressure loss is  $\Delta P_{minichannel}$ . The overpressure created by the vapor slug is scaled by the dynamic pressure  $(1/2)\rho_0 U_0^2$ :

$$\Delta P_{slug} = \bar{\lambda} \frac{L}{D_H} \frac{\rho_m U_m^2}{2} = \frac{\alpha L \bar{v} \rho_m U_m}{2 D_H^2} \quad (9)$$

$$\frac{\Delta P_{slug}}{\frac{1}{2} \rho_0 U_0^2} = \bar{\lambda} \frac{L}{D_H} \frac{\bar{\rho} U_m^2}{\rho_0 U_0^2} = \frac{\alpha L \bar{v} \rho_m U_m}{\rho_0 U_0^2 D_H^2} \quad (10)$$

If the overpressure created by the vapor slug is higher than the minichannel pressure loss, the slug can grow and purge the minichannel. This condition can be written as Eq. 11 and in non-dimensioned form as Eq. 12:

$$\Delta P_{slug} > \Delta P_{channel} \quad (11)$$

$$\frac{\Delta P_{slug}}{\frac{1}{2} \rho_0 U_0^2} > K_1 \quad (12)$$

Thus  $K_1$  is the critical threshold to be reached. Viscosity, density, and average velocity of the two-phase flow to be purged must be determined. With the average vapor quality, it is possible to estimate the product between the density and average velocity of the two-phase flow. Thus, if we consider Eq. 13, the solution of the enthalpy equation gives Eq. 14. The heated perimeter for

a rectangular microchannel ( $d + 2e$ ) will henceforth be referred to as  $\delta$  for the purpose of mathematical simplification:

$$\rho_0 U_0 L_V \frac{d\chi_V}{dz} = \frac{Q_W(d + 2e)}{A_H} \quad (13)$$

$$\chi_V(z) = \frac{Q_W \delta z}{A_H L_V \rho_0 U_0} \quad (14)$$

The average vapor quality ( $\bar{\chi}_V$ ) is obtained by the continuous averaging of the vapor quality along the minichannel. It can also be defined as the ratio between the average vapor mass flow rate and the total liquid flow injected (Eq. 16):

$$\bar{\chi}_V = \frac{1}{L} \int_{z=0}^{z=L} \chi_V(z) dz = \frac{Q_W \delta L}{2 A_H L_V \rho_0 U_0} \quad (15)$$

$$\bar{\chi}_V = \frac{\bar{m}_V}{\dot{m}_0} = \frac{\rho_m U_m}{\rho_0 U_0} \quad (16)$$

$$\rho_m U_m = \frac{Q_W \delta L}{2 A_H L_V} \quad (17)$$

The average viscosity  $\bar{\nu}$  is estimated from the Dukler correlation (Eq. 18) for a homogeneous medium. Using the average vapor quality, it is deduced that the average two-phase flow viscosity is  $\nu_0/2$ :

$$\begin{aligned} \bar{\nu}(z) &= \nu_V \chi_V(z) + \nu_L [1 - \chi_V(z)] \\ &= \nu_L - \chi_V(z) [\nu_L - \nu_V] \end{aligned} \quad (18)$$

The criterion which must be satisfied in order to allow vapor slug expansion is given by Eq. 19. When it is expressed using the inlet control parameters (heat flux,  $Q_W$ ; liquid inlet velocity:  $U_0$ ), we obtain

$$\frac{\alpha L \nu_0 \rho_m U_m}{2 \rho_0 U_0^2 D_H^2} > K_1 \quad (19)$$

$$\frac{Q_W}{U_0^2} > K_1 \frac{4 \rho_0 A_H L_V D_H^2}{\alpha \nu_0 \delta L^2} \quad (20)$$

The threshold of Eq. 20 will be referred as  $K_2$  in further calculations. The relation between  $K_1$  and  $K_2$  is given by Eq. 21 which only depends on physical and geometric parameters. The uncertainty of the threshold is only due to the uncertainty of the hydraulic diameter of the minichannel:

$$\frac{K_2}{K_1} = \frac{\alpha \nu_0 \delta L^2}{4 \rho_0 A_H L_V D_H^2} \quad (21)$$

Using this theoretical threshold, it is possible to link the critical pressure loss to a critical heat flux through Eq. 22. There exists a critical pressure loss for a given heat flux, fluid, and geometry which destabilizes the two-phase flow:

$$\frac{\Delta P_{\text{channel}}^c}{Q_W^c} = \frac{\rho_0}{2} \frac{K_2}{K_1} = \frac{\alpha \nu_0 \delta L^2}{8 A_H L_V D_H^2} \quad (22)$$

## Key Research Findings

Research over the last decade has provided a huge amount of data on flow boiling instabilities in microchannels. As far as we know today, the instabilities which occur in microchannels appear in the same way as in classical channels (see Table 2). Scaling laws have been evidenced for the stability transition criteria, such as the oscillation frequency of the instabilities, as has been shown in the previous sections. This enables us to conclude that all flow boiling instabilities in microchannels have at least one origin, which is space confinement. However, other phenomena, such as coupling with the experimental loop or the injection device, can lead to other supplementary instabilities.

## Future Directions for Research

The literature provides studies on flow boiling in single and parallel microchannels. Both configurations lead to flow instabilities which are clearly identified. The specificity of flow instabilities in microchannels is the appearance of intermittent dry out which can lead to vapor recoil. New experiments on a smaller scale need to be performed to

investigate the phenomena which occur at the scale of a bubble. In such confinements where the bubble size is close to or bigger than the hydraulic diameter, the physics involved does not seem to be the classical physics used to model or study pool boiling or flow boiling in ducts. The physical description required to build the theory and the models needs to be close to the triple line.

Such instabilities also appear for different gravity levels, which is also a research subject investigated over the last decade. The ESA (European Space Agency) and CNES (French Space Agency) currently fund research programs on boiling on a microscale either in pool boiling at the scale of a bubble or for flow boiling. The objective is to enable the industrial development of compact heat exchangers working in microgravity. Experiments must be performed in microgravity, using, for example, parabolic flights (Novespace<sup>®</sup>) during which it is possible to create microgravity conditions ( $\pm 0.05$  g) lasting about 20 s.

## Cross-References

- ▶ [Boiling and Evaporation in Microchannels](#)
- ▶ [Bubble Dynamics in Microchannels](#)
- ▶ [Pressure-Driven Two-Phase Flows](#)

## References

1. Wu HY, Cheng P (2003) Two large-amplitude/long-period oscillating boiling modes in silicon microchannels. In: 1st international conference on microchannels and minichannels. ASME, Rochester, pp 629–633
2. Qu W, Mudawar I (2003) Measurement and prediction of pressure drop in two-phase micro-channels heat sinks. *Int J Heat Mass Transf* 46:2737–2753
3. Hetsroni G, Mosyak A, Segal Z, Pogrebnyak E (2003) Two-phase flow patterns in parallel micro-channels. *Int J Multiphase Flow* 29:341–360
4. Peles YP (2003) Two-phase boiling flow in microchannels – instabilities issues and flow regime mapping. In: 1st international conference on microchannels and minichannels, Rochester
5. Bergles AE (1976) Review of instabilities in two-phase systems. In: Kakac S, Mayinger F (eds) *Two-phase flows & heat transfer*. NATO advanced study institute, Istanbul Washington, DC, Vol 1, pp 383–423
6. Fritz W (1935) Maximum volume of vapor bubbles. *Phys Z* 36:379
7. Brutin D, Topin F, Tadrist L (2003) Experimental study of unsteady convective boiling in heated minichannels. *Int J Heat Mass Transf* 46(16): 2957–2965
8. Brutin D, Tadrist L (2004) Pressure drop and heat transfer analysis on flow boiling in a minichannel: influence of the inlet condition on two-phase flow stability. *Int J Heat Mass Transf* 47(10–11):2365–2377
9. Brutin D, Tadrist L (2006) Destabilization mechanisms and scaling laws of convective boiling in a minichannel. *J Thermophys Heat Transf Underpress* 20(4):850–855
10. Bergles AE (2003) Critical heat flux in microchannels: experimental issues and guidelines for measurements. In: 1st international conference on microchannels and minichannels, Rochester
11. Li HY, Lee PC, Tseng FG, Pan C (2003) Two-phase flow instability of boiling in a double microchannel system at high heating powers. In: 1st international conference on microchannels and minichannels. ASME, Rochester, pp 615–621

---

## Flow by Surface Acoustic Waves

Yandong Gao<sup>1</sup> and Dongqing Li<sup>2</sup>

<sup>1</sup>Department of Mechanical Engineering,  
University of California at Davis, Davis,  
CA, USA

<sup>2</sup>Department of Mechanical and Mechatronics  
Engineering, Faculty of Engineering, University  
of Waterloo, Waterloo, ON, Canada

## Synonyms

Liquid handling; Micro-/nanofluidics; Surface acoustic waves

## Definition

Surface acoustic wave (SAW) devices are widely used for frequency filtering in mobile communications [1]. Recently published works [2–10] have demonstrated the use of SAWs to manipulate liquid flow in microfluidic devices. A SAW is excited by the application of a radiofrequency (rf) signal to an interdigital transducer (IDT) on a piezoelectric substrate such as quartz or LiNbO<sub>3</sub>. The

wavelength of the SAW, having a typical value of a few micrometers, is determined by the geometry of the IDT. The amplitudes of the SAW are typically about a nanometer, depending on the applied rf power. As a SAW propagates on the surface of a piezoelectric solid, any viscous materials such as liquids located at the solid surface will absorb most of its energy, which is indicated by an exponentially decaying amplitude. The interaction between the SAW and the liquid creates an acoustic radiation pressure (ARP) in the direction of propagation of the SAW in the liquid. This induces liquid currents or jets called acoustic streaming. This can lead to the flow of the liquid if the amplitudes of the SAWs are large enough [2].

## Overview

The piezoelectric chip generating the SAW is coupled to microfluidic devices. The flow actuated by the SAWs is noninvasive. There are no mechanical moving parts inside. It can comprise sealed containers without external plumbing. SAWs have been used to manipulate droplets [2–4] and to mix and pump liquids [5–10].

Wixforth et al. [3] have shown that droplets can be split, merged, mixed, and actuated along predetermined trajectories using SAWs. Because of the nonlinear interaction between a SAW and a droplet, only droplets of certain size are agitated by a given SAW wavelength and power. This effect can be used to dispense droplets of a certain size out of others. When the SAW amplitude reaches a critical value, the pulse excitation even causes droplet ejection [4]. The ability of SAWs to stir and mix liquids is also used to eliminate nonuniformities in concentrations, as in a micromixer [5–8]. A higher applied rf power on the IDTs leads to a significant improvement in the mixing efficiency. However, the temperature also increases with the higher applied voltage [8]. Another feature of flow by SAWs is the rapid decay of the induced velocity field away from the IDTs. Guttenberg et al. [9] have shown that the velocity decreases with the inverse third power of the distance from the ultrasound generator.

## Cross-References

- ▶ [Acoustic Streaming](#)
- ▶ [Transport of Droplets by Acoustics](#)

## References

1. White RM, Voltmer FW (1965) Direct piezoelectric coupling to surface elastic waves. *Appl Phys Lett* 7:314–316
2. Wixforth A (2003) Acoustically driven planar microfluidics. *Superlattice Microst* 33:389–396
3. Wixforth A et al (2004) Acoustic manipulation of small droplets. *Anal Bioanal Chem* 379:982–991
4. Bennes J et al (2005) Droplet ejector using surface acoustic waves. *IEEE Ultrasonic Symposium*, Rotterdam, pp 823–826
5. Zhu X, Kim ES (1998) Microfluidic motion generation with acoustic waves. *Sensor Actuat A* 66:355–360
6. Yang Z et al (2001) Ultrasonic micromixer for microfluidic systems. *Sensor Actuat A* 93:266–272
7. Sritharan K et al (2006) Acoustic mixing at low Reynold's numbers. *Appl Phys Lett* 88:054102
8. Tseng W et al (2006) Active micro-mixers using surface acoustic waves on Y-cut 128° LiNbO<sub>3</sub>. *J Micromech Microeng* 16:539–548
9. Guttenberg Z et al (2004) Flow profiling of a surface-acoustic-wave nanopump. *Phys Rev E* 70:056311
10. Renaudin A et al (2006) SAW nanopump for handling droplets in view of biological applications. *Sens Actuators B* 113:389–397

## Flow Cytometer Lab-on-a-Chip Devices

Jennifer R. Lukes<sup>1</sup> and Jongin Hong<sup>2</sup>

<sup>1</sup>Department of Mechanical Engineering and Applied Mechanics, University of Pennsylvania, Philadelphia, PA, USA

<sup>2</sup>Department of Chemistry, Chung-Ang University, Seoul, South Korea

## Synonyms

Microfabricated Coulter counter; Microfabricated flow cytometer; Micromachined Coulter counter; Micromachined flow cytometer; Miniaturized fluorescence-activated cell sorting devices

## Definition

Flow cytometry is a popular technique for counting and sorting individual cells or particles. Also, it is used for measurement of various physicochemical characteristics and distribution of cell populations. A flow cytometer Lab-on-a-Chip is a microfluidic tool for flow cytometry that is made using microfabrication techniques. It incorporates many components and functionalities of a typical room-sized laboratory onto a small chip.

## Overview

Reynolds' late nineteenth-century principles of laminar flow and twentieth-century advances in flow microscopy, cell counting techniques, and ink-jet technology form the intellectual foundations of flow cytometry [1]. Moldavan (1934) was the first to suggest an instrument for identifying single cells using a microscope with a photodetector. Before Coons (1941) directly labeled antibodies with fluorescent dyes, there was no technique for visualizing cells and identifying their physical structure and orientation. Microscopes equipped with cameras or photodetectors enabled the precise quantitative analysis of fluorescence intensity patterns within the field of view [1]. Kamensky and Melamed (1965) developed a microscope spectrometer that measured and recorded ultraviolet absorption and the scatter of blue light arising from the flow of cells. Then, in 1967, they modified the spectrometer to create a spectrophotometric cell sorter with electronic actuation, which separated cells of predetermined optical properties from a large population of cells in suspension. In particular, the monoclonal antibody technique, which was invented by Georges Köhler and Cesar Milstein in 1975, also led to a vast increase in the number of cellular constituents that could be specifically stained and used to classify cells.

Wallace Coulter invented a nonoptical means of counting and measuring the size of particles suspended in a conducting fluid (1953). In this approach, cells displaced conducting solution while flowing through an orifice, resulting in

increases of electric resistance measured across the orifice. Crosland-Taylor (1953) was the first to introduce the principle of hydrodynamic focusing, in which particles injected into a faster stream of fluid flowing in the same direction could be spatially confined. Fulwyler (1965) developed an electronic cell sorting device that combined Coulter methodology with ink-jet technology. The device added a charge to the droplets containing cells differently according to the cell volume measured in a Coulter aperture, thereby allowing deflection of the droplets under an electrostatic field. Van Dilla et al. (1969) developed the first fluorescence-detection cytometer with the principle of hydrodynamic focusing. The cytometer, which included a photomultiplier and an argon ion laser, was configured with the axes of flow, illumination, and detection all orthogonal to each other.

Improvements on the above pioneering works in flow cytometry and related fields have led to the development of modern flow cytometers for various applications. Currently, there are a number of commercial flow cytometers that can sort up 10,000 cells per second without affecting cell viability. Through different staining techniques and minor modifications of conventional flow cytometry, analytical capabilities have been extended from single molecules to large biological particles, including carbohydrates, lipids, cholesterol, proteins, ions, chromosomes, DNA/RNA, islet cells, and embryonic stem cells. Although conventional flow cytometers provide rapid and reliable analytical cell sampling capabilities, complex optical components like focused laser beams, various optical filters/photodetectors, and complicated electronics make the conventional flow cytometer bulky and expensive. Moreover, its operation still relies on specialized personnel, complex preparation procedures, and a relatively high volume of cells or particles to be analyzed.

Over the past decade, the drawbacks of conventional flow cytometers coupled with the increased need for miniaturization and sophisticated analysis have motivated the development of the micromachined flow cytometer. It has many potential benefits including disposability, smaller size, lower consumption of sample,

reagents and power, enhanced performance, and inexpensive instrumentation. Also, the integration of the microfluidic and detection systems on a single chip can enhance the reliability and functionality of the flow cytometer. For example, Miyake et al. (1991) were the first to report a multilayered flow chamber that could generate a hydrodynamically focused narrow stream of fluorescent dyes and particles within a water sheath. Similarly, Sobek et al. (1994) demonstrated a micromachined flow cytometer fabricated on quartz wafers and consisting of two symmetric parts bonded together to define the geometry of a sheath flow chamber and a detection channel. Later, Larsen et al. (1997) and Koch et al. (1999) presented designs for micromachined Coulter counters that could count individual particles; however, electric testing of these designs was not performed. Alternatively, Altendorf et al. (1996) demonstrated a benchtop optical flow cytometer utilizing silicon V-groove flow channels, in which a laser diode and a photodiode detector were used for cell counting. Nowadays, the goal of novel micromachined flow cytometers is to enable more precise and rapid manipulation of cells or particles and to take advantage of different driving forces for controlling fluid flows. Also required is the integration of optics and electronics to perform detection and sorting of cells or particles of interest. Herein, we present the basic principles of flow cytometer operation and discuss recent progress in micromachined flow cytometers. We recommend that the audience read [1, 2] for understanding these fields.

## Basic Methodology

### Basic Principles

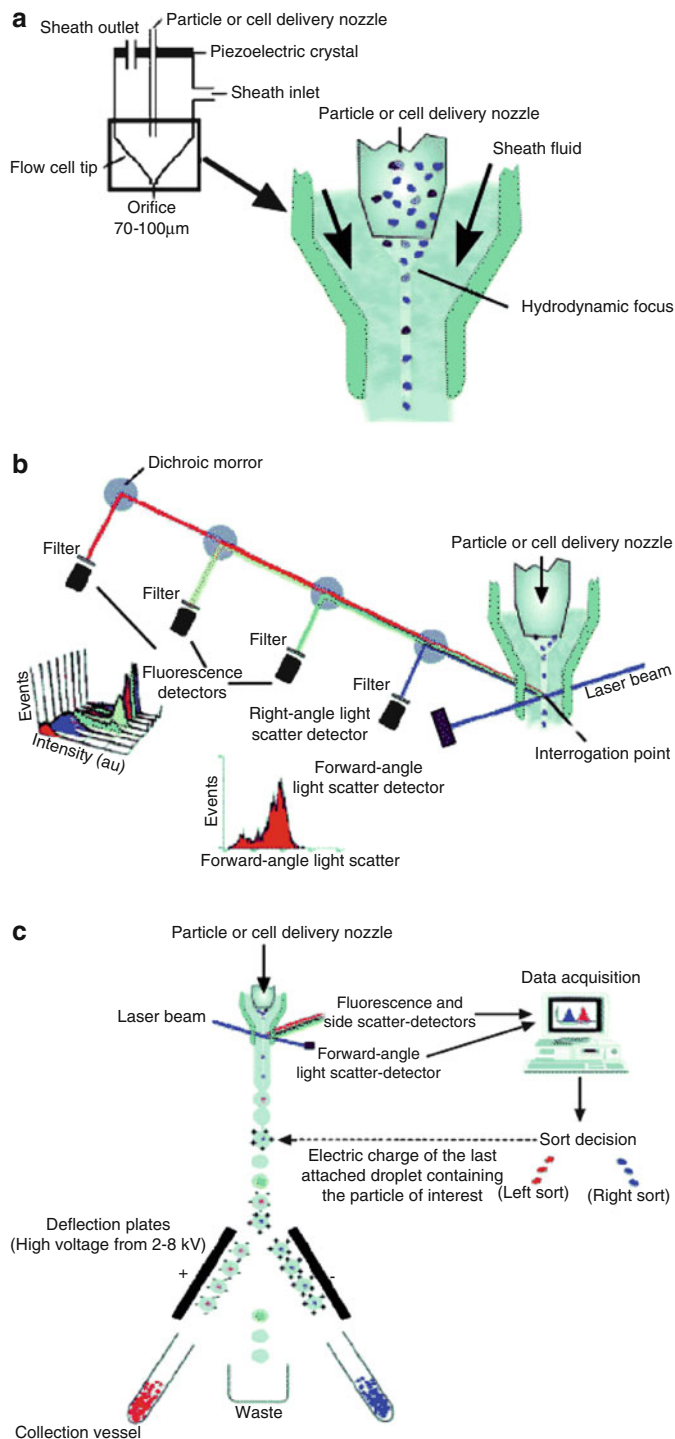
A flow cytometer is an instrument for counting and sorting suspended cells or particles in a stream of fluid and analyzing their physico-chemical characteristics. A flow cytometer has several key components: (a) a flow cell that carries the suspended single cells through the instrument and past the light source; (b) a light or excitation source, typically a laser that emits

light at a specific wavelength; (c) a detector that is capable of measuring the light signals from the cells; (d) data analysis electronics that characterize the multiparametric properties of the cells; and (e) a sorter that is able to separate each cell according to the predetermined optical properties. The basic operation principles of a flow cytometer are shown in Fig. 1. Before suspension in a sample reservoir, cells or particles can be combined with various fluorescent probes that stain cellular components to elucidate functions of interest. The suspended cells or particles are aspirated into a flow cell through a nozzle by air pressure applied on top of the sample or a syringe controlled by a precise motor. A flow cell delivers the sample stream to the center of the sheath flow and then accelerates the flow to squeeze the central sample flow into a narrow stream and to maintain a cell spacing within the surrounding fluid sheath. This phenomenon, called hydrodynamic focusing, is the keystone of a flow cytometer (Fig. 1a).

Every single cell or particle is then intercepted as it flows by a fixed light source like a laser beam and then the light is either scattered or absorbed. Scattered light is either reflected or refracted. In most flow cytometers, there are two types of scatter; forward-angle scatter and right-angle scatter. Forward-angle scatter is the amount of light scattered at small angle ( $< 10^\circ$ ) in the forward direction with respect to the direction of the laser beam and is known to be related to the size of the particle. Right-angle scatter consists of photons scattered at  $90^\circ$  with respect to the incident laser beam and depends primarily on the cell structure and granularity. Absorbed light of the appropriate wavelength may be re-emitted as fluorescence if the cell contains a naturally fluorescent substance or fluorescent dyes are added to the sample. The fluorescent signal helps to identify cells of interest. The scattered or re-emitted light is collected by a number of detectors where the stream passes through the light beam: one photodetector in line with the light beam (a forward scatter detector) and other photodetectors perpendicular to it (side scatter and fluorescent detectors). A set of dichroic mirrors and filters split the optical signals in spectral wavelength ranges. The resulting electric

### Flow Cytometer Lab-on-a-Chip Devices,

**Fig. 1** Basic principles of a flow cytometer: (a) flow cell and the principle of hydrodynamic focusing, (b) flow cytometer optics, (c) principle of electrostatic sorting-based droplet formation [3]



pulses are digitized and then the data is stored, analyzed, and displayed through a computer system (Fig. 1b).

The amount of scattered or fluorescent light subsequently needs to be displayed for interpretation. These profiles are normally displayed as single dimension (histogram) or two dimensions (cytogram). A histogram displays a frequency distribution of the cell for any particular parameter, whereas a cytogram displays the data in two dimensions like a spatial map. Both histograms and cytograms can represent the population distribution of scattered and fluorescent signals received from a large number of cells or particles. Also, multiple fluorescent dyes can be used simultaneously in a flow cytometer. Therefore, this allows a multiparametric analysis at the single cell level and so it can be used to select and purify a specific subset of cells or particles within a population.

The most common method for sorting is the stream-in-air configuration in which a continuous stream of cells or particles emerging from a nozzle is converted into droplets containing single cells using mechanical vibration of the nozzle tip. If a stream of liquid is vibrated along its axis, the stream will break up into droplets. The characteristics of this droplet formation are governed by an equation:  $v = f \cdot \lambda$ , where  $v$  is the velocity of the stream,  $f$  is the frequency of the vibration applied, and  $\lambda$  is the distance between droplets [1]. After forming the droplets in a regular pattern, a charge is added to the droplets. Then, the charged droplets are deflected by a strong electric field into different collecting chamber (Fig. 1c).

### Coulter Counter

The Coulter counter is a resistive pulse technique of particle sizing invented in 1953. The measurement principle is as follows. A particle passes through a pore and displaces conducting fluid in that pore (Fig. 2). The resistance of a pore  $R_p$  increases by  $\delta R_p$  when a particle enters since the particle displaces conducting fluid. Assuming that the current density is uniform across the

pore,  $\delta R_p$  can be estimated for a pore aligned along the  $z$ -axis by [5]

$$\delta R_p = \rho \int \frac{dz}{A(z)} - R_p \quad (1)$$

where  $A(z)$  represents the cross-sectional area occupied by fluid at a particular  $z$ -position of the pore containing a particle and  $\rho$  is the resistivity of the fluid. The particle resistivity is assumed infinite in this analysis. For a spherical particle of diameter  $d$  in a pore of diameter  $D$  and length  $L$ , the relative change in resistance is expressed as [5]

$$\frac{\delta R_p}{R_p} = \frac{D}{L} \left[ \frac{\arcsin(d/D)}{\sqrt{1 - (d/D)^2}} - \frac{d}{D} \right] \quad (2)$$

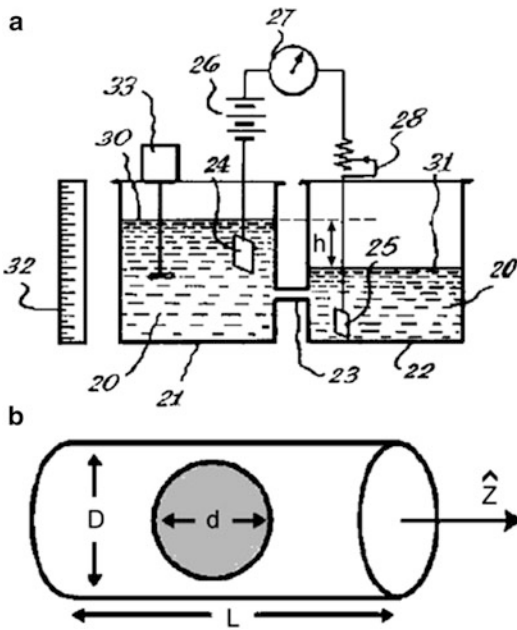
where  $L$  is the pore length. For cases where cross section  $A(z)$  varies quickly, i.e., when  $d \ll D$ , Debolis and Bean (1970) formulated an equation based on approximate solution to the Laplace equation:

$$\frac{\delta R_p}{R_p} = \frac{d^3}{LD^2} \left[ \frac{D^2}{2L^2} + \frac{1}{\sqrt{1 + (D/L)^2}} \right] F \left( \frac{d^3}{D^3} \right) \quad (3)$$

where  $F(d^3/D^3)$  is a numerical factor that accounts for the bulging of the electric field lines into the pore wall. If  $R_p$  is the dominant component of measurement circuit, then relative changes in the current are equal in magnitude to those in the resistance.

### Fabrication

We briefly describe the general methods to fabricate flow cytometers. Conventional flow cytometers contain flow chambers or cuvettes made from glass or quartz tubes, with an injector inserted into the middle of the tube. Recently, microfabricated flow cytometers have been developed using photolithography and micromachining techniques. The two kinds of micromachining



**Flow Cytometer Lab-on-a-Chip Devices, Fig. 2** Coulter counting: (a) schematic overview of the Coulter counter from the original patent. A conductive liquid suspending the particles to be analyzed (20) is moved through a small aperture (23) from one vessel (21) into the other (22) by different levels of liquid (30, 31). The impedance over the aperture is measured using two electrodes (24, 25) that are connected to a readout circuit, which consists of a battery (26), current meter (27), and variable resistor (28). The instrument is equipped with an agitator (33) to keep the particles suspended and a graduated scale alongside the vessel (32) to measure the change of volume, [4] and (b) a schematic diagram of spherical particle of diameter  $d$  in a pore of diameter  $D$  and length  $L$  [5]

techniques are surface micromachining, where thin layers of new materials are added to a substrate, and wet bulk micromachining, where a substrate is etched isotropically or anisotropically depending on etchants. Typical substrates are silicon, glass, and quartz. In addition, soft microlithography can replicate microfluidic components by casting polymer against a master mold. The master mold is a positive relief structure that hollows out negative relief structures in the cured polymer cast against it. Poly(dimethylsiloxane) (PDMS), which is an optically transparent and mechanically soft elastomer, is the most

commonly used for fabricating microfluidic systems. The soft lithography is very suitable for demonstrating prototype devices at the early stages of development. Further information in this area can be found in microfabrication techniques.

## Key Research Findings

### Hydrodynamic Focusing

The microfluidic device design and the relative flow rate of sheath and sample play important roles in hydrodynamic focusing. Lee et al. [6] proposed a theoretical model to predict the width of focused center flow inside a microfabricated flow cytometer [6]. Based on potential flow theory, they derived the equation for flow inside a planar microfabricated flow cytometer under the two-dimensional situation shown in Fig. 3a. The flow is considered laminar, and the diffusion and mixing between focused stream and sheath flows is assumed negligible. With these assumptions, conservation of mass yields

$$\dot{m}_{in} = \rho_1 \bar{v}_1 \cdot D_1 + \rho_2 \bar{v}_2 \cdot D_2 + \rho_3 \bar{v}_3 \cdot D_3 \quad (4)$$

$$\dot{m}_{out} = \rho_a \bar{v}_a \cdot D_a \quad (5)$$

$$\bar{v}_2 \cdot D_2 = \bar{v}_c \cdot d \quad (6)$$

where  $\dot{m}_{in}$  and  $\dot{m}_{out}$  are mass flow rates (per unit depth) of the inlet and outlet flows;  $D_1$ ,  $D_2$ , and  $D_3$  are the width of inlet channels 1, 2, and 3, respectively;  $\bar{v}_1$ ,  $\bar{v}_2$ , and  $\bar{v}_3$  are average velocities in sections 1, 2, and 3;  $\bar{v}_a$  is the average velocity inside the outlet section; and  $\bar{v}_c$  and  $d$  are velocity and width of focused beam, respectively. If the sheath flow rate is much higher than the sample flow rate, the final output flow will be dominated by the sheath flow and then the velocity profile can be approximated as a parabolic flow of just the sheath fluid. It follows that

$$v_c = v_{max} = 1.5 \bar{v}_a \quad (7)$$

Therefore, the width of the focused center stream can be derived as

$$d = \frac{\bar{v}_2}{v_c} \cdot D_2 = \frac{\rho_a D_a}{1.5(\rho_1(\bar{v}_1/\bar{v}_2)(D_1/D_2) + \rho_2 + \rho_3(\bar{v}_3/\bar{v}_2)(D_3/D_2))} \tag{8}$$

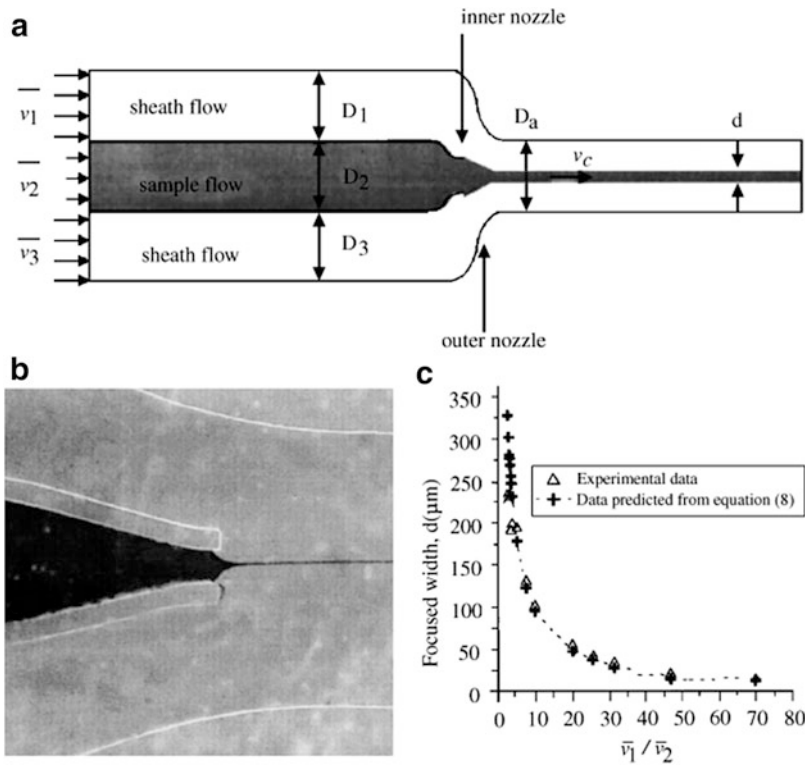
This expression indicates that the width of the focused stream is inversely proportional to the ratio of sheath flow rate to sample flow rate and proportional to volumetric flow rate of the sample flow. Lee et al. also performed experiments showing that two-dimensional hydrodynamic focusing could achieve a focused stream with width less than 10 μm when the sample was injected at the middle of the outer nozzle and the ratio of sheath flow rate to sample flow rate was increased (Fig. 3b). Their experimental results agree well with theoretical predictions.

Chung et al. (2003) investigated the difference between two- and three-dimensional hydrodynamic focusing using numerical simulation based on Poiseuille flow, which is pressure-driven flow between stationary parallel plates with no contribution from gravity, and experimental

observations with scanning confocal microscopy. Two- and three-dimensionally focused streams were achieved by planar and two-level channel geometries using poly(dimethylsiloxane) (PDMS). They found that two-dimensional focusing was not as successful as three-dimensional focusing. That is, three-dimensional focusing better confined sample particles in the vertical direction and made detection signals more stable.

Although hydrodynamic focusing with sheath fluid serves as a standard technology in conventional and microfabricated flow cytometers, a large amount of sheath fluid is required to process a small amount of sample, and continuous pumping of sheath fluid at high flow rates is needed to generate a narrow sample stream. Further reduction in the size and volume of the whole system is also limited. Alternative methods are

F



**Flow Cytometer Lab-on-a-Chip Devices,**

**Fig. 3** Hydrodynamic focusing for microfabricated flow cytometers: (a) schematic diagram of a 2-dimensional microfabricated flow cytometer for a theoretical approach, (b) photograph of focused sample stream inside a flow cytometer, and (c) variation of the width of the focused stream as a function of the relative flow rates of sample and sheath [6]

electrokinetic focusing, which uses direct current (DC) at high voltages, and dielectrophoretic focusing, which uses alternating current (AC) to focus particles and liquids into a narrow stream. These topics are of significant research interest but are beyond the scope of this entry.

### Optical Detection

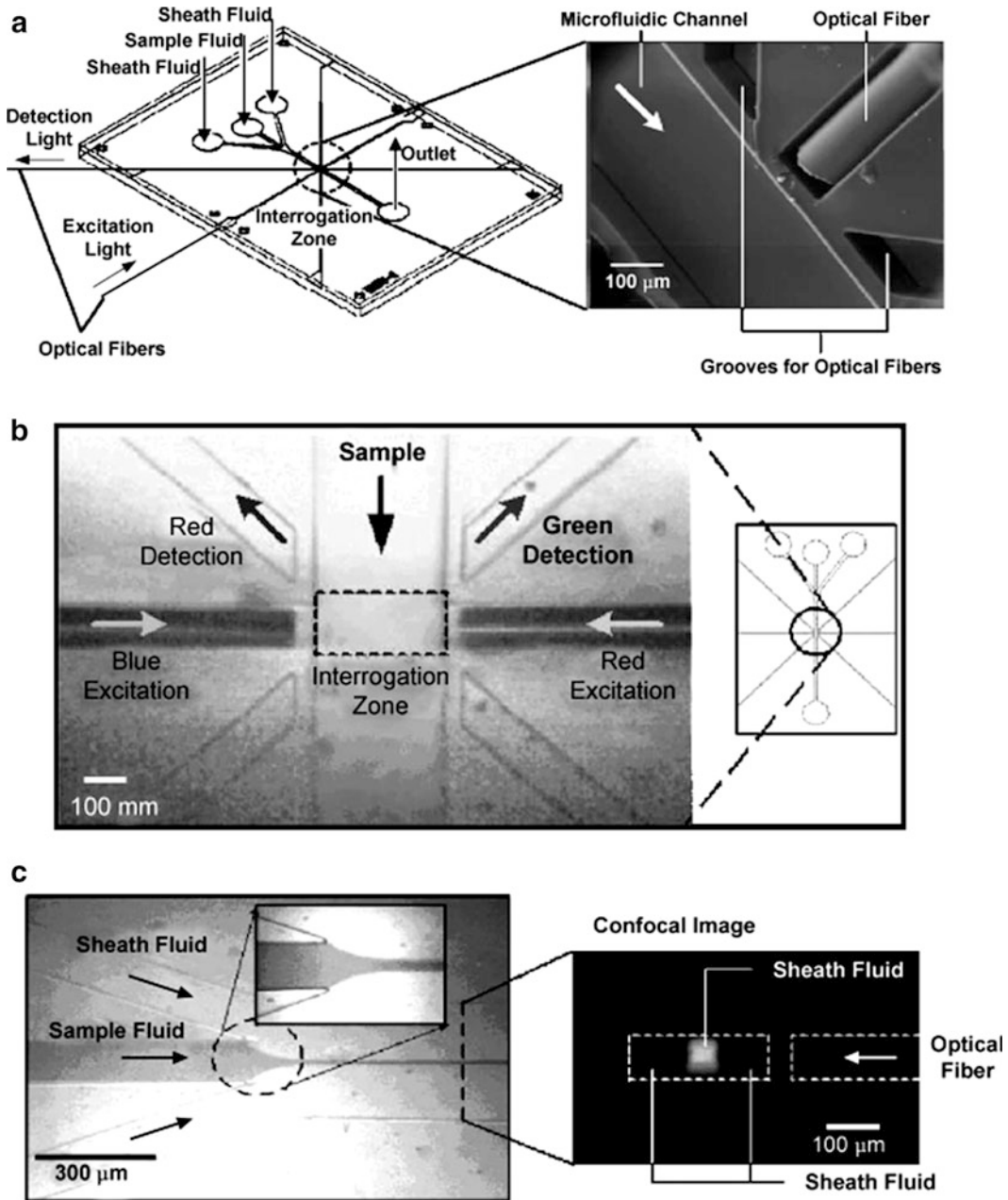
Micromachined flow cytometers open new opportunities to integrate optical components and solid-state devices with the microfluidic platform. Tung et al. [7] investigated the feasibility of silicon-based PIN photodiodes, which consisted of P-N junctions with an intrinsic region in the middle combined with self-aligned optical fibers for multicolor excitation and multiangle fluorescence detection in PDMS-based flow cytometers [7]. Replacing photomultiplier tubes (PMTs) and avalanche photodiodes (APDs) with PIN photodiodes for fluorescence detection in flow cytometry presented significant technical challenges, since the fluorescent signals generated from biological cells only produce a few nA of current in the PIN photodiodes. Thus, Tung et al. applied a lock-in amplification technique to increase the signal-to-noise ratio (S/N). At a single interrogation point, multicolor laser excitation and multiangle fluorescence detection were demonstrated to detect hydrodynamically focused fluorescent microspheres and biological particles (Fig. 4).

Lee et al. (2003) proposed a novel approach to integrate polymeric optical waveguides onto microfabricated flow cytometers. Instead of inserting optical fibers through microfabricated grooves, they developed a new method to embed photoresist (SU-8)-based optical waveguides with a thin layer of spin-on-glass (SOG). The seamless configuration and large difference in refractive indices between SU-8 (1.80) and SOG (1.36) enhanced the efficiencies of light guiding and coupling. The working principle is that the detection light can propagate in the waveguide by total internal reflection. Light intensity, which changes when cells or particles pass through the interrogation point, is collected by the other waveguide buried on the other side of the microfluidic channel. The advantage of

this method is that it permits counting and analysis of cells and particles without microscopes and delicate optical alignment.

### Electrical Detection

In optics-based flow cytometry, molecular level detection of individual cells or particles is enabled by tagging biomarkers with various fluorescent probes. These probes inherently alter the cells/particles: tagging requires an incubation step, antigenic exposure risks triggering cell differentiation, and non-surface probes require membrane permeabilization. Although some leukocytes can be separated without the use of probes by their forward scatter and side scatter signals, the efficiency is not as high as that of fluorescence-based optical detection. Thus, new label-free detection methods are emerging in the field of microfabricated flow cytometers. Saleh and Sohn [5] were the first to present a microfabricated Coulter counter on quartz substrate utilizing a four-point measurement of the current through the pore (Fig. 5) [5]. The Coulter counter was able to detect latex colloidal particles as small as 87 nm in diameter and 500 nm-diameter colloids with a resolution of  $\pm 10$  nm, although its sensitivity depends on the relative size of the pore and the particle to be measured. Also, Saleh and Sohn in 2003 corrected off-axis effects due to particles traveling off the central axis of the pore. Off-axis particles take longer to transit the pore due to the parabolic distribution of fluid velocity within the pore, causing wider pulses and large changes in electric resistance due to the nonuniform distribution of electric current density. They proposed that off-axis effects can be effectively removed in the data analysis of a given population by the nearly linear correlation between height  $\Delta R$  and width  $\tau$  in measured resistance pulses. Nieuwenhuis et al. [8] presented the integrated Coulter counter that has a controllable liquid aperture, defined by a nonconductive sheath liquid surrounding the conductive sample stream, whereas microfabricated flow cytometers reported before had a fixed Coulter aperture [8]. The dynamic Coulter aperture to the particle size enables to achieve optimal sensitivity and to prevent clogging.

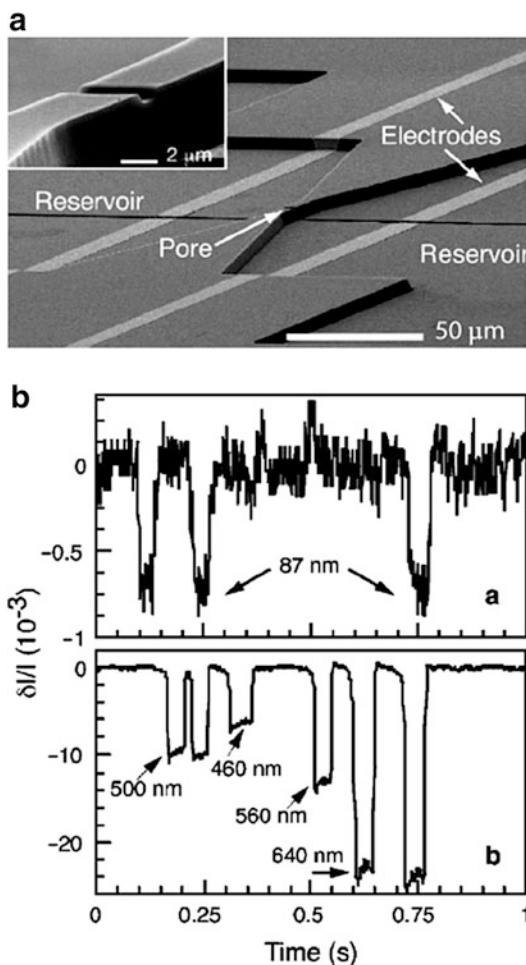


**Flow Cytometer Lab-on-a-Chip Devices, Fig. 4** Integrated optical components on a PDMS-based flow cytometer: (a) design of PDMS observation channel with embedded optical fibers (arrangement shown with 45° angle between excitation and detection optical fibers),

(b) arrangement of optical fibers for two-color excitation/detection experiment, and (c) optical and confocal microscope photos demonstrating hydrodynamic focusing (the water containing fluorescein is excited using a blue ( $\lambda = 440$  nm) laser) [7]

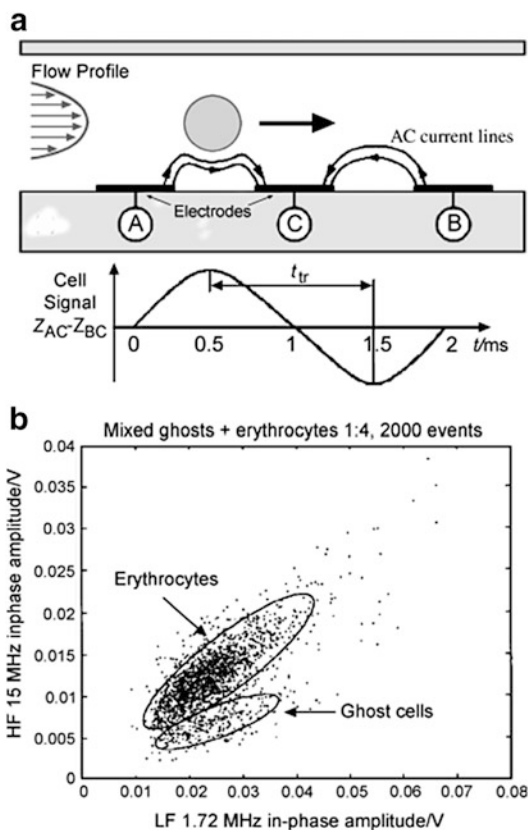
Impedance spectroscopy of living biological cells over a wide frequency range gives various information such as cell size, membrane

capacitance, and cytoplasm conductivity as a function of frequency. At low frequencies, the cell membrane offers a significant barrier to



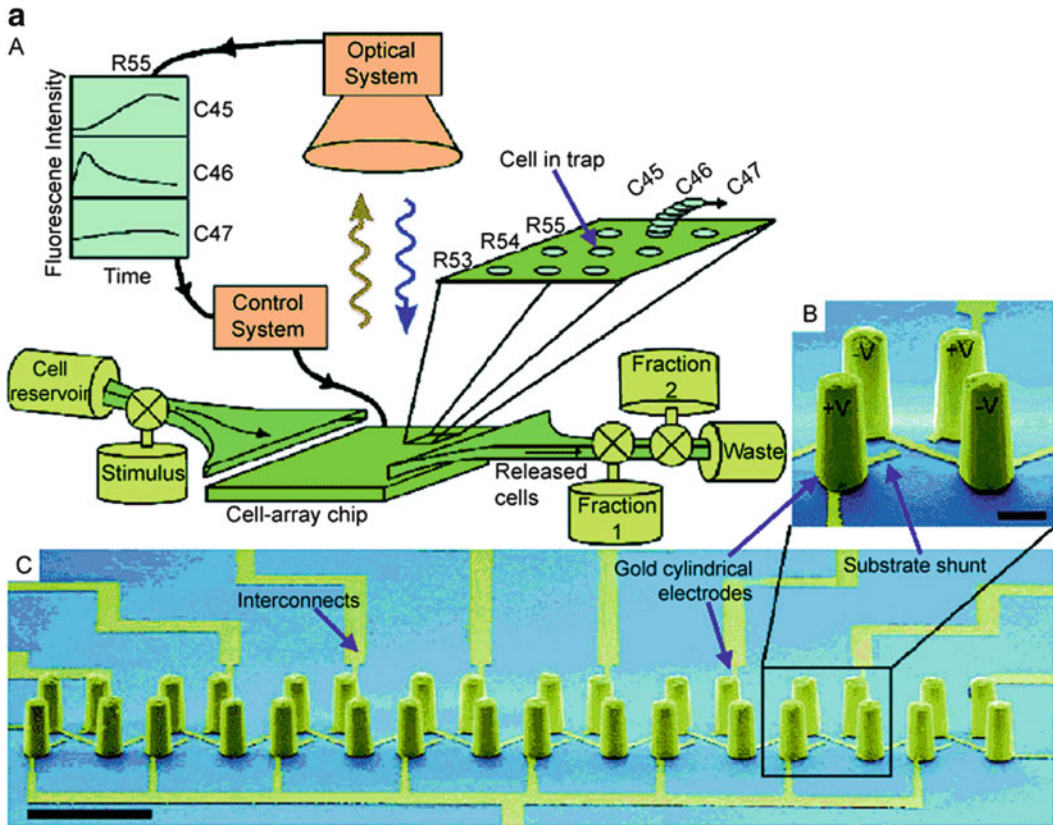
**Flow Cytometer Lab-on-a-Chip Devices, Fig. 5** Microfabricated Coulter counter: (a) scanning electron microscope image of the Coulter counter. The 3.5  $\mu\text{m}$ -deep reservoirs and the inner Ti/Pt electrodes, which control the voltage applied to the pore but pass no current, are only partially shown. The inset shows a magnified view of this device's pore, which has dimensions  $5.1 \times 1.5 \times 1.0 \mu\text{m}^3$ , and (b) relative changes in baseline current versus time for a monodisperse solution of 87 nm diameter latex colloids and a polydisperse solution of latex colloids with diameters 460, 500, 560, and 640 nm [5]

current flow and so the cell size can be measured as in Coulter counting. At intermediate frequencies, the decrease in plasma membrane polarization reduces the capacitance of the cell. This effect is known as  $\beta$ -dispersion or dielectric relaxation. At high frequencies, the plasma membranes are minimally polarized and so, above the  $\beta$ -relaxation

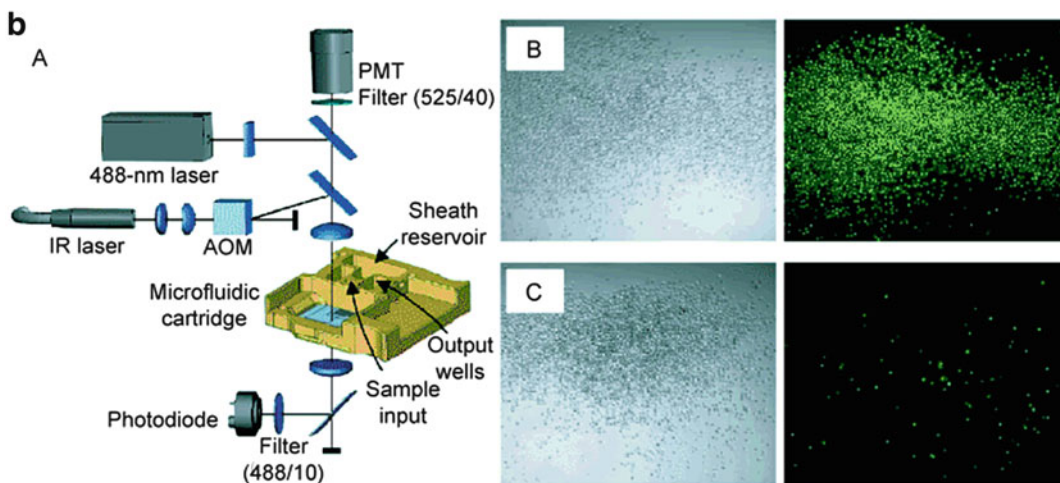


**Flow Cytometer Lab-on-a-Chip Devices, Fig. 6** Micromachined impedance flow cytometer: (a) side schematic view of the microchannel showing a particle passing over three electrodes (A, B, and C). The impedance signal is measured differently ( $Z_{AC} - Z_{BC}$ ). As the distance between two measurement areas and time  $t_{tr}$  separating the signal spikes are known, the speed of the particle can be calculated, and (b) signal in-phase amplitude of 2,000 erythrocytes and ghost cells recorded simultaneously for two frequencies [9]

frequency, the signal contains information about the heterogeneous structure and dielectric properties of the cell interior. Renaud et al. (2001) demonstrated successfully that a microfabricated cell impedance analyzer could discriminate between cell types and particle sizes with the rate of over 100 samples per second [9]. Simultaneous impedance measurements at multiple frequencies enabled the differentiation of subpopulations in the mixture of normal erythrocytes and erythrocyte ghost cells, illustrating the capability of identifying different cell types (Fig. 6). Recently, they



F



**Flow Cytometer Lab-on-a-Chip Devices, Fig. 7** Cell sorting: (a) a dielectrophoresis-based cell trapping and sorting system, (A) schematic representation of the system, showing single cells loaded onto the cell-array chip and one cell, in row 55 and column 46, being sorted by the control system into the fraction collectors after acquisition of dynamic luminescence information from the entire array, (B) pseudocolored scanning electron micrograph

(SEM) showing a single trap consisting of four electroplated gold electrodes arranged trapezoidally along with the substrate interconnects, and (C) SEM of a completed  $1 \times 8$  trap array. Scale bars: B.  $20 \mu\text{m}$ , (C)  $100 \mu\text{m}$  [12], and (b) an optically switched microfluidic fluorescence-activated cell sorter, A. schematic representation of the cell sorter instrument and the microfluidic cartridge. The near-infrared laser and

proposed a model to determine the influence of different cell properties including size, membrane, capacitance, and cytoplasm conductivity on the impedance spectrum in their flow cytometers and showed the discrimination between unlabelled neutrophils (granular, 12–15  $\mu\text{m}$  diameter, multilobed nucleus), lymphocytes (agranular, 5–10  $\mu\text{m}$ , large nucleus), and monocytes (agranular, 12–18  $\mu\text{m}$  diameter, U-shaped nucleus) [10].

### Cell Sorting

The ability of high-speed sorting based on the predetermined properties of cells or particles has been an important issue in the development of microfabricated flow cytometers. Quake et al. (1999) presented disposable fluorescence-activated cell sorting (FACS) of microbeads and bacterial cells in a microfluidic device based on electrokinetic switching of liquid streams [11]. When a fluorescently labeled cell was detected in the input channel, the sample stream flowing from an inlet to a waste port was quickly switched by reversing the electric field to deliver target particles selectively to a sample collector. This technique demonstrated sorting of fluorescent microbeads and *E. coli* at the rate of  $\sim 10$  beads/s and 20 cells/s, respectively. Later, Fu et al. integrated pneumatically actuated components which enabled self-contained and automated cell trapping and sorting at a higher rate (26–44 cells/s)

Voldman et al. [12] introduced an innovative dynamic array cytometer for single-cell assays and sorting based on the principle of dielectrophoresis, in which forces arise on particles in a nonuniform electric field due to induced polarization or charge dipoles (Fig. 7a) [12]. Their asymmetric extruded quadrupole geometry allowed noncontact trapping of multiple single cells, holding them against disrupting fluid flow

and increasing the trapping efficiency. Also, the novel dielectrophoretic trap could be physically arrayed and electrically addressed. By controlling the potential of one electrode in each trap, selected subpopulations of cells could remain trapped or be released from the trap based on the fluorescence information.

Wang et al. [13] described a high-throughput cell sorter with all-optical control switch for live cells (Fig. 7b) [13]. The optical forces, which depend on the optical power and relative optical properties of the particle and its surrounding fluidic medium, were used to deviate the cell from the flow stream to a sufficient degree to that it was directed toward the target output channel. They have shown that sorting runs of cell populations ranging from as few as 1,000 cells up to 280,000 cells can be completed in less than an hour.

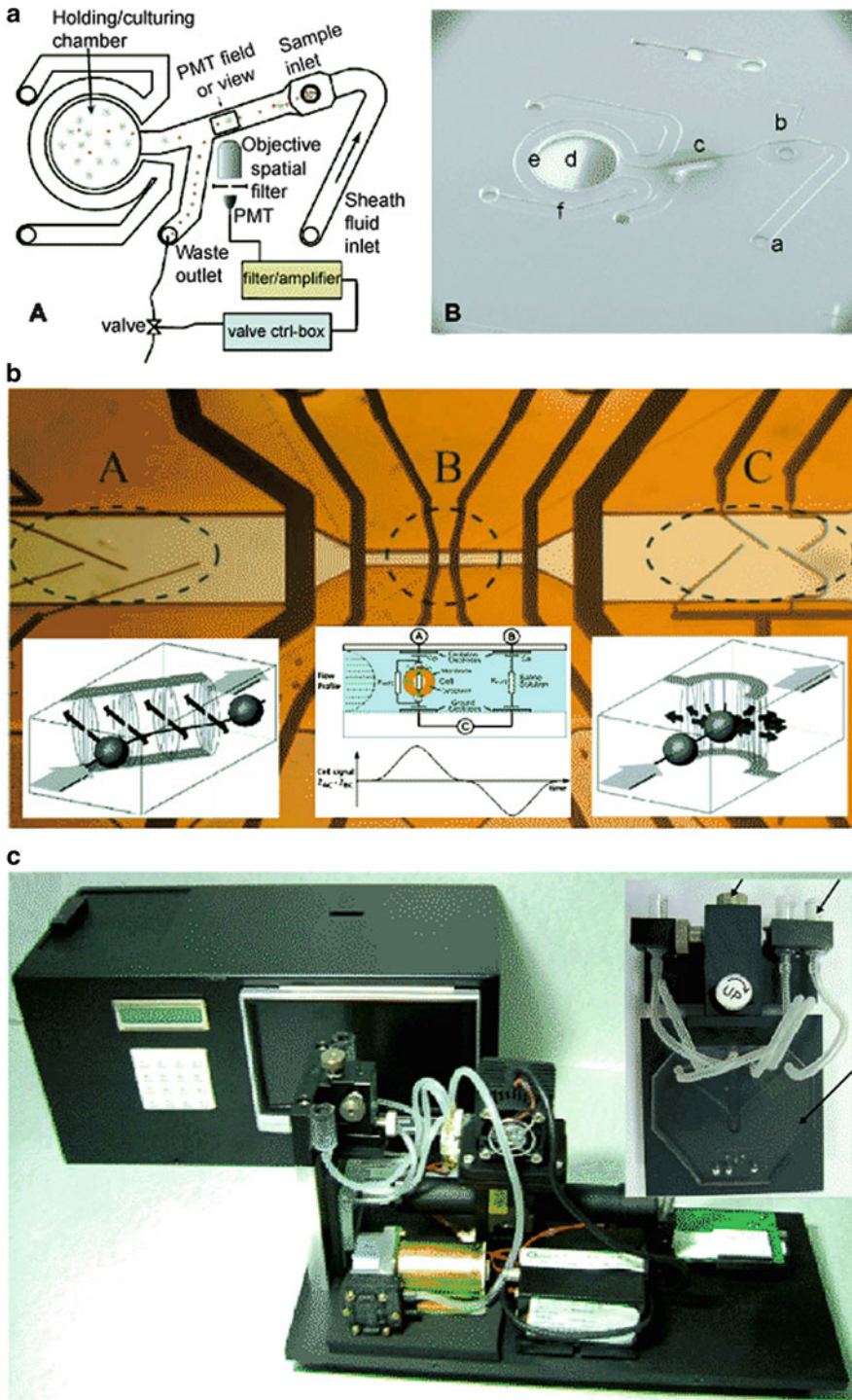
### Flow Cytometer Lab-on-a-Chip

A flow cytometer Lab-on-a-Chip should incorporate many components and functionalities of a typical room-sized laboratory onto a small chip. Although the perfect flow cytometer Lab-on-a-Chip has not yet emerged, we introduce novel examples for this issue. Recently, Wolff et al. [14] designed and developed a new pressure-driven microfabricated FACS device with advanced functional components including a chamber for holding and culturing the sorted cells and monolithically integrated waveguides for cell analysis (Fig. 8a) [14]. They achieved a 100-fold enrichment of fluorescent beads at a throughput of 12,000 cells per second while sorting fluorescent latex beads from chicken red blood cells. In particular, a new structure for coaxial sample sheathing and hydrodynamic focusing was built on the principle of the *smoking chimney*, where the sample was sheathed and

---

**Flow Cytometer Lab-on-a-Chip Devices, Fig. 7** (continued) 488 nm laser are focused through the same lens onto the microfluidic chip. The presence of a cell in the analysis region is detected by a photodiode and the fluorescence of that cell is measured by the PMT. Based on a gating of the fluorescent signal, the AOM is triggered to optically switch the cell (GFP-positive cells are switched

to the collection well). Sample is loaded directly onto and off the cartridge by pipette. Windows on the bottom of the collection wells permit viewing of the sorted populations. IR, infrared. (B, C) Bright-field (*left*) and fluorescence (*right*) images of the resulting cell populations in the collection well (B) and waste well (C) are shown for a typical sort of the GFP-expressing HeLa cells [13]



**Flow Cytometer Lab-on-a-Chip Devices, Fig. 8** Flow cytometer Lab-on-a-Chip: (a) setup and SEM image of the second-generation micro cell sorter chip with integrated holding/culturing chamber (a sheathing buffer inlet,

b chimney sample inlet c detection zone, d holding/culturing chamber, e sieve to allow diffusion of nutrients and confinement of cells, f channel for draining excess liquid during sorting and for feeding fresh media to the cells

carried downstream from the inlet like a wisp of smoke from a chimney. Renaud and coworkers (2005) have developed a microfabricated impedance flow cytometer that incorporates deflective dielectrophoresis barriers and controlled pressure-driven liquid flows (Fig. 8b) [15]. The integrated flow cytometer had the following capabilities:

- Cells trapped in electric cages could be subjected to two or more different fluids for cell transfection.
- Cells could be brought into an adjacent liquid (reagent) stream and washed shortly afterward.
- Cells could be characterized by the opacity, which is the ratio of the impedance magnitude at a high frequency to a low frequency.

Lee and coworkers (2006) presented a compact cell counting/sorting system with several essential components including a micromachined flow cytometer chip device, an optical detection system, and a data analysis and control system to achieve the functions of cell sample injection, optical signal detection, and cell collection. Its dimensions were 37 cm in length, 16 cm in width, and 18 cm in height (Fig. 8c) [16].

### Future Directions for Research

We can envision that the future flow cytometer Lab-on-a-Chip devices will miniaturize and integrate monolithically a variety of optical components like light sources, photodetectors, filters, waveguides, and lenses that can detect multiple fluorescence colors simultaneously. Other potential approaches without optical components include integrated flow cytometers based on electrochemical impedance detection, electrokinetic focusing/switching/sorting, MEMS-based filtering/pumping/switching, and

electromagnetic isolation. Also, future cytometers may combine optical components with nonoptical components monolithically for high-throughput multiparametric analysis of cells or particles.

### Cross-References

- ▶ [Cell Assays in Microfluidics](#)
- ▶ [Cell Sorting](#)
- ▶ [Control of Micro-fluidics](#)
- ▶ [Electrokinetic Focusing](#)
- ▶ [Electrokinetic Motion of Cells and Nonpolarizable Particles](#)
- ▶ [Fluorescence Measurements](#)
- ▶ [Fluorescent Labeling](#)
- ▶ [Lab-on-a-Chip Devices for Particle and Cell Separation](#)
- ▶ [Lab-on-a-Chip Devices for Sample Extractions](#)
- ▶ [Lab-on-Chip Devices for Separation-Based Detection](#)
- ▶ [Microfluidic Systems for High-Throughput Screening](#)

### References

1. Givan AL (2001) Flow cytometry: first principles. Wiley, New York
2. Huh D, Gu W, Kamotani Y, Grotberg JB, Takayama S (2005) Microfluidics for flow cytometric analysis of cells and particles. *Physiol Meas* 26:R73–R98
3. Bernas T, Grègori G, Asem EK, Robinson JP (2006) Integrating cytomics and proteomics. *Mol Cell Proteomics* 5(1):2–13
4. Coulter WH (1953) Means for counting particles suspended in a fluid. US Patent 2,656,508
5. Saleh OA, Sohn LL (2001) Quantitative sensing of nanoscale colloids using a microchip Coulter counter. *Rev Sci Instrum* 72(12):4449–4451
6. Lee GB, Hung CI, Ke BJ, Huang GR, Hwei BH, Lai HF (2001) Hydrodynamic focusing for a micromachined flow cytometer. *Trans ASME J Fluids Eng* 123:673–679
7. Tung YC, Zhang M, Lin CT, Kurabayashi K, Skerlos SJ (2004) PDMS-based opto-fluidic micro flow

**Flow Cytometer Lab-on-a-Chip Devices, Fig. 8** (continued) during cultivation; g, waste outlet) [14], (b) integrated impedance flow cytometer (A cell dipping electrodes, B detection electrodes, C sorting/trapping

electrodes) [10, 15], and (c) a photograph of the cell counting/sorting system incorporated with a microfabricated flow cytometer chip [16]

- cytometer with two-color multi-angle fluorescence detection capability using PIN photodiodes. *Sens Actuators B* 98:356–367
8. Nieuwenhuis JH, Kohl F, Bastemeijer J, Sarro PM, Vellekoop MJ (2004) Integrated Coulter counter based on 2-dimensional liquid aperture control. *Sens Actuators B* 102:44–50
  9. Gawad S, Schild L, Renaud P (2001) Micromachined impedance Spectroscopy flow cytometer for cell analysis and particle sizing. *Lab Chip* 1:76–82
  10. Cheung KC, Renaud P (2006) BIOMEMS for medicine: on-chip cell characterization and implantable microelectrodes. *Solid-State Electronics* 50:551–557
  11. Fu AY, Spence C, Scherer A, Arnold FH, Quake SR (1999) A microfabricated fluorescence-activated cell sorter. *Nat Biotechnol* 17:1109–1111
  12. Voldman J, Gray ML, Toner M, Schmidt MA (2002) A microfabrication-based dynamic array cytometer. *Anal Chem* 74:3984–3990
  13. Wang MM, Tu E, Raymond DE, Yang JM, Zhang H, Hagen N, Dees B, Mercer EM, Forster AH, Kariv I, Marchand PJ, Butler WF (2005) Microfluidic sorting of mammalian cells by optical force switching. *Nat Biotechnol* 23(1):83–87
  14. Wolff A, Perch-Nielsen IR, Larsen UD, Friis P, Goranovic G, Poulsen CR, Kutter JP, Telleman P (2003) Integrating advanced functionality in a microfabricated high-throughput fluorescent-activated cell sorter. *Lab Chip* 3:22–27
  15. Cheung K, Gawad S, Renaud P (2005) Impedance spectroscopy flow cytometry: on-chip label-free cell differentiation. *Cytometry A* 65A:124–132
  16. Yang SY, Hsiung SK, Hung YC, Chang CM, Liao TL, Lee GB (2006) A cell counting/sorting system incorporated with microfabricated flow cytometric chip. *Meas Sci Technol* 7:2001–2009
  17. Van Dilla MA, Trujillo TT, Mullaney PF, Coulter JR (1969) Cell Microfluorometry: A Method for Rapid Fluorescence Measurement. *Science* 163:1213–1214
  18. Sobek D, Senturia SD, Gray ML (1994) Microfabricated Fused Silica Flow Chambers for Flow Cytometry', *Solid-State Sensor and Actuator Workshop*, Hilton Head, South Carolina, June 13–16, pp. 260–263
  19. Larsen UD, Blankenstein G, Branebjerg J (1997) "Microchip Coulter Particle Counter" Transducers '97: 1997 International Conference on Solid-state Sensors and Actuators, Chicago, June 16–19, 1997
  20. Koch M, Evans AGR, Brunnschweiler A (1999) Design and fabrication of a micromachined Coulter counter *J. Micromech. Microeng.* 9 159–61
  21. Altendorf E, Iverson E, Schutte D, Weigl B, Osborn T, Sabeti R, Yager P (1996) Optical flow cytometry utilizing microfabricated silicon flow channels *Proc. SPIE* 2678, 267–76
  22. Lee GB, Lin CH, Chang GL (2003) Micro flow cytometers with buried SU-8/SOG optical waveguides, *Sensors and Actuators A* 103 165–170
  23. Gawad S, Schild L, Renaud PH (2001) Micromachined impedance spectroscopy flow cytometer for cell analysis and particle sizing. *Lab Chip Sep*;1(1):76–82.
  24. Moldavan A (1934) Photo-electric technique for the counting of microscopical cells. *Science* 80(2069): 188–189. doi:10.1126/science.80.2069.188
  25. Coons AH, Creech HJ, Jones RN (1941) Immunological properties of an antibody containing a fluorescent group. *Exp Biol Med* 47(2):200–202. doi: 10.3181/00379727-47-13084P
  26. Kamensky A, Melamed MR (1969) Rapid multiple mass constituent analysis of biological cells. *Ann N Y Acad Sci* 157:310–323
  27. Crosland-Taylor PJ (1953) A device for counting small particles suspended in a fluid through a tube. *Nature (London)* 171:37–38. doi: 10.1038/171037b0
  28. Fulwyler MJ (1965) Electronic separation of biological cells by volume. *Science* 150:910–911. doi: 10.1126/science.150.3698.910
  29. Miyake R, Ohki H, Yamazaki I, Yabe R (1991) Micro electro mechanical systems, 1991, MEMS '91, Proceedings. An investigation of micro structures, sensors, actuators, machines and robots. *IEEE*. doi: 10.1109/MEMSYS.1991.114808
  30. Deblois RW, Bean CP (1970) Counting and sizing of submicron particles by the resistive pulse technique. *Rev Sci Instrum* 41(7):909–915. doi: 10.1063/1.1684724
  31. Chung S, Park SJ, Kim JK, Chung C, Han DC, Chang JK (2003) Plastic microchip flow cytometer based on 2- and 3-dimensional hydrodynamic flow focusing. *Microsyst Technol* 9:525–533. doi: 10.1007/s00542-003-0302-2
  31. Saleh OA, Sohn LL (2002) Correcting off-axis effects in an on-chip resistive-pulse analyzer. *Rev Sci Instrum* 73:4396. doi: 10.1063/1.1519932

---

## Flow in Channels with 3D Elements

Zheming Wu<sup>1</sup> and Dongqing Li<sup>2</sup>

<sup>1</sup>Goldman Sachs, Hong Kong, China

<sup>2</sup>Department of Mechanical and Mechatronics Engineering, Faculty of Engineering, University of Waterloo, Waterloo, ON, Canada

## Synonyms

Flow and mass transport through rough microchannels; Flow in microchannels with 3D roughness

## Definition

Electrokinetic or pressure-driven liquid flow in microchannels with three-dimensional (3D) surface roughness generated by manufacturing techniques or by adhesion of biological particles from the liquid.

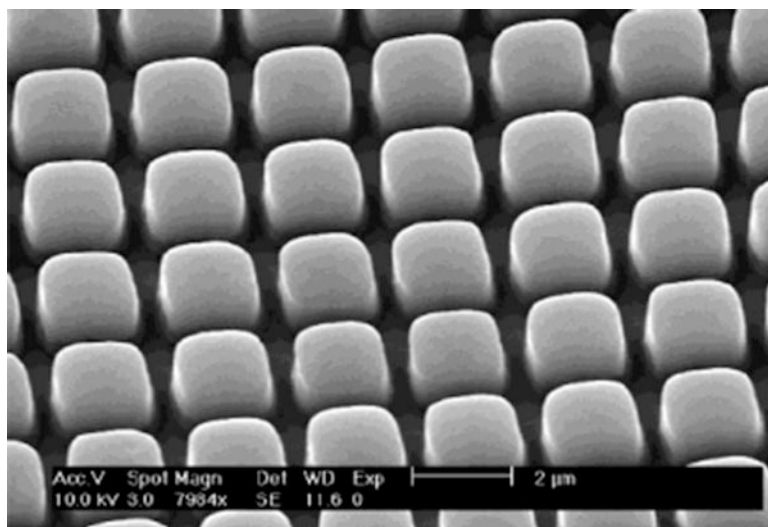
## Overview

Fundamental understanding of liquid flow through microchannels is important to the design and operation of lab-on-a-chip devices. The microchannel surfaces may exhibit certain degrees of roughness generated by the manufacturing techniques or by adhesion of biological particles from the liquids. The reported surface roughness elements range from 0.1 to 2  $\mu\text{m}$  [1–3]. Microfabrication techniques such as photolithography can also make 3D elements inside microchannels (see Fig. 1). The surface roughness of microchannels not only increases the reaction-sensing surface area but also plays an important role in determining the flow characteristics. In early experimental investigations of flow and heat transfer in microtubes and trapezoidal microchannels, the increase in flow friction and decrease in heat transfer attributed to surface roughness effects were observed [1–3].

For low Reynolds number pressure-driven flow through microchannels, the pressure drop over the microchannels is greatly increased by the existence of the 3D surface roughness elements, and periodical fluid expansions and compressions between rough elements are generated. These were clearly predicted by the 3D numerical simulations developed by Hu et al. [4]. The roughness elements act on the flow in two ways: causing the expansion and compressions of the streamlines and obstructing the flow directly, both giving energy losses of the fluids.

The roughness on channel walls also significantly influences the electrokinetic flows [5]. The electrical field is distorted by the presence of the nonconducting surface roughness elements, which makes the electroosmotic slip velocity of the liquid nonuniform [5]. The electroosmotic flow in a rough microchannel induces a periodic pressure field between rough elements that makes the central flow velocity smaller than that in the near-wall region and hence reduces the overall flow rate. The induced pressure field causes an exchange of liquid between the rough element gaps and the central flow, causing an even-out effect [5]. The flow congestion and flow circulation can be obtained in microchannels with heterogeneously charged 3D elements (i.e., with different zeta potentials), and a tidal wavelike

**Flow in Channels with 3D Elements, Fig. 1** An example of a silicon surface with microfabricated, symmetrically arranged prism elements



concentration field is found in heterogeneous channels with oppositely charged rough elements [6]. The electrokinetic flow behaviors in rough microchannels were verified by using the current monitoring technique and particle tracking technique [7].

As an application, the flow in rough microchannels was applied theoretically in the nucleic acid extraction process [8], which is the first critical step for many nucleic acid probe assays. Using a microchannel with 3D prismatic elements on the channel wall can dramatically increase the surface area-to-volume ratio and hence enhance the nuclei acid adsorption on the wall. The opportunity for molecule adsorption is also increased due to the induced pressure resisting the central bulk electroosmotic flow. It is found that decreasing the electroosmotic flow velocity or the channel height enhances nuclei adsorption.

## Cross-References

- ▶ [AC Electro-Osmotic Flow](#)
- ▶ [Combined Pressure-Driven Flow and Electroosmotic Flow](#)
- ▶ [Electrokinetic Flow in Porous Media](#)
- ▶ [Electroosmotic Flow \(DC\)](#)
- ▶ [Electroosmotic Flow over Heterogeneous Surfaces](#)

## References

1. Mala GM, Li D (1999) Flow characteristics of water through microtubes. *Int J Heat Fluid Flow* 20:142
2. Qu W, Mala GM, Li D (2000) Pressure-driven water flows in trapezoidal silicon microchannels. *Int J Heat Mass Trans* 43:353
3. Qu W, Mala GM, Li D (2000) Heat transfer for water flow in trapezoidal silicon microchannels. *Int J Heat Mass Trans* 43:3925
4. Hu Y, Werner C, Li D (2003) Influence of 3D surface roughness on low-Reynolds pressure-driven flow through microchannels. *Fluid Eng* 125:871
5. Hu Y, Werner C, Li D (2003) Electrokinetic transport through rough microchannels. *Anal Chem* 75:5747
6. Hu Y, Werner C, Li D (2004) Influence of the 3D heterogeneous roughness on electrokinetic transport in microchannels. *J Colloid Interface Sci* 280:527
7. Hu Y, Xuan X, Werner C, Li D (2007) Electroosmotic flow in microchannels with prismatic elements. *Microfluid Nanofluid* 3:151
8. Hu Y, Li D (2007) Modeling of nucleic acid adsorption on 3D prisms in microchannels. *Anal Chem Acta* 581:42

---

## Flow Patterns

### Definition

In single-phase flow, flow pattern means whether the flow is laminar or turbulent or whether flow separation or secondary flow exists. In multiphase flow, flow pattern refers to the internal geometry of the flow, i.e., the relative location of interfaces between the phases, such as stratified and dispersed.

### Cross-References

- ▶ [Bubble Dynamics in Microchannels](#)

---

## Flow Rate Measurements, Methods

John Collins<sup>1</sup> and Abraham P. Lee<sup>2</sup>  
<sup>1</sup>Biopico Systems Inc and University of California, Irvine, CA, USA  
<sup>2</sup>University of California, Irvine, CA, USA

### Synonyms

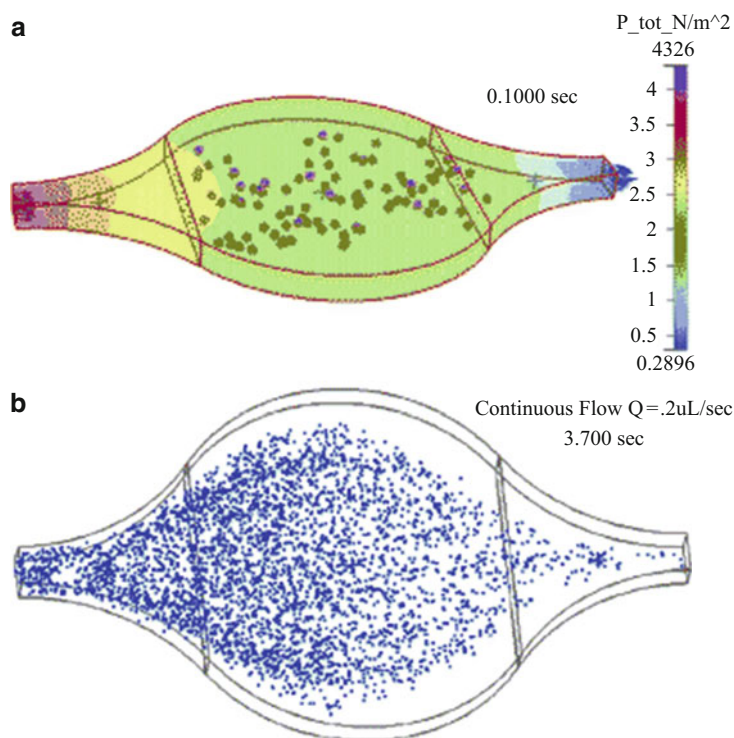
Flow measurement; Flow sensors; Fluidic pressure sensing

### Definition

In microfluidics, the volumetric flow rate is the volume of fluid flowing per unit time in the cross section of a microfluidic channel. The mass flow rate is significant in multiphase flow, where different fluid phases have different densities.

### Flow Rate Measurements, Methods, Fig. 1

A frame from a continuous flow of particles in a reaction chamber. (a) Flow of particles under a pressure gradient (the *arrows* at the inlet and outlet show the flow). (b) Flow front of high-density particles, showing a parabolic velocity profile. Note that the particles in the *middle* travel at a high velocity, thereby showing a low density, and the particles at the sides travel at a low velocity, thereby showing a high density



A fluidic pressure sensor measures the pressure drop due to the flow of fluid. Velocimetry is a technique for measuring the velocity profile of fluids by means of particles which are viscously dragged by the bulk of the fluid. Under laminar flow with no slip at the wall boundaries, a parabolic velocity distribution exists, and a good flow sensor integrates the parabolic velocity profile over the cross section of the flow.

### Overview

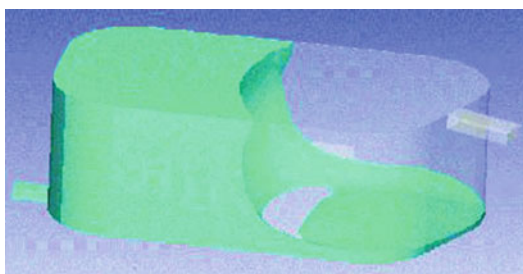
In microfluidics, control and manipulation of fluid flow can be accomplished by pressure-driven, electrokinetic, magnetohydrodynamic, centrifugal, and capillary forces. When forces such as electrokinetic and magnetohydrodynamic forces act on the walls of a microchannel, a slip in the fluid flow occurs at the walls. On the other hand, when forces such as pressure-driven forces act on the inlet or outlet, a laminar flow of fluid experiences no slip at the walls. Thus, the middle of the channel flows at a higher velocity than near the

walls. Figure 1 shows a microfluidic device used in a biosensing application. Figure 1a shows the flow of particles under a constant pressure gradient. Figure 1b shows the parabolic velocity profile of a flow front of high-density particles. Note that the particles in the middle of the channel travel with a higher velocity, thereby showing a lower density, and the particles near the walls travel with a lower velocity, thereby showing a higher density. Observing a statistical distribution of particles in a flow is equivalent to discretizing the entire fluid volume with velocity elements. This velocity profile can be integrated mathematically at any cross section of the fluid flow in order to compute the flow rate. The flow of a fluid with a velocity  $\mathbf{u}$  and pressure  $p$  at a time  $t$  is given by the Navier–Stokes partial differential Eq. 1

$$\frac{\partial \mathbf{u}}{\partial t} + (\mathbf{u} \cdot \text{grad})\mathbf{u} + \text{grad}(p) = \frac{1}{\text{Re}} \Delta \mathbf{u} \quad (1)$$

where  $\text{Re}$  is the Reynolds number, given by the ratio of inertial to viscous forces, and is very small for the laminar-flow regime of

microfluidics. Figure 2 shows the flow of a fluid under constant pressure. The bulk fluid is dispensed by drawing the flow out at the bottom outlet and venting air at the top inlet. Figure 3 shows the flow characteristics when a constant negative pressure is applied at the outlet. These calculations were based on computational fluid dynamic (CFD) simulations using the volume-of-fluid (VOF) model for the immiscible fluids air and water. A hydrophobic material with a contact angle of  $109^\circ$  was assumed in the CFD simulation, and fluidic properties of air and water were also assumed. The fluidic impedance caused by the geometry of the channel was evaluated from the pressure–flow rate characteristics. In the case of a hydrophobic wall, there is a threshold pressure that drives the flow against a hydrophobic force. A steady-state flow is obtained, and the



**Flow Rate Measurements, Methods, Fig. 2** Dispensing of fluid from a tank, where air is sent in at the inlet (*top*) and water is released at the outlet (*bottom*)

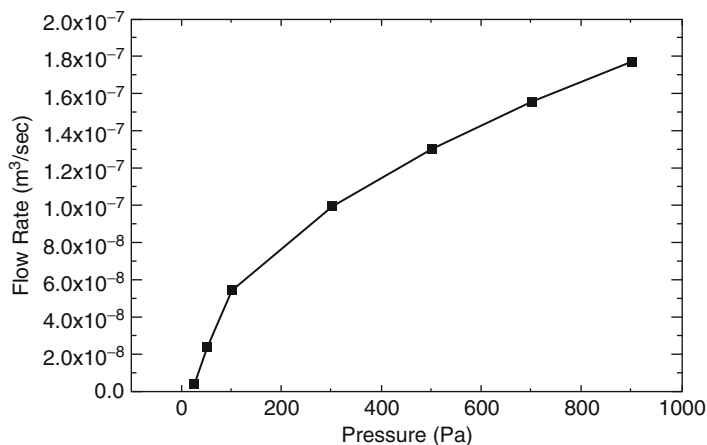
**Flow Rate Measurements, Methods, Fig. 3** Flow characteristics for a hydrophobic geometry of the kind shown in Fig. 2, showing the applied negative pressure and the flow rate at the outlet

flow is proportional to the pressure. Integration of the flow rate at every element of the cross section of a flow channel is performed in an ideal flow sensor.

The measurement of flow rates and the performance of quantitative analysis on fluids in minute volumes are greatly advancing the development of multifunctional, high-throughput lab-on-a-chip devices. Traditionally, there have been many MEMS-based flow sensors for gaseous flows. In recent times, several advancements have taken place in measuring microflows of liquids. Some examples of sensing principles for the measurement of microfluidic flow include heat transfer detection [1], molecular sensing [2], noninvasive optical techniques [3], atomic-emission detection [4], streaming-potential measurements, electrical-impedance measurements [5, 6], electrochemical redox cycling [7], amperometric sensing [8], ion-selective field-effect transistors, micromechanical sensing [9], and detection of periodic flapping motion [10]. Flow sensors are critical for controlled, precision flow to enable active micrototal analysis systems.

## Basic Methodology

Many of the well-established macroflow sensing methods such as the use of shear stress sensors, thermal anemometers, magnetohydrodynamic sensors, particle imaging, and fluorescent



imaging have been adapted and scaled down for microfluidics. However, miniaturization and integration issues have opened up new opportunities for microflow sensing. Broadly, flow sensors can be classified as either obstructive or nonobstructive to the flow. Obstructive flow sensors add fluidic resistance to the flow, and so nonobstructive flow sensors are generally preferred. These nonobstructive flow sensors can themselves be classified into invasive and noninvasive flow sensors. In invasive flow sensors, heat, electric current, or foreign substances such as fluorescent dyes or particles are added to the flow in order to perform the flow rate measurement. For example, fluorescence-correlation-spectroscopic and optical-Doppler-coherence tomographic measurements fall into this category. In noninvasive flow sensors, the sensing element does not physically make contact with the flow. Mostly, the flow sensing depends on optical parameters of the fluid, such as the refractive index, that depend on the flow rate. Sonic and radio-frequency signals can also be used for such measurements. In reality, there are no ideal noninvasive flow-sensing techniques. However, flow sensors that minimally modulate the flow optically, thermally, or electrically have been adapted for micrototal analysis applications. There is still research under way into high-sensitivity and very low-flow-rate measurements.

Time-of-flight (TOF) measurement is popular in microflow measurements. The time of flow of a pulse of temperature or of molecular tracers from one point in a microchannel to another point is characterized to measure the flow rate. An emitter and a collector are integrated into TOF sensors. Various optimizations of these sensors have been carried out, using temperature pulses or electrochemical production of molecular tracers. These sensors calculate the flow rate at one point in the cross section of the channel and are calibrated with a known flow rate. Flow measurement using microparticles captures the velocity profile at many such locations in the channel cross section and allows one to calculate the flow rate. Figure 4 shows the principle of a flow sensor using a CFD simulation of convective diffusion

of heat or molecular tracers generated at an emitter. The collector in the flow sensor records a measure of the flow. The relation between the flow sensor reading and the actual flow rate is nonlinear, and the flow sensor is calibrated for a window of operation of flow measurements.

## Experimental Techniques for Flow Sensing

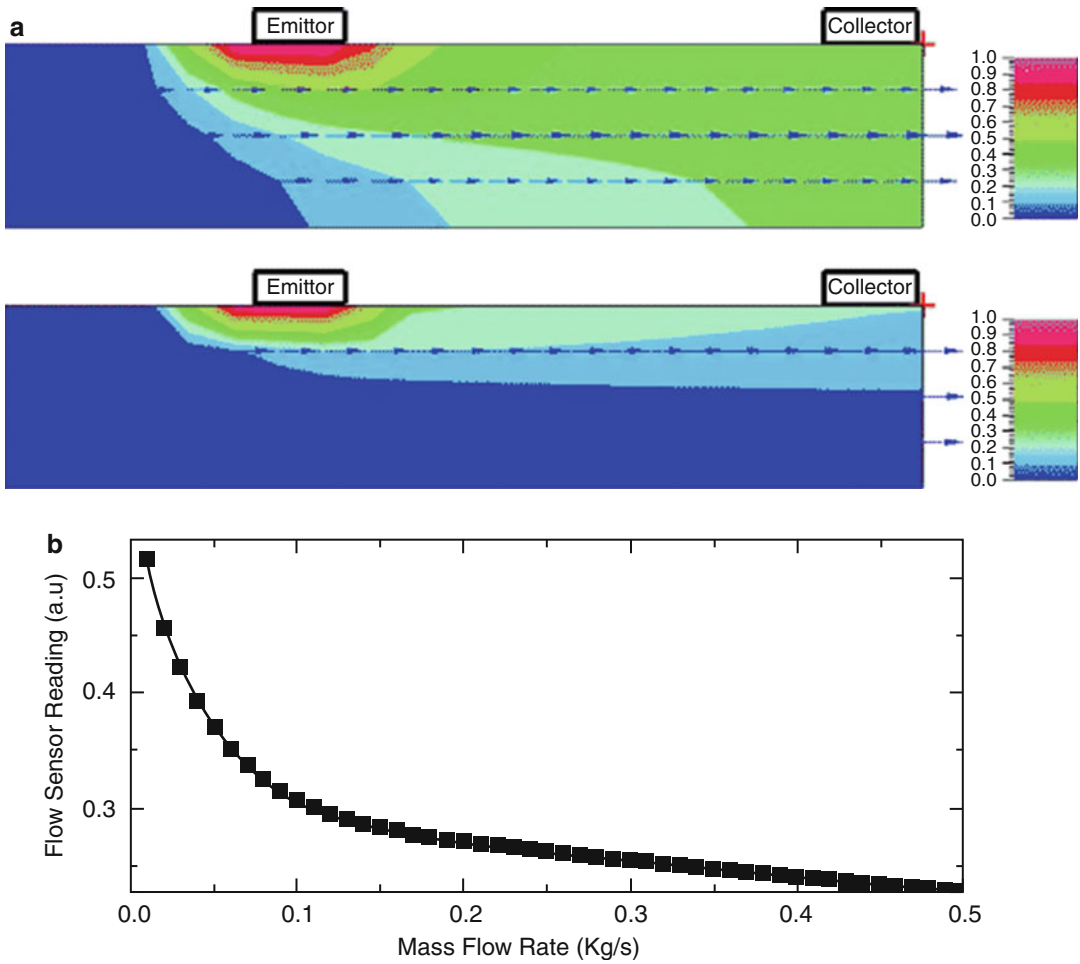
### Heat-Transfer-Detection-Based Flow Sensors

These thermal-anemometer-based flow sensors can sense very low flows in microchannels. The measurement principle is based on the thermal time of flight. The length of the heating pulse and the time of flight used in the measurement are measured in milliseconds. An example of the structure of a flow sensor is shown in Fig. 5 [1]. The structure consists of a heater in the middle, with an upstream and a downstream temperature sensor integrated into the wall of the channel. When there is no flow in the channel, heat diffuses into the two temperature sensor regions and no differential temperature is detected. An increase in the flow rate in the channel favors convection of heated fluid in the direction of the flow, and the differential temperature detected by the sensors increases.

The process flow for the fabrication of the microfluidic system includes a single or double metallization layer, a polymer layer for the fluidic system, and a glass sealing cap. There have been some efforts during fabrication to minimize the thermal-dissipation loss. The temperature difference between the two points where the sensors are located is measured with a differential current amplifier, and the flow rate is calibrated. At low flow rates, the temperature difference is a linear function of the flow rate as in Fig. 6. Measurements without heat insulation decrease the sensitivity of the flow sensor and increase the lower limit of flow rate detection. The distance between the heater and the sensors is optimized for the maximum differential temperature.

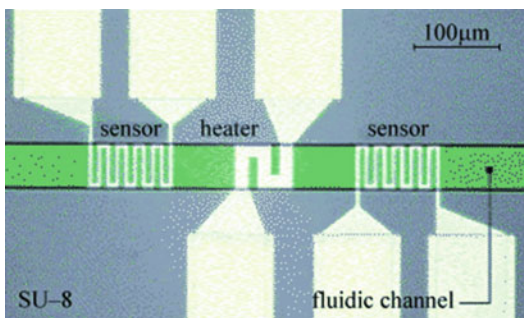
### Micromechanical Flow Sensors

Micromechanical flow meters measure shear forces produced as a result of fluid flow. The deflection of a micromechanical plate due to the



**Flow Rate Measurements, Methods, Fig. 4** Principle of a time-of-flight flow sensor using CFD simulation. (a) Convective diffusion of heat or of a molecular tracer

originating from the emitter wall. (b) Flow sensor reading, in arbitrary units, measured at the collector

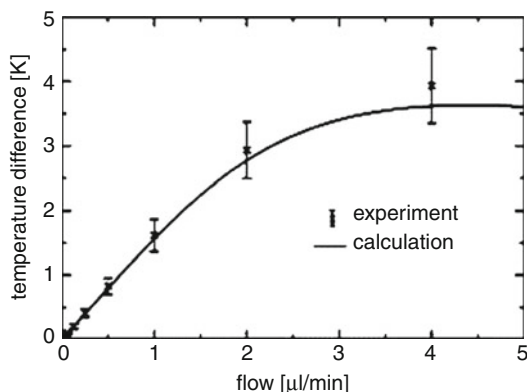


**Flow Rate Measurements, Methods, Fig. 5** Photomicrograph of a microfluidic mass flow sensor [1]

shear force can be measured optically using a system coupled to a laser deflection system. Figure 7 shows a schematic of such a plate, encapsulated in a channel. The major interaction between the fluid and the plate is through the stress field, which contains both normal (pressure) and shear stresses.

Assuming steady, unidirectional flow in the channel, the Navier–Stokes equation can be written as

$$\frac{\partial^2 u}{\partial y^2} + \frac{\partial^2 u}{\partial z^2} = \frac{1}{\mu} \frac{dP}{dx}$$



**Flow Rate Measurements, Methods, Fig. 6** Flow characteristics of a heat-transfer-based flow sensor. The lowest flow rate without heat insulation is on the order of 30 nL/min [1]

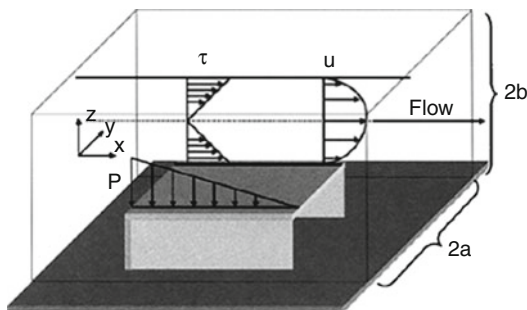
where  $u$  is the velocity of the fluid in the  $x$ -direction,  $\mu$  is the dynamic viscosity of the fluid, and  $dP/dx$  is the pressure gradient along the direction of flow. The equation can be solved for the  $x$ -component of the fluid velocity to yield a relation between the volumetric flow rate and the pressure gradient, as below:

$$\frac{dP}{dx} = \frac{3\mu Q}{4ab^3} S$$

where  $Q$  is the volumetric flow rate,  $a$  and  $b$  are half of the height and half of the width of the channel, respectively, and  $S$  is a factor depending on the geometry of the channel. The shear stress acting on the top surface of the plate is given by

$$\tau = -z \frac{3\mu Q}{4ab^3}$$

Flow was established in the microfluidic channel shown in Fig. 7 by means of a syringe pump, and the angular deflection of the plate was monitored. The encapsulated plate provided local flow information along the length of the channel. Such plates operate independently of the absolute pressure, and sensors of this kind can provide local flow information along the length of a microfluidic system. The resolution of the angular-deflection measurement system was



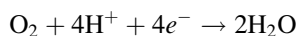
**Flow Rate Measurements, Methods, Fig. 7** Schematic of a plate encapsulated in a channel, showing the flow direction and the velocity profile for laminar flow above the device [9]

approximately 50  $\mu$ rad, yielding a flow resolution of about 1  $\mu$ L/min for the sensor. Figure 8 shows the response of the plate to a flow of ethanol [9]. The response of the flow meter was measured for flow rates ranging from 2.1 to 41.7  $\mu$ L/min.

#### Molecular Sensing

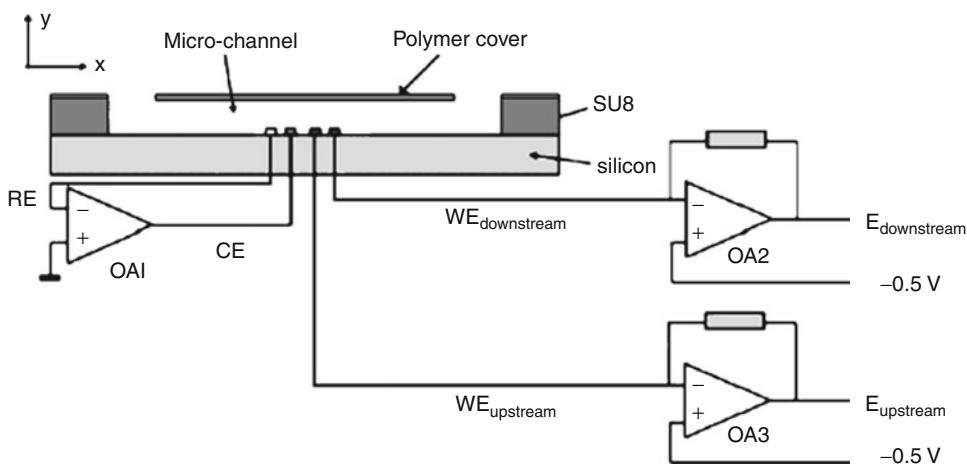
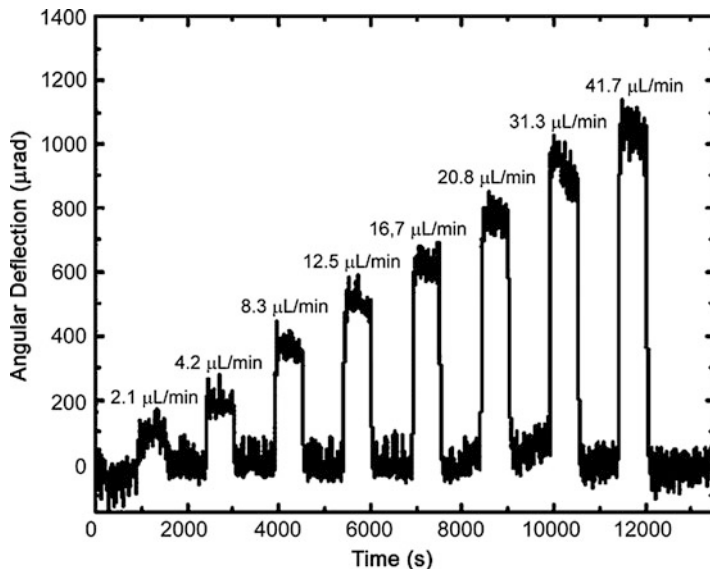
This type of electrochemical flow sensor is similar to a thermal sensor; here, molecules such as oxygen are generated by applying an electric current. One such system is based on measuring dissolved oxygen in an aqueous solution using two closely spaced integrated oxygen sensors. Figure 9 shows the geometrical details of such a flow sensor [8].

Upon application of a negative potential to the working electrodes, oxygen is reduced and a current passes through:



During measurement, the upstream amperometric oxygen sensor consumes part of the dissolved oxygen and the response of the downstream amperometric sensor is reduced, since the two sensors are closely spaced. The velocities in the  $y$ - and  $z$ -directions and diffusion along the  $x$ -direction can be neglected. The kinetics of the electrode reaction are fast enough to deplete the oxygen immediately, and the oxygen concentration at the surface of the working electrode is zero. The current passing through the

**Flow Rate Measurements, Methods, Fig. 8** Graph of the response of the plate to a flow of ethanol at eight different flow rates [9]



**Flow Rate Measurements, Methods, Fig. 9** Longitudinal cross section of a fabricated flow sensor and the related measurement setup. (The upstream and downstream oxygen sensors share a common counter

and reference electrode [8].) *RE* reference electrode, *CE* counter electrode, *WE* working electrodes, *OA* operational amplifier, *SU8* channel material

working electrode, *i*, is calculated according to Faraday’s law:

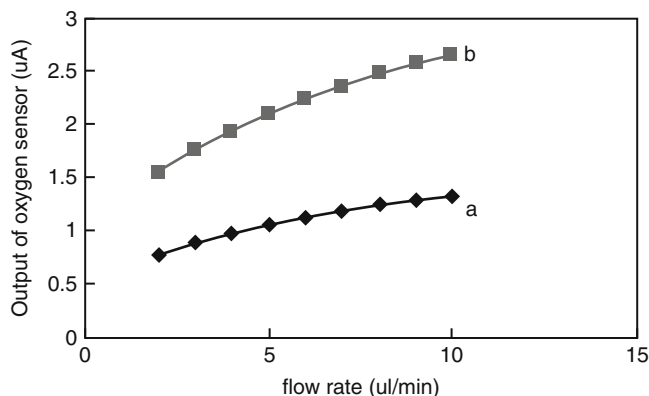
$$i = 4FAD \frac{dc}{dy}$$

where *F* is the Faraday constant, *c* is the concentration of oxygen, *D* is the diffusion coefficient, and *A* is the area of the working electrode.

The difference between the responses of the two sensors is related to the convective transportation. By comparing the outputs of the two amperometric sensors, the flow rate can be obtained. Figure 10 shows the measured amperometric response of the upstream oxygen sensor at different flow rates. For curve a, a gas mixture of 10 % oxygen and 90 % nitrogen was bubbled into a phosphate buffered saline (PBS) solution.

### Flow Rate Measurements, Methods,

**Fig. 10** Current passing through the upstream amperometric oxygen sensor at different flow rates for two solutions. *Curve a*, the solution was purged with a gas mixture of 10 % oxygen and 90 % nitrogen; *curve b*, the solution was purged with air [8]



For curve b, air was bubbled into the solution. The figure shows that the current passing through the oxygen sensors is related to both the flow rate and the oxygen concentration in the solution. The ratio of the responses of the two sensors is related only to the flow rate and is not affected by the change of the dissolved oxygen concentration. This electrochemical flow sensor can detect flow rates in the region of several microliters per minute, and the advantage of this flow sensor is that no additional tracers have to be added or produced during the flow measurement.

### Electrical-Impedance Sensing

Electrical-impedance-based flow sensing uses a pair of electrodes along the channel; this type of sensor is suitable for conducting solutions. An understanding of the electrical double layer is important for understanding the principle of operation of this flow sensor. When the flow rate is increased, the counterbalancing ions are replaced by the bulk solution, thereby lowering the average ionic concentration within the recording zone. This local concentration drop results in an increase in the real part of the impedance. Under hydrodynamic conditions, forced convection dominates the transport of ions to the electrodes within the flow channel. The electrical double layer formed across the channel, as shown in Fig. 11, is formed from two capacitances of the equivalent circuit, namely, the diffusion layer capacitance ( $C_s$ ) and the outer Helmholtz plane capacitance ( $C_e$ ). The former is due to an excess or depletion of ions in the channel, and the latter

is due to free electrons at the electrodes and is independent of the electrolyte concentration. The smaller of these capacitances dominates the admittance, since these capacitances are in series. The frequency of the applied ac voltage, the flow rate, and the conductivity of the fluid are the factors affecting the admittance of the fluidic system, and the flow-sensing principle is based on the optimization of these parameters (Table 1).

For the electrochemical oxidation of a species A to  $A^+$  in a microchannel, the convective-diffusive equation for mass transport under steady-state conditions is given by Eq. 2 below:

$$D_A \frac{\partial^2 [A]}{\partial y^2} - v_x \frac{\partial [A]}{\partial x} = 0 \quad (2)$$

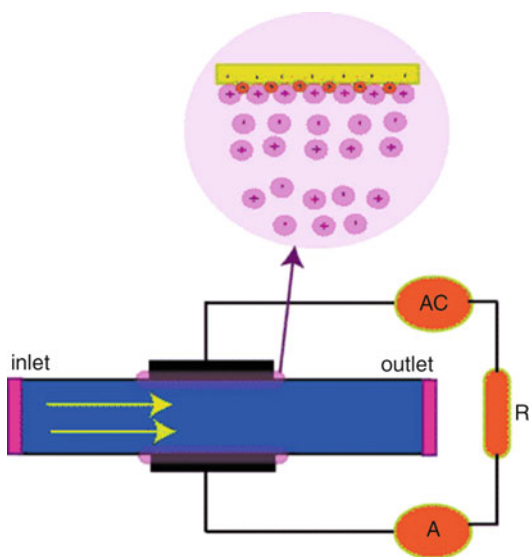
$$\frac{\partial A}{\partial t} = 0 \quad (3)$$

$$i_L = 0.925nF[A]_{\text{bulk}} D_A^{2/3} Q^{1/3} w \cdot \sqrt[3]{\frac{x_c^2}{h^2 d}} \quad (4)$$

Here  $[A]$  is the concentration of the species A,  $D_A$  is the diffusion coefficient, and  $v_x$  is the velocity in the direction of flow. The first term represents lateral diffusion in the microchannel, and the second term represents transport along the length of the channel. Under steady-state flow conditions, the boundary condition is given by Eq. 3. The solution of this equation predicts the mass-transport-limited current as a function of the flow rate  $Q$  as given by Eq. 4, where  $n$  is the number of

electrons transferred,  $F$  is the Faraday constant,  $x_e$  is the electrode length,  $h$  is the cell half-height,  $d$  is the width of the cell, and  $w$  is the electrode width. Note that the current due to the flow of electrolyte is directly proportional to the cube root of the volume flow rate of the fluid. An ac voltage signal is considered rather than a dc voltage, since the application of an ac voltage to the flow sensor does not promote any electrode reactions. Optimization of electrical parameters such as the voltage and frequency of the ac signal is an essential condition for measuring low flow rates.

A flow sensor of this type was fabricated on a glass substrate with gold surface electrodes (Fig. 12a), and the microfluidic channel was



**Flow Rate Measurements, Methods, Fig. 11** Electrical-impedance-based flow-sensing device

made of PDMS. Gold of thickness 100 nm was deposited on an adhesion layer of titanium of thickness 20 nm using e-beam deposition. A spun layer of Shipley photoresist (1827) was used for patterning the metal (Fig. 12b). PDMS channels of width 500  $\mu\text{m}$  were made from an SU8 mold. The glass and PDMS were bonded together after treatment with an oxygen plasma for 1 min. The fluidic channel was aligned with the parallel electrodes using a stereomicroscope. The measuring instrumentation was similar to that used in strain gauge and thermocouple interfaces. The microfluidic flow was maintained at a constant flow rate using a Harvard Picoplus syringe pump. This flow sensor was capable of measuring very low values of flow rate, starting at 0.05  $\mu\text{L}/\text{min}$  ( $<1$  nL/s). The response showed a cube root behavior even at very low flow rates, as shown in Fig. 13 [6]. The sensitivity after optimization was  $5.2 \cdot 10^{-4}$  mA/ $(\mu\text{L}/\text{min})$ . Fluorescent beads of diameter 2.5  $\mu\text{m}$  were sent through the channel, and video microscopy of their flow profile was performed. The flow sensor results were compared with the velocity of the beads (shown by the asterisks in Fig. 13) and showed a similar response. Figure 14 shows the magnitude and phase data for the flow condition after the impedance spectra for the solution had been divided by the no-flow spectra [5].

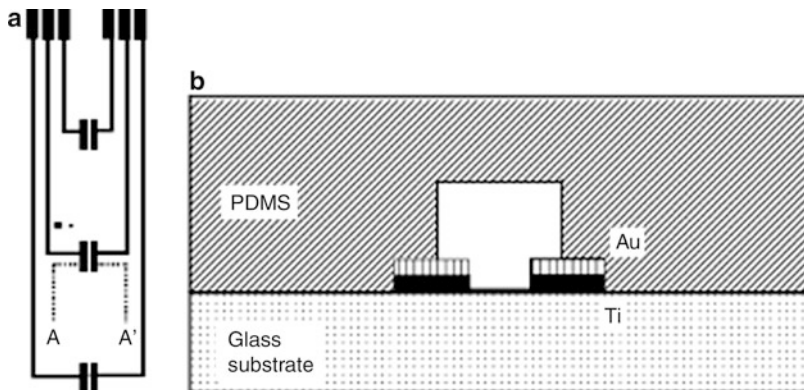
There is a need for the development of flow sensors integrated into specific applications. Integrated micrototal analysis systems would require a feedback loop for reconfigurable and programmable assays, for controlling the dosage in the case of drug delivery, for reagent concentration control in bioassays, and for advanced on-chip

**Flow Rate Measurements, Methods, Table 1** Summary of the most popular flow sensors

Method	Flow rate limit	Sensitivity	Limitations
Heat transfer	0.01 $\mu\text{L}/\text{min}$	1.4 mV/(nL/min)	Heats the sampling fluid ( $\sim 1$ K/min/ $\mu\text{L}$ ), complex fabrication
Mechanical	1.0 $\mu\text{L}/\text{min}$	50 $\mu\text{rad}/(\mu\text{L}/\text{min})$	Moving parts, complex fabrication
Molecular sensing	2.5 $\mu\text{L}/\text{min}$	–	Aqueous fluids with dissolved oxygen
Optical	0.048 $\mu\text{L}/\text{min}$	–	No integration available
Flapping frequency	0.1 mm/s	–	Reported for gas flow, complex fabrication
Impedance sensing	0.05 $\mu\text{L}/\text{min}$	$10^{-4}$ mA/ $(\mu\text{L}/\text{min})$	Limited to conducting fluids

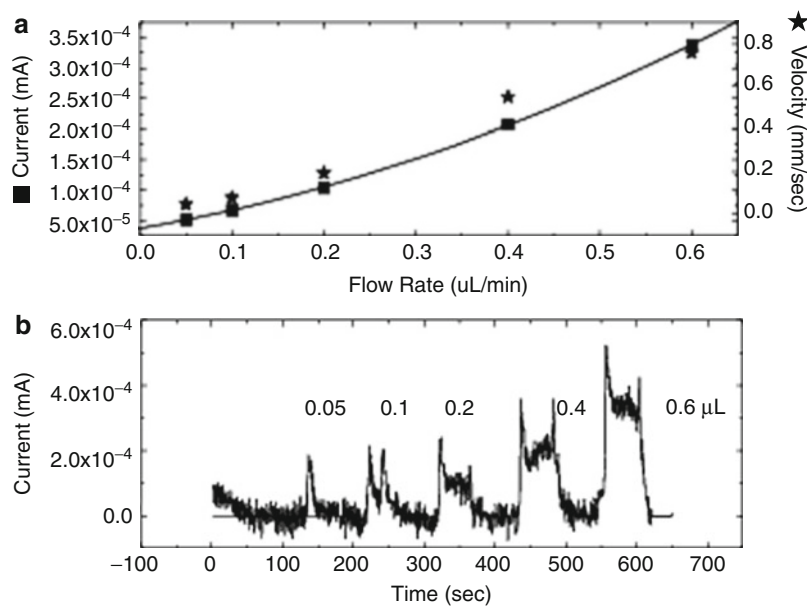
### Flow Rate Measurements, Methods,

**Fig. 12** (a) Layout of fabricated electrodes and wiring for measuring the current flow. (b) Cross section of the fabricated flow sensor through the electrodes at AA' in (a) [6]



### Flow Rate Measurements, Methods,

**Fig. 13** Response of flow sensor at very low flow rates. (a) Instantaneous current values when the flow was varied and switched. The results in (a) are replotted in (b). The velocities of beads at different flow rates of the fluid are also shown on the right axis of (a). (The peaks in (b) correspond to the flow rate values labeled) [6]



micropumps that have flow regulation built in. Moreover, it is necessary to develop linear flow sensors which require no calibration and do not affect the fluid or the flow rate.

#### Periodic-Flapping-Motion Detection

A flow sensor using this principle has been demonstrated [10] for gas flows; it works on the principle of detecting a periodic flapping motion of a planar jet impinging on a V-shaped plate downstream in the low-Reynolds-number regime. The Strouhal number  $St$ , which describes an oscillating flow by the ratio of the inertial forces due to unsteady flow to the inertial forces due to changes in velocity, was found to remain

nearly constant if the opening angle of the V-shaped plate was appropriately chosen. The Strouhal number is defined as

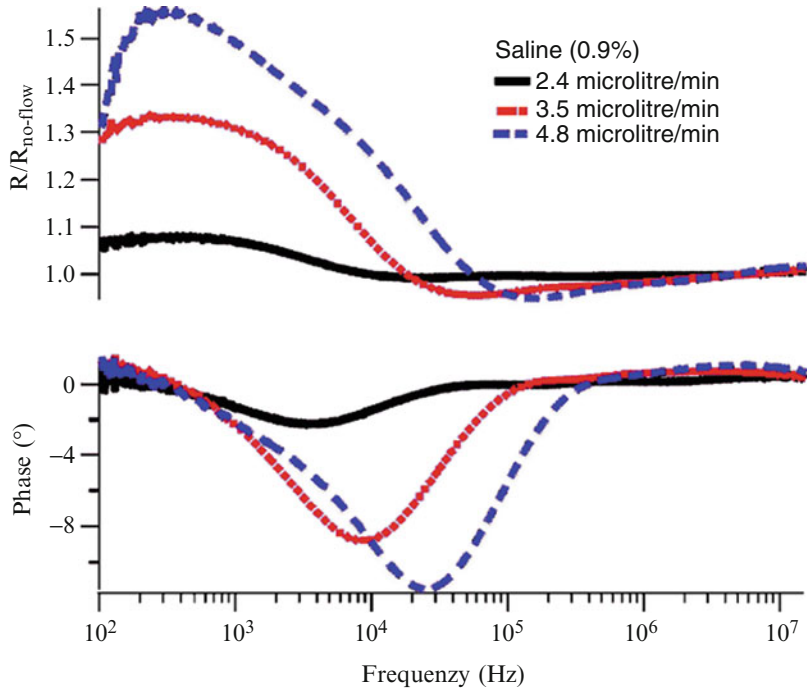
$$St = \frac{f_F L}{V_j}$$

where  $f_F$ ,  $L$ , and  $V_j$  are the flapping frequency, the length of the impinging jet, and the jet exit velocity, respectively.

Instead of sensing DC current or voltage signals induced by small volumes in the flow, this flow sensor detects the oscillation frequency of the periodic flapping jet, resulting in a higher sensitivity and a larger dynamic range than

### Flow Rate Measurements, Methods,

**Fig. 14** Magnitude and phase data for the flow condition after the impedance spectra of the solution have been divided by the no-flow spectra [5]



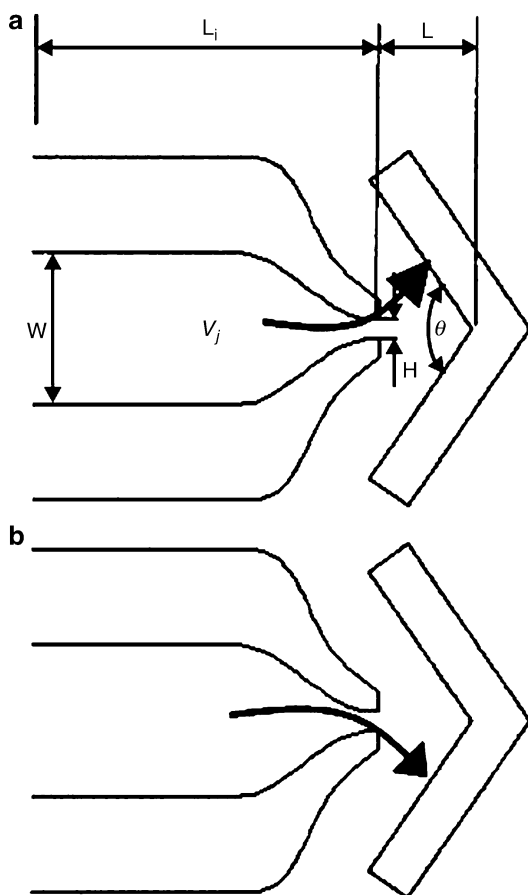
F

those of existing products. The sensor is composed of a planar convergent nozzle, a V-shaped plate downstream, and a pair of sensing resistors. A sample flow containing a dye allows the flapping motion of the impinging jet to be visualized under a microscope. The flapping motion has been confirmed experimentally even at a low flow velocity (0.15 mm/s). The flapping frequency is detected using built-in microsensing resistors driven by a constant-current circuit. Figure 15 shows a schematic of the flapping motion of the jet column for a microflow sensor with a convergent nozzle and a V-shaped plate. Even on the microscale, the flow velocity is linearly proportional to the frequency of the flapping motion, as shown in Fig. 16, and the velocity or volumetric flow rate of small amounts of flow can be measured by detecting the flapping frequency.

### Optical-Sensing-Based Flow Sensors

Backscatter interferometry, optical coherent tomography, and particle-imaging velocimetry are some of the optical techniques for flow sensing. The backscatter interferometric flow-sensing system [3] may be considered to be in this category. This system is based on synchronous

detection and measurements of the phase difference with respect to fluid-heating events upstream produced by a focused IR source. The heating upstream is repeated for several cycles using a mechanical shutter inserted into the IR beam path. The frequencies of both the shutter and the detected signals are synchronous and time-varying. However, the detected signal downstream lags behind the shutter signal by the amount of time it takes for the fluid to warm up and propagate from the heating region to the detection region. The fluid flow velocity in the microchannel can be quantified by performing Fourier decomposition of the signals and calculating the phase change between the appropriate harmonics of those signals in the Fourier domain. A block diagram of the experiment is shown in Fig. 17. The interferometric backscatter detector is based on a fiber-coupled HeNe laser that illuminates a portion of an isotropically etched channel and a position-sensitive transducer to measure fringe pattern shifts. An infrared laser with a mechanical shutter is used to heat a section of the flowing volume, and the resulting refractive-index change is detected downstream as a time-dependent perturbation. The fluid velocity is

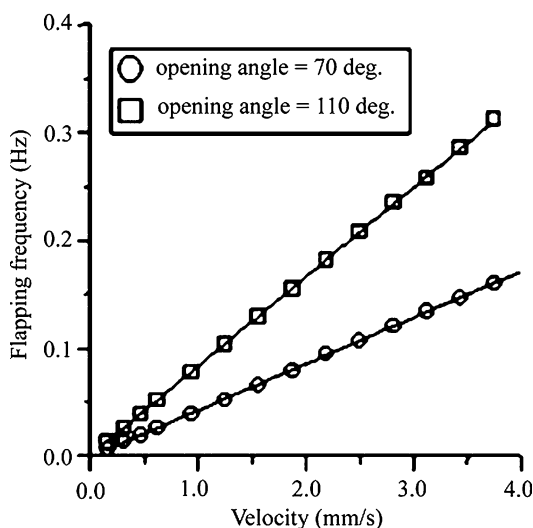


**Flow Rate Measurements, Methods, Fig. 15** Schematic representation of the flapping motion of the jet column for a microflow sensor with a convergent nozzle and a *V-shaped* plate. Periodic flapping motion occurs when the impinging jet reaches the *V-shaped* plate. (a) Jet column flaps upward, and (b) jet column flaps downward [10]

quantified by changes in the phase difference with respect to the shutter signal, as in Fig. 18. This flow sensor has been established to be suitable for flow measurements in the range 3–6  $\mu\text{L}/\text{h}$  with a detection limit of 0.127 nL/s.

#### Near-Field Heterodyne Grating-Based Flow Sensors

In this optical technique based on photothermal effects, pump light is shone on a transmission grating in front of a fluid channel and the inside liquid is heated with a pattern of the grating due to the Talbot effect [11]. Another probe light is



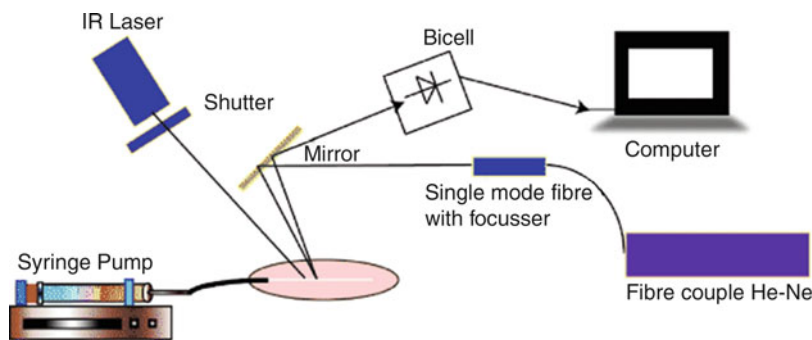
**Flow Rate Measurements, Methods, Fig. 16** The flow velocity is linearly proportional to the flapping frequency, and two sensors with different opening angles have similar behaviors [10]

similarly shone on the same place as the pump light, and the diffraction by the transmission grating (reference) and the diffraction by the temporally generated thermal grating inside the fluid channel (signal) are mixed and performed heterodyne detection. In principle, the two diffractions progress in the same direction, and therefore their combination is detected by a detector positioned at a visible diffraction spot (heterodyne detection). Figure 19 shows the application of the NF-HDG method to a microchip and the flow sensor calibration. The optimization of the grating-sample distance based on the Talbot effect enhances the signal intensity and the detectable flow rate limit is as low as 0.017 ml/min.

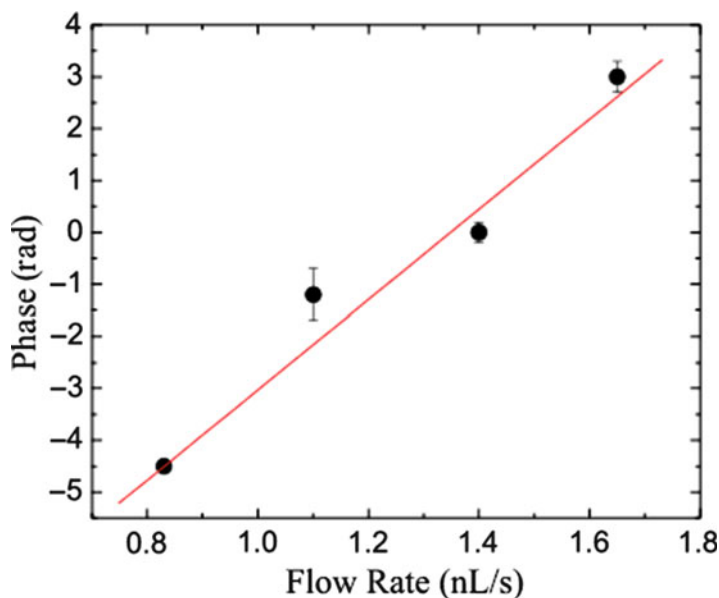
#### Integrated Optical Fiber Cantilever-Based Flow Sensors

A fiber-tip cantilever transduces flow rates to optical signal readout, and fiber-optic sensor alignment is guided by preformed microfluidic channels [12]. The sensing mechanism is based on displacement of an emitting optical fiber tip due to fluidic drag force, which reduces optical coupling to a receiving multimode fiber.

**Flow Rate Measurements, Methods, Fig. 17** Block diagram of the experimental setup for a backscatter interferometric flow-sensing system [3]



**Flow Rate Measurements, Methods, Fig. 18** Calibration curve of phase change versus flow rate in a microfluidic channel [3]

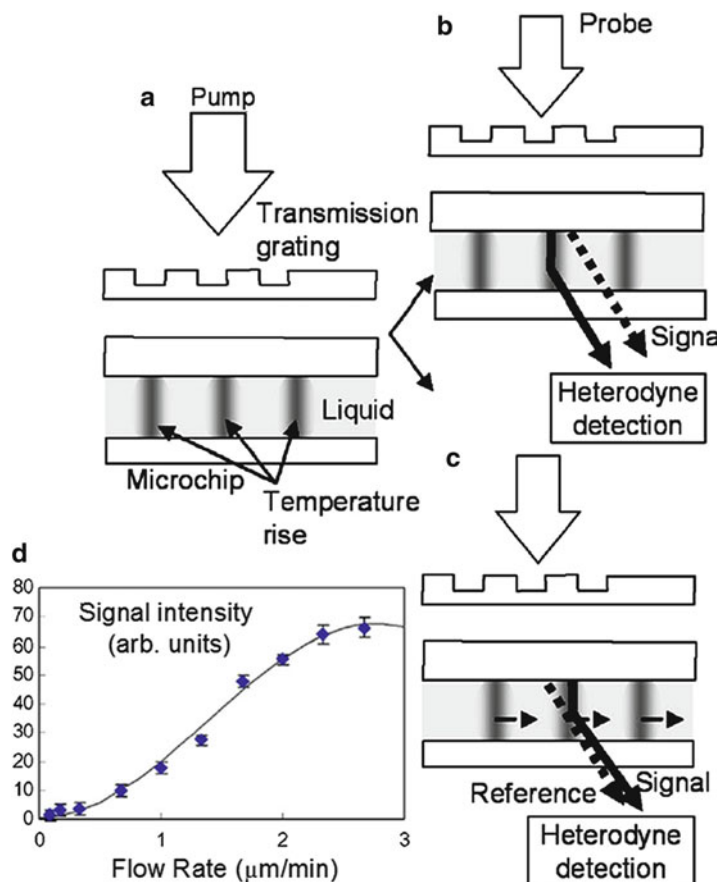


The mechanically flexible and optically transparent silica optical fiber can be thinned by hydrofluoric acid (HF) etching, and the dynamic range can be adjusted in a one-step chemical etch. Increase in volume flow rate bends the single-mode fiber-tip cantilever, which is then no longer aligned with the multimode receiving fiber, thus reducing the transmitted intensity. The drag force exerted on the fiber-tip cantilever with cylindrical cross section is given as  $FD = (\frac{1}{2})\rho AU^2 C_D$ , where  $\rho$  is the density of fluid,  $U$  is the flow velocity,  $A$  is the cross-sectional area of the cylinder in the plane normal to  $U$ ,  $C_D$  is the drag coefficient, and  $A = 2aL$  in the case of a transverse cylinder of radius  $a$  and length  $L$ . The single-mode fiber tip is aligned with

a cleaved multimode fiber and permanently fixed in place during the fabrication process so that maximum coupling efficiency is obtained for zero flow rate. Fluidic drag force bends the cantilever (Fig. 20), which results in a situation equivalent to an angular scan of the single-mode fiber's far-field distribution using a multimode fiber core as the detector. The two fibers are threaded through two 300 mm-wide alignment channels, so that the stripped part of the single-mode fiber crosses the 750 mm-wide microfluidic channel. Figure 21 shows the optical readout of the fiber cantilever sensor in response to various flow rates of distilled water. It is seen that the sensor recovers its baseline response even after transient exposure to relatively large flow rates.

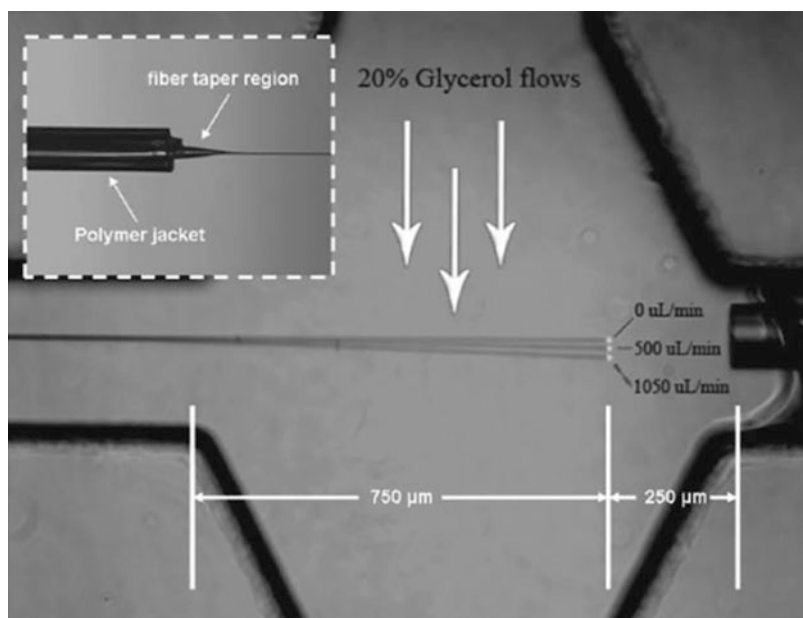
### Flow Rate Measurements, Methods,

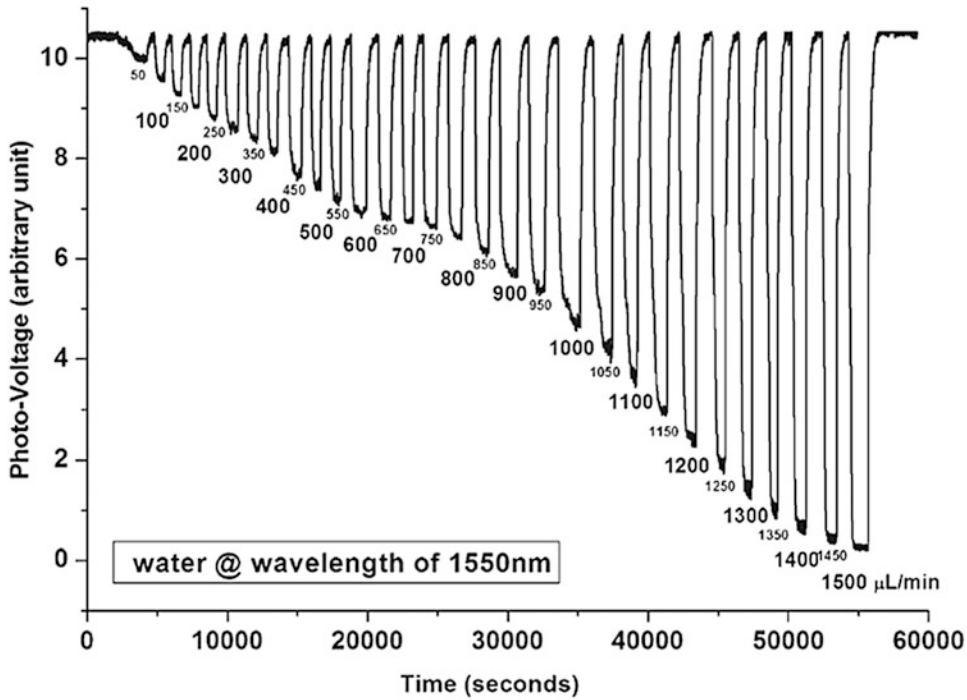
**Fig. 19** Application of the NF-HDG method [11] to a microchip. (a) A pump light beam is incident on a grating, and the liquid in the microchannel is excited by a grating pattern of the pump light. (b) A probe light beam is incident and diffracted by both the transmission grating and thermal grating in the microchannel. (c) When the fluid is in motion, the heterodyne signal intensity is changed by change in the phase relation between the reference and the signal. (d) Calibration curves of flow rate measured in the microtube at the chopper frequency 602 Hz



### Flow Rate Measurements, Methods,

**Fig. 20** Integrated micro-opto-fluidic flow sensor [12]. Displacement of the fiber tip is shown for three flow rates of a 20% glycerol–water mixture. The inset shows the fiber-tip cantilever fabricated in a one-step chemical etch





**Flow Rate Measurements, Methods, Fig. 21** Optical response of the fiber cantilever sensor to various volumetric flow rates (0–1,500 mL/min) of water

**Flow Rate Measurements, Methods, Table 2** Summary of the most popular flow sensors

Method	Flow rate limit	Sensitivity	Limitations
Heat transfer	0.01 mL/min	1.4 mV/(nL/min)	Heats the sampling fluid (~1 K/min/mL), complex fabrication
Mechanical	1.0 mL/min	50 mrad/(mL/min)	Moving parts, complex fabrication
Molecular sensing	2.5 mL/min	–	Aqueous fluids with dissolved oxygen
Optical	0.048 mL/min	–	No integration available
Flapping frequency	0.1 mm/s	–	Reported for gas flow, complex fabrication
Impedance sensing	0.05 mL/min	10 <sup>-4</sup> mA/(mL/min)	Limited to conducting fluids
Near-field heterodyne grating	0.017 mL/min	–	Use of optical fiber and grating
Integrated optical fiber cantilever	7 mL/min	–	Fabrication of thin fiber cantilever

### Key Research Findings

There have been reports on the theory of most types of flow sensor and CFD simulations and experimental validations of them. Table 2 summarizes the most popular flow sensors, with the flow rate resolution or lower limit, and their limitations.

### Commercial Microfluidic Flow Sensors

Commercial flow sensors provide high-precision thermal sensor technology to enable measurements of low flow rates with low internal volume and no moving parts. In these thermocalorimetric measurements, the liquid is heated up slightly to analyze the temperature profile and recorded by



**Flow Rate Measurements, Methods,**  
**Fig. 22** Elveflow microfluidic flow sensor

an integrated A/D converter. For example, Sensirion CMOSens<sup>®</sup> microsensor enables flow rates down to 25 nL/s. Elveflow microfluidic flow sensor (shown in Fig. 22) enables to monitor flow down to 1.2 nL/s with resolution of 1.5 pL/s. Dolomite Mitos flow sensor enables flow rate measurement down to 6.6 nL/s. GeSiM flow sensor measures small flow rates below 16 nL/s.

### Future Directions for Research

There is a need for the development of flow sensors integrated into specific applications. Integrated micrototal analysis systems would require a feedback loop for reconfigurable and programmable assays, for controlling the dosage in the case of drug delivery, for reagent concentration control in bioassays, and for advanced on-chip micropumps that have flow regulation built in. Moreover, it is necessary to develop linear flow sensors which require no calibration and do not affect the fluid or the flow rate. Though volume metering is important in several biotechnological applications, the recent trend is in developing methodology that does not depend very much on the flow rate and the research focus is in biosensing rather than flow sensing.

### Cross-References

- ▶ [Droplet-Based Lab-on-Chip Devices](#)
- ▶ [Mechanical Nanosensors](#)
- ▶ [Nanoscale Biosensors](#)
- ▶ [Time-of-Flight Filter](#)
- ▶ [Velocimetry](#)

### References

1. Scholer L, Lange B, Seibel K, Schafer H, Walder M, Friedrich N, Ehrhardt D, Schonfeld F, Zech G, Bohm M (2005) Monolithically integrated micro flow sensor for lab-on-chip applications. *Microelectron Eng* 78–79:164–170
2. Wu JA, Sansen W (2002) Electrochemical time of flight flow sensor. *Sensor Actuator A Phys* 97–98:68–74
3. Markov DA, Dotson S, Wood S, Bornhop DJ (2004) Noninvasive fluid flow measurements in microfluidic channels with backscatter interferometry. *Electrophoresis* 25(21–22):3805–3809
4. Nakagama T, Maeda T, Uchiyama K, Hobo T (2003) Monitoring nano-flow rate of water by atomic emission detection using helium radio-frequency plasma. *Analyst* 128(6):543–546
5. Ayliffe HE, Rabbitt RD (2003) An electric impedance based microelectromechanical system flow sensor for ionic solutions. *Meas Sci Technol* 14(8):1321–1327
6. Collins J, Lee AP (2004) Microfluidic flow transducer based on the measurement of electrical admittance. *Lab Chip* 4(1):7–10
7. Amatore C, Belotti M, Chen Y, Roy E, Sella C, Thouin L (2004) Using electrochemical coupling between parallel microbands for in situ monitoring of flow rates in microfluidic channels. *J Electroanal Chem* 573(2):333–343
8. Wu J, Ye J (2005) Micro flow sensor based on two closely spaced amperometric sensors. *Lab Chip* 5(12):1344–1347
9. Czaplewski DA, Ilic BR, Zalalutdinov M, Olbricht WL, Zehnder AT, Craighead HG, Michalske TA (2004) A micromechanical flow sensor for microfluidic applications. *J Microelectromech Syst* 13(4):576–585
10. Lee GB, Kuo TY, Wu WY (2002) A novel micromachined flow sensor using periodic flapping motion of a planar jet impinging on a V-shaped plate. *Exp Therm Fluid Sci* 26(5):435–444
11. Katayama K, Uchimura H, Sakakibara H, Kikutani Y, Kitamori T (2007) In situ microfluidic flow rate measurement based on near-field heterodyne grating method. *Rev Sci Instrum* 78:083101
12. Lien V, Vollmer F (2007) Microfluidic flow rate detection based on integrated optical fiber cantilever. *Lab Chip* 7:1352–1356

## Flow-Based Particle Trapping and Manipulation

Melikhan Tanyeri and Charles M. Schroeder  
Department of Chemical and Biomolecular  
Engineering, University of Illinois at  
Urbana-Champaign, Urbana, IL, USA

### Synonyms

Flow-based tweezers; Microfluidic trapping and manipulation; Microfluidic tweezers

### Definition

Controlling small particles in free solution is an essential technology for nanoscience and engineering. However, confinement and fine-scale manipulation of micro and nanoscale particles remains a significant challenge in the field. At present, particle trapping methods based on acoustic, electrokinetic, magnetic, and optical fields are utilized, but some of these methods are limited to particles with specific material properties and/or bulky micron-scale dimensions. Recently, a number of flow-based trapping and manipulation methods have been developed. This entry describes methods for flow-based control of micro- and nanoscale particles and summarizes recent advances in the field. The discussion in this entry is limited to flow-based traps and tweezers; methods utilized for particle sorting and separation are discussed in “► [Lab-on-a-Chip Devices for Particle and Cell Separation](#).”

### Physical Principles and Key Research Findings

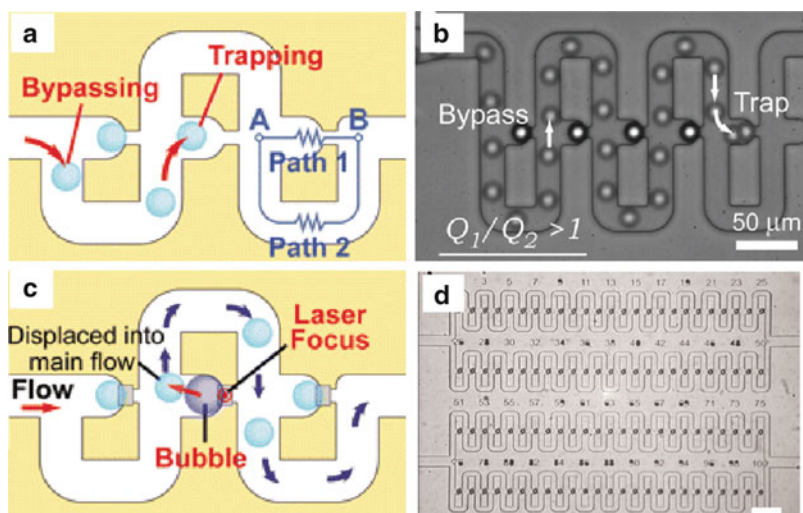
Macroscopic objects can be handled by high-precision manipulation tools such as tweezers. However, macroscopic manipulation methods are not suitable for controlling micro- or nanoscale objects with dimensions smaller than

100  $\mu\text{m}$ . To address this challenge, a wide array of confinement and manipulation techniques for micro- and nanoscale particles in solution has been developed using a variety of force fields (e.g., electric, magnetic, optical, acoustic) [1–4]. These methods have led to key advances in many fields of science and engineering including physics and materials science. Nevertheless, many of these methods impose limitations for applications in molecular and cellular biology due to the perturbative nature of the underlying force fields. From this perspective, there is a strong need for alternative trapping methods, which allow for gentle and minimally invasive handling and manipulation of biological objects.

Flow-based trapping and manipulation methods utilizing microfluidic systems have emerged as an alternative path to meet these needs. Flow-based methods employ a combination of fluid flow, distinct microchannel geometries, and physical structures within the channels of a microfluidic device to enable gentle confinement and manipulation of micro- and nanoscale objects. Modern flow-based microfluidic methods for particle trapping can be classified into two categories: contact based or contact-free. Here, a brief overview of each category is provided along with the physical principles.

#### Contact-Based Methods

Contact-based trapping and manipulation methods utilize fluid flow and various micro-patterned structures to confine particles [5, 6]. The general physical principle for this trapping method is to use hydrodynamic flow in order to capture a single particle within a pocket-like microstructure called the *trapping site* (Figs. 1 and 2). Particles are carried into trapping sites by fluid flow. Trapping sites are designed to have relatively low flow resistance, which facilitates initial transport of particles into the site. Once a particle enters the trapping site, contact between the particle and the trapping structure significantly increases the flow resistance of the trapping site, diverting the main fluid stream away from the trapping site. Physical contact between the particle and the micropatterned



**Flow-Based Particle Trapping and Manipulation, Fig. 1** (a) Schematic diagram of a contact-based microfluidic trap. When the trapping site is empty, flow resistance along the straight channel (path 1) is lower than that of the loop channel (path 2), and the main flow stream along the straight channel carries objects into the trapping site (trapping mode). If a trapping site is filled, objects will be carried along the loop channel, bypassing the occupied trap (bypassing mode). This design allows for capturing a single object at a trapping site. (b) Superimposed time-lapsed high-speed camera images showing capture of a single bead at an empty trapping site. The image shows

the path of a single bead passing through four occupied trapping sites and finally being captured by the next empty trapping site. (c) Release mechanism using microbubble. An IR laser beam is focused onto the aluminum pattern, causing localized heating and bubble formation. The formed bubble displaces the trapped particle from the trap into the main flow. The particle is then carried out of the device by the main flow. (d) A micrograph of a  $4 \times 25$  trap array device demonstrating trapping of 100 beads ( $15 \mu\text{m}$  diameter) (scale bar,  $100 \mu\text{m}$ ) (Reproduced with permission from [5] © 2007 National Academy of Sciences, U.S.A)

structure is maintained by the flowing fluid, which prevents the release of the trapped particle, thereby resulting in long-term confinement of the particle at the trapping site. Subsequent particles simply “bypass” the trapping site, which limits superfluous capture of particles.

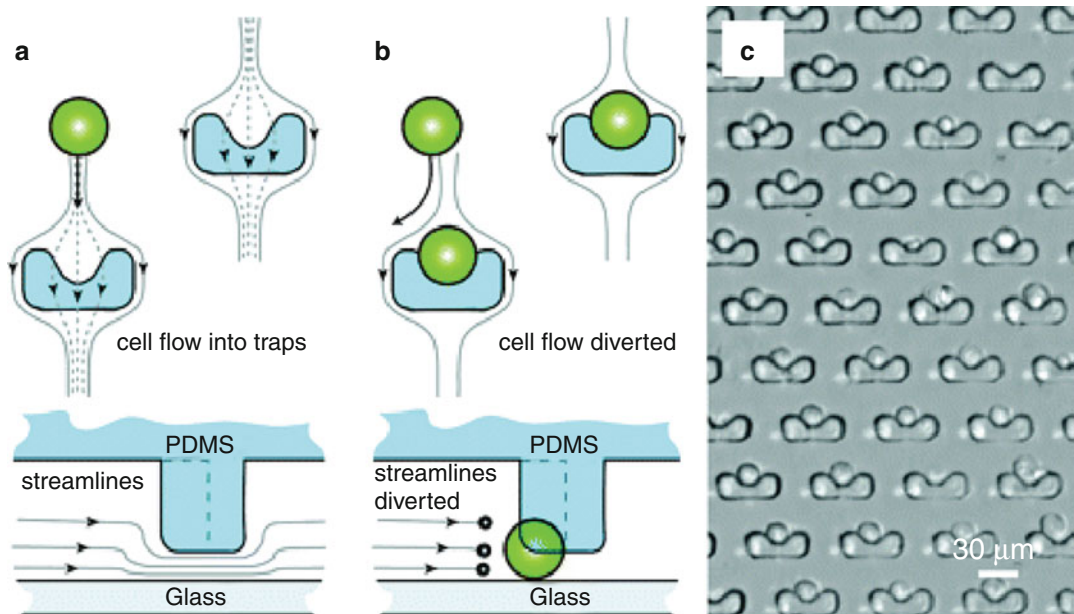
**Advantages:** The main advantages of the contact-based methods are their relatively simple design and operation and the ability to create large arrays of particles for long-term high-throughput analysis. Furthermore, by utilizing microfluidic tools, it is possible to change the microenvironment around the trapped particles during analysis and observation.

**Disadvantages:** In general, contact-based traps are passive traps such that trapped particles cannot be manipulated. Moreover, these methods often lead to irreversible capture of objects, which complicates the retrieval of trapped objects. For those methods where particle

retrieval is feasible, it is generally carried out either by using external force fields – which also allows for retrieving specific target particles [5] (Fig. 1c) – or by reversing the fluid flow direction [6]. Furthermore, the size range of particles that can be captured with these methods is fairly small and primarily depends on the design and the dimensions of the trapping site.

### Contact-Free Methods

Although contact-based methods have proved useful for biological studies, there is a strong need for contact-free, flow-based methods for precise confinement and manipulation of biomolecules and cells. To this end, a number of contact-free fluid flow-based trapping and manipulation methods have been developed. These methods rely on microvortices, microeddies, stagnation point flows, or stagnant regions within a fluid stream to confine particles for further analysis.



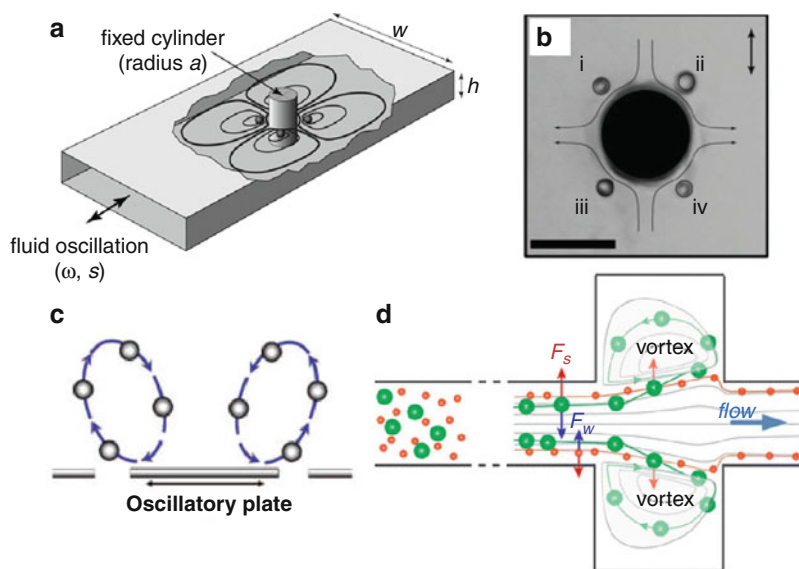
**Flow-Based Particle Trapping and Manipulation, Fig. 2** Schematic describing the trapping mechanism of a contact-based microfluidic trapping array device. (a) Fluid streams containing target particles flow through arrays of U-shaped structures which serve as trapping sites for single particles. The trapping sites are designed to have a small gap between the U-shaped structure and the microchannel. This gap facilitates transport of objects

into the U-shaped pockets by allowing for a fraction of the fluid flow through the pockets. (b) Once an object enters a pocket, it partially blocks the fluid flow through the gap, thereby effectively confining the object into the pocket. (c) A micrograph of an array of single trapped objects is shown (scale bar, 30  $\mu\text{m}$ ) (Reprinted with permission from [6] © 2006 American Chemical Society)

Below, we provide a brief overview of these methods:

- (a) **Microeddies:** In this contact-free trapping method, microeddies are generated in the vicinity of a cylindrical structure in a microchannel by low-frequency fluid oscillations [7] (Fig. 3a). The oscillations drive four symmetric steady streaming eddies adjacent to the cylindrical post. Particles in the fluid are drawn into the microeddies, and eventually a single particle is trapped near the center of each eddy without contacting any solid surface (Fig. 3b).
- (b) **Microvortices:** Microvortices within microchannels can be created by either using a dynamic structure such as an oscillating plate [8] (Fig. 3c) or by implementing contraction expansion zones in a microchannel [9, 10] (Fig. 3d). For example, a suspended microplate resonating in the lateral plane (arrows) generates two

counter-rotating elliptical microvortices near its edges (Fig. 3c). These two microvortices can be utilized to attract and confine particles suspended in the surrounding liquid medium. Similarly, microvortices created within the expansion zone of a microchannel can be used for particle trapping and manipulation (Fig. 3d). This method depends on high Reynolds number flows within microchannels where inertial forces dominate over viscous forces and particles within the flow experience lift forces transverse to the flow direction. In this case, lift forces orthogonal to the flow direction act to equilibrate microparticles near the walls of the microchannel upstream from the expansion chambers. The shear-induced lift force  $F_S$  drives particles toward channel walls. The wall-induced lift force  $F_W$  drives particles toward the channel center. The balance of these two lift forces determines the



**Flow-Based Particle Trapping and Manipulation, Fig. 3** (a) Hydrodynamic trap based on microeddies generated by low-frequency fluid oscillations around a cylinder in a microchannel. (b) Image showing four trapped microspheres using microeddies around a cylindrical post. *Arrow* indicates the direction of fluid oscillations. (Scale bar, 250  $\mu\text{m}$ ) (a, b) (Reprinted with permission from [7] © 2006 American Chemical Society). (c) Hydrodynamic trap based on microvortices

created by a resonating square microplate (Reprinted with permission from [8] © 2008 American Chemical Society). (d) Hydrodynamic trap based on microvortices created within a microchannel with sudden expansion geometry. The particles entering the vortices are effectively trapped for long time scales (Reproduced from [10] with kind permission from Springer Science + Business Media Copyright © 2013)

equilibrium position of particles along the channel width. At the channel expansion, the channel wall is no longer in close proximity, and the wall-induced lift force  $F_w$  is significantly smaller than the shear-induced lift force ( $F_s > F_w$ ), thereby causing particle migration into the vortices. Larger particles (green) experience larger lift forces and are able to migrate across fluid streamlines into the vortices while smaller particles (red) follow fluid streamlines and flow out of the system. In this manner, large particles can be captured and isolated from the rest of the sample for long time scales within these expansion chambers.

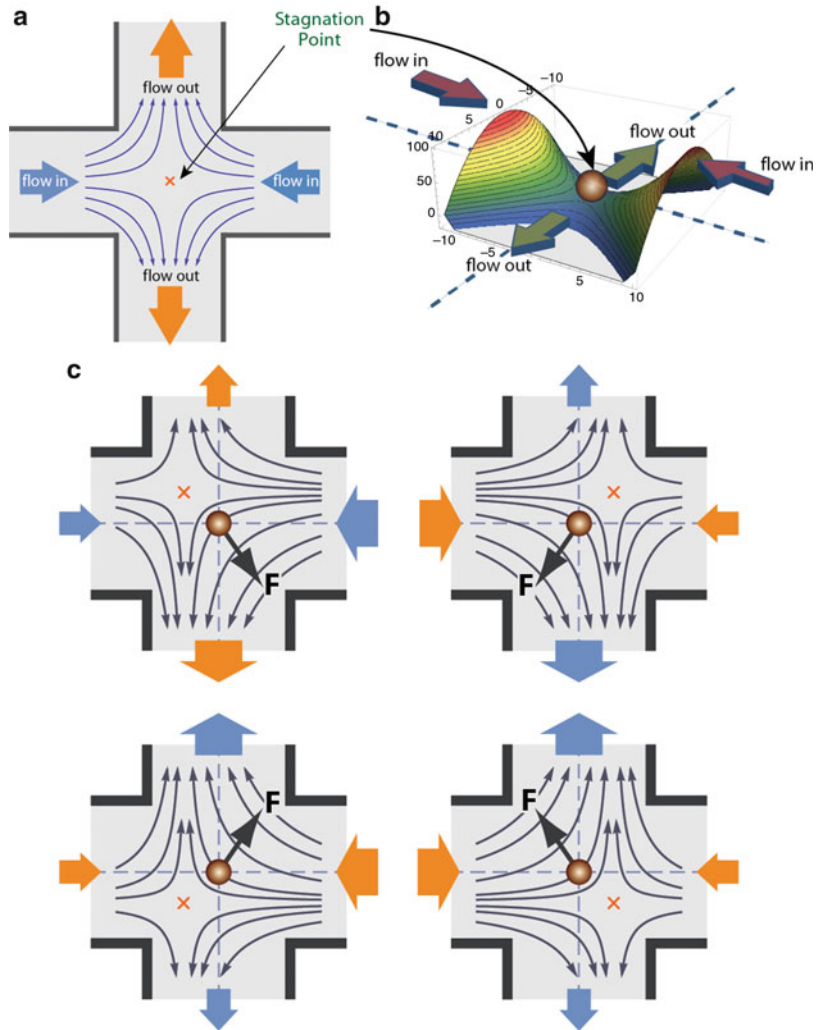
- (c) **Feedback-controlled planar extensional flow:** A single particle can be confined at the stagnation point of a planar extensional flow, which is generated at the junction of two perpendicular microchannels where two

opposing laminar streams meet [11, 12] (Fig. 4a). Planar extensional flows are potential flows with a velocity potential function which is stable along the incoming flow (flow-in) direction and unstable along the outgoing flow (flow out) direction, where the stagnation point corresponds to a saddle point (Fig. 4b). Therefore, a particle positioned at the stagnation point is passively confined along the flow-in direction. To confine the particle along the unstable flow-out direction, an automated feedback controller is used to manipulate the position of the stagnation point along this direction. By precise control over the position of the stagnation point, a single particle can be manipulated in any direction within the microchannel junction (Fig. 4c).

- (d) **Microfluidic Wheatstone bridge:** Particles can be captured by dynamically forming

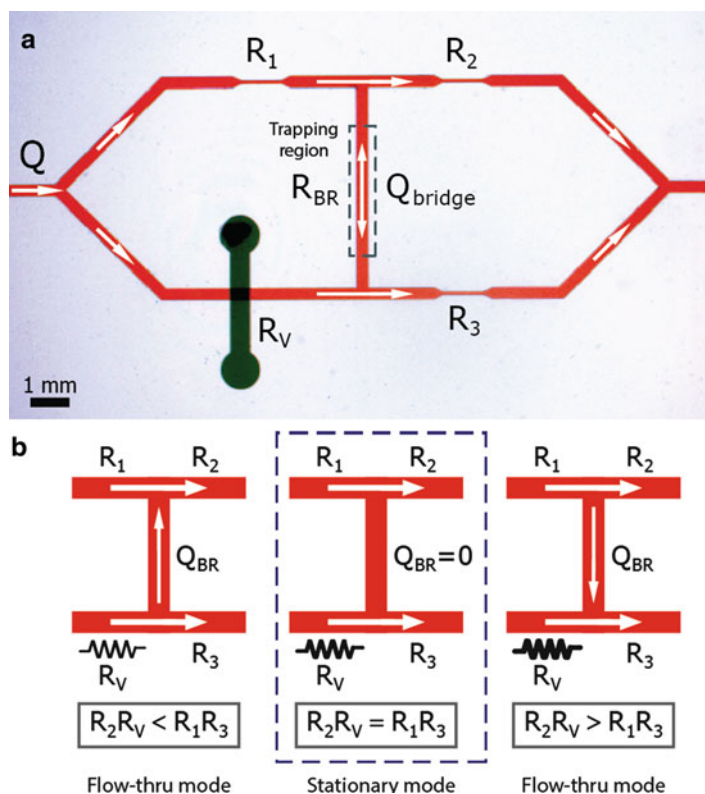
### Flow-Based Particle Trapping and Manipulation, Fig. 4

(a) Hydrodynamic trap based on a planar extensional flow generated at the intersection of two perpendicular microchannels. A planar extensional flow can be created by two opposing laminar streams meeting at the microchannel junction. (b) Planar extensional flows can be expressed as potential flows with a velocity potential function which is stable along the incoming flow (*flow-in*) direction and unstable along the outgoing flow (*flow out*) direction, where the stagnation point corresponds to a saddle point. (c) A particle at the microchannel junction can be steered toward any direction by manipulating the position of the stagnation point. In this manner, a single particle is effectively confined and manipulated using the sole action of fluid flow (Adapted with permission from [11] Copyright 2010 AIP Publishing LLC)



stagnant regions within a fluid stream [13]. One of the microfluidic architectures, capable of creating such a stagnant fluid region, is shown in Fig. 5. This device is the microfluidic analogue of a Wheatstone bridge circuit. The device consists of two parallel branches (red) which are connected by a perpendicular “bridge” channel. The bridge divides the parallel branches into four segments, each with a distinct flow resistance ( $R_1, R_2, R_3, R_v$ ). The flow rate and direction of flow within the bridge channel are controlled by a single on-chip metering valve (dark green) which

functions as a variable resistor ( $R_v$ ). Under certain conditions, by using the metering valve, the variable flow resistance ( $R_v$ ) can be set such that  $R_2 R_v = R_1 R_3$ . In this case, the pressure drop across the bridge channel is zero, and the fluid flow within the bridge completely stops ( $Q_{\text{bridge}} = 0$ ). This creates a stagnant fluid region within the bridge, thereby confining any particles present within the fluid. Dynamical adjustment of the variable flow resistance ( $R_v$ ) enables on demand sampling of particles from a sample stream within the bridge channel.



**Flow-Based Particle Trapping and Manipulation, Fig. 5** (a) Optical micrograph of the microfluidic Wheatstone bridge. Two parallel branches (red) from an inlet stream are connected by a perpendicular “bridge” channel. The bridge divides the parallel branches into four segments, each with a distinct flow resistance ( $R_1, R_2, R_3, R_v$ ). One segment contains a metering valve (dark green), which functions as a variable resistor ( $R_v$ ) to control fluid flow within the bridge. (b) Flow control in the

Wheatstone bridge. The flow rate and direction of flow in the bridge are controlled by a single on-chip metering valve. For  $R_2R_v < R_1R_3$ , flow is directed toward the upper branch (left panel). Similarly, when  $R_2R_v > R_1R_3$ , flow is directed toward the lower branch (right panel). For  $R_2R_v = R_1R_3$ , the resistance is balanced, which completely stops the flow within the bridge such that  $Q_{\text{bridge}} = 0$  (middle panel) (Reproduced from [13] with permission from The Royal Society of Chemistry)

**Advantages:** Contact-free methods allow for capturing “target” particles in a sample solution. Therefore, these methods are amenable to sorting and separation of rare particles within a sample. Furthermore, exchange of the surrounding medium of a trapped object is carried out with relative ease using these flow-based methods. Flow-based contact-free trapping methods are feasible for many different particle types with no specific requirements on the material composition or the chemical/physical nature (optical, magnetic, surface charge) of the trapped object.

**Disadvantages:** Despite their numerous advantages, modern contact-free methods often

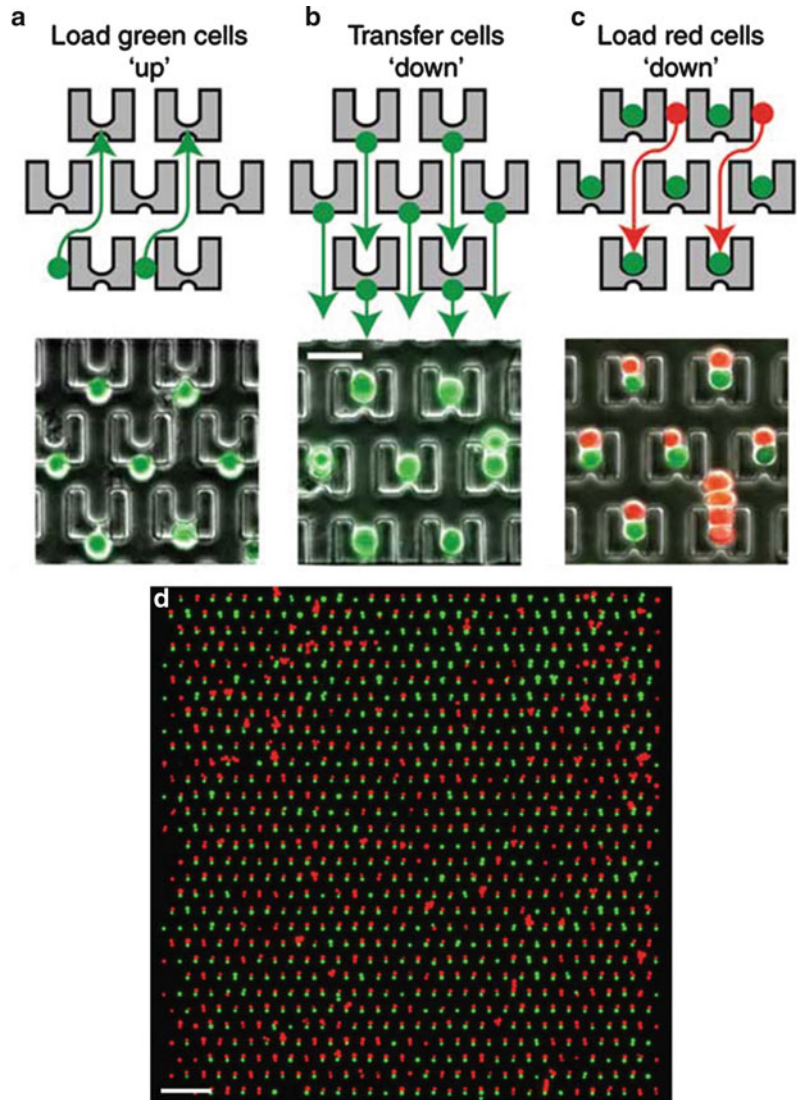
suffer from low throughput. Although it is possible to design trap arrays allowing for multiplexed assays, contact-based methods offer more convenient platforms for analyzing large number of samples.

## Examples of Application

Particle trapping is a pervasive technology with important applications in biology and medicine. Current methods have led to key advances in many fields of science and engineering including physics, biotechnology, and materials science.

### Flow-Based Particle Trapping and Manipulation,

**Fig. 6** Using U-shaped microfluidic structures, two different cell types (shown in *red* and *green*) can be paired up side by side in a single trapping site using fluid flow. A large array of cell pairs can be created within a single microfluidic device for high-throughput analysis of cell-cell interactions (Reprinted from [14] by permission from Macmillan Publishers Ltd: Nature Methods, copyright (2009))



Flow-based confinement and manipulation methods offer a new platform for observation of molecules, cells, and particles without surface immobilization, eliminates potentially perturbative optical, magnetic, and electric fields. Examples provided below highlight different applications for each category of flow-based trapping:

### Contact-Based Methods

Contact-based methods using fluid flow are utilized to create dense arrays of cell pairs for

conducting high-throughput cell-cell interactions studies [14] (Fig. 6). Using this microfluidic trapping method, pairing and fusion of different cell types including fibroblasts, myeloma cells, B cells, mouse embryonic stem cells, and mouse embryonic fibroblasts have been demonstrated in a high-throughput format. In comparison with commercial fusion techniques, this method provides improved efficiency of cell pairing and fusion and enables on-chip culturing of the fused cells for long time scales.



**Flow-Based Particle Trapping and Manipulation, Fig. 7** Time-lapse image of the relaxation dynamics of an individual single-stranded DNA molecule (ssDNA,  $L = 18 \mu\text{m}$ ) studied by the hydrodynamic trap based on a planar extensional flow. A single fluorescently labeled

DNA molecule is trapped and stretched with the hydrodynamic trap. The flow is stopped subsequently, allowing for relaxation of the DNA molecule (molecule relaxing *right to left*) (Adapted from [15] with permission from The Royal Society of Chemistry)

### Contact-free Methods

Microvortices created within the expansion zone of a microchannel are used for label-free isolation and enrichment of rare cells within an aqueous sample, where there is sufficient size difference between rare cells and the rest of the sample. This method allows for cell separation in a high-throughput, size, and density-based manner, where target cells are concentrated from tens of milliliters of volume into smaller microliter scale volumes [9]. In this manner, isolation of cancer cells from the human blood (circulating tumor cells, CTCs) has been demonstrated using a microfluidic device generating massively parallel laminar microscale vortices.

The hydrodynamic trap based on feedback-controlled planar extensional flow enables free-solution trapping, manipulation, stretching, and sorting of objects ranging from single molecules to individual cells [11, 12]. For instance, a microfluidic device generating a planar extensional flow at a cross-slot is used to effectively trap, isolate, and stretch individual DNA molecules in free solution, which reveals the stretching and relaxation dynamics of individual DNA molecules [15] (Fig. 7). This method allows for long time scale observation of single-molecule dynamics, which is generally not accessible using alternative methods.

### Cross-References

- ▶ [Dielectrophoretic Motion of Particles and Cells](#)
- ▶ [Lab-on-a-Chip Devices for Particle and Cell Separation](#)
- ▶ [Manipulating Cells, Techniques](#)
- ▶ [Optical Tweezers for Manipulating Cells and Particles](#)
- ▶ [Particle Manipulation Using Ultrasonic Fields](#)

### References

1. Nilsson J, Evander M, Hammarstrom B, Laurell T (2009) Review of cell and particle trapping in microfluidic systems. *Anal Chim Acta* 649(2): 141–157
2. Johann RM (2006) Cell trapping in microfluidic chips. *Anal Bioanal Chem* 385(3):408–412
3. Yi CQ, Li CW, Ji SL, Yang MS (2006) Microfluidics technology for manipulation and analysis of biological cells. *Anal Chim Acta* 560(1–2):1–23
4. Karimi A, Yazdi S, Ardekani AM (2013) Hydrodynamic mechanisms of cell and particle trapping in microfluidics. *Biomicrofluidics* 7(2):021501
5. Tan WH, Takeuchi S (2007) A trap-and-release integrated microfluidic system for dynamic microarray applications. *Proc Natl Acad Sci U S A* 104(2): 1146–1151
6. Di Carlo D, Aghdam N, Lee LP (2006) Single-cell enzyme concentrations, kinetics, and inhibition analysis using high-density hydrodynamic cell isolation arrays. *Anal Chem* 78:4925–4930

7. Lutz BR, Chen J, Schwartz DT (2006) Hydrodynamic tweezers: I. Noncontact trapping of single cells using steady streaming microeddies. *Anal Chem* 78(15):5429–5435
8. Lin CM, Lai YS, Liu HP, Chen CY, Wo AM (2008) Trapping of bioparticles via microvortices in a microfluidic device for bioassay applications. *Anal Chem* 80(23):8937–8945
9. Mach AJ, Kim JH, Arshi A, Hur SC, Di Carlo D (2011) Automated cellular sample preparation using a centrifuge-on-a-chip. *Lab Chip* 11(17):2827–2834
10. Zhou J, Kasper S, Papautsky I (2013) Enhanced size-dependent trapping of particles using microvortices. *Microfluidics Nanofluidics* 14, 10.1007/s10404-013-1176-y
11. Tanyeri M, Johnson-Chavarria EM, Schroeder CM (2010) Hydrodynamic trap for single particles and cells. *Appl Phys Lett* 96:224101
12. Tanyeri M, Ranka M, Sittipolkul N, Schroeder CM (2011) A microfluidic-based hydrodynamic trap: design and implementation. *Lab Chip* 11(10):1786–1794
13. Tanyeri M, Ranka M, Sittipolkul N, Schroeder CM (2011) Microfluidic Wheatstone Bridge for rapid sample analysis. *Lab Chip* 11(24):4181–4186
14. Skelley AM, Kirak O, Suh H, Jaenisch R, Voldman J (2009) Microfluidic control of cell pairing and fusion. *Nat Methods* 6(2):147–152
15. Brockman C, Kim SJ, Schroeder CM (2011) Direct observation of single flexible polymers using single stranded DNA. *Soft Matter* 7:8005–8012

---

## Fluid Metering

Cheng-Tsair Yang and Chun-Min Su  
Flow Measurement Laboratory Center for  
Measurement Standards, Industrial Technology  
Research Institute, Hsinchu, Taiwan

### Synonyms

Fluid metrology; Fluid quantification; Measurement standards; Weights and measures

### Definition

Fluid metering concerns the measurement of fluids, liquids in particular, in the form of flow rate and/or fluid volume. Apart from accuracy and precision, the uncertainty and traceability of

measurements are important factors to be considered. For micro- and nanofluidic applications, the fluid may flow in channels with dimensions of a few millimeters or below, with flow rates ranging typically from microliters to nanoliters per minute, and the fluid may be dispensed in volumes on the order of microliters to picoliters.

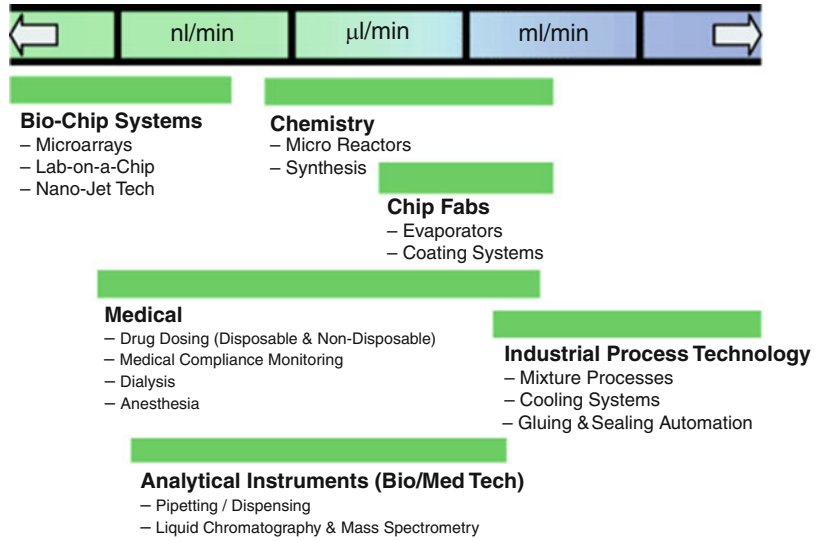
### Overview

Microfluidics is bringing about innovations in biotechnology, medicine, energy, and many other industries and is one of the major branches of nanobiotechnology research [1]. However, the lack of reliable and accurate flow metering or even flow monitoring is one of the key challenges to related applications that are delaying the commercial success of many innovations, because microfluidic products, especially those for medical use, must pass certification processes to prove their capability, reliability, safety, etc. Therefore, for accurate and reliable measurement, all metering techniques and devices should be traceable to basic SI units and/or international measurement standards. In the case of microscale fluid metering, the accuracy still needs to be improved, and the traceability chain and measurement standards need to be well established.

Fluids in capillaries or microchannels which are millimeters to micrometers in diameter or width can flow in a continuous form. Sometimes, however, in many applications, the fluid is dispersed into discrete droplets, for example, in the case of a liquid that is injected onto a microarray chip. Therefore, in this entry, metering of fluids is categorized into continuous flow rate measurement and droplet volume measurement.

### Metering of Continuous Fluid Flow

In the case of flow in microscale pathways, some important parameters in macroscale fluid mechanics remain important, but the features of the flow are very different. The influences of viscosity and surface effects are much more significant compared with fluid flow in traditional pipelines or channels. That is, the ratio of the inertial force to the viscous force

**Fluid Metering,****Fig. 1** Flow rate ranges suitable for various industries

(Reynolds number) is in general smaller than unity, and the ratio of the inertial force to surface tension (Weber number) is also small, so that accurate microfluidic metering is somewhat more difficult than metering for macroscopic flows. For gas flows, the effect of the Knudsen number, defined as the ratio of the molecular mean free path to the channel size, is high and cannot be ignored for microscale channels, and hence the fluid metering discussed here will be for liquids only. The Reynolds number  $Re$ , the Weber number  $We$ , and the Knudsen number  $Kn$  are expressed as follows:

$$\begin{aligned} Re &= \frac{\text{inertial force}}{\text{viscous force}} = \frac{\rho UL}{\mu}, \\ We &= \frac{\text{inertial force}}{\text{surface force}} = \frac{\rho U^2 L}{\sigma}, \\ Kn &= \frac{\text{molecular mean free path}}{\text{channel size}} = \frac{\lambda}{L}, \end{aligned} \quad (1)$$

where  $\rho$  and  $\mu$  are the density and dynamic viscosity, respectively, of the fluid,  $U$  is the mean fluid velocity in a channel with a characteristic length  $L$ ,  $\sigma$  is the surface tension, and  $\lambda$  is the molecular mean free path.

The flow rate in microfluidics, which is a key parameter in microbioassays, drug delivery, biomedical microfluidic systems, etc., ranges from

some milliliters per minute to nanoliters per minute or even less.

As shown in Fig. 1, the flow rate for medical uses ranges from about 1 nl/min to about 10 ml/min in the case of anesthesia, dialysis, and drug dosing. For analytical instruments for biomedical technology such as liquid chromatography and mass spectrometry, the flow rate is mainly in the range of nanoliters per minute to microliters per minute. For nanobiotechnology applications, such as microarrays for high-throughput diagnosis and labs-on-a-chip for biochemical analysis, the required flow rate reduces to less than 1 nl/min, a level typically referred to as *subnanoliter per minute*.

Many technologies have been developed to monitor or measure fluid flow in microdevices. The underlying mechanisms of these devices are based mainly on thermal or mechanical principles; examples of the variables to be measured are temperature, differential pressure, and drag force, which translate to thermal changes, deflection of cantilever beams, and shear strain, respectively. Most of these microflow sensors are manufactured by microelectromechanical systems (MEMS) processes without moving parts, and the flow rate measurements are mainly translated from velocity detection. For example, because flows in microchannels are in most

cases laminar, the pressure drop  $\Delta p$  along a channel can be expressed as follows:

$$\Delta p = \text{Re} \cdot f \cdot \frac{\mu L}{2D_h^2} U, \quad (2)$$

where  $f$  is the friction coefficient,  $L$  is the channel length,  $D_h$  is the hydraulic diameter, and  $U$  is the mean flow velocity. From Eq. 2, we can see that  $\Delta p$  is a linear function of  $U$ , and the flow rate, which is the product of the flow velocity and the channel cross section, can be determined by measuring the pressure difference.

Because direct measurement of flow rate by using microscale devices is difficult, most microflow sensors are designed to meter flow velocity. This is convenient and useful. For instance, a carbon nanotube (CNT) has been used as a flow sensor which generates a voltage when a polar liquid flows over it. The voltage produced shows a logarithmic dependence on the flow velocity, and the sensor exhibits a dynamic range of operation covering six orders of magnitude, from 100 nm/s to some cm/s [2]. This level of dynamic range is virtually impossible to achieve with traditional macroscale flow meters. Theoretically, multiplying the metered velocity by the cross-sectional area of the microchannel or capillary gives the flow rate. However, because of the uncertainty in the measurement of areas in such small dimensions, the flow rate or fluid quantity is usually obtained by use of some built-in conversion after calibration.

### Metering of Discrete Droplet Volumes

The measurement of discrete droplet volumes is now playing a more and more important role in various applications such as pipettes, drug dispensing systems, inkjet printer heads, and microarray biochip spotters. The purpose of dispensing is to deliver a certain amount of a liquid sample, buffer solution, or frequently used library compound from a storage vial or mother plate to a cultivation container, test tube, assay plate, or microarray chip for subsequent handling. Applications in this field today are showing a trend toward a decrease in the volume of liquid to be handled, a trend that is promoted by the common

interests of reducing the cost and increasing the speed and is made possible by the advancement of micro- and nanofluidic technologies.

The instrument most often used to dispense a measured volume of liquid is a pipette (also called a pipet or pipettor). It is commonly used in research in chemistry and molecular biology, as well as in medical tests, and the typical range of liquid volume that pipettes can handle is from 0.1 to 20  $\mu\text{l}$ . For applications in which dispensing speed and cost-effectiveness are of particular concern, such as microarray biochips, automated dispensing is a prerequisite, and the liquid volume delivered goes down to nanoliters or even picoliters. The technologies used to deliver such tiny amounts of liquid are many and can in general be categorized into contact dispensing, noncontact dispensing, and true contactless dispensing [3].

The dispensed liquid volume is one of the key parameters that need to be properly controlled in order for experiments and tests to be well conducted. In fact, experiments may fail simply because an erroneous liquid volume has been introduced, resulting mainly from an operator's poor technique or the use of uncalibrated instrument. For applications such as high-throughput screening, making sure that the liquid volume delivered is well controlled becomes even more important, since a small difference leads to a relatively large deviation, and the accuracy of the dispensed volume can substantially affect the analysis results. Therefore, measurement of the dispensed liquid volume is indispensable for satisfactory quality control of related products.

The method of measuring macroscale liquid volumes is simple and straightforward. The mass of the dispensed liquid is measured by a balance with appropriate precision and then divided by its density. When the performance of a dispensing tool such as a piston-operated volumetric apparatus is evaluated, water is typically adopted as the working fluid, and the temperature is, in general, the only variable that needs to be monitored and controlled. The procedure suggested by the international standard ISO 8655-6 [4] is generally followed to ensure that the measurement uncertainty is within the acceptable range. However,

for micro- and nanoscale droplet dispensing, the traditional weighing method encounters difficulties in yielding accurate and consistent measurement results. Therefore, the International Organization for Standardization (ISO) published a new standard, ISO 8655-7 [5], in 2005, detailing the use of nongravimetric methods, in particular photometric and titrimetric methods, for the assessment of equipment performance. Many other methods for measuring or monitoring liquid volume have also been proposed, such as methods based on droplet images, fluorescent intensity, electric impedance, and interference fringes. These methods are somewhat specific and require further justification of their traceability when used in fluid metering; thus, they will not be discussed here.

## Basic Methodology

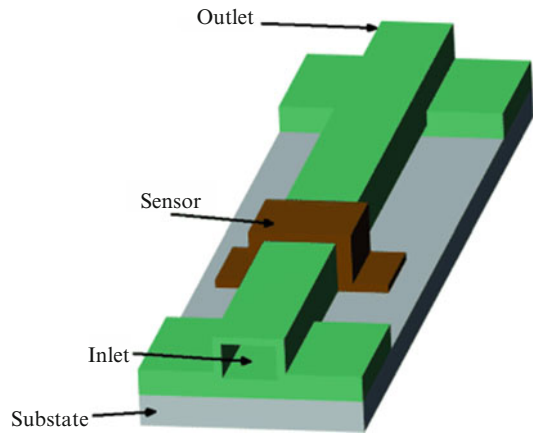
### Continuous Fluid Flow Measurement

Since thermal transfer accompanies the mass transfer of a fluid flow, microflow sensors based on thermal effects are the most common. An example of a MEMS thermal flow sensor is shown in Fig. 2.

When the sensor is heated and fluid flows through the sensor, heat will be taken away downstream. We can use this effect to measure the fluid flow. One application of the thermal effect is similar to the hot-wire anemometry used to measure wind velocity. Let us imagine that the sensor is made of tungsten wire, which will produce heat when electric power is supplied. If we try to keep the wire at a constant temperature, a higher current is needed for a faster fluid velocity. When thermal balance is reached, the heat generated by the electric power equals that dissipated owing to fluid flow. Therefore,

$$\begin{aligned} I^2 R_w &= h \cdot A \cdot (T_w - T_0) \\ &= \text{Nu} \cdot (k_f/d) \cdot A \cdot (T_w - T_0), \end{aligned} \quad (3)$$

where  $I$  is the electric current;  $R_w$  is the resistance at the working temperature  $T_w$ ;  $h$  is the heat transfer coefficient;  $A$  and  $d$  are the



**Fluid Metering, Fig. 2** Example of a MEMS structure for metering the flow rate in a microchannel, based on the theory of constant-temperature anemometry

cross-sectional area and diameter, respectively, of the wire;  $\text{Nu}$  is the dimensionless heat transfer rate (Nusselt number);  $k_f$  is the coefficient of heat conduction; and  $T_0$  is the fluid temperature. The dimensionless heat transfer rate can usually be expressed as

$$\text{Nu} = A' + B' \text{Re}^n, \quad (4)$$

where  $A'$ ,  $B'$ , and  $n$  are empirical constants, usually determined by calibration. For a given working fluid and wire, the Nusselt number can then be expressed in terms of the mean fluid velocity  $U$  as follows:

$$\text{Nu} = a + bU^n, \quad (5)$$

where  $a$  and  $b$  are constants to be determined. The resistance  $R_w$  at the working temperature  $T_w$  can be obtained from the following equation:

$$R_w = R_0 \cdot [1 + \alpha(T_w - T_0)]. \quad (6)$$

Thus, we have

$$\frac{(R_w - R_0)}{R_0} = \alpha(T_w - T_0), \quad (7)$$

where  $R_0$  is the resistance at a fluid temperature  $T_0$  and  $\alpha$  is the temperature coefficient of resistance.

Equation 3 can be rewritten as the following equations:

$$I^2 R_w = A \cdot (k_f/d) \cdot (T_w - T_0) \cdot (a + bU^n), \tag{8}$$

$$I^2 R_w^2 = A \cdot R_w \cdot (k_f/d) \cdot \frac{(R_w - R_0)}{\alpha R_0} \cdot (a + bU^n). \tag{9}$$

If the fluctuation in fluid temperature remains insignificant and the resistance  $R_w$  is made constant by keeping  $T_w$  constant with a feedback circuit, the relationship between the voltage drop in the wire  $V_w$  and the fluid velocity can be formulated as

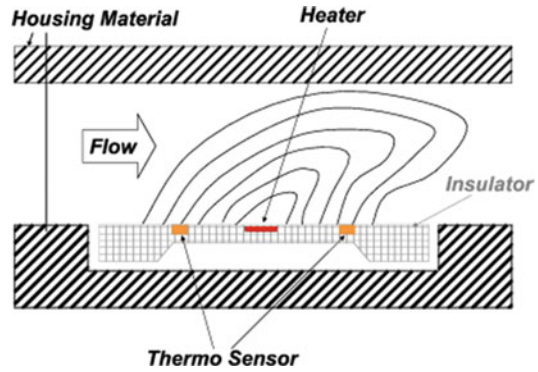
$$V_w^2 = I^2 R_w^2 \propto (a + bU^n). \tag{10}$$

The coefficients can be determined by a calibration process, and the fluid velocity can then be obtained by measuring the voltage drop. When the fluid velocity has been obtained, the volumetric flow rate can be calculated by multiplying the velocity by the cross-sectional area.

A sensing line embedded in the wall of a microchannel is more complicated than a single tungsten wire, but the analysis is the same. In order to successfully integrate a suitable metering element, various sensing structures need to be designed and tested. Linearity, reliability, and sensitivity to velocity variation are key features to be concerned with. Generally, a design with high temperature coefficient of resistance in Eq. 6 is preferred, since this should increase the sensitivity of the sensor.

Another approach to measuring fluid flow, which also applies thermal principles, is illustrated in Fig. 3.

A resistor providing a continuous heating power of a few milliwatts is placed in the flow channel. At both the left and right sides of the resistor, two thermosensors are embedded symmetrically to measure the temperature. If the fluid in the channel is still, the temperature field, represented by the isotherms, is symmetric, and

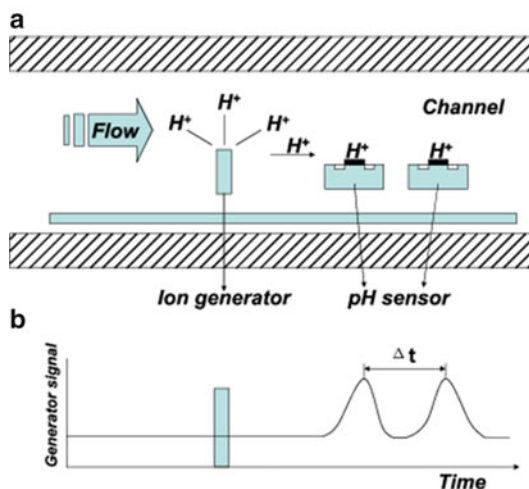


**Fluid Metering, Fig. 3** Illustration of the operational principle of a microflow sensor that uses a heating element to heat the fluid and two thermosensors to measure the temperatures upstream and downstream of the element. The temperature difference is used to determine the flow rate

the two sensors will measure the same temperature. When the fluid flows at some velocity, the isotherms will be distorted, and hence the thermosensors will measure different temperatures, which are then used to determine the fluid velocity. The temperature field affected by the fluid flow can be simulated numerically by using the Navier-Stokes equations with a boundary condition of constant flow velocity.

The concept of *time of flight* has also been adopted, similarly to its use in ultrasonic flowmeters for macroscale flows. A heat pulse is generated upstream by a laser or electric coil, and the heated fluid is detected downstream. The time difference is used to determine the velocity and then the volumetric flow rate. However, diffusion of heat in the fluid results in a broadened temperature distribution when the fluid reaches the sensors and hence results in difficulty in determining the transit time accurately. An ion generator can be used to replace the heater for the purpose of determination of the time of flight [6].

As shown in Fig. 4,  $H^+$  or  $OH^-$  ions are generated on demand by an upstream ion generator, and two pH-sensitive sensors located downstream are used to detect the time of flight of ions flowing from the upstream sensor to the downstream sensor.

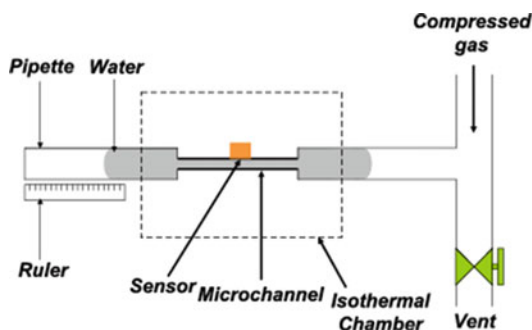


**Fluid Metering, Fig. 4** Illustration of the operational principle of a microflow sensor that uses an ion generator and two pH sensors to measure the flow rate. The ions follow the fluid flow, and the difference of the arrival times at the two sensors determines the flow velocity

### Verification of Flow Rate Measurement

As mentioned earlier, most metering devices in fact measure the flow velocity. When a measurement is made with a microflow sensor, if the flow in the microchannel can be resolved simultaneously by using high-resolution velocimetry, such as by means of a microresolution particle image velocimetry ( $\mu$  PIV) system that has been calibrated by use of a calibrated interferometer and timer, traceability can be achieved by comparing the results. For devices that indicate a flow rate or fluid quantity on a panel, however, direct tracing back to reference standards is faster and more reliable. For example, a flow sensor or flow controller such as a syringe pump can be calibrated by use of a standard flow rate system that has been certified and is traceable to basic physical standards such as standards of time, length, mass, and luminous intensity.

Some researchers have tried to set up calibration facilities to verify the metering performance of their microflow sensors. A simple way is to connect the sensor to a pipette with a scale [7].



**Fluid Metering, Fig. 5** Schematic diagram of an experimental setup for the calibration of a microflow sensor. The liquid, driven by compressed air, flows through the sensor under test into a pipette with a scale. The liquid volume collected in the pipette within a certain time interval is used to determine the flow rate

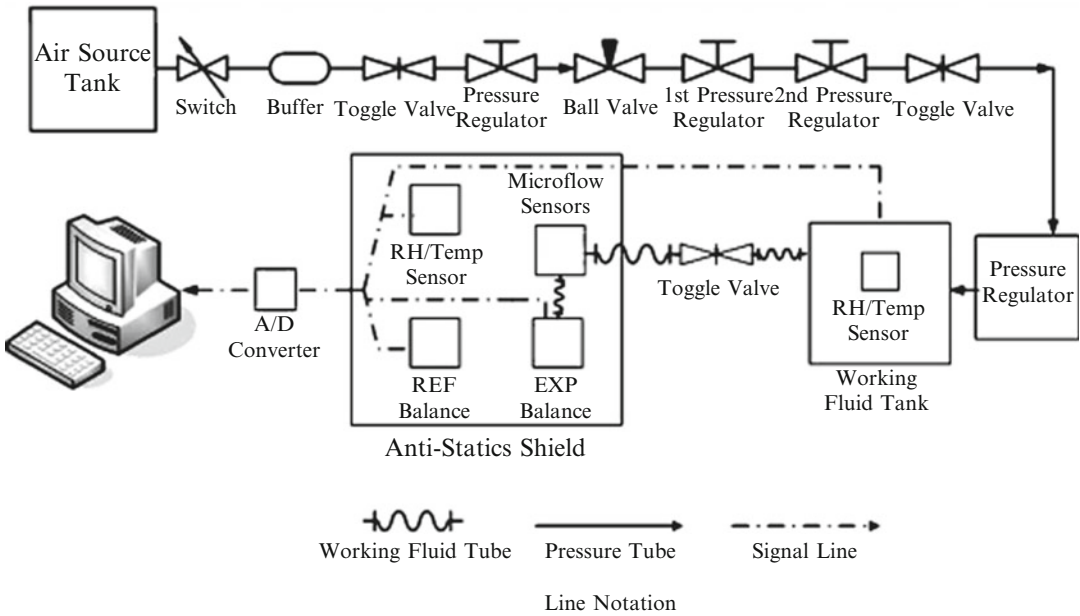
As shown in Fig. 5, the liquid is pushed by compressed air, and the scale is read over a time interval to obtain a reference flow rate. The meter error  $E$  can be easily estimated by direct comparison:

$$E = Q_m - Q_s = Q_m - \left( \frac{\Delta l \cdot \pi d_i^2}{4\Delta t} \right), \quad (11)$$

where  $Q_m$  is the meter reading of the microflow sensor and  $Q_s$  is the reference standard obtained from the distance of travel  $\Delta l$  of the liquid/air interface during a time interval  $\Delta t$  and the inner diameter  $d_i$  of the pipette.

In another approach, which is a little more complicated [8], a glass capillary is placed on a cooled metal plate to stabilize the temperature of the fluid, and then an infrared laser pulse heats up a mass of liquid. Because the refractive index is a function of temperature, instruments that are sensitive to the change of refractive index are installed downstream to detect the heated liquid. However, thermal diffusion makes it complicated to accurately determine the arrival time of the heated mass of liquid.

For a standard of flow rate metering, traceability is the top priority; the measurement



**Fluid Metering, Fig. 6** Diagram of a twin-balance weighing system serving as a primary standard for microflow sensor calibration

uncertainty should be sufficiently small, and a system that features simple operation, low measurement uncertainty, and high repeatability is desirable. Therefore, approaches based on weighing are, above all others, favorable candidates for such a purpose. As shown in Fig. 6, a gravimetric primary metering standard has been set up to achieve these requirements [9]. Liquid water is driven by a pneumatic pressure control mechanism to obtain flow rates down to less than a microliter per minute. The measurement capability depends on the weighing of the collection beaker, the stability of the pressure difference, the time interval, and the variation of the ambient temperature. Buoyancy variation and liquid evaporation are critical concerns for measurements associated with such a small quantity of liquid.

In this setup, a liquid in a reservoir tank is pushed into 1/8 in. connection pipes or microchannels by a preset air pressure. The air pressure must be well controlled, for example, by using a two-stage valve system followed by

a pressure modulator. The liquid flows through the microflow sensor to be verified and then into a collection tank installed on a high-precision balance. To eliminate buoyancy effects due to changes in the air density during calibration, a twin-balance arrangement has been adopted. This means that a similar collection tank is installed on another balance, and the difference between readings before and after the calibration period is used for buoyancy compensation. Both the balances are well covered with a glass shield to avoid any influence from the ambient air flow. In addition, the liquid in the collection tank is covered with low-volatility oil to eliminate evaporation. The oil should be full to the edge of the collection tank, which is placed inside a larger beaker. The oil will overflow into the larger beaker so as to maintain a constant outlet pressure and reduce possible weight variations.

After the fluid meter has been connected in series between the reservoir and the collection beaker, calibration can begin when the fluid

flow reaches steady state. The recorded weights before and after a preset time interval are used to

calculate the mass flow rate. The mass flow rate is expressed accurately as follows:

$$\begin{aligned}
 q_m &= \frac{m_1 - m_0}{t} = \frac{V_{cv} \times \rho_{l,1} + W_1 + (V_{\text{tank}} + \Delta V_{\text{tank}}) \times \rho_{a,1}}{t} - \frac{(V_{cv} \times \rho_{l,0} + W_0 + V_{\text{tank}} \times \rho_{a,0})}{t} \\
 &= \frac{V_{cv} \times (\rho_{l,1} - \rho_{l,0}) + (W_1 - W_0)}{t} + \frac{V_{\text{tank}} \times (\rho_{a,1} - \rho_{a,0}) + \Delta V_{\text{tank}} \times \rho_{a,1}}{t} \\
 &= \frac{V_{cv} \times (\rho_{l,1} - \rho_{l,0}) + (W_1 - W_0)}{t} + \frac{(W_1 - W_0)/\rho_{l,1} \times \rho_{a,1} + V_{\text{tank}} \times (\rho_{a,1} - \rho_{a,0})}{t}, \\
 &= \frac{V_{cv} \times (\rho_{l,1} - \rho_{l,0})(W_1 - W_0)}{t} + \frac{(W_1 - W_0)/\rho_{l,1} \times \rho_{a,1} + V_{\text{tank,ref}} \times (\rho_{a,1} - \rho_{a,0})}{t} \\
 &= \frac{V_{cv} \times (\rho_{l,1} - \rho_{l,0}) + (W_1 - W_0)(1 + \rho_{a,1}/\rho_{l,1})}{t} + \frac{(W_{\text{ref},1} - W_{\text{ref},0})}{t} \\
 &= f(V_{cv}, \rho_{l,1}, \rho_{l,0}, W_1, W_0, \rho_{a,1}, W_{\text{ref},1}, W_{\text{ref},0}, t)
 \end{aligned} \tag{12}$$

where  $q_m$  is the mass flow rate in g/min;  $m$  is the liquid mass in the collection beaker in g;  $W$  is the reading from the balance in g;  $V_{cv}$  is the control volume between the outlet of the fluid meter and the collection beaker in  $\text{cm}^3$ ;  $\rho_l$  and  $\rho_a$  are the density of the liquid and air, respectively, in  $\text{g}/\text{cm}^3$ ; and  $t$  is the collection time in minutes. The subscripts 0 and 1 represent the initial and final conditions, respectively, and ref denotes the reference balance. A total of nine variables are considered in the equation. The volume flow rate  $q_v$  can be obtained by dividing the mass flow rate by the liquid density:

$$\begin{aligned}
 q_v &= \frac{q_m}{\rho_{l,1}} \\
 &= g(V_{cv}, \rho_{l,1}, \rho_{l,0}, W_1, W_0, \rho_{a,1}, W_{\text{ref},1}, W_{\text{ref},0}, t).
 \end{aligned} \tag{13}$$

The density of liquid water is a function of its temperature  $T_1$  and can be determined from the following formula:

$$\begin{aligned}
 \rho_l &= 0.99985308 + 6.32693 \cdot 10^{-5} \times T_1 \\
 &\quad - 8.523829 \cdot 10^{-6} \times T_1^2 \\
 &\quad + 6.943248 \cdot 10^{-8} \times T_1^3 \\
 &\quad - 3.821216 \cdot 10^{-10} \times T_1^4
 \end{aligned} \tag{14}$$

A check standard, used to confirm the reliability of the calibration, is always necessary. For example, a circular capillary can be used, and the Hagen-Poiseuille formula can be applied to obtain the theoretical flow rate:

$$q_v = \frac{\pi r_0^4 \cdot \Delta p}{8 \nu \cdot \Delta l}, \tag{15}$$

where  $r_0$  is the inner radius of the capillary tube,  $\Delta p$  is the pressure difference between two detection points a distance  $\Delta l$  apart, and  $\nu$  is the dynamic viscosity. Periodically connecting this capillary to the calibration standard and measuring the flow rate simultaneously for comparison is important.

### Volume Measurement of Discrete Droplets

The gravimetric method is suitable for measuring the volume of liquid dispensed by pipettes, and it is commonly adopted to assess the performance of such instruments. Trained personnel are required to carry out such tests. The balances used for this purpose may have a precision of four to seven decimal places, depending on the volume to be measured and the desired accuracy. It should be well established that the experimental setup is free from environmental disturbances

such as vibration and air flow. Two points need to be addressed when the gravimetric method is used. The first one is the determination of the Z-factor, which is the transformation factor between the volume  $V$  and mass  $m$  of liquid. The volume dispensed is determined by the following equation:

$$V = m \cdot Z. \tag{16}$$

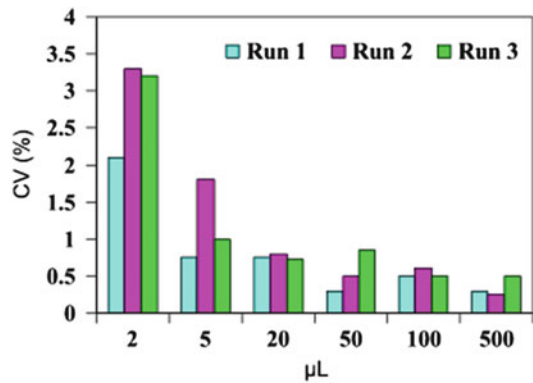
The Z-factor has units of microliters per milligram ( $\mu\text{l}/\text{mg}$ ), and its value, dependent on barometric pressure and temperature, is tabulated in the literature [4]. For example, at one atmosphere, the value of the Z-factor for temperatures between  $15\text{ }^\circ\text{C}$  and  $30\text{ }^\circ\text{C}$  ranges from 1.0020 to 1.0054. The second point is the error due to evaporation, which inevitably takes place during the measuring process. Especially for small volumes below  $50\ \mu\text{l}$ , the evaporation rate should be calculated, and the design of the weighing vessel and the test cycle time are important. The mean volume  $\bar{V}$  in the case of multiple dispensing can be calculated from the following equation:

$$\bar{V} = (\bar{w} + \bar{e} \cdot t) \cdot Z, \tag{17}$$

where  $\bar{w}$  is the average weight,  $\bar{e}$  is the average evaporation rate, and  $t$  is the test cycle time.

For the measurement of very small volumes of liquid, the gravimetric method becomes difficult to implement with accuracy.

As demonstrated in Fig. 7, which shows the results for a pipette checked using the gravimetric method, the coefficient of variation (CV, defined as the ratio of the standard deviation to the mean) for a run consisting of ten measurements of a given volume increases considerably when the dispensed liquid volumes are less than  $5\ \mu\text{l}$ . Evaporation, buoyancy, vibration, and the effects of static electricity are the primary causes of these results. A possible alternative method to determine microscale droplet volumes is one based on measurement of the concentration of a liquid solution. Two practices, also recommended by the ISO standard [5], are commonly used, namely, the photometric and titrimetric methods.



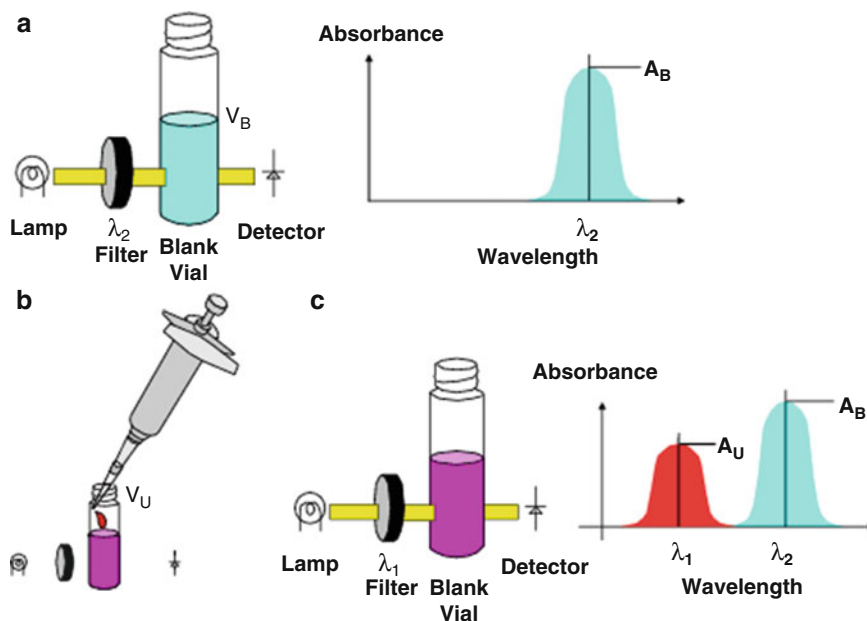
**Fluid Metering, Fig. 7** Performance verification results for measurements of dispensed liquid volumes conducted by the gravimetric method

The theory of operation of the photometric method for determining dispensed liquid volumes is based on the Beer-Lambert law, which can be written as follows:

$$A(\lambda) = \log_{10} \left( \frac{I(0)}{I(l)} \right) = -\log_{10}(T(\lambda)) = \varepsilon(\lambda)lC, \tag{18}$$

where  $A$  is the absorbance, which is a function of the wavelength  $\lambda$  of the incident light;  $I(0)$  and  $I(l)$  are the intensities of the incident and transmitted light, respectively;  $l$  is the length of material that the light travels through;  $T$  is the transmittance;  $\varepsilon$  is the molar absorptivity; and  $C$  is the molar concentration of the material. Equation 18 implies that for a given substance and a fixed wavelength of light, the absorbance of the sample has a linear relationship to its molar concentration and the path length. Although a setup with a single-dye, single-wavelength design is feasible for determining the volume of liquid delivered, a dual-dye, dual-wavelength ratiometric photometry technique is generally used since it enables the measurement to be independent of the path length.

The measurement procedure using the dual-dye, dual-wavelength photometric method is shown in Fig. 8. A test vial is loaded with a blank solution of known volume ( $V_B$ ) and



**Fluid Metering, Fig. 8** Measurement procedure using the dual-dye, dual-wavelength photometric method for the determination of dispensed liquid volume

concentration ( $C_B$ ), with a peak absorbance ( $A_B$ ) at a wavelength  $\lambda_2$ . A drop of the sample solution, which has a peak absorbance at another wavelength  $\lambda_1$  and nearly zero absorbance at  $\lambda_2$ , with a known concentration ( $C_S$ ) and an unknown volume ( $V_U$ ), is dispensed into the test vial, and it is mixed fully with the blank solution. The absorbance ( $A_U$ ) of the mixture at the wavelength  $\lambda_1$  is then measured. With a knowledge of the extinction coefficients of the blank and sample solutions  $\varepsilon_B$  and  $\varepsilon_S$ , respectively, the unknown droplet volume can be calculated using the following formula derived from the Beer-Lambert law:

$$V_U = V_B \left[ \frac{\frac{A_U}{A_B}}{\frac{\varepsilon_S C_S}{\varepsilon_B C_B} - \frac{A_U}{A_B}} \right]. \quad (19)$$

The sources that need to be taken into consideration in the evaluation of the measurement uncertainty of the photometric method include

instrument-related uncertainties, for example, imprecision and drift in absorbance readings; reagent-related uncertainties, for example, uncertainties in the volume and temperature of the reagents, incomplete mixing, pH dependence, and evaporation; and system-related uncertainties, for example, system nonlinearity.

The principle of the titrimetric method is based on the chemical equivalence of two solutions. In general, any titration system can be used. A test solution with a known concentration  $C_D$  and an unknown volume  $V_U$  is dispensed into a titration vessel containing a receiver liquid, followed by a titration process with a titration solution of known concentration  $C_T$ . An auxiliary solution may be required to adjust the pH value before the titration starts. The equivalence point  $E_Q$  (in milliliters) is determined by potentiometric detection, for example, with a silver electrode. The unknown volume can be calculated using the following formula:

$$V_U = E_Q \times \frac{C_T}{C_D}. \quad (20)$$

The titrimetric method described here is, according to ISO 8655-7 [5], suitable for measuring dispensed liquid volumes greater than 500  $\mu\text{l}$ . This is not satisfactory, since our goal here is to measure liquid volumes of a few microliters or under. However, a technique based on the principle of titration of two liquids and measurement of the pH value of the resulting solution has been demonstrated to be feasible for the characterization of liquid volumes in the nanoliter range [10]. The long test cycle time and some issues in the evaluation of the uncertainty of this technique are, however, yet to be resolved.

Verification of measurements conducted by the photometric or titrimetric technique can be done easily by comparing the results with results from the gravimetric method if the volume dispensed is sufficiently large. However, for the measurement of small liquid volumes where the gravimetric method is no longer applicable, verification can be difficult. In that case, cross-validation between various measuring techniques and/or comparison with a calibrated dispenser is essential.

### Key Research Findings

According to ISO GUM, which is a guide to the expression of uncertainty in measurements, the measurement uncertainty of the primary flow rate calibration system described above can be estimated as follows:

$$\begin{aligned} & \left[ \frac{u_c(q_m)}{q_m} \right]^2 \\ &= \left[ \frac{\partial f}{\partial V_{cv}} \frac{u(V_{cv})}{q_m} \right]^2 + \left[ \frac{\partial f}{\partial \rho_{1,1}} \frac{u(\rho_{1,1})}{q_m} \right]^2 \\ &+ \left[ \frac{\partial f}{\partial \rho_{1,0}} \frac{u(\rho_{1,0})}{q_m} \right]^2 + \left[ \frac{\partial f}{\partial W_1} \frac{u(W_1)}{q_m} \right]^2 \\ &+ \left[ \frac{\partial f}{\partial W_0} \frac{u(W_0)}{q_m} \right]^2 + \left[ \frac{\partial f}{\partial \rho_{a,1}} \frac{u(\rho_{a,1})}{q_m} \right]^2 \\ &+ \left[ \frac{\partial f}{\partial W_{ref,1}} \frac{u(W_{ref,1})}{q_m} \right]^2 + \left[ \frac{\partial f}{\partial W_{ref,0}} \frac{u(W_{ref,0})}{q_m} \right]^2 \\ &+ \left[ \frac{\partial f}{\partial t} \frac{u(t)}{q_m} \right]^2. \end{aligned} \tag{21}$$

Similarly,

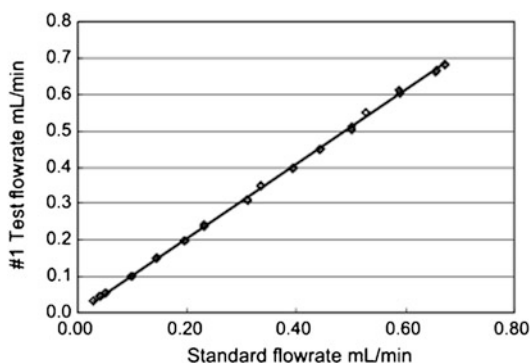
$$\begin{aligned} & \left[ \frac{u_c(q_v)}{q_v} \right]^2 \\ &= \left[ \frac{\partial g}{\partial V_{cv}} \frac{u(V_{cv})}{q_v} \right]^2 + \left[ \frac{\partial g}{\partial \rho_{1,1}} \frac{u(\rho_{1,1})}{q_v} \right]^2 \\ &+ \left[ \frac{\partial g}{\partial \rho_{1,0}} \frac{u(\rho_{1,0})}{q_v} \right]^2 + \left[ \frac{\partial g}{\partial W_1} \frac{u(W_1)}{q_v} \right]^2 \\ &+ \left[ \frac{\partial g}{\partial W_0} \frac{u(W_0)}{q_v} \right]^2 + \left[ \frac{\partial g}{\partial \rho_{a,1}} \frac{u(\rho_{a,1})}{q_v} \right]^2 \\ &+ \left[ \frac{\partial g}{\partial W_{ref,1}} \frac{u(W_{ref,1})}{q_v} \right]^2 + \left[ \frac{\partial g}{\partial W_{ref,0}} \frac{u(W_{ref,0})}{q_v} \right]^2 \\ &+ \left[ \frac{\partial g}{\partial t} \frac{u(t)}{q_v} \right]^2, \end{aligned} \tag{22}$$

where  $u$  denotes the standard uncertainty of the variable within the accompanying parentheses and the partial differential of each variable is the sensitivity coefficient. Each variable could contribute its measurement uncertainty to the final combined standard uncertainty  $u_c$ , in the form of a type A or type B uncertainty, defined in ISO GUM. If we consider a gravimetric system, that system could be a measurement standard for flow rates of 0.1 mg/min–10 g/min (0.1  $\mu\text{l}/\text{min}$ –10 ml/min) at temperatures of 15–26  $^\circ\text{C}$  and pressures of 1–60 kPa, and the relative expanded uncertainty of the system is smaller than 1.1 %.

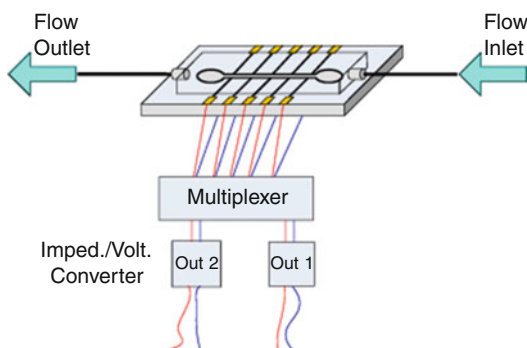
An example of a calibration is shown in Fig. 9, where flow rates obtained from a meter under test, denoted by squares along with a linear fit, have been plotted against those of a calibration system. Because the instruments used to measure the nine variables can have their own calibration chains, the traceability of the microflow meter has therefore been established.

If flow rates down to 1 nl/min are required, the gravimetric method is no longer practical owing to the limits of balances and evaporation or leakage during the long time required for calibration.

Therefore, a chip-based, time-of-flight-type microflow rate calibrator, as shown in Fig. 10, has been proposed [9]. When an interface formed by two fluids that have different dielectric constants and are insoluble in each other, for example, a water/air or water/oil interface, passes



**Fluid Metering, Fig. 9** Example of calibration of a microfluidic meter using the gravimetric method



**Fluid Metering, Fig. 10** Schematic of a chip-based volumetric microflow rate calibrator. Electrode nodes are used to detect a liquid/air or liquid/liquid interface passing through the microchannel

through an electrode node, the potential changes owing to the change in equivalent capacitance. In contrast to other approaches of this kind, which generally suffer from the effects of diffusion, the determination of the time of flight in this calibrator can be more precise, since the interface follows the flow faithfully and does not change over time while moving in the microchannel. The volume between any two electrode nodes could be obtained from a calibrated flow rate determined by a primary system and the time interval between two detection signals. This calibrator can thus be traced back to the primary standard and be used to calibrate lower flow rates.

In principle, the capability to determine small dispensed liquid volumes using concentration

measurement increases as the amount of diluent or receiver liquid in the test container is reduced, as long as taking measurements remains possible with the instruments used. This feature is a consequence of the scalability of these methods. However, the use of a large volume is essential in order to obtain measurements with low uncertainty, and it is virtually inevitable, to a certain degree, that the uncertainty becomes higher as the liquid volume handled becomes lower. This is a trade-off and requires elaborate consideration when these methods are to be used.

## Future Directions for Research

Accurate micro- and nanoscale fluid metering is important since it serves as a basis for evaluating the performance of microfluidic devices and thus is critical to the quality control of those devices and systems using them. Establishment of a traceability chain and evaluation of the measurement uncertainty for flow rate and droplet volume metering instruments are important, especially for levels of liquid quantity that cannot feasibly be dealt with by gravimetric methods. Moreover, reliable methods to measure extremely small liquid volumes, for example, 10 nl or below, are yet to be developed.

## Cross-References

- ▶ [Droplet Dispensing](#)
- ▶ [Flow Rate Measurements, Methods](#)
- ▶ [Nanofluidics in Carbon Nanotubes](#)
- ▶ [Picoliter Flow Calibration](#)
- ▶ [Pyroelectric Flow Sensors](#)
- ▶ [Thermocapacitive Flow Sensor](#)
- ▶ [Thermoelectric Flow Sensors](#)

## References

1. Whitesides G (2003) The right size in nanobiotechnology. *Nat Biotechnol* 21(10):1161–1165
2. Ghosh S, Sood AK (2003) Carbon nanotube flow sensors. *Science* 299:1042–1044
3. Comiey J (2002) Nanolitre dispensing - on the point of delivery. *Drug Discov World* 2002:33–44

4. ISO 8655-6:2002(E) Piston-operated volumetric apparatus – part 6: gravimetric methods for the determination of measurement error
5. ISO 8655-7:2005(E) Piston-operated volumetric apparatus – part 7: non-gravimetric methods for the assessment of equipment performance
6. Poghossian A, Yoshinobu T, Schoning MJ (2003) Flow-velocity microsensors based on semiconductor field-effect structures. *Sensors* 3:202–212
7. Wu S, Lin Q, Yuen Y, Tai YC (2001) MEMS flow sensors for nano-fluidic applications. *Sens Actuators A* 89(1–2):152–158
8. Markov DA, Bornhop DJ (2001) Nanoliter-scale non-invasive flow-rate quantification using micro-interferometric back-scatter and phase detection. *J Anal Chem* 371:234–237
9. Yang CT, Lin WT, Yang FR, Feng CC (2005) A metrological traceability system for microflowrate measurement. *ASME IMECE2005-29443*, Orlando
10. Cavallaro A, Saggere L (2005) Picoliter fluidic flow characterization using ion-selective measurement. *ASME IMECE2005-82646*, Orlando

---

## Fluidic Assembly

Nathan B. Crane, Jose Carballo, Qi Ni, Onursal Onen and Rasim O. Guldiken  
 Department of Mechanical Engineering,  
 University of South Florida, Tampa, FL, USA

### Synonyms

Assembly; Directed assembly; Fluidic assembly; Self-assembly

### Definition

Fluid-assisted assembly refers to a number of processes that utilize a fluid medium or fluidic forces to assemble components. Fluid-assisted assembly processes often use a fluidic medium to overcome the challenges with grasping and releasing microscale components using traditional methods. These processes can utilize capillary, viscous, magnetic, electrical, and gravitational forces. This category encompasses both stochastic self-assembly processes and directed processes.

### Overview

Assembly is the process of positioning components and fixing them in their desired positions. In general, this requires control over the orientation and position of every component. At the macroscale, this is accomplished by sequentially grasping, positioning, and releasing each component. Most traditional assembly models are based on kinematics.

As part dimensions decrease, it becomes increasingly difficult to handle them by traditional methods. Instead, at the microscale, many systems are made with little or no assembly of submillimeter components. To do this, each process and material used in manufacturing the system must be compatible with all the previous processes. When it works, this approach avoids the assembly problem, but it comes with penalties in cost and performance.

The root of microscale assembly processes is the difficulty with grasping and releasing small components. At these size scales, electrostatic, capillary, and van der Waals forces dominate over gravity. This makes part release very complicated. However, in a fluid environment, many of these forces are reduced. The buoyancy of a fluid environment also reduces the effects of gravity. This permits the parts to be manipulated by small forces that might otherwise be negligible. Some types of fluidic assembly entirely eliminate the grasping of the parts and utilize stochastic interactions to position the parts [1].

### Basic Methodology

Fluidic assembly systems can generally be categorized into three key categories:

1. Fluid Gripping – Fluid forces replace mechanical grasping to implement the traditional, grasp, position, and release assembly methods.
2. Fluid Actuation – Fluid forces such as surface tension and viscous shear are used to position a part and/or hold it into its desired position.
3. External Field – Fluids serve as a medium to support external fields that act on the assembly objects. External fields include electrical, magnetic, and acoustic.

The latter two methods can both be utilized with two very different control methods. Some systems that rely on a self-assembly approach in random interactions are used to bring the parts into position, and the parts and assembly environment are designed to create the forces that hold them together. The assembly system is simplified because there is no need for a control system and the associated actuation to guide the parts. However, most systems require the assembly of multiple parts with controlled orientation and sequence. It is difficult to design the bonding and agitation systems that can complete this process reliably without errors. Alternatively, a feedback system can be implemented to control the motion of the components. This facilitates the assembly of more complex systems, but requires more complexity in the assembly equipment.

The basic concepts of each assembly type are summarized below.

**Fluidic Gripping**

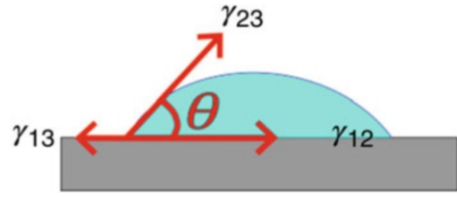
Fluidic gripping utilizes the surface interaction between the liquid and the surroundings. The surface tension effect of the liquids starts to dominate gravity when the characteristic length is less than the capillary length ( $\sqrt{\frac{2}{\rho g}}$ ). The wetting property of the grasped parts and the surface tension of the liquid determine the gripping force in most cases. The surface tension can be created from liquid–liquid or liquid–gas interfaces.

Most common fluidic grippers use capillary bridge configuration. Surface energy minimization results in a finite contact angle between the liquid and the solid surface which is defined by Young’s equation (Fig. 1):

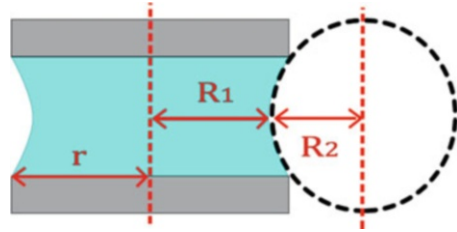
$$\text{Cos}(\theta) = \frac{\gamma_{13} - \gamma_{12}}{\gamma_{23}} \tag{1}$$

When  $\theta$  is less than  $90^\circ$ , wetting of the solid is energetically favorable and gripping is made possible.

Another effect of surface tension can be observed from the physical shape of the capillary bridge. The Laplace pressure ( $\Delta P$ ) is expressed as



**Fluidic Assembly, Fig. 1** The contact angle between a liquid and a solid with the surface tensions illustrated



**Fluidic Assembly, Fig. 2** A capillary bridge with the principle radii of curvature illustrated

$$\Delta P = P_{in} - P_{out} = \gamma * \left( \frac{1}{R_1} + \frac{1}{R_2} \right) \tag{2}$$

where  $R_1$  and  $R_2$  are the principle radii at the minimum of the capillary bridge (Fig. 2).

Laplace pressure quantifies the pressure difference between the inside and outside of the liquid. For a convex surface profile, the pressure outside is always greater than the inside of the drop ( $R_1 > 0 > R_2$ ).

When the aspect ratio of the gripping droplet is much less than unity ( $R_1 \gg R_2$ ), Laplace pressure can be used to approximate the gripping force by substituting

$$F = \Delta P * A = \Delta P * \pi r^2 \tag{3}$$

In this case, the force is exerted by pressure through the contact area ( $A = \pi r^2$ ).

When the aspect ratio of the gripping droplet is within the same magnitude ( $|R_1| \sim |R_2|$ ), the energy approach can be used to predict the gripping force. Using the simplest case where both the gripper and part have a flat surface and the same wetting properties, the maximum gripping force ( $F$ ) between the gripper and the part can be

approximated by the normal component of the surface tension force:

$$F = 2 * \pi * r * \sin(\theta) * \gamma \quad (4)$$

Here, the surface tension ( $\gamma$ ) acts at the contact line of both the gripper and the part.

Detailed study was carried out by Lambert et al. [2] and the authors suggested that it is necessary to combine both effects when calculating the dynamic gripping force since both the contact angle and the Laplace pressure are changing during gripping. They showed that in micro gripping, as the gap of the capillary bridge increases, the force due to wetting energy increases and the force due to Laplace pressure decreases while the total gripping force stays constant. The study also investigated other key parameters such as the geometry of the gripper, the surface tension of the liquid, and the volume of the liquid used during gripping.

When the ambient environment is in liquid phase, immiscible liquid droplet can be used to grasp parts. Also, gas bubbles have been used instead of droplets for submerged parts.

Capillary bridge gripper can provide large adhesion force; it also has the benefit of self-aligning given the correct geometry. It is important to point out that chemical coatings and surface roughness can change the wetting of the solid dramatically. By doing so, small droplets can form patches on a non-wettable surface. Single or multiple droplets can be used to align components in similar processes by means of capillary averaging. The accuracy of the alignments is usually in the range of micrometers. Moreover, a number of self-assembly processes (stochastic and deterministic) involve the deposition of liquid drops in predetermined sites and then grasp the parts when they are in contact. This is critical to many surface mount technology (SMT) assembly processes. Compared to traditional mechanical grippers, fluidic grippers offer softer contact between the gripper and the parts. The gripping force can vary over a large range. Also, lower cost is possible since the number of mechanical actuators is limited.

Although capillary grippers provide excellent characteristics in the microscale, there are still several limitations: the solid surfaces (grripper fixture and the part that is being grasped) have to have good wetting properties. It is more likely to operate in a liquid–gas system since releasing can be challenging in a liquid–liquid system. Also, the cycling life may be limited since every releasing step will decrease the volume of the gripping fluid. In general, the releasing of components is done by applying shear force to the capillary bridge. Some unconventional methods including vibration input, surface tension modulation via electrowetting, and use of thermal input to evaporate/freeze the gripping droplet have been demonstrated by researchers and some examples can be found in [2].

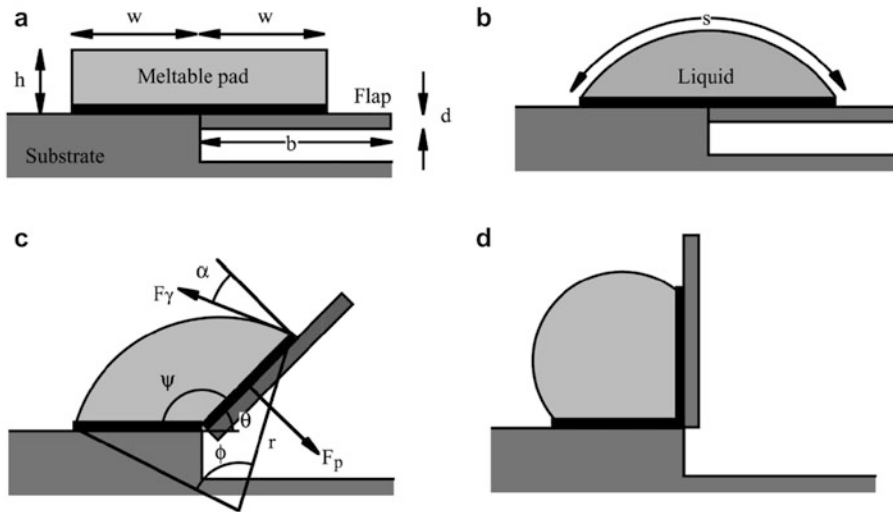
### Fluid Actuation

Surface tension can also provide a method to rotate parts out of plane to assemble 3D structures as illustrated in Fig. 3. Capillary folding is usually nonreversible; a variety of features can be fabricated through different steps. Due to the advancement in surface micromachining; multiple layers of predefined patterns can be created onto a planar substrate. Then the bonding material is deposited in solid form. When a specific trigger (usually thermal) is supplied, the bonding material goes through phase change from solid to liquid. Surface tension of the liquid provides a torque to rotate the planar parts to create 3D structures.

Neglecting gravity, the maximum rotating torque ( $T$ ) can be approximated by

$$T = \gamma * W * \left\{ \sin \left[ \frac{(\theta + \phi)}{2} \right] - \frac{\sin \left( \frac{\phi}{2} \right)}{2 * \cos \left( \frac{\theta}{2} \right)} \right\} \quad (5)$$

(see [3] for detailed derivation). Variations include hinged/non-hinged flaps, parts with/without liming mechanism, and open/closed final structures.



**Fluidic Assembly, Fig. 3** Surface tension powered rotation [3]. Solder is placed over hinged components. When the solder reflows, the surface tension bends the hinge.

Mechanical stops and/or solder volume can be used to control the equilibrium angle (Figure reproduced with permission of the publisher)

Capillary folding can be done in parallel. As such, it is well-suited for assembling/actuating a large number of parts in a single step. Design parameters include the surface tension of the bonding material, the wetting of the substrate/parts, and the trigger supplied. The material compatibility needs to be carefully considered in order to make the process practical.

Fluidic forces are also exerted on solids at a fluid/fluid interface. Lateral capillary force causes failure of many microstructures during fabrication and release. Constructively, lateral capillary force can be used to assemble large number of identical parts in repeated array.

Individual droplets or bubbles can also be actuated to drive assembly if parts are located on or in the droplets. Tools available for the manipulation of droplets include electrowetting, mechanical vibration, thermal capillary flow, acoustic radiation, and surface roughness modification. Parts can be transferred with the droplet along programmable paths, and the fabrication and equipment requirement is relatively simple compared to other processes. The limitation will be the part size relative to droplet size, control over part orientation, and the speed which the parts can be actuated.

### External Fields

External fields such as electric, magnetic, and acoustic fields can be employed for assembly in fluidic environment, while fluid properties such as buoyancy, surface tension, electrical insulation, viscosity, and interfaces can assist. Various tasks can be accomplished using the advantages of each specific external field, and complex assemblies can be formed through feedback control.

**Magnetic:** Magnetic forces are noncontact forces having long-distance action and high-energy density with favorable scaling at the microscale [10]. Forces are also independent from the assembly medium and the surface chemistry, which makes the method component oriented rather than medium oriented. Magnetic field strength and the component volume are the two main factors in force scaling. Orientation control can be achieved by adjusting direction of the field, magnetic characteristics of components, and/or the shape of the components [1]. External magnetic fields are effective in long-range manipulation and positioning, while short-range magnetic forces are suitable for assembly and fine positioning. External fields require multi-axis magnet assemblies that might increase the cost, but each magnet assembly can

be reused. Short-range forces only require proper material selection and magnetization. Magnetic force-driven microrobots can be actuated and controlled by external magnetic fields to manipulate nonmagnetic components. Both two- and three-dimensional assemblies are possible with careful design and magnet assemblies.

**Electric Fields:** Electric field assembly can be employed with attractive and repulsive properties of uncharged particles (electrophoresis, EP) or with dielectric properties of components (dielectrophoresis, DEP). Electric field-mediated assembly is usually utilized with metal electrodes. The assembly can be accomplished either on top of the electrodes or at desired locations. Electric field-mediated assembly is mostly restricted to two-dimensional assemblies.

Similar to magnetic field, attractive and repulsive forces are possible. In EP, charges of the component determine the type of attraction, and in DEP the key parameter is the difference of dielectric properties between the components and the medium. DEP generates an attractive force on components with higher polarizability than the surrounding medium (positive DEP). Repulsive force is observed if it is lower (negative DEP) [1]. The direction of the dielectrophoretic forces is independent of the electric field direction and depends on the dielectric properties of the particle, frequency of the applied field, and conductivity of the medium as seen in Eq. 1 [1].  $a$  is the radius of the particle,  $K(\omega)$  is the Clausius–Mossotti factor,  $E_{rms}$  is the root mean square value of the electric field,  $\epsilon_p$  and  $\epsilon_m$  are the permittivities of the particle and medium,  $\sigma_p$  and  $\sigma_m$  are the conductivities of the particle and medium, and  $\omega$  is the angular frequency. Frequency-dependent dielectric properties of materials, cells, and other components allow tailoring of assembly to use attractive and repulsive forces only by changing the frequency.

$$F_{DEP} = 2\pi\epsilon_0\epsilon_m a^3 \text{Re}[K(\omega)] \nabla E_{rms}^s K(\omega)$$

$$= \frac{\epsilon_p - \epsilon_m - \frac{j}{\omega(\sigma_p - \sigma_m)}}{\epsilon_p + 2\epsilon_m - \frac{j}{\omega(\sigma_p + 2\sigma_m)}} \quad (6)$$

**Acoustic Fields:** Acoustic field-mediated assembly utilizes several different acoustic excitation types such as mode shapes, surface acoustic waves, Faraday waves, and standing wave patterns. Acoustic forces usually require more complex design to manipulate components by using pressure waves in fluids. Pressure wave fields can be generated with bulk piezoelectric transducers, surface acoustic wave devices, and vibration modes (or mode shapes) of vibrating surfaces. Carefully positioned or custom-fabricated transducers with accompanying electrical peripherals are essential. Acoustic forces depend on the magnitude, phase, and direction of the acoustic field [1]. Manipulation and handling of components is easy to achieve by acoustic fields; on the other hand, orientation and position control is not.

External field-mediated assembly techniques offer flexible and robust control of micro components in fluidic systems. Simultaneous use of multiple fields helps eliminate the disadvantages of individual methods and enables more complex assemblies. Most external field assemblies do not require closed-loop control; however, methods like magnetic robots and manipulation of individual components to target locations with external fields require manual or closed-loop control systems.

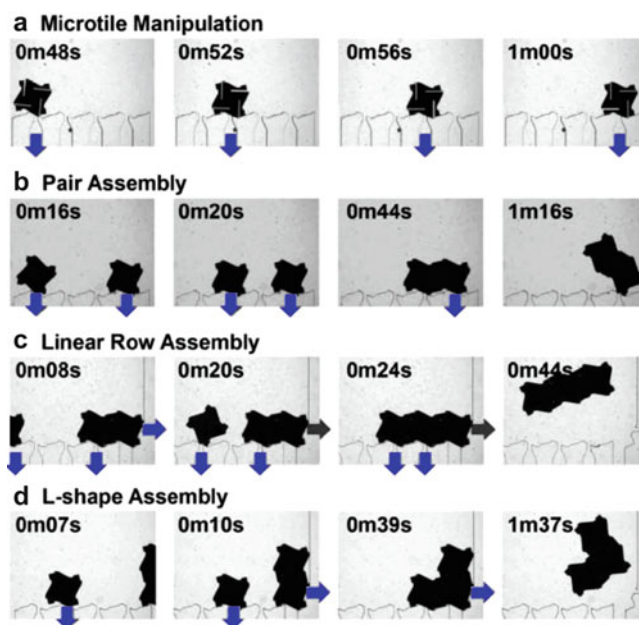
## Key Research Findings

### Fluid Flow Field Control

Modulation of fluid velocity fields is one direct way to manipulate components [4]. Final component positions were designed to be flow sinks; hence, fluid viscous (drag) forces worked as the transporting mechanism. Valve control allowed for reconfiguring the location of flow sinks and thus for redirecting assembly locations after previous flow sinks have been filled to add components or to create different assemblies. Furthermore, assembly components were designed with internal channels and valves for fluid to flow through. Once assembled, internal valves would control the direction of the fluid through the components. This would allow for parts to relocate fluid sinks and to grow a structure in 3D.

### Fluidic Assembly,

**Fig. 4** Fluid-driven assembly inside a microfluidic chamber [8]. Fluid flow in and out of the chamber ports permits control over the component bonding arrangements (Figure reproduced with permission of the publisher)



Another way of regulating fluid flow for noncontact component manipulation was created by mechanical oscillation. Within a fluid environment, a tool capable of oscillating its tip at high frequencies would then create local streamlined flow. Tool oscillation parameters could be adjusted to define whether the local flow would repel, attract, or rotate components. For this technique, there was no contact between the tool and the manipulated component. This concept is attractive for manipulating cells and live organisms [5].

### Microfluidics

Sorting can be seen as a preliminary assembly step. Particle sorting has been known as a common application for microfluidic devices and could be integrated into a microfluidic assembly system. While most sorting methods utilize spherical components, railed microfluidic channels have been created to sort and control orientation of non-geometric components [6]. Furthermore, concept of space confinement within a microfluidic channel has been applied to the assembly of microscale components into structures that resemble polymer chains [7].

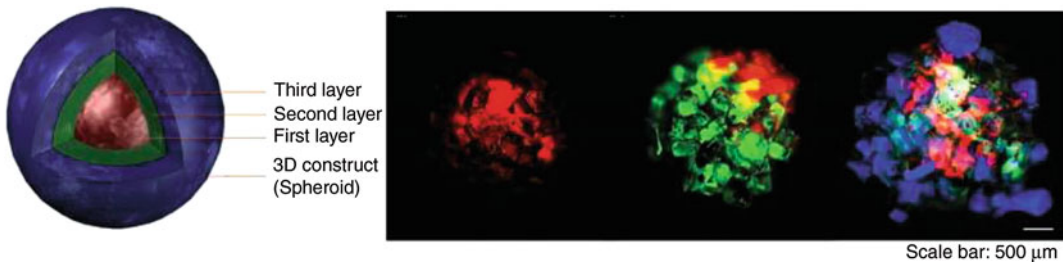
While microfluidic channels are capable of achieving 1D actuation, microfluidic chambers

have harnessed fluidic forces for actuation in 2D. The use of variable flow sinks for controlling fluid flow fields (described above) has also been proposed in microfluidic chambers (Fig. 4) [8]. Such systems are attractive for their potential of creating complex free-floating structures. Component placement has been achieved at locations within a microfluidic chamber [9]. Sequential valve switching allowed for internal chamber flow to generate zero-force nodes, where components would reach a stable equilibrium.

While the spaces within these channels and chambers are limited, assembly products can be ejected and used for further assembly of larger structures. Current microfabrication allows for complex microfluidic systems to be built in parallel. An array of assembly systems can be used to expand the complexity and size limits that an individual system can achieve.

### Colloidal

At the nanoscale, colloidal assembly systems rely on fluid flows caused by natural convection for positioning colloidal particles. Convective assembly patterns are controlled by evaporation rate and contact line geometry. Coatings with monolayer precision have been created through



**Fluidic Assembly, Fig. 5** Morphology and merged three-layer fluorescent images of assembled spheroids [11] (Figure reproduced with permission of the publisher)

convective assembly. During evaporation, colloidal particles arrange themselves while suspended on fluid–air interface. Besides using natural convective flows during droplet evaporation, several methods have been employed to modify flow and placement of suspended particles, acquiring desirable positioning strategies [10]. As a result, nanoparticles assembled into crystalline arrangements are attractive as nanoscale-lithography masks through subsequent deposition and etching processes. They also have potential for data storage applications as well as patterning of proteins. Furthermore, colloidal assemblies serve as the building elements for larger, more complex structures (i.e., one approach to high precision of microscale assembly).

### Assembly of Magnetic Hydrogels

Linear and spherical assembly of magnetic micro size hydrogels was reported by Xu et al. [11]. Gelatin methacrylate and PEG hydrogels were magnetized by loading them with magnetic nanoparticles. Linear assembly is done using a static magnetic field formed by parallel sheet magnets and 3D spherical assembly was done using the magnetic tip of a rod. Multilayered assembly was achieved in 3D as presented in Fig. 5. Cell encapsulation with the assembled microgels was also presented in the same study.

### Dielectrophoretic Assembly of Resistors Between Electrodes

Dielectrophoresis was used for assembly of 15  $\mu\text{m}$  by 2  $\mu\text{m}$  size, three-terminal silicon metal oxide semiconductor field-effect transistors between electrodes as illustrated in Fig. 6 [12].

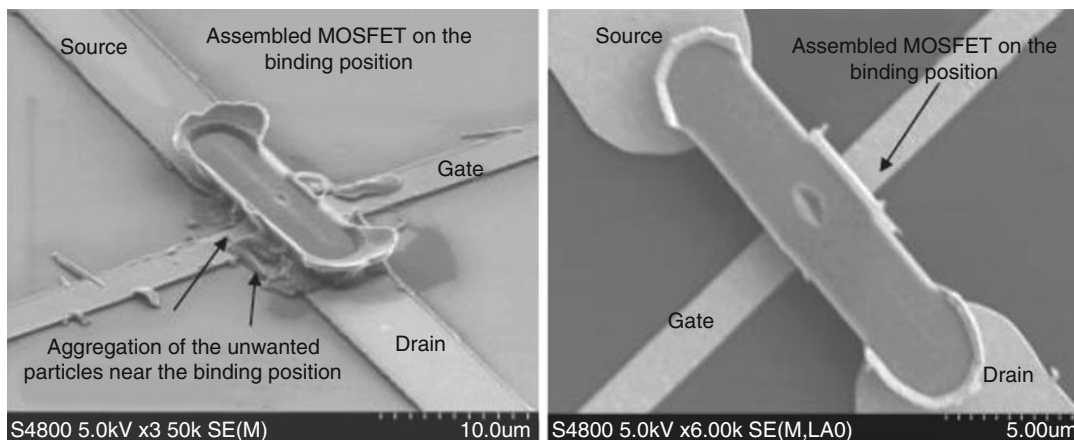
A combined positive and negative DEP approach was used for positioning and assembly of the transistors. Negative DEP was used to position particles on top of metal electrodes. Positive DEP between the resistors and the metal electrodes led to assembly by either leaving the DEP voltage on or with the help of chemicals during drying process.

### Self-Propelled Magnetic Field-Actuated Microrobots

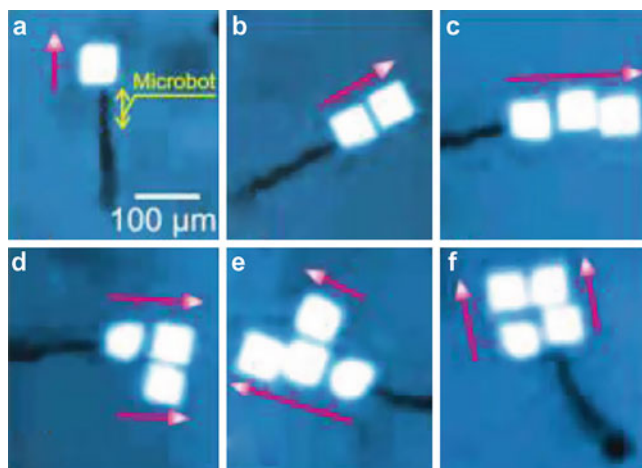
Self-propelled tubular microrobots were reported to use manually controlled assembly, which are composed of rolled Ti/Fe/Pt thin films [13]. Magnetic field was used for untethered control of microrobots by adjusting the external magnetic field, using mechanical actuator containing a NdFeB permanent magnet placed underneath the suspension. The rotation or movement of the magnet enables various assembly tasks to be completed. The microrobots were self-propelled with bubble formation by platinum catalytic decomposition of hydrogen peroxide into oxygen and water inside the microrobot. Easy control and high propulsion power was reported with transportation of large-size components (compared with microrobot) and numerous small components at the same time (up to 60 particles) by one robot. The robots were used to manipulate and assemble both metal and polymer components in different configurations as seen in Fig. 7.

### Acoustic Field Assembly Using Vibrational Mode Shapes

Microscale hydrogels were assembled by acoustic excitation as illustrated in Fig. 8 [14].



**Fluidic Assembly, Fig. 6** FESEM images of the assembled transistor device with unwanted particles and close-up image [12] (Figure reproduced with permission of the publisher)



**Fluidic Assembly, Fig. 7** Optical images of a microbot assembling four nanoplates in different configurations [13] (Figure reproduced with permission of the publisher)

Specific mode shape patterns are formed and components are forced to move to nodes and antinodes at resonant frequencies of the droplets and structures on which the droplets are placed. Microgels and microbeads of various sizes in a droplet were successfully assembled by excitation at various frequencies and intensities. The control over individual components is not possible; however, a high number of components can be robustly manipulated. Both single- and double-layer structures (with a second assembly on top of the first assembly) were reported. The hydrogels used in the study are capable of encapsulating cells and proteins to create biological assemblies.

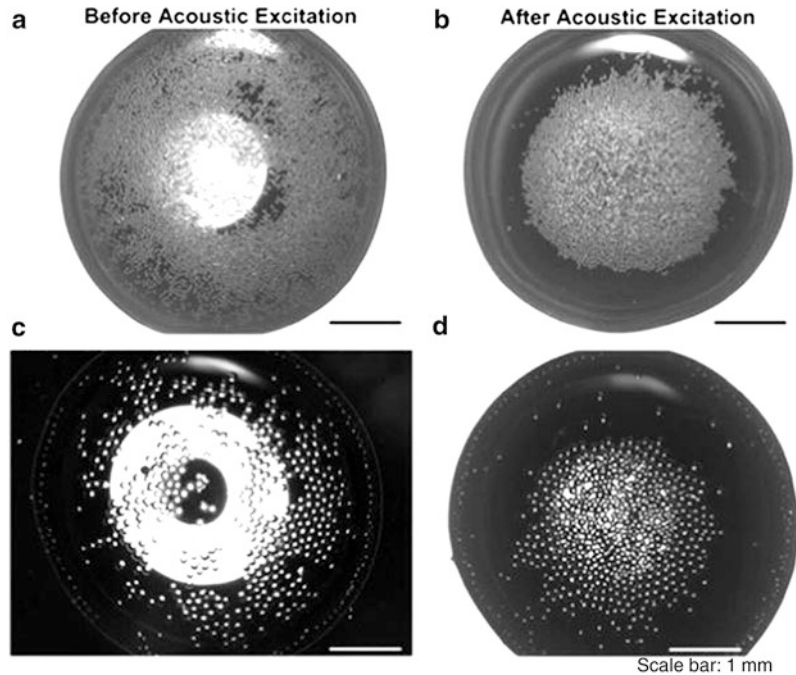
### Future Directions for Research

Fluidic assembly is still a relatively young area of scientific study. Much of the current work has focused on the development of new assembly processes. Demonstrations of these methods have largely focused on demonstrating basic capabilities by assembling simple systems with relatively few unique parts. The largest assemblies consist primarily of arrays of repeated elements.

Future research is likely to move towards the controlled integration of larger varieties of components into more complex systems. This advancement will require the integration of

**Fluidic Assembly,**

**Fig. 8** Acoustic assembly of microbeads. (a) Distributed 50  $\mu\text{m}$  microbeads before excitation and (b) after excitation. (c) Distributed 100  $\mu\text{m}$  microbeads before excitation and (d) after excitation [14] (Figure reproduced with permission of the publisher)



greater control over the orientation of components and the sequence in which they assemble through enhanced sensing and feedback control. This favors the use of directed assembly processes over purely self-assembled systems. This can be accomplished using external field assembly methods and some fluidic force methods if they are integrated with feedback controls.

One area of particular opportunity is in the assembly of biological systems. A fluidic environment is required to maintain cell viability and the cells are of sizes that are not easily handled by traditional means. While fluidic assembly methods would be very attractive, living tissues are very complex assemblies consisting of multiple cell types, support materials, and many system constraints. Significant advances are required in the control of assembly processes in order to assemble living tissues from cells.

**Cross-References**

- ▶ [Acoustic Streaming](#)
- ▶ [Control of Micro-fluidics](#)
- ▶ [Dielectrophoresis](#)

- ▶ [Digital Microfluidics](#)
- ▶ [Electrophoresis](#)
- ▶ [Electrowetting](#)
- ▶ [Electrowetting, Applications](#)
- ▶ [Hydrophilic and Hydrophobic Patterning](#)
- ▶ [Self-Assembled Monolayer](#)
- ▶ [Self-Assembly](#)
- ▶ [Self-Assembly Fabrication](#)
- ▶ [Surface Tension, Capillarity, and Contact Angle](#)

**References**

1. Crane NB, Onen O, Carballo J, Ni Q, Guldiken R (2013) Fluidic assembly at the microscale: progress and prospects. *Microfluid Nanofluid* 14(3–4):383–419
2. Lambert P (2007) Capillary forces in microassembly [electronic resource]: modeling, simulation, experiments, and case study/Pierre Lambert. Springer, New York
3. Syms R, Yeatman E, Bright V, Whitesides GM (2003) Surface tension-powered self-assembly of microstructures—the state-of-the-art. *J Microelectromech Syst* 12(4):387–417
4. Kalontarov M, Krishnan M, Erickson D (2009) Fluid dynamically driven assembly in three dimensions for programmable matter. In: volume 9: heat transfer, fluid flows, and thermal systems, parts A, B and C, vol 2009, no 43826. pp 1491–1495

5. Hagiwara M, Kawahara T, Arai F (2012) Local streamline generation by mechanical oscillation in a microfluidic chip for noncontact cell manipulations. *Appl Phys Lett* 101(7):074102
6. Park W, Lee HS, Park H, Kwon S (2009) Sorting microparticles by orientation using wedged-fin and railed microfluidics. In: *TRANSDUCERS 2009–2009 international solid-state sensors, actuators and microsystems conference*, Denver, Colorado, pp 429–432
7. Vanapalli SA, Iacovella CR, Sung KE, Mukhija D, Millunchick JM, Burns MA, Glotzer SC, Solomon MJ (2008) Fluidic assembly and packing of microspheres in confined channels. *Langmuir: ACS J Surf Colloids* 24(7):3661–3670
8. Tolley MT, Kalontarov M, Neubert J, Erickson D, Lipson H (2010) Stochastic modular robotic systems: a study of fluidic assembly strategies. *IEEE Trans Robot* 26(3):518–530
9. Schneider TM, Mandre S, Brenner MP (2011) Algorithm for a microfluidic assembly line. *Phys Rev Lett* 106(9):094503 (4 pp.)
10. Mastrangeli M, Abbasi S, Varel C, Van Hoof C, Celis J-P, Böhringer KF (2009) Self-assembly from milli- to nanoscales: methods and applications. *J Micromech Microeng: Struct Devices, Syst* 19(8):83001
11. Xu F, Wu C-AM, Rengarajan V, Finley TD, Keles HO, Sung Y, Li B, Gurkan UA, Demirci U (2011) Three-dimensional magnetic assembly of microscale hydrogels. *Adv Mater (Deerfield Beach, Fla)* 23(37):4254–4260
12. Lee SW, Bashir R (2005) Dielectrophoresis and chemically mediated directed self-assembly of micrometer-scale three-terminal metal oxide semiconductor field-effect transistors. *Adv Mater* 17(22):2671–2677
13. Solovev AA, Sanchez S, Pumera M, Mei YF, Schmidt OG (2010) Magnetic control of tubular catalytic microrobots for the transport, assembly, and delivery of micro-objects. *Adv Funct Mater* 20(15):2430–2435
14. Xu F, Finley TD, Turkeydin M, Sung Y, Gurkan UA, Yavuz AS, Guldiken RO, Demirci U (2011) The assembly of cell-encapsulating microscale hydrogels using acoustic waves. *Biomaterials* 32(31):7847–7855

---

## Fluidic Diodes

### Definition

Fluidic devices exhibiting different hydrodynamic properties for the two different fluid flow directions.

In the *forward* direction, fluid passes through a fluidic diode easily, encountering very small hydraulic resistance (dissipation). In the other, *reverse* direction, the resistance is high. When supplied with an alternating fluid flow, this difference in properties results in the ► [fluidic rectification](#) effect. The simplest way to obtain the diode properties is to use a moving component blocking the available flow path in one of the two directions. More robust, easier to make, and capable of operating at a higher frequency are no-moving-part diodes.

### Cross-References

- [Fluidic Rectification](#)
- [Valve-Less Rectification Pumps](#)

---

## Fluidic Pumping

### Definition

A method of generating nonreturn (or nearly nonreturn) fluid flow by processing the supplied alternating flow.

Fluidic devices need a supply of the fluid with which they operate. Sometimes, there is an available external fluid source, and in other cases, the fluid may be provided from a pressurized vessel. Most often, however, the fluidic circuits are supplied with fluid flow from a fluidic pump. This consists of two essential parts: an alternator producing an alternating flow, usually by motion of a reciprocating plunger, piston, or diaphragm, and a rectifier, which changes the alternating flow into a one-way or nonreturn flow.

### Cross-References

- [Fluidic Rectification](#)
- [Valve-Less Rectification Pumps](#)

---

## Fluidic Rectification

### Definition

The process of converting an alternating fluid flow into a one-way flow.

Usually, fluidic devices need for their operation a source of one-way fluid flow. Much easier to generate, however, is an alternating flow produced by the reciprocating motion of a displacing component. The simplest way to rectify an alternating flow is using a nonreturn valve with a moving component blocking the available flow path. In the so-called valveless pumps, the rectification effect is obtained by using inertial effects in fluids on one of the three basic sorts of devices: ► [fluidic diodes](#), fluidic jet-type rectifiers, and traveling-wave rectifiers.

### Cross-References

- [Fluidic Diodes](#)
- [Jet-Type Rectifier](#)
- [Traveling-Wave Pump](#)
- [Valve-Less Rectification Pumps](#)

---

## Fluorescence

### Definition

Fluorescence is the property whereby some atoms and molecules absorb light at a particular wavelength and subsequently emit light of longer wavelength after a brief interval termed the fluorescence lifetime. Photons from an external source are absorbed by the fluorophore, and this produces excited singlet-state electrons. However, the time taken for these electrons to return to the lower energy level is known as the excited-state lifetime. The emission of light occurs as fluorescence from an excited electron singlet state, where all the electrons in the molecule are spin-paired. The

return to ground states occurs with the emission of photons. Emission rates are fast, being in the region of  $10\text{ s}^{-1}$ , and fluorescence lifetimes are relatively short. Many fluorophores have subnanosecond lifetimes, and, therefore, the fluorescence emitted by these dyes is short-lived.

### Cross-References

- [Fluorescent Labeling](#)
- [Fluorescent Thermometry](#)
- [Photometer](#)

---

## Fluorescence Lifetime

### Definition

The fluorescence lifetime of an excited dye molecule represents the average time a fluorophore remains in its excited state and is given by the inverse of the total rate at which radiative and nonradiative relaxation to the ground state occurs.

### Cross-References

- [Fluorescent Thermometry](#)

---

## Fluorescence Measurements

Gea O. F. Parikesit

Quantitative Imaging Group, Delft University of Technology, Delft, The Netherlands

### Synonyms

Fluorescence microscopy; Fluorescence visualization; Fluorescent microscopy; Fluorescent visualization

## Definition

Fluorescence is the phenomenon where a molecule absorbs energy from incoming light and instantaneously emits another light, in which the emitted light has a longer wavelength than the absorbed light. Fluorescence measurements are methods to quantitatively visualize and characterize a physical, biological, or chemical process, based on the characteristics of fluorescence that occurs during the process.

## Overview

Fluorescence is a type of luminescence, which is light that is not generated by high temperature. In fluorescence, a molecule (usually called as a fluorochrome, a fluorophore, or a fluorescent dye) absorbs energy from incoming light and instantaneously emits another light, where the emitted light has a longer wavelength than the absorbed light [1]. The molecule stops emitting light immediately when there is no more incoming light. The fluorescence signals can be measured to quantitatively visualize and characterize a physical, biological, or chemical process. Fluorescence measurements are very useful because they are sensitive and specific to the studied process. Moreover, the fluorescently visualized process can be imaged in detail and analyzed further using various image processing and analysis techniques. This advantage, along with the high spatial measurement capabilities allowed by optical microscopy, is highly crucial for investigations in very small scale such as in microfluidics and nanofluidics. Several methods to measure fluorescence signals, in particular related to quantitative visualization and characterization of phenomena in microfluidic and nanofluidic channels, will be reviewed in this entry.

The fluorescence phenomenon occurs in three steps: excitation of the fluorochrome by the energy absorbed from incoming light (it occurs in 10 s); vibrational relaxation of the fluorochrome, where the energy of the fluorochrome is lowered from the original excited state to the lowest excited state (it occurs in 10 s); and

emission of light with longer wavelength from the fluorochrome (it occurs in 10 s) [1]. The various energy levels involved in the fluorescence phenomenon are illustrated in the so-called Jablonski diagram, as shown in Fig. 1.

Both the energy absorbed from the incoming light and the energy contained in the emitted light occur in discrete amounts, which are termed quanta, and can be expressed by the equation

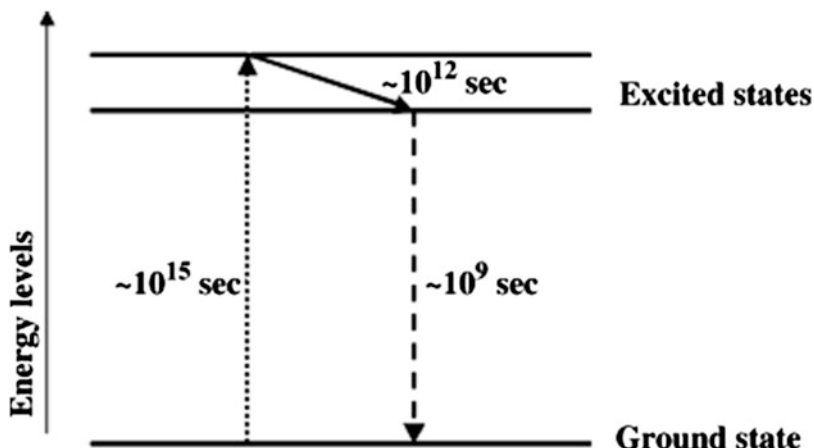
$$E = hf = h \frac{c}{\lambda}, \quad (1)$$

where  $E$  is the energy,  $h$  is Planck's constant ( $6.626,068 \cdot 10^{-34} \text{ m}^2 \text{ kg s}^{-1}$ ),  $f$  is the light frequency,  $c$  is the speed of light in vacuum, and  $\lambda$  is the light wavelength. In general, fluorescence measurements are performed using lights with wavelengths ranging from ultraviolet to visible, which is between 250 and 750 nm. The difference of wavelengths between the excitation and emission light is caused by the second step in the fluorescence phenomenon, which is the vibrational relaxation of the fluorochrome. In this step, some of the absorbed energy is transformed into changes in structural arrangement of the fluorochrome molecule. The shift of wavelength from the excitation light to the emission light is termed as the Stokes shift. Once a fluorochrome molecule reaches its original state, it can be excited again, and the fluorescence signal can be generated repeatedly using a continuous excitation light.

Fluorochrome molecules are usually characterized using their quantum yield and ► [fluorescence lifetime](#). Quantum efficiency is a measure of the efficiency of the fluorochrome's fluorescence emission compared to all possible energy relaxation pathways. This dimensionless parameter is expressed as the ratio between the number of photons (i.e., the smallest discrete amount of light) emitted and the number of photons absorbed. Hence, in general, fluorochromes with higher quantum efficiency are preferred. The fluorescence lifetime ( $\tau$ ) is the time that a fluorochrome molecule remains in the excited state before generating the emission light. The decaying of the fluorescence intensity coming

### Fluorescence Measurements,

**Fig. 1** The Jablonski energy diagram of the fluorescence phenomenon. The *dotted line* illustrates the excitation of the fluorochrome molecule, the *solid line* represents the vibrational relaxation of the excited fluorochrome molecule, and the *dashed line* shows the emission of light with longer wavelength



from a fluorochrome molecule after a pulse excitation light is given by an exponential function:

$$I(t) = I_0 e^{-\frac{t}{\tau}}, \quad (2)$$

where  $I(t)$  is the fluorescence intensity at time  $t$  and  $I_0$  is the initial fluorescence intensity immediately after the pulse excitation. Therefore, the fluorescence lifetime can also be defined as the time in which the fluorescence intensity from the fluorochrome molecule decays to  $1/e$  of the initial intensity.

The fluorescence signal given by the emission light can be significantly reduced by two different phenomena: quenching and photobleaching. In quenching, the excited fluorochrome molecule loses its energy non-radiatively, for example, through collisions with other molecules. Meanwhile photobleaching is the irreversible destruction of the fluorochrome molecules using very intense excitation light. For imaging purposes, both quenching and photobleaching should generally be avoided. However, for quantitative visualization of transport phenomena in microfluidics and nanofluidics, these phenomena can be useful, as we will discuss later.

Fluorescence signals are also influenced by characteristics of the environments surrounding the fluorochrome molecule. One of the most common environmental factors is the concentration of other molecules, which causes quenching as described above. Another factor is the pH of the aqueous medium containing the fluorochromes.

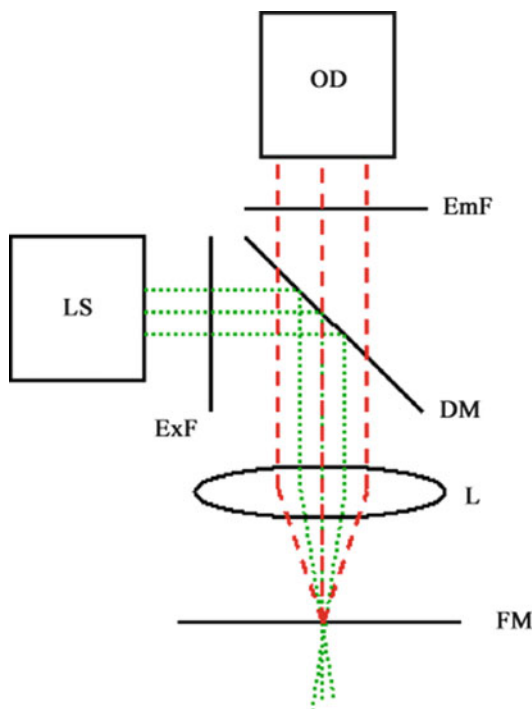
In most imaging applications, the sensitivity of fluorochromes to different pH levels is unwanted. In biological and chemical measurements, however, the pH of the medium can provide extra information of the investigated process. To measure the pH level, two different types of fluorochromes are typically used; each is being sensitive to different pH levels. In this so-called ratio-metric measurement method, the emission light's intensity ratio between the two fluorochromes indicates the actual pH level of the medium.

Below we will describe the optical microscopy setups for performing fluorescence measurements. Afterward we will discuss the application of the fluorescence measurements to quantitatively visualize and characterize transport of fluid and individual biological molecules in microfluidic and nanofluidic studies.

## Basic Methodology

### Fluorescence Microscopy Setup

In general, the fluorescence measurements can be done without using an optical microscope. Fluorescence signals given by bulk materials can readily be measured using standard macroscale optical methods. For measurements in very small scales, such as the investigations performed in microfluidics and nanofluidics, however, an optical microscope is necessary. Here we start by describing the most common fluorescence



**Fluorescence Measurements, Fig. 2** The basic anatomy of a common fluorescence microscopy setup. *LS* light source, *OD* optical detector, *ExF* excitation filter, *EmF* emission filter, *DM* dichroic mirror, *L* lens, *FM* position of fluorochrome molecules

microscopy setup. Figure 2 illustrates the basic anatomy of a fluorescence microscopy setup. The light that is used in the setup usually comes from a mercury (Hg) arc-discharge lamp, located at the back of the microscope. The emission light generated from the fluorescence measurements is then imaged to an optical detector, typically a digital CCD (charge-coupled devices) camera, for further processing and analysis.

Among the most important elements of the setup are the set of optical filters, which separate the excitation light from the emission light [1]. It comprises mainly the excitation filter, the emission filter, and a dichroic mirror (also known as a dichromatic beam splitter, which splits two lights with different wavelengths to two different paths). The excitation filter serves to ensure that only the light with a certain range of wavelengths illuminates, and eventually excites, the

fluorochrome molecules. The filter absorbs all the light with wavelengths outside the desired range. After passing the excitation filter, the light is directed by the dichroic mirror onto the fluorochrome molecules. With the help of the lens near the molecules, the excitation light is focused toward the molecules. After excitation, the fluorochrome molecules eventually generate the emission light, which is then again collected by the same lens near the molecules. The collected emission light then passes through the dichroic mirror; a dichroic mirror is designed so that it reflects light with the same range of wavelengths as the excitation light, while it transmits light with the same wavelengths as the emission light. To ensure that only the emission light reaches the detector, the emission filter is used. This filter absorbs noises that have the same range of wavelengths as the excitation light, such as excitation light scattered by objects near the fluorochrome molecules.

A fluorescence microscope setup that uses such optical filter set, as depicted in Fig. 2, is known as an epi-fluorescence microscope [1]. The word epi-fluorescence means that both the excitation light path and the emission light path use the same lens near the fluorochrome molecules. When excitation light illuminates the fluorochrome molecules, the lens serves as a condenser lens, which focuses the light into the object plane. Meanwhile, when the fluorochrome molecules generate emission light, the lens serves as an objective lens, which gathers light from the object plane into optical detectors. Therefore, by using the epi-fluorescence microscope setup, we can keep the fluorochrome molecules in the object plane always in focus, simultaneously for the excitation light path and the emission light path.

The fluorochrome molecules, which are exactly in the focal plane of the lens, can be imaged clearly in the optical detector. Other molecules, however, will be imaged poorly because they are out of focus. The transition between being in focus and out of focus occurs gradually, such that there is a range of space in which the molecules can still be imaged clearly even though

they are not exactly in focus. This range of space, termed depth of focus [1], can be expressed as

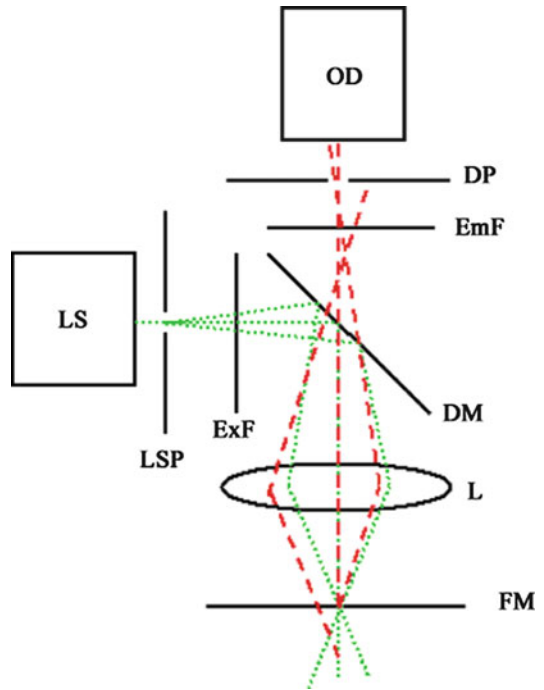
$$Z = \frac{n\lambda}{(NA)^2}, \tag{3}$$

where  $Z$  is the depth of focus for a lens,  $n$  is the refractive index of the medium containing the fluorochrome molecules,  $\lambda$  is the wavelength of the emission light, and  $NA$  is the numerical aperture of the lens, which in turn is defined as  $NA = n(\sin \theta)$  with  $\theta$  as the maximum angle that can be captured by the lens.

The notion of depth of focus is important in microfluidic and nanofluidic studies, because it influences the spatial resolution of the measurement. Let us consider a microfabricated channel with a channel depth of  $d$ , in which fluorochrome molecules are being contained and measured. If  $Z > d$ , then all the fluorochrome molecules are always in focus, and they all are imaged clearly in the optical detector. Consequently, in microfluidic channels, where the fluorochrome molecules are typically much smaller than the channel depth  $d$ , the position of the fluorochrome molecules along the channel depth cannot be resolved anymore. Hence, multiple molecules that are positioned near each other cannot be distinguished from each other, and three-dimensional measurements (for instance, to characterize the transport of fluid inside such channels) cannot be performed. In nanofluidic channels, however, where the fluorochrome sizes are more similar to the channel depth  $d$ , the measurements can be described as a quasi-2D problem, and it is not required anymore to resolve along the channel depth.

Meanwhile, if  $Z < d$ , then only fluorochrome molecules within the depth of field are imaged clearly in the optical detector. By scanning the position of the microfabricated channels relative to the lens, the positions of fluorochrome molecules along the channel depth can be resolved, and a 3D measurement can be performed.

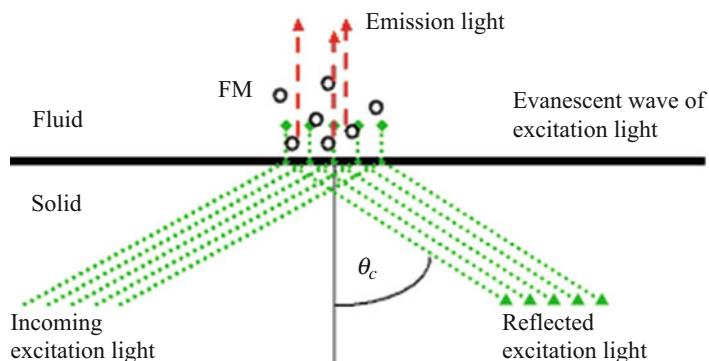
If all the emission light, from both the fluorochrome molecules in focus and the fluorochrome molecules out of focus, is collected by the microscope setup, then the setup is termed as having



**Fluorescence Measurements, Fig. 3** The schematic concept of a confocal fluorescence microscope configuration. *LS* light source, *OD* optical detector, *ExF* excitation filter, *EmF* emission filter, *DM* dichroic mirror, *L* lens, *FM* position of fluorochrome molecules, *LSP* light-source pinhole, *DP* detector pinhole. Note that the emission light coming from out-of-focus fluorochrome molecules is blocked away by the detector pinhole

a wide-field configuration. Emission light from molecules that are out of focus is typically not wanted in fluorescence measurements, because it serves as a background signal that reduces the measurement quality. To eliminate this background, another type of configuration, termed the confocal configuration [1, 2], is used. Figure 3 provides the schematic concept of a confocal configuration.

In a confocal configuration, a pair of pinholes is positioned near the optical filter set: one pinhole (called a light-source pinhole) is located prior to the excitation filter, while another pinhole (called a detector pinhole) is located after the emission filter. Their positions are arranged such that the lens images the light-source pinhole into a single point in the object plane, and this point in the object plane is imaged, again by the



**Fluorescence Measurements, Fig. 4** The schematic concept of TIRF. *FM* fluorochrome molecules. Note that only fluorochrome molecules that reside very close to the

solid-fluid interface is illuminated by the excitation light and generates the emission light; the other fluorochrome molecules are not involved in the measurement

same lens, exactly into the detector pinhole. Using this configuration, the light-source pinhole ensures that a smaller volume in the object plane is illuminated by the excitation light; thus spatial resolution in excitation is improved compared to the wide-field configuration. Moreover, the detector pinhole ensures that emission light generated by fluorochrome molecules that are out of focus is eliminated; hence background fluorescence signals are removed from the measurements. There is a trade-off, however, between the advantages described above and the longer time required in measurements with a confocal configuration [1, 2]. Because a smaller excitation volume is obtained in a confocal configuration, the excitation volume needs to be scanned through the whole object; in case of measurements in microfluidic and nanofluidic channels, this means scanning along the depth, length, and width of the channels. Multiple pinholes can then be used to reduce the scanning time, where the pinholes perform fluorescence measurements on several excitation volumes simultaneously.

Compared to macroscale fluidic channels, the surface-to-volume ratio in microfluidic and nanofluidic channels is significantly larger, and consequently the physical effects caused by channel surfaces become more prominent. Therefore, it also becomes increasingly important to understand microfluidic and nanofluidic phenomena at these surfaces. A particular fluorescence

microscope setup that is suitable for this kind of measurements is the so-called TIRF (total internal reflection fluorescence) setup. Figure 4 illustrates the concept of TIRF.

In a TIRF microscopy setup, the fluorochrome molecules reside near a solid-fluid interface. The excitation light is illuminating the fluorochrome molecules from a steep angle, coming from the solid side toward the fluid medium. When this angle is larger than a certain critical angle  $\theta_c$ , then almost all of the excitation light is reflected back from the solid-fluid interface toward the solid side. This critical angle is expressed as

$$\theta_c = \sin^{-1}\left(\frac{n_f}{n_s}\right), \quad (4)$$

with  $n_f$  as the refractive index at the fluid medium and  $n_s$  the refractive index at the solid side. Hence only a very small amount of the excitation light goes through the solid-fluid interface. This small amount of excitation light, termed as evanescent wave, decays rapidly as it travels away from the solid-fluid interface toward the fluid medium. In effect, the excitation light only illuminates a very thin region in the fluid medium, with depth of only tens of nanometers, near the solid-fluid interface. Consequently, only fluorochrome molecules very near to the solid-fluid interface are excited and fluorescence measurements can be performed in detail on the surface.

### Flow Visualization

To be able to design devices based on microfluidics and nanofluidics, it is crucial to quantitatively visualize the flow of fluids in the microfluidic and nanofluidic channels. There have been many flow visualization methods being developed for macro-scale fluid flow (e.g., hot-wire anemometry), but most of them are not suitable for micro- and nano-scale measurements because they are too intrusive for micro- and nanoscale fluid flows [3]. Fluorescence measurements are very suitable for quantitatively visualizing flow in micro- and nanoscales, because it is nonintrusive and it allows for measurements with a high spatial resolution.

Fluorescence-based flow visualization methods can be categorized into two types: particle-based methods and scalar-based methods [3]. In particle-based methods, the fluid motion is deduced from the observed motion of fluorescence particles embedded in the fluid. The fluorescence particles are typically formed as microspheres, where fluorochrome molecules coat each sphere (see, e.g., the FluoSpheres from Invitrogen, CA, USA). To infer the fluid flow, the motion of the fluorescence particles must be processed and analyzed. When a CCD camera is used in the setup, the image sequence capturing the particles motion can be processed and analyzed digitally in a computer. Several analysis methods are available: the most popular is the so-called Micro-PIV (microscale particle image velocimetry). This method analyzes patterns of particle ensembles and infers the fluid motion by performing correlation analysis between the recorded patterns. Micro-PIV is derived from its macroscale counterpart, PIV. Another particle-based method that can be used is PTV (particle tracking velocimetry), in which individual particles are tracked and the path lines of the individual particles are analyzed to infer the fluid flow.

In scalar-based methods, the velocity of a conserved scalar is being observed and analyzed to infer the fluid flow. The fluorescence signals themselves can be used as the scalar by preparing a fluid solution containing the fluorochrome molecules. Due to the typically short

fluorescence lifetime of fluorochrome molecules, however, it is difficult to visualize the fluid motion using only fluorescence; as soon as the excitation light is terminated, no emission light is generated anymore. Therefore, a modification to this method is needed.

The first type of modification is performed by inducing photobleaching on the fluorochrome molecules. Prior to the measurement, the whole fluidic channel is illuminated and all the fluorochrome molecules generate emission light. Exactly at the beginning of the measurement, another excitation light with much higher intensity illuminates a certain region of the fluidic channel for a very short time. To shape this certain region, for example, in a straight line across the channel width, a line-shaped aperture is positioned before the excitation filter. This extra excitation induces photobleaching but only to fluorochrome molecules that are located within the straight light. Hence the motion of the photobleached region can be analyzed to infer the fluid flow. The main disadvantage of this method is that it needs an extra light source for inducing the photobleaching.

The second type of modification is done by using the so-called caged-fluorescent dyes. The caged-fluorescent dyes are fluorochrome molecules that have been modified chemically so that they become nonfluorescent. When a certain light (normally ultraviolet light) is exposed to the caged-fluorescent dyes, however, the chemical modification is reversed and the original fluorochrome molecules become fluorescent again. Prior to the measurement, the caged-fluorescent dyes fill the fluidic channels. Exactly when the measurement starts, the ultraviolet light illuminates a certain region of the fluidic channel (e.g., in a shape of a line, as in the photobleaching method described above). Therefore, only caged-fluorescent dyes located within that certain region is transformed back into the original fluorochrome molecules, and the molecules' motion can be studied to deduce the fluid flow. As in the photobleaching method, this method also requires an extra light source to perform measurements.

### Single-Molecule Detection

As we go from microfluidics to nanofluidics and the sizes of tracer particles are more and more reduced to the limit of a single-molecule of fluorochromes, the distinction between the scalar-based and particle-based methods becomes obsolete [3, 4]. In turn, the small dimensions of the microfluidic and nanofluidic channels also allow for increased sensitivity in the fluorescence detections: the background signal (caused by sample impurities and scattered photons) scales linearly with the size of the detection volume, while the fluorescence signal of each fluorochrome single-molecule is independent of the detection volume.

One of the most important applications of the single-molecule fluorescence detection in microfluidics and nanofluidics is the investigation on individual DNA (deoxyribonucleic acid) molecules [4]. DNA molecules are usually tagged using the so-called intercalating cyanine dyes. These fluorochrome molecules, popularly known as TOTO and YOYO, are virtually nonfluorescent in solution but form highly fluorescent complexes with DNA molecules, with >1,000-fold fluorescence enhancement [5]. The fluorescence signal of the DNA-dye complexes has been shown as insensitive to DNA base composition, and the fluorescence intensity is linearly proportional to the DNA length, which allows for fluorescence-based sizing of the DNA molecules. When tagged using these dyes, the motion of DNA molecules inside microfluidic and nanofluidic channels can be imaged and studied in detail.

### Key Research Findings

Fluorescence measurements are very useful in general because of its sensitivity and specificity to the investigated physical, biological, or chemical process. Moreover, the fluorescently visualized process can be imaged in detail and analyzed further using various image processing and analysis techniques. This advantage, along with the high spatial measurement capabilities allowed by optical microscopy, is highly crucial for

investigations in very small scale such as in microfluidics and nanofluidics.

Fluorochrome molecules are usually characterized using their quantum yield and fluorescence lifetime. Quantum efficiency is a measure of the efficiency of the fluorochrome molecules, which is expressed as the ratio between the number of photons emitted and the number of photons absorbed. In general, fluorochrome molecules with higher quantum efficiency are preferred. Meanwhile, the fluorescence lifetime is defined as the time in which the fluorescence intensity from a fluorochrome molecule decays to  $1/e$  of the initial intensity, after a pulse excitation is introduced. This parameter is related to the speed and the temporal resolution that can be achieved during fluorescence measurements.

For fluorescence measurements in very small scales, such as the investigations performed in microfluidics and nanofluidics, an optical microscope is necessary. Among the most important elements of the setup are the set of optical filters, which separate the excitation light from the emission light. When both the excitation light path and the emission light path use the same lens near the fluorochrome molecules, the setup is termed as an epi-fluorescence microscopy setup.

Depth of focus is defined as a range of space in which the fluorochrome molecules can still be imaged clearly even though they are not exactly in focus. This parameter is important in microfluidics and nanofluidics, as it influences the spatial resolution of the measurement. Emission light from fluorochrome molecules that are out of focus is typically not wanted in fluorescence measurements, because it serves as a background signal that reduces the measurement quality. To eliminate this background, the confocal configuration can be used. Meanwhile, to perform detailed fluorescence measurements on surfaces, the so-called TIRF (total internal reflection fluorescence) microscopy setup is usually used.

The main application of fluorescence measurements in microfluidics and nanofluidics is for quantitatively visualizing fluid flow. Two particle-based methods are commonly used: PIV, which uses the pattern of particles motion

to induce the fluid motion, and PTV, which tracks individual particles to achieve the same objective. Alternatively, scalar-based methods can also be used, where the fluorescence signal itself serves as the observed scalar. Due to the typically short fluorescence lifetime of fluorochrome molecules, however, it is difficult to visualize the fluid motion using only fluorescence. Hence modifications are required, for example, by inducing photobleaching and by using caged-fluorescent dyes.

As we go from microfluidics to nanofluidics, the distinction between the scalar-based and particle-based methods becomes obsolete, and in turn, the small dimensions of the microfluidic and nanofluidic channels also allow for increased sensitivity in the fluorescence detections. This, along with the invention of intercalating cyanine dyes, spurs other major applications of fluorescence measurements in microfluidics and nanofluidics: the investigation on individual DNA molecules.

### Future Directions for Research

Fluorescence measurements are very important in studies on microfluidics and nanofluidics, with main applications on flow visualization and single-molecule detection. To achieve measurements with higher spatial resolution, which becomes more significant with the rapid development of nanofluidics, research efforts should be focused on developing more advanced fluorescence microscopy setups. The particularly useful setups will be the ones that can break the classic optical diffraction limit.

### Cross-References

- ▶ [Confocal Microscopy, Detection](#)
- ▶ [Evanescent Wave](#)
- ▶ [Evanescent Wave Microscopy](#)
- ▶ [Fluorescent Labeling](#)
- ▶ [Fluorescent Thermometry](#)
- ▶ [Micro-PIV-Based Diffusometry](#)
- ▶ [Microscale Flow Visualization](#)

- ▶ [Surface Plasmon Resonance Sensors](#)
- ▶ [Visualization Based on Molecular Tagging Methods](#)

### References

1. Murphy DB (2001) *Fundamentals of light microscopy and electronic imaging*. Wiley-Liss, New York
2. Pawley JB (2006) *Handbook of biological confocal microscopy*. Springer, Berlin
3. Sinton D (2004) *Microscale flow visualization*. *Microfluid Nanofluid* 1(1):2–21
4. Dittrich PS, Manz A (2005) Single-molecule fluorescence detection in microfluidic channels—the Holy Grail in  $\mu$ TAS? *Anal Bioanal Chem* 382(8):1771–1782
5. Rye HS, Yue S, Wemmer DE, Quessada MA, Haugland RP, Mathies RA, Glazer AN (1992) Stable fluorescent complexes of double-stranded DNA with bis-intercalating asymmetric cyanine dyes: properties and applications. *Nucleic Acids Res* 20(11):2803–2812

---

### Fluorescence Resonance Energy Transfer (FRET)

Miao Wu and W. Russ Algar  
Department of Chemistry, University of British Columbia, Vancouver, BC, Canada

### Synonyms

Electronic energy transfer (EET); Förster resonance energy transfer (FRET)

### Definition

Fluorescence resonance energy transfer (FRET) is a non-radiative, through-space excitation energy transfer process. The electronic excitation energy of a donor molecule is transferred to a ground-state acceptor through dipole–dipole interactions without involvement of a photon or molecular contact. Efficient FRET requires close proximity and suitable alignment between the transition dipoles of the donor and acceptor, as well as overlap between the donor emission spectrum and acceptor absorption spectrum.

## Overview

FRET was first elucidated by Theodor Förster between 1946 and 1948 [1]. Many researchers, including the International Union of Pure and Applied Chemistry (IUPAC), recognize FRET as *Förster resonance energy transfer* rather than *fluorescence resonance energy transfer*. The tribute to Förster notwithstanding, it is argued that the “fluorescence” terminology is incorrect because no photon is emitted during the energy transfer process. However, there is some value to the *fluorescence resonance energy transfer* terminology, which can be used to distinguish between energy transfer from optically excited donors and energy transfer from excited-state donors formed as the products of chemical or enzyme-catalyzed reactions. The latter two processes also follow the mechanism elucidated by Förster and are commonly referred to as *chemiluminescence resonance energy transfer* (CRET) and *bioluminescence resonance energy transfer* (BRET), respectively. In practice, both the “Förster” and “fluorescence” terminology are widely accepted expansions of the FRET acronym. Despite Förster’s breakthrough in the mid-twentieth century, it was not until the 1990s that improvements in fluorescence instrumentation and the availability of fluorescent materials made it possible for the full potential of FRET to be realized [2]. Currently, FRET is one of the most powerful and widely utilized fluorescence techniques, with numerous applications in biology, biochemistry, biophysics, and bioanalysis.

Physically, the FRET process is summarized in Eq. 1, where  $D$  represents the donor fluorophore,  $A$  represents the acceptor chromophore, and  $*$  indicates an excited electronic state.



The rate of energy transfer between the donor and acceptor,  $k_{\text{FRET}}$ , is given by Eq. 2, where  $\tau_{\text{D}}$  is the inverse decay rate of the donor,  $\tau_{\text{D}}^{-1} = k_0 = k_{\text{r}} + k_{\text{nr}}$  (the sum of the radiative,  $k_{\text{r}}$ , and non-radiative decay rates,  $k_{\text{nr}}$ ),  $R_0$  is the Förster distance, and  $r$  is the distance separating the donor and acceptor. The Förster distance is

the separation at which  $k_{\text{FRET}} = k_0$ . A Jablonski diagram for FRET is shown in Fig. 1a.

$$k_{\text{FRET}} = \frac{1}{\tau_{\text{D}}} \left( \frac{R_0}{r} \right)^6 \quad (2)$$

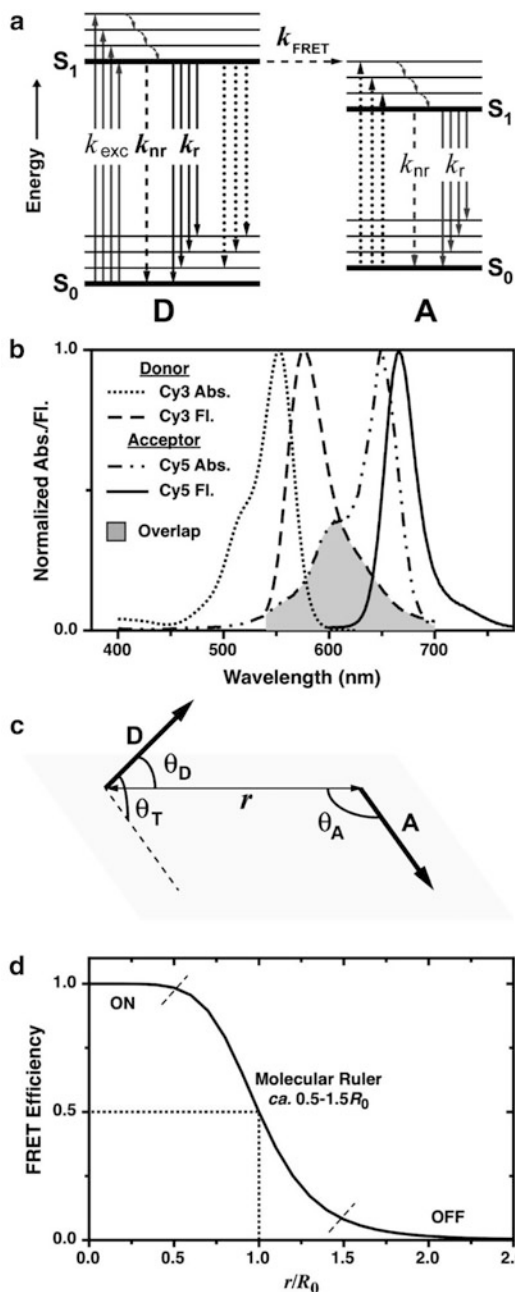
Equation 2 appears simple because the details of the FRET interaction are contained within the Förster distance ( $R_0$ ) parameter, Eq. 3, where  $\Phi_{\text{D}}$  is the quantum yield of the donor,  $\kappa^2$  is the orientation factor,  $J(\lambda)$  is the spectral overlap integral,  $N_{\text{A}}$  is Avogadro’s number, and  $n$  is the refractive index of the medium between the donor and acceptor [3].

$$\begin{aligned} R_0^6 &= \frac{9(\ln 10)\Phi_{\text{D}}\kappa^2 J(\lambda)}{128\pi^5 N_{\text{A}} n^4} \\ &= (8.79 \times 10^{-28} \text{ mol}) n^{-4} \Phi_{\text{D}} \kappa^2 J(\lambda) \end{aligned} \quad (3)$$

The spectral overlap integral, Eq. 4, measures the degree of resonance between the donor and acceptor, where  $F_{\text{D}}(\lambda)$  is the donor emission spectrum and  $\varepsilon(\lambda)$  is the wavelength-dependent molar absorption coefficient of the acceptor. For the numerical constant in Eq. 3, the wavelength,  $\lambda$ , and  $\varepsilon(\lambda)$  should be in units of cm and  $\text{mol}^{-1} \text{ cm}^2$  ( $= 10^3 \text{ M}^{-1} \text{ cm}^{-1}$ ), respectively. An example of spectral overlap is illustrated in Fig. 1b for a Cy3–Cy5 FRET pair.

$$J(\lambda) = \frac{\int F_{\text{D}}(\lambda)\varepsilon_{\text{A}}(\lambda)\lambda^4 d\lambda}{\int F_{\text{D}}(\lambda) d\lambda} \quad (4)$$

The orientation factor determines, in part, the strength of the coupling between the donor and acceptor transition dipole moments and is a function of their relative alignment. The interaction is strongest for collinear dipoles ( $\kappa^2 = 4$ ) and weakest for perpendicular dipoles ( $\kappa^2 = 0$ ), where  $0 \leq \kappa^2 \leq 4$ . The orientation factor is calculated via Eq. 5, where  $\theta_{\text{T}}$  is the angle between the donor emission and acceptor absorption transition dipoles, and  $\theta_{\text{D}}$  and  $\theta_{\text{A}}$  are the angles the donor and acceptor dipoles make to the vector connecting them. These angles are



**Fluorescence Resonance Energy Transfer (FRET), Fig. 1** (a) Jablonski diagram illustrating FRET and related processes, including excitation of the donor, radiative (solid line) and non-radiative (dashed lines) relaxation on the donor and acceptor, vibrational relaxation (short curved arrows) and transitions associated with FRET (dotted lines). Processes that determine the FRET efficiency are indicated in bold. (b) Illustration of spectral overlap between Cy3 (donor) emission and Cy5 (acceptor) absorption. (c) Definition of the angles used to calculate

illustrated in Fig. 1c. In the case of a dynamic isotropic distribution of donor and acceptor orientations (i.e., random rotation), the orientation factor takes on a value of  $\kappa^2 = 2/3$ ; in the case of a static isotropic distribution of orientations,  $\kappa^2 = 0.476$ .

$$\kappa^2 = (\cos \theta_T - 3 \cos \theta_D \cos \theta_A)^2 \quad (5)$$

The FRET efficiency,  $E$ , is given by Eq. 6 and is the ratio of the rate of FRET to all processes that depopulate the donor excited state [3]. From Eq. 2, the FRET efficiency reduces to a function of the Förster distance,  $R_0$ , and donor–acceptor separation,  $r$ . The relative distance dependence of FRET,  $E$  vs.  $r/R_0$ , is illustrated in Fig. 1d. At donor–acceptor separations equal to the Förster distance,  $r = R_0$ , the energy transfer efficiency is  $E = 50\%$ . It can also be seen that, for  $0.5R_0 < r < 1.5R_0$ , the FRET efficiency is very sensitive to the donor–acceptor separation and can serve as a spectroscopic “molecular ruler” to accurately measure distances at the biomolecular length scale.

$$E = \frac{k_{FRET}}{k_r + k_{nr} + k_{FRET}} = \frac{R_0^6}{r^6 + R_0^6} \quad (6)$$

### Basic Methodology

#### Measuring FRET Efficiencies

The most common method of measuring FRET efficiency is through either quenching of the donor emission intensity or a decrease in its fluorescence lifetime, Eq. 7 [3]. The relevant terms include  $F$ , the fluorescence intensity, and  $\tau$ , the fluorescence lifetime, where the subscript D denotes a quantity measured for donor alone and the subscript DA denotes a donor quantity measured in the presence of acceptor. When the donor exhibits a multi-exponential fluorescence

**Fluorescence Resonance Energy Transfer (FRET), Fig. 1** (continued) the orientation factor from the relative alignment of the donor and acceptor transition dipoles. (d) FRET efficiency as a function of the relative distance between the donor and acceptor

lifetime, the amplitude weighted lifetime should be used to calculate the FRET efficiency. Figure 2 shows model composite fluorescence spectra for a Cy3–Cy5 FRET pair with different energy transfer efficiencies, illustrating the quenching of Cy3 donor fluorescence and a decrease in its fluorescence lifetime.

$$E = 1 - \frac{F_{DA}}{F_D} = 1 - \frac{\tau_{DA}}{\tau_D} \quad (7)$$

When the acceptor is fluorescent, the FRET efficiency can also be measured from the combination of the FRET-quenched donor emission and FRET-sensitized acceptor emission, Eq. 8. The subscript AD denotes an acceptor quantity measured in the presence of donor, and  $\Phi$  is a quantum yield.

$$E = \frac{(F_{AD} - F_A)}{(\Phi_A/\Phi_D)F_{DA} + (F_{AD} - F_A)} \quad (8)$$

Equation 8 is advantageous in that it does not require a donor-only reference state and is ratiometric, providing greater reliability when donor/acceptor concentration cannot be easily controlled. The drawbacks to Eq. 8 are the need for reliable estimates of the donor and acceptor quantum yields and the necessity of correcting  $F_{AD}$  for any directly excited acceptor fluorescence,  $F_A$  (measured in the absence of donor). The fluorescence intensities in Eq. 8 must be integrated over the full donor and acceptor emission spectra (or corrected accordingly), whereas the donor fluorescence measurements in Eq. 7 can be made at a single wavelength or across a narrow band of wavelengths. Figure 2 also shows FRET sensitization of Cy5 fluorescence in the Cy3–Cy5 FRET pair.

Another method of calculating the FRET efficiency is via the change in the fluorescence intensity of the acceptor. This method is based on Eq. 9, where  $\varepsilon_D(\lambda_{exc})$  and  $\varepsilon_A(\lambda_{exc})$  are the donor and acceptor molar absorption coefficients at the excitation wavelength. A large variety of other mathematical formulas have been developed to calculate FRET efficiency in many different

experimental formats. Many of these formulas are adaptations of Eqs. 7, 8, and 9.

$$E = \frac{\varepsilon_A(\lambda_{exc})}{\varepsilon_D(\lambda_{exc})} \left( \frac{F_{AD} - F_A}{F_A} \right) \quad (9)$$

It should be noted that quantitative measurements of FRET efficiency are primarily useful for distance measurements; however, there are many experiments in which distance information is not the main objective, e.g., binding isotherms. In such cases, the transition from  $E_{min}$  to  $E_{max}$  (or vice versa) can provide important qualitative and quantitative information. Changes in acceptor fluorescence intensity, donor fluorescence intensity, or the ratio between the two ( $F_{AD}/F_{DA}$ ) can be used similarly, without formal calculation of FRET efficiency, when distance information is not the objective. Specific examples where quantitative measurement of FRET efficiency is both important and unimportant are provided later in this entry.

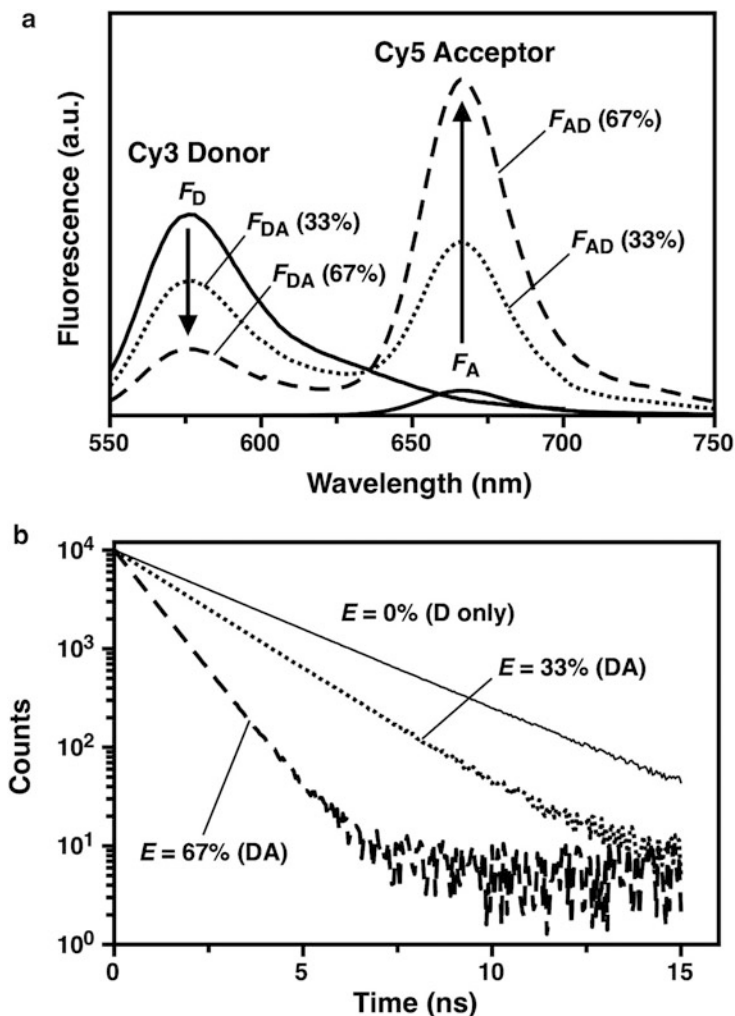
### Selection of FRET Pairs

Many different combinations of fluorophores can be used as a FRET pair. Table 1 lists a few popular examples but these serve only as a starting point. Online tools are available to assist in fluorophore selection on the basis of excitation and emission spectra and help researchers evaluate spectral overlap, select a suitable excitation wavelength, and estimate donor–acceptor emission crosstalk in the context of specific optical filter sets. Selection of an acceptor with a large Stokes shift can help reduce crosstalk between measurements of donor and acceptor fluorescence. Popular online spectral databases include those offered by the University of Arizona and many commercial vendors of fluorescent dyes (e.g., BD Biosciences, BioLegend, eBioscience, Life Technologies). Caution should be exercised when evaluating spectral overlap from normalized spectra, which do not account for differences in quantum yield or molar absorption coefficient between candidate donors and acceptors. Most Förster distances are in the range of 2.0–7.0 nm.

In many microfluidic applications, a fluorescent acceptor is preferable to a dark quencher (i.e., a nonfluorescent acceptor). The potential

**Fluorescence Resonance Energy Transfer (FRET), Fig. 2**

Model data for the change in the emission spectra for a Cy3 donor paired with a Cy5 acceptor (1:1 ratio) at different FRET efficiencies (0 %, 33 %, 67 %). Note the small direct excitation of Cy5 in the absence of FRET. Increases in FRET efficiency are reflected by progressive quenching of the Cy3 fluorescence and sensitization of Cy5 fluorescence. The model data is for excitation at 520 nm, where  $\epsilon_{520, \text{Cy3}} = 79,500 \text{ M}^{-1} \text{ cm}^{-1}$  ( $\epsilon_{\text{max, Cy3}} = 150,000 \text{ M}^{-1} \text{ cm}^{-1}$ ),  $\Phi_{\text{Cy3}} = 0.15$ ,  $\epsilon_{520, \text{Cy5}} = 7,500 \text{ M}^{-1} \text{ cm}^{-1}$  ( $\epsilon_{\text{max, Cy5}} = 250,000 \text{ M}^{-1} \text{ cm}^{-1}$ ), and  $\Phi_{\text{Cy5}} = 0.28$ . (b) Model data for the change in Cy3 donor lifetime with increasing FRET efficiency. In this example,  $T_0 = 2.7 \text{ ns}$  and is a monoexponential decay



**Fluorescence Resonance Energy Transfer (FRET), Table 1** Approximate Förster distances for three common FRET pairs

FRET pair	$R_0$ (nm)
Fluorescein–tetramethylrhodamine	5.0–5.5
Cyan fluorescent protein (CFP)–yellow fluorescent protein (YFP)	~5.0
Cy3–Cy5	5.0–6.0

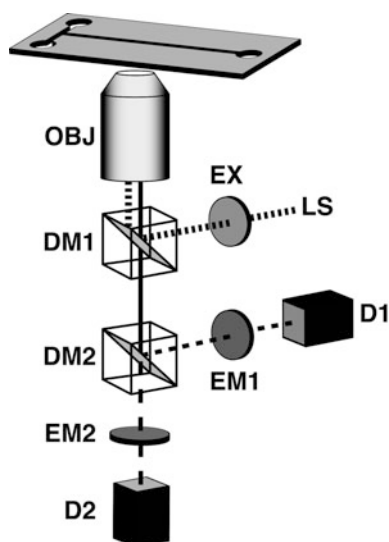
disadvantage of a dark quencher is the challenge of distinguishing between loss of donor fluorescence due to FRET and loss of donor fluorescence due to dilution and/or other non-FRET mechanisms. Observation of FRET-sensitized acceptor fluorescence, or changes in the acceptor/donor

fluorescence ratio, can be more reliable. Dark quenchers also tend to have lower molar absorption coefficients (and thus smaller spectral overlap integrals) than fluorescent dye acceptors. Nonetheless, a potential advantage of dark quenchers is more facile multiplexed FRET, that is, the parallel observation of multiple spectrally distinct FRET pairs. For example, for two FRET pairs with dark quencher acceptors,  $D_1-Q_1$  and  $D_2-Q_2$ , the emission crosstalk between  $D_1$  and  $D_2$  can be quite small; however, for two FRET pairs with fluorescent acceptors,  $D_1-A_1$  and  $D_2-A_2$ , the emission crosstalk can be extensive, particularly between  $A_1$  and  $D_2$ . Both fluorescent acceptors and dark quenchers have been successfully used in microfluidic FRET experiments.

## Instrumentation for Microfluidic FRET Experiments

Commercial or home-built fluorescence microscopes are the most commonly utilized instruments for measuring FRET in microfluidic applications. An objective lens is used to focus excitation light onto a region of interest along the channel and collect fluorescence from that same region. Common excitation sources include lasers, which can help maximize sensitivity by virtue of their high-intensity monochromatic radiation; high-power light-emitting diodes (LEDs); and arc lamps, which provide the greatest flexibility in wavelength selection. The excitation wavelength should be chosen to provide efficient excitation of the donor with minimal direct excitation of a fluorescent acceptor (when applicable). Band-pass excitation filters are used to select a narrow band of excitation wavelengths from polychromatic sources and cleanup laser lines. With arc lamp and LED sources, both the center position and bandwidth of the excitation filter determine the level of direct excitation of the acceptor.

Fluorescence emission collected by the objective lens is separated from the excitation light using a dichroic mirror. The dichroic mirror passes wavelengths of light longer than a certain threshold and reflects wavelengths of light shorter than this threshold. The threshold is selected based on the donor emission. If a fluorescent acceptor is paired with the donor, a second dichroic mirror is used to split the fluorescence into donor and acceptor channels. The reflected and transmitted light from the second dichroic mirror is directed through band-pass emission filters to photodetectors. The band-pass filters should be optimized to transmit either donor or acceptor fluorescence with minimal crosstalk. Due to the red-tailed emission of fluorescent dyes, there is often a compromise between choosing the spectral position and bandwidth of the acceptor emission filter for maximum fluorescence signal and shifting or narrowing the bandwidth for minimum crosstalk. Common detectors include photomultiplier tubes (PMTs), avalanche photodiodes (APDs), and charge-coupled device (CCD) or scientific-grade



**Fluorescence Resonance Energy Transfer (FRET), Fig. 3** Basic setup for microfluidic FRET measurements. *OBJ* objective lens, *DM* dichroic mirror, *LS* light source, *EX* excitation filter, *EM* emission filter, *D* photodetector

complementary metal-oxide semiconductor (sCMOS) cameras for imaging. A generic setup for a FRET experiment is illustrated in Fig. 3. Confocality can be implemented by inserting a pinhole in front of the detector(s) to eliminate out-of-focus light, i.e., fluorescence that does not originate from the plane of the microfluidic channel. A confocal design generally provides a superior signal-to-background ratio and better image resolution, but is not a necessity.

An important consideration for measuring dynamic processes via FRET is the acquisition time for fluorescence measurements, which must be shorter than the time scale of the process of interest. Dynamic processes that occur over time scales faster than minutes generally preclude the use of slower measurement techniques such as fluorescence lifetime imaging microscopy (FLIM) or methods based on photobleaching. The latter include determination of FRET efficiencies from changes in bleaching kinetics or the use of bleaching to generate donor-only or acceptor-only reference states in situ. However, an important advantage of microfluidic methods is that dynamic processes can be measured as a function of position along a length of channel

where reagents mix and react. Since this property tends to create standing patterns of fluorescence, snapshots of fast processes (milliseconds to seconds) can be obtained without being limited by acquisition times, potentiating the use of a slower measurement technique such as FLIM (assuming the residence time in the detection volume is much longer than the fluorescence lifetime). Photobleaching methods, however, require continuous excitation of static fluorophores and are not compatible with the transport of dyes in microfluidic flow. Such methods could potentially be used with fluorophores immobilized or trapped within a microfluidic chip (e.g., solid-phase assays or staining of adherent cells).

## Key Research Findings

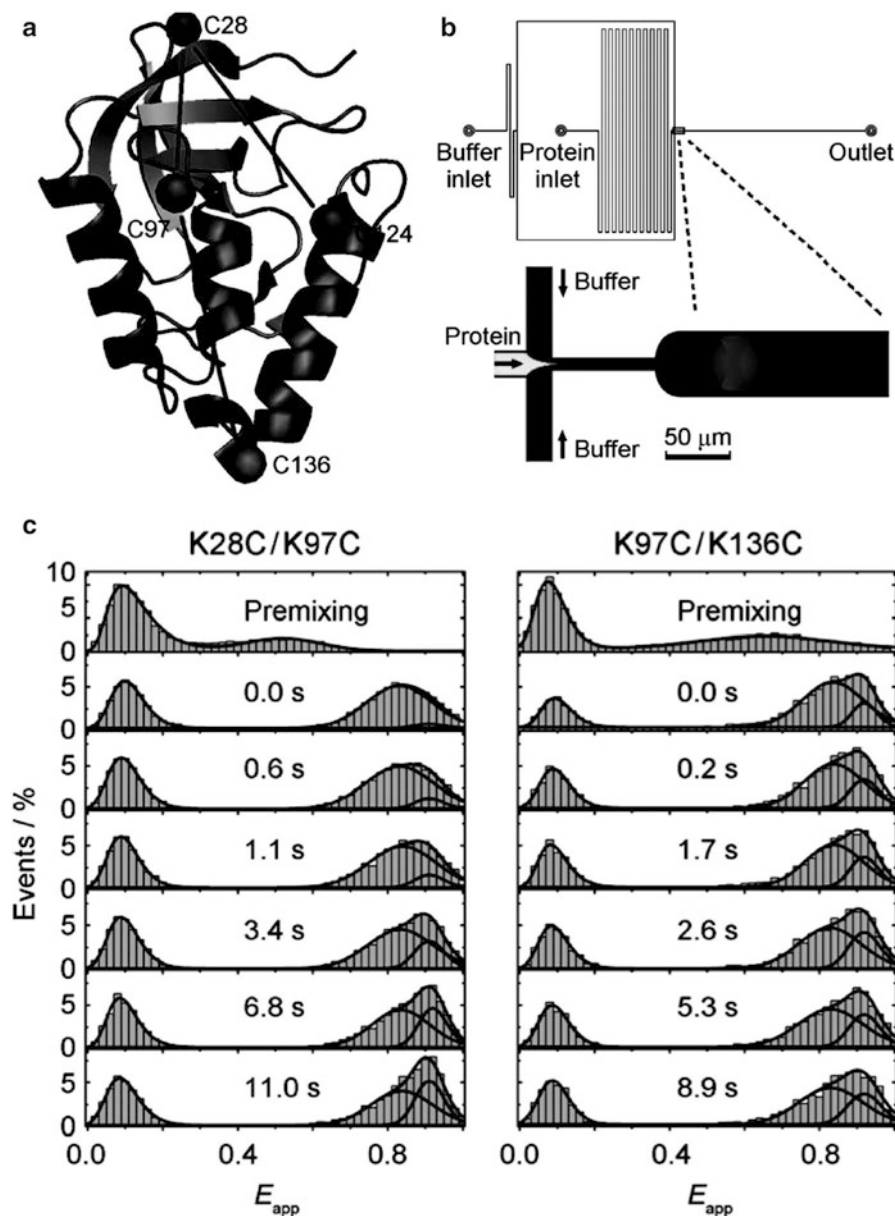
This section highlights representative examples of how microfluidics can add value to FRET experiments and vice versa.

### Protein Folding

FRET is one of the best known methods for studying protein folding. Protein dimensions and conformational changes are commensurate with the range of FRET, which can be used to study the equilibrium folding of ensembles of protein under different conditions or their folding dynamics at the level of single proteins. Microfluidic chips are advantageous for such experiments in that they can provide higher throughput, better control over solution conditions, and require smaller sample sizes. For example, single-pair FRET (spFRET; the analog of single-molecule fluorescence detection) and a microfluidic laminar-flow mixer have been used to measure the unfolded and folded subpopulations of staphylococcal nuclease (SNase) protein [4]. In this application of FRET, three mutants of SNase were expressed with cysteine residues at different sites (Fig. 4a), and these residues were labeled with Alexa Fluor 546 (AF546; donor) and Alexa Fluor 647 (AF647; acceptor) dyes. The positions of the cysteine residues were selected so that changes in the conformation of the  $\beta$ -sheet

domain,  $\alpha$ -helical domain, or the whole SNase protein would induce a change in FRET efficiency, depending on the mutant. For fluorescence detection, the microfluidic mixer (Fig. 4b) was mounted on a confocal microscope equipped with a 532 nm laser source and suitable dichroic and band-pass filters to isolate AF546 and AF647 fluorescence at two separate APDs. Protein was initially unfolded due to the presence of denaturant in the mixer and refolded in the detection channel as the denaturant was rapidly diluted with native buffer. This process was monitored via the detection of single proteins as they moved through the laser focus in the detection channel to generate FRET efficiency histograms (Fig. 4c) as a function of folding time. Two FRET efficiency distributions were observed, which corresponded to folded and unfolded states. The  $\alpha$ -helical domain of SNase folded faster (folding relaxation lifetime,  $0.6 \pm 0.2$  s) than the  $\beta$ -sheet domain ( $4.5 \pm 0.8$  s).

To study ensemble protein folding, a microfluidic chip can be designed to produce a linear concentration gradient of a denaturant such as sodium dodecyl sulfate (SDS) across 100 channels and a temperature gradient along each channel (Fig. 5a) [5]. FRET has been combined with such a chip to observe the folding states of  $\alpha$ -synuclein, an intrinsically disordered protein that is implicated in neurodegenerative disease. This protein is known to adopt an alpha helical structure upon binding to lipid membranes or SDS micelles. By labeling mutant cysteine residues on the protein with Alexa Fluor 488 (donor) and Alexa Fluor 594 (acceptor), the folded state of the protein was mapped, via FRET, as a function of SDS concentration (0–2.5 mM, 100 data points) and temperature (21–47 °C, 100 data points). The chip was imaged using an epifluorescence microscope equipped with an LED excitation source. The folding map (Fig. 5b) revealed four protein structural domains: (i) unstructured ( $E = 0.45$ ), (ii) a kinked structure with two helical domains ( $E = 0.9$ ), (iii) a fully extended helical structure ( $E \sim 0$ ), and (iv) a kinked-two-helix structure bound to SDS micelles. The high density of data points, which was enabled by the microfluidic



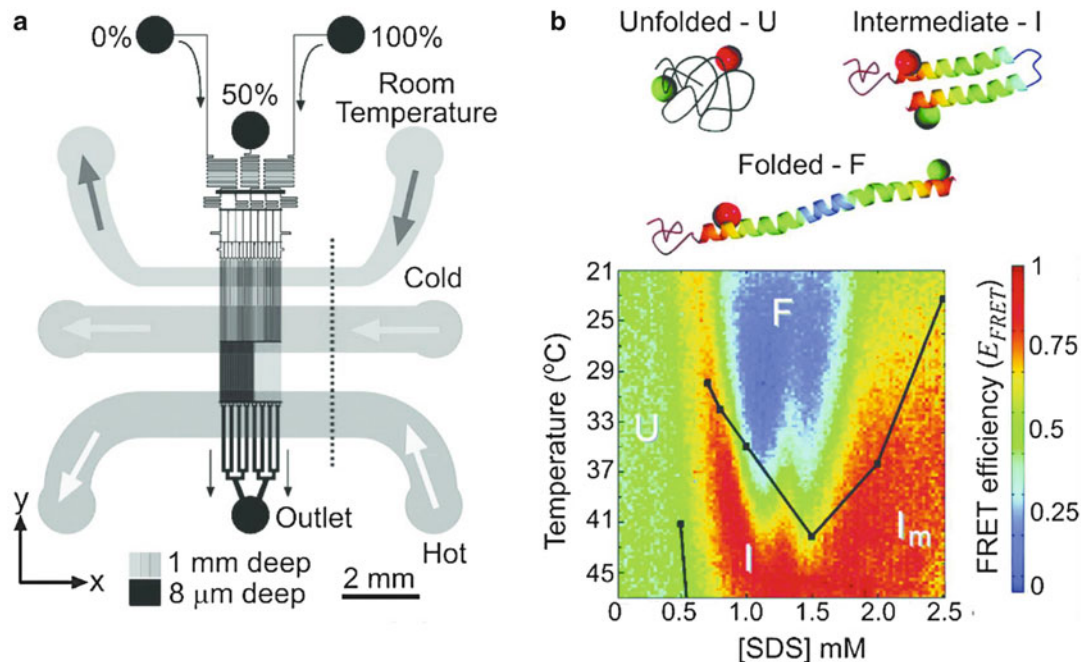
**Fluorescence Resonance Energy Transfer (FRET), Fig. 4** (a) Positions of cysteine residues used for donor/acceptor labeling on mutants of SNase. (b) Microfluidic chip used for mixing and spFRET detection. (c) FRET histogram for refolding of two of the SNase mutants

( $\beta$ -sheet folding, K28C/K97C;  $\alpha$ -helix folding, K97C/K136C) (Reprinted with permission from Zhi et al. [4]. Copyright 2011 Wiley-VCH Verlag GmbH & Co. KGaA, Weinheim)

format, revealed details previously unobserved in non-microfluidic experiments with fewer data points, including conditions where three conformational states and two assembly states (micelles vs. monomers) coexisted.

### Binding Kinetics

Another application of FRET is the measurement of binding kinetics. While FRET can provide an optical signal for binding, a microfluidic chip can provide fast, efficient mixing with spatially



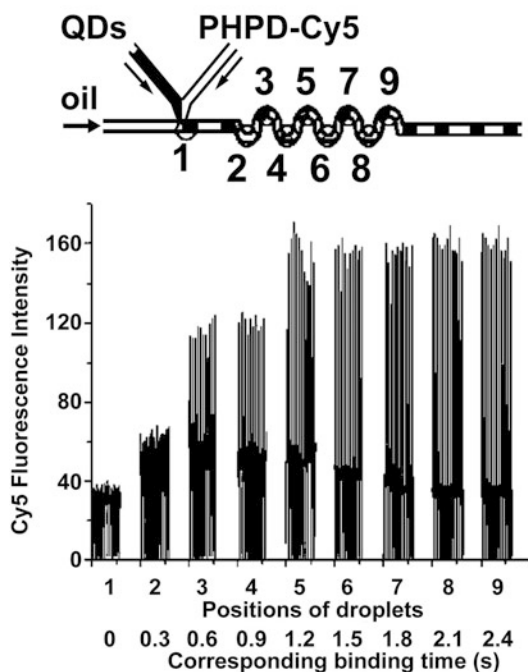
**Fluorescence Resonance Energy Transfer (FRET), Fig. 5** (a) Microfluidic chip for producing gradients of denaturant (SDS) and temperature. The percentage of the feed solution (100 % = 2.5 mM SDS) for dilution is indicated. (b) Folding map showing the conditions

where  $\alpha$ -synuclein is folded (*F*), unfolded (*U*), intermediate (*I*), and micelle associated (*I<sub>m</sub>*) (Reprinted with permission from Vandelinder et al. [5]. Copyright 2009 American Chemical Society)

resolved observation of the process. Droplet microfluidics is one such technology and has been combined with FRET to monitor the fast binding kinetics between a CdSe/ZnS core/shell quantum dot (QD) and a peptide appended with a dendritic tetra-hexahistidine motif [6]. Polyhistidine sequences spontaneously assemble to the ZnS shell, with equilibrium binding being reached within 100 s for a single hexahistidine sequence. When the peptide is labeled with a Cy5 dye (acceptor) at its opposite terminus, the association kinetics with the QD (donor) can be measured through the evolution of FRET using a standard fluorometer. However, the assembly kinetics of the dendritic tetra-hexahistidine peptide are too rapid to monitor using this methodology. A microfluidic Y-junction provides the necessary temporal resolution (Fig. 6). Peptide and QD solution were combined into single droplets within an oil-filled microfluidic channel and traversed a serpentine mixing region where Cy5 fluorescence was measured at different points

along the channel length (1 mm increments correlating to 0.3 s of mixing time). The fluorescence was observed via an electron multiplying CCD (EMCCD) camera mounted on an inverted fluorescence microscope. The time to reach equilibrium binding was determined from the position where the FRET-sensitized Cy5 fluorescence saturated (Fig. 6). For the dendritic tetra-hexahistidine peptide, the binding time was 1.5 s, with half-maximum binding reached within 0.6 s. The equilibrium binding and half-maximum times for a single hexahistidine motif were >150 s and 48 s, respectively.

Continuous flow microfluidics can also be combined with FRET to measure binding kinetics, such as in the case of DNA polyplex assembly [7]. These complexes, which comprise cationic polymers and DNA, are prospective vectors for gene therapy. Binding must be stable enough to prevent premature dissociation, but must not be so stable as to preclude intracellular release of the gene. The challenge of understanding polyplex



**Fluorescence Resonance Energy Transfer (FRET), Fig. 6** Schematic of the microfluidic Y-junction and serpentine mixing region, indicating points along the channel where FRET-sensitized Cy5 fluorescence was measured. The corresponding fluorescence intensity is shown below for droplets flowing past each measurement point. PHPD-Cy5 is the dendritic tetra-hexahistidine peptide (Reprinted with permission from Wang et al. [6]. Copyright 2012 American Chemical Society)

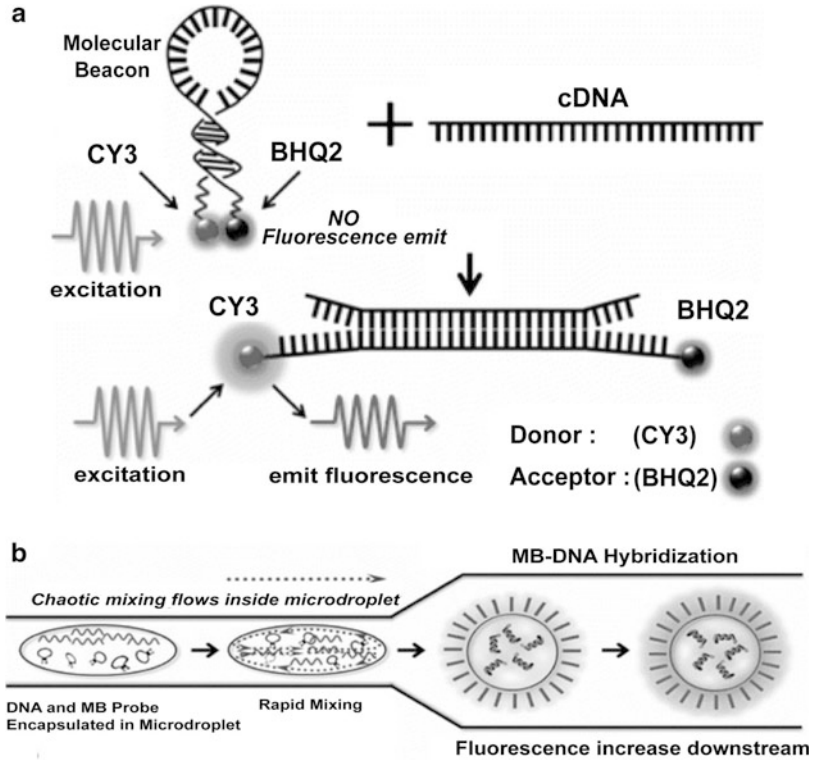
assembly has been addressed using a microfluidic T-junction with laminar flow to generate precisely controlled diffusive mixing between DNA conjugated with QDs (donor) and cationic chitosan polymer labeled with Cy5 (acceptor). The distribution of FRET-sensitized Cy5 fluorescence across the width and length of the channel provided information about the assembly process with millisecond time resolution. Assembly started immediately at the interface between the two solutions and occurred in two stages. In the first stage, the Cy5 fluorescence intensity was proportional to the square root of mixing time, indicating a diffusion controlled process. At approximately 625 ms, a flocculation stage began and was accompanied by a change in the diffusivity of the DNA that corresponded to 20-fold compaction in its size.

### Bioassays

The development of bioassays based on microfluidic devices, i.e., the lab-on-a-chip concept, is of tremendous interest. While much effort has been directed at interfacing microfluidic devices with, for example, mass spectrometers, a myriad of FRET methods have been developed for detecting a wide array of analytes. These FRET methods are suitable for integration with microfluidic devices for on-chip detection. For example, molecular beacon probes are a well-known FRET technology and have been combined with a microfluidic picoliter drop generator for the rapid detection of target DNA sequences [8]. Molecular beacons comprise a DNA hairpin (also called a stem-loop structure) labeled at opposite termini with donor and acceptor dyes (Fig. 7a). In the absence of target DNA complementary to the loop, the self-complementary stem region remains hybridized and maintains the donor and acceptor in close proximity for efficient FRET. Upon hybridization with target (cDNA), the stem opens and linear double-stranded DNA is formed, separating the donor and acceptor with loss of FRET. A molecular beacon complementary to a portion of the breast cancer-related BRCA1 gene was labeled with Cy3 (donor) and black hole quencher 2 (BHQ2, acceptor). A second molecular beacon complementary to the hepatitis C virus gene was labeled with fluorescein (donor) and black hole quencher 1 (acceptor). Using the microfluidic generator, target DNA and molecular beacons were encapsulated in 137 pL droplets and driven by pressure flow through a sawtooth-edge serpentine region of the microfluidic channel to generate rapid mixing via chaotic advection (Fig. 7b). Hybridization was complete within 10 s. BRCA1 could be detected at concentrations between 125 nM and 2  $\mu$ M with 2  $\mu$ M molecular beacon, or at concentrations as low as 500 fM with 2.5 nM molecular beacon [8]. The recovery of FRET-quenched fluorescence in the microfluidic channels was visualized using a cooled monochrome CCD camera with filter sets for Cy3 and fluorescein. The major advantages of the microfluidic FRET format were the small sample size and speed of analysis, which compared very

**Fluorescence Resonance Energy Transfer (FRET), Fig. 7**

(a) Molecular beacon (MB) concept. (b) Detection of target DNA in microdroplets (Reprinted with permission from Hsieh et al. [8]. Copyright 2009 the authors)



favorably with the hours of hybridization often needed with heterogeneous DNA assay formats (e.g., DNA microarray chips).

Heterogeneous FRET assays can also be integrated with microfluidic chips. A simple glass-polydimethylsiloxane (PDMS) microfluidic channel has been used to assemble and carry out solid-phase FRET-based DNA hybridization assays on-chip [9]. The glass substrate was modified with biotin prior to assembly of the PDMS channel. Streptavidin-modified QDs (donor) and biotinylated probe were injected into the channel in sequence to create a layer of bioselective interfacial chemistry. Sample containing Cy3 (acceptor)-labeled complementary target was then injected and rapidly hybridized with immobilized probe within the confines of the channel. As injection proceeded, probe sites along the channel length hybridized with target until all the local probe sites were saturated or all targets had been captured. Consequently, the length of channel along which FRET-sensitized Cy3 fluorescence was observed was

proportional to the amount of target injected. It was possible to detect 5 fmol of target DNA without a direct dependence on the measured fluorescence intensity. FRET was imaged off-line using an upright fluorescence microscope equipped with a 405 nm laser source, which raster scanned the microfluidic chip to detect fluorescence with a PMT and appropriate filters for the QD and Cy3.

**Cellular Analysis**

In addition to bioassays, FRET-based probes are widely used for cellular analysis, which is a rapidly expanding area of interest in microfluidics. A microfluidic device has been designed to produce stepwise gradients of an apoptosis-inducing anticancer drug, etoposide, in microchambers seeded with cultured HeLa cells [10]. The cells expressed a fusion protein with cyan fluorescent protein (CFP; donor) attached to yellow fluorescent protein (YFP; acceptor) through a peptide linker containing the Asp-Glu-Val-Asp (DEVD) sequence

recognized and cleaved by caspase-3. This protease is a key effector of apoptosis and its activity could be observed via the fluorescence intensity ratio of the CFP and YFP. Initially, in the protein fusion, there was efficient FRET between the CFP and YFP. When apoptosis was induced, hydrolysis of the peptide linker by caspase-3 separated the CFP and YFP, resulting in the loss of FRET. Cells were imaged in the microfluidic chip every 12 h over 2 days, and the YFP/CFP fluorescence ratio decreased (up to 80 %) over time and as the concentration of etoposide increased. The microfluidic device was advantageous in that it required smaller quantities of both etoposide and cells and quickly generated a concentration gradient of the former. Intracellular FRET provided a faster response than the conventional assay format, and use of an epifluorescence microscope platform provided high-sensitivity, real-time detection of apoptosis via imaging of individual cells. Band-pass filters were used to isolate CFP and YFP fluorescence. No explicit corrections were made for crosstalk and the FRET efficiency was not calculated.

In another example of cellular analysis, a microfluidic chip was designed for the integrated analysis of micro RNA (miRNA) expression in single cells, including cell capture, cell lysis, reverse transcription, and real-time quantitative polymerase chain reaction (RT-qPCR) [11]. The chip was capable of running 300 RT-qPCR reactions in parallel, including an optically multiplexed analysis of two genes in parallel. TaqMan probes, a commercialized FRET-based technology, were used to follow the RT-qPCR amplification. The microfluidic format ameliorated the high reagent cost and low throughput associated with traditional RT-qPCR while also improving the sensitivity and precision of the method. Measurements were made using commercially available RT-PCR instrument equipped with a flatbed thermocycler, a xenon arc lamp, and suitable excitation and emission filters for the TaqMan probes. The device was used to generate 3,300 single-cell measurements of miRNA expression, miRNA coregulation, and single nucleotide variation.

## Future Directions for Research

A major focus of contemporary microfluidic research is the development of systems for single-cell analysis. In these endeavors, fluorescence methods remain the best option for in situ analysis of cellular biomarkers. Many future applications will likely utilize FRET to observe ligand–receptor interactions, clustering of cell surface receptors, cellular enzyme activity, and other biological process as part of on-chip, high-throughput analyses of single cells. Such analyses are essential for uncovering cell-to-cell variability in heterogeneous biological systems that may have distinct subpopulations. In this context, a particularly exciting prospect is the combination of microfluidic single-cell analysis with spFRET, which could provide a powerful platform for correlating protein folding with subpopulations that have differences in gene expression or molecular factors.

Future research is also likely to make greater use of fluorescent nanoparticles such as QDs, which offer distinct advantages over fluorescent dyes. For example, the superior brightness of QDs and their resistance to photobleaching facilitates spFRET, while their narrow, continuously tunable fluorescence emission and broad light absorption facilitate spectral multiplexing to detect and correlate multiple biomarkers associated with single cells. Further, more sophisticated multifunctional FRET probes can be constructed using nanoparticles, which can serve as a nanoscale scaffold for the assembly of biomolecules and the transport of therapeutics. The preparation of such probes is not trivial, and microfluidic platforms will enable the use of smaller amounts of these materials in conjunction with higher-throughput analysis.

Beyond FRET, the ability of microfluidic platforms to offer automated delivery of small volumes of reagents with high precision and rapid mixing suggests benefits for bioanalyses based on CRET and BRET. Elimination of the need for an excitation source may help reduce the footprint of the instrumentation associated with the readout of microfluidic chips, which is substantially larger than the chips themselves, and reduce electrical

requirements for field deployable or point-of-care bioanalysis systems. Notwithstanding such developments, future use of microfluidics and FRET to study fundamental biological processes will likely see greater utilization of more advanced fluorescence imaging modalities, such as FLIM and multispectral/hyperspectral imaging, to provide even greater amounts of information per measurement. Microfluidics and FRET have much to offer one another and are a powerful combined platform for basic and applied research.

## Cross-References

- ▶ [Confocal Microscope](#)
- ▶ [Confocal Microscopy, Detection](#)
- ▶ [Fluorescence](#)
- ▶ [Fluorescence Lifetime](#)
- ▶ [Fluorescence Measurements](#)
- ▶ [Fluorescent Labeling](#)
- ▶ [Quantum Dot](#)
- ▶ [Quantum Efficiency](#)

## References

1. Förster T (1993) Intermolecular energy migration and fluorescence {Ann. Phys. 2, 55 (1948, translation)}. In: Mielczarek EV, Greenbaum E, Knox RS (eds) Biological physics. American Institute of Physics, New York
2. Sun Y, Wallrabe H, Seo SA, Periasamy A (2011) FRET microscopy in 2010: the legacy of Theodor Förster on the 100th anniversary of his birth. *Chem Phys Chem* 12(3):462–474
3. Lakowicz JR (2006) Principles of fluorescence spectroscopy, 3rd edn. Springer, Boston
4. Zhi Z, Liu P, Wang P, Huang Y, Zhao XS (2011) Domain-specific folding kinetics of staphylococcal nuclease observed through single-molecule FRET in a microfluidic mixer. *Chem Phys Chem* 12(18): 3515–3518
5. Vandellinder V, Ferreón ACM, Gambin Y, Deniz AA, Groisman A (2009) High-resolution temperature-concentration diagram of  $\alpha$ -synuclein conformation obtained from a single Förster resonance energy transfer image in a microfluidic device. *Anal Chem* 81(16):6929–6935
6. Wang J, Jiang P, Han Z, Qiu L, Wang C, Zheng B, Xia J (2012) Fast self-assembly kinetics of quantum dots and a dendrimeric peptide ligand. *Langmuir* 28(21): 7962–7966
7. Ho YP, Chen HH, Leong KW, Wang TH (2009) The convergence of quantum-dot-mediated fluorescence resonance energy transfer and microfluidics for monitoring DNA polyplex self-assembly in real time. *Nanotechnology* 20(9):095103
8. Hsieh ATH, Pan PJH, Lee AP (2009) Rapid label-free DNA analysis in picoliter microfluidic droplets using FRET probes. *Microfluid Nanofluid* 6(3):391–401
9. Tavares AJ, Noor MO, Vannoy CH, Algar WR, Krull UJ (2012) On-chip transduction of nucleic acid hybridization using spatial profiles of immobilized quantum dots and fluorescence resonance energy transfer. *Anal Chem* 84(1):312–319
10. Dai W, Zheng Y, Luo KQ, Wu H (2010) A prototypic microfluidic platform generating stepwise concentration gradients for real-time study of cell apoptosis. *Biomicrofluidics* 4(2):024101
11. White AK, VanInsberghe M, Petriv OI, Hamidi M, Sikorski D, Marra MA, Piret J, Aparicio J, Hansen CL (2011) High-throughput microfluidic single-cell RT-qPCR. *Proc Natl Acad Sci U S A* 108(34): 13999–14004

---

## Fluorescence Yield

### Definition

The ratio of the number of molecules that fluoresce to the total number of excited molecules.

### Cross-References

- ▶ [Fluorescence Measurements](#)
- ▶ [Lab-on-a-Chip Devices for Chemical Analysis](#)

---

## Fluorescent Labeling

Elizabeth Tully and Richard O’Kennedy  
Applied Biochemistry Group, School of  
Biotechnology and Biomedical Diagnostics,  
Institute National Centre for Sensor Research,  
Dublin City University, Dublin, Ireland

### Synonyms

Biomolecule detection; Luminescent labels

## Definition

► **Fluorescent probes** are relatively small molecules that are used to label biomolecules such as proteins, antibodies, and nucleic acids. They contain functional groups and specific physical and chemical characteristics that confer suitability for their use as detection moieties. To date, thousands of fluorescent probes are known each with varying spectral properties. Fluorophores may be intrinsic or extrinsic in nature. Intrinsic fluorophores are naturally occurring, whereas extrinsic fluorophores are added to generate a fluorescence signal to facilitate measurement of a specific target molecule. Fluorescent labels have provided excellent sensitivity for a range of assay systems that can be applied to the determination of almost any analyte.

## Overview

The use of fluorescence to facilitate measurements in biological systems has increased dramatically and includes applications in spectroscopy, flow cytometry, clinical chemistry, in situ hybridization, immunoassays, immunocytochemistry, immunohistochemistry, and microarrays. ► **Luminescence** is the emission of light from any substance occurring when an electron returns from an electronically excited state to ground state. There are two main categories of luminescence, fluorescence, and phosphorescence, and these are dependent on the nature of the excited state. ► **Fluorescence** is the property whereby some atoms and molecules absorb light at a particular wavelength and subsequently emit light of longer wavelength after a brief interval, termed the fluorescence lifetime [1]. Photons from an external source are absorbed by the fluorophore, and this produces excited singlet state electrons. However, the time taken for these electrons to return to the lower energy level is known as the excited state lifetime. The emission of light occurs as fluorescence from an excited electron singlet state, where all the electrons in the molecule are spin-paired. The return to ground states occurs, with the emission of photons.

Emission rates are fast being in the region of  $10 \text{ s}^{-1}$ , and fluorescence lifetimes are relatively short. Many fluorophores have sub-nanosecond lifetimes, and, therefore, the fluorescence emitted by these dyes is short-lived. ► **Phosphorescence** is the emission of light from triplet-excited states, whereby one set of electron spins is unpaired. This means that electrons in the excited orbital have the same spin as the ground state electrons. Therefore, transition to ground state is not possible, and emission rates are slow (in the region of  $10\text{--}10 \text{ s}^{-1}$ ). Phosphorescent lifetimes have durations in the millisecond range. Following exposure to light, phosphorescent substances glow for several minutes as the excited phosphors return to the ground state very slowly.

Fluorescence-based detection has a number of major advantages over other light-based investigative methods. Changes in concentration can be monitored very rapidly, and samples are not affected or destroyed in the process. Fluorescence typically occurs from aromatic molecules, e.g., naturally occurring fluorescent substances such as quinine, fluorescein, rhodamine B, acridine orange, and 7-hydroxycoumarin. In contrast to aromatic organic molecules, atoms are generally nonfluorescent in the condensed phase. The lanthanides, however, a group of elements including terbium and europium do not follow this rule. Fluorescence occurs in these molecules as a result of electron transitions between orbitals. Lanthanides exhibit long decay times due to the shielding effect of electron transitions between the orbitals and also low emission rates because of their low extinction coefficients.

A fluorescence emission spectrum is a plot of fluorescence intensity versus wavelength (nm) or wavenumber ( $\text{cm}^{-1}$ ). Emission spectra vary widely from fluor to fluor and are dependent on chemical structure and environmental conditions, e. g., pH, buffer components, solvent polarity, and dissolved oxygen. A number of processes are involved in fluorescence emission which can have an effect on the fluorescence characteristics of a fluorophore. These include collisions with quenchers, rotational and translational diffusion, and complex formation with solvent/solute. Fluorescent molecules absorb

photons of energy at one wavelength and subsequently emit energy at another wavelength. During the absorption process (excitation), the quantum energy levels of some fluorophores increase with photon uptake. This absorption band is not isolated at a discrete (single) photon energy level but spread over a range of wavelengths, giving rise to a peak of maximal absorbance. The extinction coefficient ( $E$ ) is the absorbance peak maximum and is specific for each fluorophore. The ratio of total photon emission over the entire range of fluorescence to the total photon absorption (range 0–1) is known as the quantum yield ( $Q$ ). The higher the quantum yield the brighter the luminescence (photon emission) will be. Another characteristic that is an important consideration for fluorophores is the size of its Stokes shift. Stokes law states that the emission wavelength of a given fluorophore should be longer and of lower energy than the excitation wavelength, so that the emission spectrum should be separated sufficiently from its excitation spectrum.

The intensity of emitted fluorescence can be decreased by a number of processes, and this is known as quenching. Collisional quenching occurs when the excited state fluorophore is deactivated upon contact with some other molecule in solution. Fluorophores can form nonfluorescent complexes with quenchers, and static quenching can occur in the ground state since no diffusion or molecular collisions are occurring. Quenching can also happen by other nonmolecular mechanisms such as attenuation of the incident light by the fluorophore itself or another absorbing species in the sample [2]. Another problem encountered with fluorescent labels is over-labeling. As the level of probe attachment to biological molecule is increased, decreases in emission intensities can occur. This is because fluorophores self-quench at high label levels, due to the energy transfers from excited state molecules to ground state dimers.

In immunoassays, antibodies and antigens can be labeled directly with a fluorescent molecule. Fluorescence-based detection is a safe, rapid, noninvasive technique suitable for a wide range of biological applications. Fluorescence-

based detection of antibody-antigen binding interactions was traditionally performed with organic fluorescent tags such as FITC, cyanine 3 and 5, and rhodamine [2]. Most organic fluorophores have narrow excitation spectra and broad emission bands. Therefore, multiplexing of assays is difficult as spectral overlap can take place. Quenching, photobleaching, and autofluorescence can also often occur, affecting the generated signal, giving rise to skewed or invalid results. Another problem associated with the use of organic fluorescent probes is that conjugation strategies must be tailored to both the target molecule for labeling and the fluorescent dye. Therefore, the efficiency of labeling is often compromised, whereby over or under labeling can occur. There are many techniques for the direct and indirect labeling of biomolecules with fluorescent tags for biological applications. The selection of an appropriate fluorescent tag is dependent on a number of parameters such as sample type, mode of action, immobilization strategy, excitation and emission characteristics of the fluorophore, and the type of analyte being detected.

The evolution of novel fluorophores that exhibit greater stability and brightness has led to improved sensitivity and reproducibility in biological monitoring. The advent of inorganic fluorophores such as quantum dots, nanocrystals, and functionalized nanoparticles has revolutionized fluorescence-based detection methods. Novel fluorescent probes have higher quantum yields and high resistance to photodegradation, and the main advantages of such probes are their narrow predictable emissions, extreme photostability, and brightness. Functionalization of the polymer shell of such molecules is generally quite simple and allows direct coupling of the probe to biomolecules. For example, silica nanoparticles are easy to modify, through either NHS activation, silanization, or carboxyl modification facilitating conjugation to biomolecules. Recombinant proteins and antibody fragments can also be specifically engineered with fluorescent tags, but these tags can often change the binding properties of the molecule due to changes in structure and conformation.

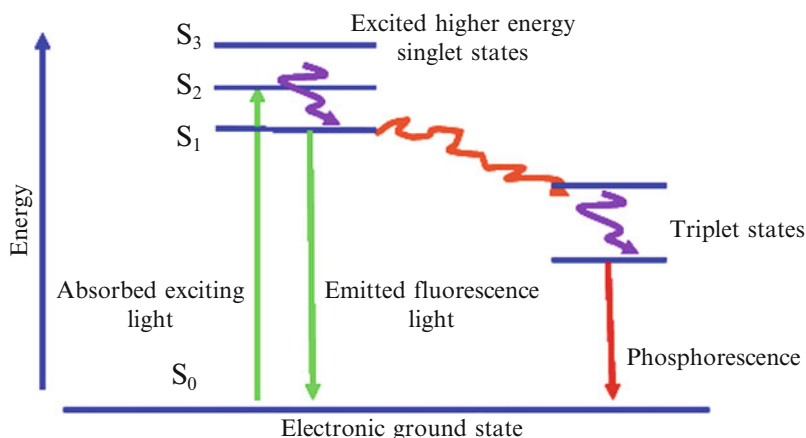
## Basic Methodology

Detection of labels for use in biological applications can be performed by either spectrophotometric or radioactive methods. Labels can alternatively be indirectly detected through another labeled substance. The use of spectrophotometric probes includes both chromogenic (colored) labels and fluorescent labels. Chromogenic labels are mainly used for the non-covalent staining of structural features within cells as the colored pigments in the dye bind to specific areas in the cell. However, there are a number of problems associated with these tags. The sensitivity of visible wavelength dyes is generally not sufficiently sensitive for detection of low concentrations of antigen, and even if a biomolecule is covalently modified with the chromogen, a relatively large amount of dye is required. Biomolecules can also be labeled with radioactive probes. Radioactive probes are detected with highly specialized equipment, and there are certain safety considerations that must be addressed when working with such materials.

However, with fluorescent labels, sensitivity can be increased dramatically. Fluorescence-based detection is a simple safe and effective way of labeling molecules for biological applications. Fluorescent tags have a number of attributes including large quantum emission yield upon excitation and easy conjugation to biomolecules via reactive groups that make them highly suitable for biological detection. The availability of multiple tags directed to specific reactive groups on biomolecules allows multiplexing of assays, whereby different probes can be used to detect for multiple antigens on a biomolecule in tissue or cells (Fig. 1).

## Fluorescent Labels

The physical and chemical properties exhibited by an ideal fluorescent label are shown in Table 1. These include high quantum yield and a large Stokes shift to ensure good separation of excitation and emission wavelengths. A large Stokes shift will increase the fluorescent signal generated as interference from Rayleigh-scattered excitation light is decreased. The aromatic ring



**Fluorescent Labeling, Fig. 1** Jablonski diagram (Adapted from [14]). When a photon provided by an external light source is absorbed by a fluorophore, it is excited from a vibrational level in the electronic ground state ( $S_0$ ) to a higher electronically excited state. The electronic state of an organic molecule can be either a singlet state whereby all electrons in the molecule are spin-paired or a triplet state where one set of electrons is unpaired. The excited singlet states ( $S_{1-3}$ ) are reached

after initial absorption. A molecule in this energy level will quickly fall to the lowest vibrational level of this state by energy loss through collision. Fluorescence occurs as photon of light is emitted, returning the fluorophore to ground state. The Jablonski diagram shows the possible routes by which an excited molecule can return to ground state via unstable triplet states. A quick return to ground state results in fluorescence, whereas a delayed return is known as phosphorescence

**Fluorescent Labeling, Table 1** List of ideal properties of fluorescent probes

Properties	Ideal fluorescent probe
Light emitted	Narrow band of emission
Stability	Emits brightly Photostable
Stokes shift	Large shift Good distance between excitation and emission wavelengths
Quantum yield	High quantum yield, approaching 1
Fluorescence lifetime	Long lifetime
Light source	Broad excitation range Inexpensive

system contained in most fluorophores generates the luminescence, and as the ring gets larger, the emission shifts to red and the quantum yield increases. Aromatic ring constituents affect the fluorescent behavior of each dye. Ring activators, i.e., electron donating groups, increase the quantum yield of a fluorophore, whereas electron withdrawing groups decrease it. The presence of heavy atoms can also diminish the quantum yield by enhancing the probability of the excited singlet state going into triplet transition. Energy decay from a triplet-excited state causes phosphorescence instead of fluorescence. The phosphorescent band is located at longer wavelengths and hence at lower energies, relative to the fluorescence spectrum. The energy transition to the triplet state is an opposite reaction to that of fluorescence and so a decrease in potential luminescence is caused. Polycyclic structures in the aromatic ring system are important to maintain fluorescent properties. Coplanar structures, i.e., rings in the same dimensional plane, show the greatest fluorescence. Malachite green and rhodamine have very similar structures, yet the oxygen bridges on upper phenyl rings of rhodamine confer a planar shape, thus enhancing its luminescent qualities [2].

Intrinsic fluorophores are naturally occurring whereby the intrinsic fluorescence originates within the aromatic amino acids such as tryptophan, tyrosine, and phenylalanine. The indole groups of tryptophan residues are the dominant source of UV absorbance/emission in proteins.

Fluorescence emission from phenylalanine is observed only when the sample protein lacks both tyrosine and tryptophan residues, and this is a very rare occurrence. Emission of tryptophan is very sensitive to local environmental changes and can be used as a reporter group for protein conformational changes. Spectral shifts are observed on binding of ligands and on protein-protein association. The emission maximum of proteins reflects the average exposure of tryptophan residues to the aqueous phase. Tryptophan fluorescence is subject to quenching by iodide, acrylamide, and disulfide groups and also by nearby electron-deficient groups and protonated histidine residues. Extrinsic fluorophores are added to samples to provide fluorescence and change the spectral properties. In addition, the molecule of interest is often nonfluorescent or the intrinsic fluorescence is too weak. Proteins with weak intrinsic fluorescence can be labeled with fluorophores that have longer excitation and emission wavelengths than their constituent aromatic amino acids. There are huge numbers of such fluorophores available. Reagents are available that can be used for both the covalent and non-covalent labeling of proteins. In the case of covalently bound probes, a variety of reactive groups are available for effective coupling with amine, sulfhydryl, and histidine side chains in proteins. Ideally, for labeling of biomolecules, each fluorophore should have several analog forms each with a different reactive group suitable for coupling to a different specific functional group on the target molecule. Popular organic labels include derivatives of fluorescein, rhodamine, coumarins, and Texas Red, as shown in Table 2.

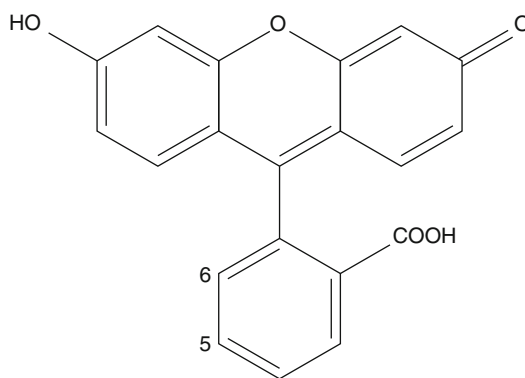
### Common Fluorophores

Fluorescein and rhodamine are common fluorophores used for the fluorescent labeling of proteins in biological applications. This is due to a number of advantageous properties such as long absorption maxima, insensitivity to solvent polarity, high molar extinction coefficient, and the availability of a wide variety of reactive derivatives. Fluorescein derivatives are characterized by a multi-ring aromatic structure, due to the planar nature of an upper, fused, three-ring system (Fig. 2). Derivatives of the basic structure

**Fluorescent Labeling, Table 2** List of common organic fluorophores

Fluorophore	Mr (Da)	$\lambda_{ex}$ (nm)	$\lambda_{em}$ (nm)	Fluorescent lifetime (ns)	Quantum yield (Q)	Reacts with
Fluorescein isothiocyanate	389	494	520	~4.1	0.75	Amines
NHS-fluorescein	457	491	518	~4.0	0.75	Amines
Iodoacetamidofluorescein	515	491	520	~4.0	0.75	Sulfhydryls
Fluorescein-5-maleimide	427	490	515	~4.0	0.75	Sulfhydryls
Fluorescein-5 thiosemicarbazide	421	492	516	~4.0	0.75	Aldehyde/ ketone
5-(((2-(carbohydrazino)methyl)thio)acetyl)-aminofluorescein	493	490	516	~4.0	0.75	Aldehyde/ ketone
Tetramethylrhodamine-5-(6)-isothiocyanate	444	544	570	~1.5	0.25	Amine
NHS rhodamine	528	546	579	~1.5	0.25	Amine
Lissamine rhodamine sulfonyl chloride	577	556	576	~2.1	0.25	Amine
Texas Red sulfonyl chloride	577	556	576	~4.2	0.25	Amine
Tetramethylrhodamine-5-(6)-iodoacetamide	569	540	567	~	0.25	Sulfhydryls
Lissamine rhodamine B sulfonyl hydrazine	573	560	585	~	0.25	Sulfhydryls
Texas Red hydrazine	621	580	604	~	0.25	Sulfhydryls
7-amino-4-methyl-coumarin-3-acetic acid	233	345	450	~	0.49	Amines (using EDC activation)
Succinimidyl-7-mino-4-methyl-coumarin-3-acetic acid	330	345	450	~	0.49	Amines
Sulfosuccinimidyl-7-mino-4-methyl-coumarin-3-acetic acid	431	345	450	~	0.49	Amines
4,4-difluoro-5,7-dimethyl-4-bora-3a,4a-diaza-S-indacene-3-proponic acid, succinimidyl ester (BODIPY FL C3-SE)	389	502	510	~	0.8	Amines
4,4-difluoro-5,7-diphenyl-4-bora-3a,4a-diaza-S-indacene-3-proponic acid (BODIPY 530/550 C3)	416	535	552	~	0.8	Amines
Cyanine 3	767	550	570	~0.2	~0.25	Amines
Cyanine 5	792	649	670	~0.3		Amines

of fluorescein involve substitution of carbons number 5 or 6 of the lower ring, for modification and labeling of biomolecules. The effective excitation wavelength range is between 488 and 495 nm, while the emission spectrum lies between 518 and 525 nm, depending on the derivative. The quantum yield of fluorescein derivatives can be up to 0.75. However, quick photobleaching can be observed when the dye is dissolved in buffers, exposed to light or pH variations, or subjected to long-term storage. Amine-reactive fluorescein derivatives such as fluorescein isothiocyanate (FITC) react under slightly alkaline conditions with primary amines in biomolecules to form stable highly fluorescent derivatives. FITC is synthesized by modification of the lower ring at carbon position 5 or 6. Isothiocyanates react with nucleophiles such as

**Fluorescent Labeling, Fig. 2** Structure of fluorescein

amines, sulfhydryls, and the phenolate ion of tyrosine side chains. They form a stable product on reaction with biomolecules at primary amines. FITC is almost entirely selective for modifying

N-terminal amines in proteins. The reaction involves the attack of a nucleophile on the central electrophilic carbon of the isothiocyanate group. The resulting electron shift creates a thiourea linkage between FITC and the biomolecule. FITC is water soluble above pH 6.0, and isothiocyanate reagents are reasonably stable in aqueous solution for short periods but degrade over time.

The main applications of FITC are as follows:

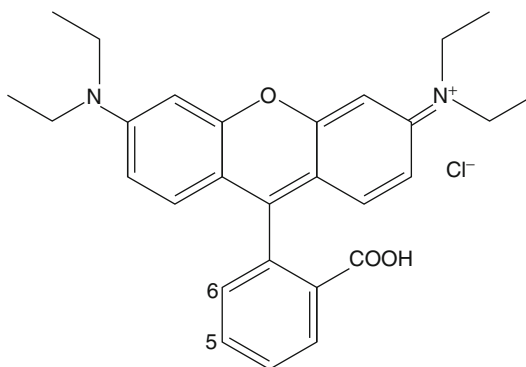
- Labeling of antibodies to detect antigens in cells, tissues, immunoassays, blots, chips, and microarrays
- Detecting proteins after electrophoretic separations
- Microsequencing analysis of proteins/peptides
- Identification of molecules separated by capillary zone electrophoresis
- Labels in flow cytometry

NHS-fluorescein is an amine-reactive carboxy-succinimidyl ester group at carbon position 5 or 6 of the lower ring and is more stable than FITC. The NHS ester reaction proceeds rapidly at slightly alkaline pH values, resulting in stable amide-linked derivative. It has similar properties to FITC with the extinction coefficient dependent on environmental conditions such as pH or buffer. NHS-fluorescein is insoluble in aqueous solution; therefore, all stock solutions should be made up in an organic solvent. The optimal pH for NHS ester functionality is 7–9. NHS-fluorescein is also available with a long-chain spacer. This may be useful for reducing steric hindrances around the fluorescent molecule encountered during labeling, thus minimizing quenching effects.

Sulfhydryl-reactive derivatives of FITC contain sulfhydryl groups on the lower ring structure. These groups direct the labeling to more limited sites on target molecules. Coupling through sulfhydryl residues instead of amines can avoid active centers in proteins, preserving functional activity. Sulfhydryl-reactive sites are naturally available through free cystine side chains generated by the reduction of disulfides or the use of thiolation reagents. Iodoacetamidofluorescein is an intense fluorophore derived by modification of a sulfhydryl-reactive iodoacetyl group at carbon

5 or 6. Iodoacetyl groups react with sulfhydryls under slightly alkaline conditions to yield stable thioether linkages. They do not react with unreduced disulfides in cystine residues. It is important to protect these reagents from light since the light-catalyzed breakdown of iodoacetyl groups causes quenching. The molar extinction coefficient is dependent on environmental factors such as pH. These reagents are soluble in organic solvent and aqueous solution above pH 6.0. Fluorescein-S-maleimide has a sulfhydryl-reactive maleimide group on the lower ring structure. It forms stable thioether bonds that are pH controlled and has fluorescent properties close to fluorescein. If no –SH groups are available, disulfides can be reduced with thiolation reagents. Fluorescein-S-maleimide is soluble in aqueous solution above pH 6.0 at low concentrations.

Fluorescent derivatives of fluorescein with hydrazide groups on carbon 5 or 6 can be used to label aldehyde- or ketone-containing molecules. Hydrazides react with aldehyde and ketone functional groups to form hydrazone linkages. Many biomolecules have no aldehyde or ketone groups in their native state, except for those with sugar residues such as carbohydrates, glycoproteins, and RNA. These molecules can be oxidized with sodium periodate to produce reactive formyl groups. Modification reagents that generate aldehydes upon coupling to a molecule can also produce hydrazide-reactive sites. DNA and RNA can be modified with hydrazide-reactive probes by reacting cytosine residues with bisulfite to form sulfone intermediates. Fluorescein-5-thiosemicarbazide is a hydrazide derivative of fluorescein and is involved in a spontaneous reaction with aldehyde-/ketone-containing molecules to form covalent hydrazone linkages. It can also label cytosine residues in DNA/RNA by way of bisulfite activation. This derivative is soluble in organic solvents and aqueous solutions above pH 7.0. However, it is prone to photobleaching and so protection from light is essential. It is useful for the site-directed labeling of antibodies through carbohydrate side chains. 5-(((2-(carbohydrazino)methyl)thio)acetyl)-aminofluorescein is another derivative of fluorescein that has a longer spacer arm on carbon 5. It is very similar to



**Fluorescent Labeling, Fig. 3** Structure of rhodamine

fluorescein-5-thiosemicarbazide and reacts with aldehydes/ketones in the same way. It can label cytosine residues and is soluble in organic solvents and aqueous solutions above pH 7.0.

Rhodamine derivatives obtain their fluorescent character from a planar multi-ring aromatic structure. They are very similar to fluorescein but with a nitrogen atom replacing oxygen on the outer ring as shown in Fig. 3. Activated rhodamine probes have reactive groups made through substitution on carbon 5 or 6 of the lower ring. Alterations to the basic rhodamine structure modulate its fluorescence characteristics, giving rise to an intense and stable fluorescence. There are a number of derivatives of the basic rhodamine structure.

These include the following:

Tetramethylrhodamine derivative	2 methyl groups on each nitrogen on the outer ring
Rhodamine B	2 ethyl groups on each nitrogen on the outer ring plus a carboxylate at position 3
Rhodamine G6	2 methyl groups on each nitrogen on the outer ring plus an ethyl ester on a carboxylate at position 3
Sulforhodamine B	2 ethyl groups on each nitrogen on the outer ring plus a sulfonate at positions 3 and 5 (Lissamine rhodamine B)
Sulforhodamine 101 (Texas Red)	Intense luminescent properties in the far red region of spectrum

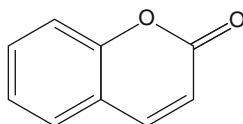
The basic characteristics of rhodamine probes are as follows. The effective excitation

wavelength is in the visible light spectrum (500–590 nm), and associated emission wavelengths occur from high 500 s to early 600 s, i.e., the orange-to-red portion of the visible spectrum. The quantum yield of rhodamine derivatives is generally lower than fluorescein, typically being 0.25. However, rhodamine probes exhibit slower bleaching in that the intensity fades slowly when dissolved in buffers or exposed to light. The red emission of rhodamine probes is in stark contrast to fluorescein so this makes it ideal for double staining when used in conjunction with FITC. A number of amine-reactive derivatives are commonly used, and these include tetramethylrhodamine (TMR)-isothiocyanate, NHS rhodamine, Lissamine rhodamine sulfonyl chloride, and Texas Red sulfonyl chloride. Coupling through sulfhydryls instead of amines can help to avoid interference with active centers in biomolecules, thus minimizing the effect on the biological activity. Reaction sites are available via free cystine side chains and the use of thiolation reagents. An example of a sulfhydryl-reactive probe is TMR-iodoacetamide.

Finally, another group of derivatives are the aldehyde-/ketone-reactive probes. This group is based on the activation of a sulfonyl hydrazine group of carbon number 5. They are based on Lissamine and Texas Red structures and used to label aldehyde-/ketone-containing molecules (with sugars). The most common aldehyde-/ketone-reactive probes are Lissamine rhodamine B hydrazine and Texas Red hydrazine.

### Coumarin Derivatives

Coumarins are naturally occurring substances found in Tonka beans, lavender oil, and sweet clover, and many are inherently fluorescent. The basic structure of a coumarin molecule is shown in Fig. 4. Some coumarin derivatives are also highly fluorescent, e.g., 7-amino-4-methyl-coumarin-3-acetic acid (AMCA) has a carboxylate group that is easily functionalized for conjugation [3]. It gives rise to an intense fluorescence in the blue region of visible spectrum. Coumarins are also good donors for excited state energy transfer to fluorescein. Their emission spectra are in a region that does not overlap with other major probes and

**Fluorescent Labeling,****Fig. 4** Structure of coumarin

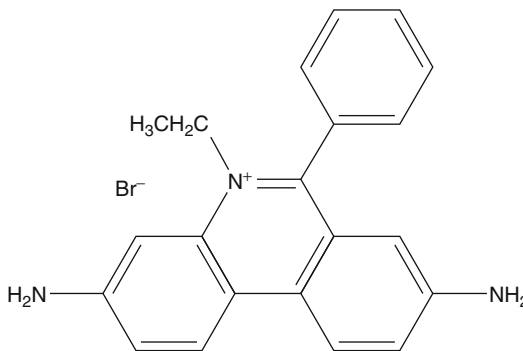
are therefore suitable for double-staining applications. The main advantages of coumarin probes are a large Stokes shift, a good quantum yield of  $\sim 0.49$ , and an activity over a wide pH range (3–10). Coumarin derivatives are easily coupled to biomolecules via a carbodiimide reaction with EDC. The most common probes are NHS-AMCA and sulfo-NHS-AMCA, which have similar properties. Coumarin labels are highly useful for double-labeling techniques since their emission wavelengths are sufficiently distant from the more common organic fluorophores. Therefore, coumarins are highly appropriate for use in multiplexed immunostaining applications.

**BODIPY Derivatives**

4,4-Difluoro-4-bora-3a-4a-diaza-s-indacene (BODIPY) has a fused multi-ring structure. Modifications at 1, 3, 5, 7, and 8 carbon positions cause spectral shifts in excitation and emission wavelengths and functional sites for coupling. BODIPY derivatives have a high quantum yield ( $\sim 0.8$ ) and are relatively insensitive to pH changes. One disadvantage of BODIPY probes is the relatively small Stokes shift (20 nm maximum), which can cause problems since excitation at suboptimal wavelengths is required to prevent interference and light scattering from the excitation source. BODIPY is suitable for use with molecules with only one free amine group, since the label is easily quenched by excess presence of dye.

**DNA Labels**

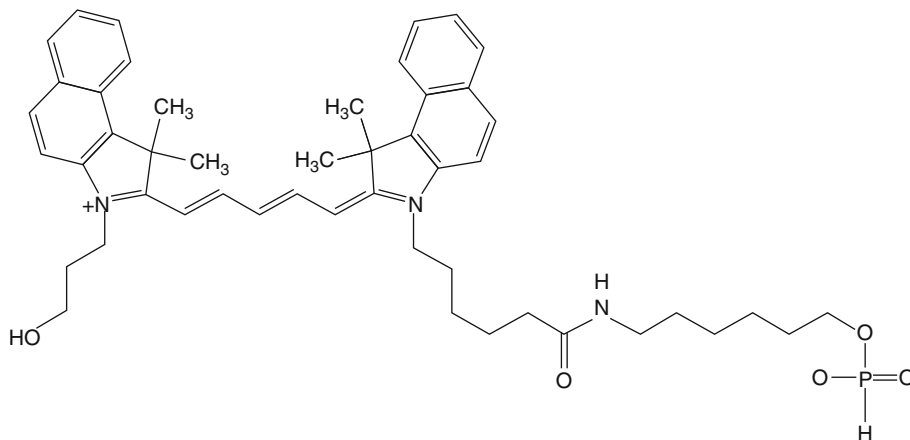
There are numerous probes available that spontaneously bind to DNA, displaying enhanced emission. Ethidium bromide weakly fluoresces in water, but this intensity is greatly increased upon binding to DNA (Fig. 5). The mode of binding is due to the intercalation of the planar aromatic ring between base pairs of double-helical DNA. Acridine orange also binds to

**Fluorescent Labeling, Fig. 5** Structure of ethidium bromide

DNA by intercalation, and 4',6-diamidino-2-phenylindole (DAPI) binds into the minor groove of DNA. Fluorescence is most enhanced when adjacent to *adenine-thymine-rich* regions of DNA. These labels are used to image DNA on agarose gels using a UV transilluminator for molecular biological applications.

**Non-covalent Fluorescent Probes**

Some dyes are weakly fluorescent or nonfluorescent until the occurrence of a particular event, i.e., enzymatic cleavage. An example of this is 7-umbelliferyl phosphate, a coumarin derivative, and a nonfluorescent phosphate ester that becomes highly fluorescent upon hydrolysis. It can be used to measure the activity of alkaline phosphatase in ELISA and enzyme-amplified DNA assays. Some dyes become fluorescent upon reacting with amines. Fluorescamine is one such dye and can be used for protein labeling, but more common applications of this dye are the determination of protein concentration and as a tracking dye in protein sequencing. Anionic dyes can be used to bind to residues of proteins, which carry positive charges. Upon binding, the fluorescent intensity can be either enhanced or quenched. In the case of enhancement, changes in microenvironment can cause changes in hydrophobicity of a given biomolecule. Probes that are nonfluorescent in water may be highly fluorescent in apolar media. Non-covalent probes can also be used in a quenching capacity, for example, at pH 3.1;



**Fluorescent Labeling, Fig. 6** Structure of cyanine 5

eosin Y exhibits strong green fluorescence, whereas on binding to protein, the fluorescence is quenched. Another example is the non-covalent binding of the near-infrared anionic dye IR-125 to casein. This was investigated with the use of steady-state and picosecond laser fluorescence measurements. In an aqueous borate buffer, minimal fluorescence emission from the dyes was observed. When casein was added to the solution, enhancements in the fluorescence emission were found. The reason for this is that the dye distributes between the hydrophobic core of the protein and the interstitial aqueous solution. The dye molecules residing in the interior of the protein exhibit enhancements in their fluorescence due to a more favorable microenvironment.

### Near-Infrared (NIR) Fluorescent Probes

NIR detection of biomolecules has a number of advantages including low fluorescence background, since very few naturally occurring molecules can undergo electronic transitions in this low energy region of the spectrum. Scatter is also reduced at higher wavelengths at this end of the spectrum, and sample photodecomposition is reduced. Excitation is usually by a cheap, stable laser diode, which increases sensitivity. NIR probes have high quantum yields, large Stokes shifts, photochemical stability, and a high tolerance to quenching. Good examples of NIR probes are the group of cyanine dyes. These molecules have emission maximums between 600 and

800 nm. The quantum yields of these probes in aqueous solutions are very low. However, on binding to analytes, changes in absorption and emission wavelengths are increased as the fluorescent lifetime increases. Cyanine dyes can label proteins by covalent and non-covalent binding. The non-covalent attachment of cyanine is useful for the detection of large proteins, as the positive charge of dyes can be used for non-covalent labeling. Figure 6 shows the basic structure of a cyanine dye.

Cyanine derivatives with alkyl  $\text{SO}_3^-$  groups and active groups such as isothiocyanate, iodoacetamide, and N-succinimidyl can be used for covalent attachment to biomolecules. Dicarboxyanine dyes (adding a  $-\text{CH}=\text{CH}-$  entity to the polymethine chain of cyanine) cause a large red shift (up to 100 nm) in absorption maximum. Dicarboxyanine dyes with NHS esters are suitable for the covalent labeling of molecules with primary/secondary amines, under slightly alkaline conditions. Cyanine dye fluorophores are bright fluorescent dyes that contain a  $-\text{CH}$  group linking two nitrogen-containing heterocyclic rings as shown in Fig. 6. They can be functionalized with NHS ester, maleimide, isothiocyanate, and hydrazine chemistries for biomolecule attachment. They exhibit high molar extinction coefficients and favorable quantum yields. The small size of these dyes reduces steric hindrance and, therefore, loss of activity. Cyanine dyes can be used for standard fluorescence,

fluorescence resonance energy transfer (FRET), time-resolved fluorescence (TRF), and fluorescence polarization applications. The favorable properties of cyanine dyes include good aqueous stability, tolerance to organic solvents, pH insensitivity (range pH 3–10), low nonspecific binding, and high photostability. They are suitable for labeling via a range of amine, thiol, and aldehyde groups. The sensitivity of fluorescence detection is often limited by autofluorescence of biological samples. This is decreased as the excitation wavelength becomes longer, and, therefore, detectability over background is increased. Longer wavelength probes can be excited with simple excitation sources such as LEDs. Cyanine dyes have absorption and emission wavelengths above 650 nm. They also have a small Stokes shift with the absorption maximum shifted from the emission maximum. The charged side chains of cyanine dyes are used for improved water solubility and to prevent self-association, the main cause of self-quenching.

### Lanthanides

Long-lifetime probes are those with fluorescent lifetimes greater than those of traditional organic probes (1–10 ns). Lanthanides are transition metals with fluorescent lifetime decay times between 0.5 and 3 ms [4]. Transition metal-ligand complexes are made up of metal and organic ligands. They contain mixed singlet-triplet states and have intermediate lifetimes of 400 ns to  $\mu$ s. Their absorption coefficients are very low and emissive rates very slow, giving rise to long lifetimes. They are not directly excited but use chelated organic liquids as conduits. Lanthanides can substitute chemically for calcium in calcium-dependent proteins. They can be used with proteins that do not have intrinsic binding sites. They are particularly useful in immunoassay applications. Biological samples can exhibit autofluorescence, which can be limiting, since autofluorescence from the sample decays on a nanosecond timescale, as does the fluorescence of most probes. However, due to the long decay time of lanthanides, they continue to emit following the disappearance of autofluorescence. Time-gated detection can be used with lanthanides

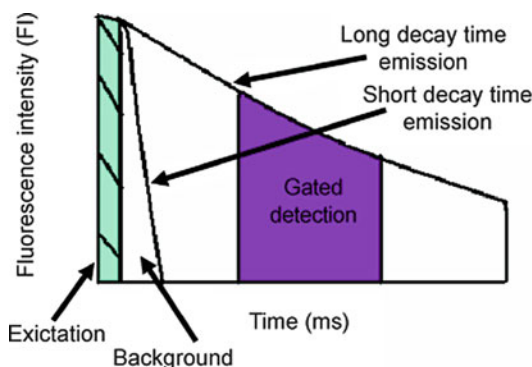
whereby steady-state intensity measurements are taken over a period of time following pulsed excitation. This principle of time-gated detection of long lifetime probes is illustrated in Fig. 7.

### In Vivo Labeling

The green fluorescent protein (GFP) from the jellyfish, *Aequorea victoria*, is a versatile reporter for monitoring gene expression and protein localization in a variety of cells and organisms [5]. GFP emits bright green light on excitation. The chromophore in GFP is intrinsic to the primary structure of the protein, and fluorescence from GFP does not require additional gene products, substrates, or other factors. GFP fluorescence is stable and species independent and can be monitored noninvasively using the techniques of fluorescence microscopy, fluorescence-activated cell sorting (FACS), flow cytometry, and fluorescence resonance energy transfer (FRET). Since the first use of the green fluorescent protein (GFP) in living organisms, over ten years ago, live cell fluorescence microscopy has become an indispensable tool for cell biologists. In recent years, many fluorescent reporters suitable for in vivo experiments have been developed, including a wide range of fluorescent proteins in various colors. The technique of in vivo labeling of genes and proteins for microarray purposes is a useful tool in the development of the field of gene and protein expression analysis. In vivo labeling methods give accurate pictures of what is happening in the natural dynamic environment, and these techniques are becoming a vital tool for fluorescence-based detection, especially for microarray applications.

### Fluorescent Labeling of Biomolecules

A standard protocol for the fluorescent labeling of biomolecules is difficult to derive as optimization of labeling condition such as buffer, pH, and concentration is highly specific for each dye. Gel filtration can be used to remove azide, which interferes with the labeling process or for buffer exchange and is often found as a preservative in biological preparations. Typically, phosphate-buffered saline comprising of 0.13 mM  $\text{NaH}_2\text{PO}_4$ , 0.528 mM  $\text{Na}_2\text{HPO}_4$ , and



**Fluorescent Labeling, Fig. 7** Principle of time-gated fluorescence detection. Time-gated fluorescence detection is used to monitor the fluorescence of a sample as a function of time after excitation by a flash or pulse of light. This figure shows a schematic of the system used with the lanthanides whereby steady-state intensity measurements of emitted fluorescence are taken over a period of time following pulsed excitation. Time resolution is optically gated, whereby short laser pulse acts as a gate for the detection of emitted fluorescence and only fluorescence that arrives at the detector at the same time as the gate pulse is collected. In time-gated detection systems, the detector is turned on after excitation and the fluorescence intensity generated is integrated. This method is useful for long lifetime probes

0.51 mM NaCl, pH 7.4, or 0.5 M carbonate buffer, pH 9.6, are used for labeling reactions. The amount of fluorescent labeling reagent used for each reaction is dependent on the amount of protein to be labeled. By using the appropriate molar ratio of labeling reagent to protein, the extent of conjugation can be controlled. For protein concentrations in the range of 2–5 mg/ml, a 10 M excess is used; for concentrations <2 mg/ml, a 15 M excess is used; and for protein concentrations <1 mg/ml, 20 M excess of dye is used. The fluorescent label is generally dissolved in an organic solvent, as most fluorescent dyes are insoluble in aqueous solution, at concentration of 10 mg/ml. Taking into account the molar ratio of dye and biomolecule, the correct volume of label can be determined and added to the protein stock. The tubes are incubated end on end and left to react overnight at 4 °C, in the dark to avoid any photobleaching. The following day the fluorescent conjugate is purified to remove unreacted dye, by either gel purification, spin column

centrifugation, or dialysis. The conjugate concentration and dye/protein ratio are then determined spectrophotometrically. The level of label incorporation can be measured by determining the absorbance at or near the characteristic extinction maximum of the label. It is also important to determine the dye/protein ratio for all derivatives prepared with tags. The equations below are used to calculate this information.

$$\frac{A_{280} - (A_{\max} \times CF) \times DF}{E_{\text{protein}}} \quad (1)$$

$$\frac{A_{\max}}{E_{\text{dye}} \times \text{Prot. Conc}} \times DF \quad (2)$$

$A_{\max}$  = absorbance of the conjugate at the excitation maximum wavelength for the dye;  $A_{280}$  = absorbance of the conjugate at 280 nm;  $CF$  = correction factor, i.e.,  $A_{280}$  dye/ $A_{\max}$  dye;  $DF$  = dilution factor;  $E_{\text{protein}}$  = protein molar extinction coefficient;  $E_{\text{dye}}$  = dye protein molar extinction coefficient.

### Biotinylation

Another efficient method of labeling biomolecules for fluorescence applications is biotinylation. Biotin is a B vitamin, which binds with high affinity to avidin and streptavidin. It is the strongest non-covalent binding reaction with an affinity constant ( $K_d$ ) of  $10 \text{ M}^{-1}$ . It can be easily conjugated to proteins since many derivatives are available. Analogs of biotin are also available with an extended spacer arm that reduces steric hindrances, thus improving binding capability. Biotin forms a stable amide bond with primary amines at pH 7–9. The optimal biomolecule concentration for successful biotinylation is approximately 1–2 mg/ml. However, for less concentrated solutions of biomolecule, this can be adjusted once the molar excess of both dye and biomolecule is taken into account. Unreacted biotin is removed from the biomolecule post-conjugation by ultrafiltration, microcentrifugation, or dialysis. Silica-encapsulated quantum dots or nanoparticles can be coupled directly to streptavidin through a carbodiimide-mediated coupling reaction.

This theoretically yields a high number of streptavidin molecules, typically up to 20, binding to the inorganic label. Biotinylated biomolecules can then be coupled directly to streptavidin-labeled fluorescent tags.

### Novel Fluorophores

The main advantages of novel inorganic fluorescent probes such as nanoparticles and quantum dots are their narrow predictable emission, extreme photostability, multiple tunable colors, brightness, broad excitation, large Stokes shift, and high quantum yields [6]. Functionalization of the polymer shell of such molecules is generally quite simple and allows direct coupling of the probe to biomolecules. Silica nanoparticles are easy to modify, through either NHS activation, silanization, or carboxyl modification. Quantum dots are nanocrystalline semiconductors that exhibit unique light-emitting properties that can be customized by changing the size or composition of the dots. Quantum dots are typically 2–8 nm in size and covered with a layer of organic material that allows functionalization of the surface for biomolecule attachment. The color is determined by the size of the particles and the composition of the material used, which in turn dictate the optical properties. One of the main advantages of nanocrystalline fluorophores is that they absorb light over a broad spectral range. By absorbing all wavelengths shorter than their emission wavelength (blue wavelengths), only a single light source is required for the excitation of multiple colored dots. This simplifies instrumentation, lowering costs and enabling multiplexing of assays. The narrow emission spectra of nanocrystals give rise to sharper colors and high spectral resolution, which improves assay sensitivity since nanocrystals emit more light than their constituent dye. Quantum dots are not liable to photobleaching, exhibit excellent photostability, and, relative to conventional fluorophores, are up to 100 times more stable [6]. It is this photostability that allows repeated interrogation of the materials over longer periods. Quantum dots have high excitation cross sections, whereby they absorb much of the light with which they are irradiated, and high quantum yields in that they

reemit more than 50 % of the light they absorb [7]. This gives rise to strong fluorescence signals, thus increasing detection sensitivity. The potential uses of quantum dots in biological applications include drug delivery, diagnostics, drug discovery, genetic analysis, and observation of biomolecular interactions. Multiple proteins or biomolecules can be identified by multiplexing different colored quantum dots in microarray applications.

Organic fluorescent labels such as FITC, Cy5, and rhodamine can exhibit high optical background in immunoassay applications, which reduces sensitivity [8]. The use of long-decay fluorescent probes and time-resolved detection allows for a significant decrease in background and, therefore, an increase in sensitivity. The lanthanide chelates, such as europium and terbium, have traditionally been used as probes for the time-resolved fluorescent detection of analytes. Functionalized derivatives of these dyes are available commercially for both homogeneous and heterogeneous assays. However, an enhancement step is often necessary such as dissociative enhancement (DELFA) or addition of enzyme labels to improve performance, resulting in an enzyme-amplified lanthanide luminescence system. Another group of structures, the metalloporphyrins are particularly suitable for biological applications, due to their relatively long decay times, and provide a realistic alternative to fluorescent lanthanide chelate labels. Phosphorescent metalloporphyrins, such as the water-soluble platinum and palladium complexes of coproporphyrin, have a number of advantages as labels for immunoassay development. These include high quantum yields of up to 40 %, simple laser excitation at 532 nm, broad red emission (600–750 nm), and long phosphorescent lifetimes (10–1,000  $\mu$ s). The platinum and palladium porphyrins can have either isothiocyanate-reactive groups or maleimide-reactive groups, allowing conjugation to be tailored exactly to suit the substance being labeled. There are two main conjugation strategies for porphyrin attachment to proteins. The first involves the activation of the porphyrin by carbodiimide, followed by nucleophilic attack of the primary amino groups of the biomolecule to produce bioconjugates via the

amide bond. The second method employs carbodiimide to preactivate the porphyrin in the presence of an active ester, which results in a porphyrin derivative with active functional groups that can react with the amino groups of a biomolecule. Novel derivatives of platinum and palladium coproporphyrin were used to make phosphorescent conjugates of antibodies, avidin, biotin, and NeutrAvidin. These labels and conjugates were evaluated in solid-phase immunoassays using commercial phosphorescence-based detectors. Successful use of these probes was reported for a number of plate-based assay formats [9].

Ruthenium complexes are designed specifically to have long fluorescence lifetimes close to 500 ns. These labels are laser-excitabile metal-ligand complexes and can be used to label amines on biomolecules under mild conditions. The main advantages of these dyes as protein labels include high photostability, good water solubility, a lack of dye-dye interactions, and large Stokes shifts. In addition, the fluorescence signal of such long-lived fluorophores can be gated to eliminate the emission from short-lifetime fluorophores and autofluorescence from cells and biomolecules, to further improve sensitivity. Castellano et al. [10] described the development and characterization of highly luminescent ruthenium complexes for covalent linkage to human serum albumin (HSA) and human immunoglobulin (hIgG). The conjugation reactions were performed at 4 °C in the dark using a thiol-reactive ruthenium complex, dissolved in an organic solvent. Unreacted dye was removed by gel filtration and dialysis, and the conjugates were characterized spectroscopically. Ruthenium metal-ligand complexes were also used in ► [fluorescence resonance energy transfer \(FRET\)](#) immunoassays. The antigen ruthenium-labeled HSA was reacted with an anti-HSA antibody, labeled with a nonfluorescent absorber, reactive blue 4. The conjugation of ruthenium dye to HSA employed a simple covalent linkage using a 10 M excess of dye. The association of Ru-labeled HSA to the anti-HSA antibody was detected by a change in the spectral parameters of Ru-HSA. The intensity and decay time of Ru-labeled antigen decreased upon

binding to the acceptor-labeled antibody. Antibodies labeled with NHS-functionalized ruthenium complexes have also been used for the electrochemiluminescence detection of interferon alfa-2b in human serum. Labeled antibodies were prepared by incubating the antibody with the Ru-NHS ester at a molar excess of 10 for 1 h at room temperature with agitation. Unreacted dye was removed by dialysis.

Fluorescent nanoparticles exhibit considerable advantages in detection over organic fluorescent dye molecules and quantum dots. The superiority of nanoparticles is apparent in their stability, brightness, and ease of functionalization for bioconjugation. Ow et al. [11] described a class of highly fluorescent core-shell nanoparticles, up to 20 times brighter and photostable than their constituent fluorophore. The fabrication of such molecules employs a microemulsion technology. This method encapsulates fluorescent dye molecules into a silica matrix, giving rise to dye-doped nanoparticles with high intensity of fluorescent signal. The excellent photostability of doped nanoparticles is due to exclusion of oxygen by the silica encapsulation. Surface modification post-fabrication allows efficient conjugation to biomolecules. Silica is easy to modify, through either NHS activation, silanization, or carboxyl modification [5]. SEM, TEM, and fluorescence spectroscopy were used to characterize the doped nanoparticles to determine size uniformity, quantum yield, fluorescent lifetime, and fluorescent intensity. Each nanoparticle encapsulates thousands of fluorescent dye molecules in the protective silica matrix, providing a highly amplified and reproducible signal for fluorescence-based bioanalysis. Traditional immunoassays employ the use of one or more fluorescent dye molecules linked to an antibody to trace the antibody-antigen binding interaction. Nanoparticles have been successfully conjugated to antibodies, proteins, streptavidin, and avidin. The efficiency of the conjugation process can be monitored and the conjugation rate predicted, with respect to the initial ratio of biomolecule to nanoparticle (NP) by applying mathematical formulae which take into account the size of the nanoparticles,

their capacity for binding (mg protein present per  $\text{mm}^2$  of nanoparticle surface), and the mean diameter of the nanoparticles.

## Key Research Findings

The use of fluorescence in immunoassay for the detection of medically and biologically important analytes has become an important tool in diagnostics. Sun [7] showed the use of quantum dots as novel fluorescent probes for a glass chip-based sandwich immunoassay. Carboxyl-coated quantum dots were linked to antibodies via EDC chemistry. Glass chips were silanized for the immobilization of capture antibodies, and a sandwich assay was successfully developed on the chip, with detection using laser confocal scanning microscopy and array software. Luminescent quantum dot bioconjugates were also prepared using engineered polyhistidine terminated proteins. A recombinant single chain antibody fragment (scFv) specific for trinitrotoluene (TNT) was conjugated to CdSe-ZnS quantum dots through a carboxy terminal histidine tail, and the conjugated scFv were used to detect TNT in a competitive immunoassay.

The use of nanoparticles to improve the performance and sensitivity of immunoassays is an emerging technology. Seydack [6] reported on the use of nanoparticles in immunoassays with improved detection limits, multiplexing of assays, reduction in photobleaching, signal amplification, and improved sensitivity. Both dye-doped and metallic-enhancement nanoparticles are easily fabricated for use as fluorescent tags in immunosensing technologies. The preparation and characterization of tetramethylrhodamine (TMR), ruthenium, and fluorescein-doped nanoparticles was reported by Lian et al. [5], and the application of such molecules in solid-phase and biochip applications was shown. The applications of nanoparticles in immunoassay formats include direct and indirect binding assays for the detection hIgG, using avidin nanoparticles in direct comparison with Texas Red and quantum dots [5]. DNA microarray technology was also explored, using genomic

DNA from *Pseudomonas aeruginosa*. Dilutions of DNA were printed on gamma amino propyl silane (GAPS) slides, and post-hybridization labeling with avidin nanoparticles versus streptavidin-Cy5 was investigated. Clusters of arrayed DNA were imaged, and under the same conditions, the nanoparticle spots were much brighter. Lian et al. also investigated the use of nanoparticles in a protein microarray application with high detection sensitivity reported. The use of europium (III) chelate-doped nanoparticles as donors in homogeneous proximity assays has also been reported. Antibody fragment-coated nanoparticles are prepared by activation of the carboxyl groups on the nanoparticles with EDC/NHS chemistry. Covalent linkage occurs between the activated carboxyl groups on the nanoparticle surface and amino groups on the Fab. Lochner et al. [12] show the principle of nanoparticle-enhanced fluorescence. This phenomenon occurs when the surface of a metallic nanoparticle is illuminated, generating an electromagnetic field. The interaction of this field with nearby fluorophores results in a fluorescent enhancement effect. Silanized plates were used to couple silver nanoparticles on the surface, and Fc-specific antibody fragments were used to immobilize antigen-specific antibodies. Fluorescein-labeled antigen was detected in the sample only in the presence of the silver colloid.

Tully et al. [13] described a fluorescence-based immunoassay for the detection of a *Listeria monocytogenes*-derived protein, internalin B, using quantum dots as fluorescent labels. A polyclonal antibody-based competitive assay with a limit of detection of 12 ng/ml was developed. The multicolor sensitivity and stability of quantum dots makes them ideal for the analysis of complex samples for histology, pathology, and cytology in immunostaining applications. Quantum dots are similar in size to organic dyes so can be substituted for current fluorescence-based techniques [6]. The main advantage of quantum dots for the immunostaining of *L. monocytogenes* is the ability to multiplex without the need for multiple excitation sources, thus facilitating double or triple immunostaining of bacterial cells surface components.

## Future Directions for Research

Fluorophores can be covalently attached to macromolecules, and the emission of these fluorescent probes can be from UV to NIR. Probes are available with short (nanosecond) to long (micro- to millisecond) lifetimes. Future trends in fluorescent labeling for biological applications lie with a number of emerging technologies. Labels with better spectral properties such as larger Stokes shift, greater stability, solubility in aqueous solution, and high brightness are constantly being developed. The evolution of these tags coupled with advances in functionalization methods for inorganic probes is giving rise to a new generation of sophisticated probes suitable for high-throughput screening in diagnostics. Metallic nanoparticles and inorganic probes are highly complex, spectroscopically tailored tags that improve assay sensitivity, reproducibility, and multiplexing capabilities. Easily functionalized nanoparticles, quantum dots, and nanocrystals are consistently brighter and more robust and will provide important reagents in the future for fluorescence-based detection. Another key group of fluorescent tags are those genetically engineered into biological molecules through in vivo labeling and the cloning of naturally fluorescing moieties. Further development of existing tags and generation of novel probes, as outlined, will have a very significant influence in the area of fluorescence-based analysis in the near future.

**Acknowledgments** The financial support of Enterprise Ireland and Science Foundation Ireland is gratefully acknowledged.

## References

1. Lakowicz JR (1999) Principles of fluorescence spectroscopy, 2nd edn. Kluwer/Plenum Publishers, New York
2. Hermanson GT (1996) Bioconjugate techniques. Academic, London
3. O’Kennedy R, Thornes RD (eds) (1997) Coumarins biology, applications and mode of action. Wiley, Chichester
4. Handl HL, Gillies RJ (2005) Lanthanide-based luminescent assays for ligand-receptor interactions. *Life Sci* 77:361–371

5. Lian W, Litherland S, Badrane H, Tan W, Wu D, Baker HV, Gulig PA, Lim DV, Jin S (2004) Ultrasensitive detection of biomolecules with fluorescent dye-doped nanoparticles. *Anal Biochem* 334:135–144
6. Seydack M (2005) Nanoparticle labels in immunosensing using optical detection methods. *Biosens Bioelectron* 20:2454–2469
7. Sun C, Yang J, Li L, Wu X, Liu Y, Liu S (2004) Advances in the study of luminescence probes for protein. *J Chromatogr B* 803:173–190
8. Wolfbeis OS (ed) (1993) Fluorescence spectroscopy: new methods and applications. Springer, Berlin/Heidelberg/New York
9. O’Riordan T, Soini A, Soini J, Papkovsky DB (2002) Performance evaluation of the phosphorescent porphyrin label: solid-phase immunoassay of  $\alpha$ -fetoprotein. *Anal Chem* 74(22):5845–5850
10. Castellano F, Dattelbaum JD, Lakowicz JR (1998) Long-lifetime Ru (II) complexes as labeling reagents for sulfhydryl groups. *Anal Biochem* 255:165–170
11. Ow H, Larson DR, Srivastava M, Baird BA, Webb WW, Wiesner U (2005) Bright and stable core-shell silica fluorescent nanoparticles. *Nanoletters* 5(1): 113–117
12. Lochner N, Lobmaier C, Writh M, Leitner A, Pittner F, Gabor F (2003) Silver nanoparticle enhanced immunoassay: one step ‘real-time’ kinetic assay for insulin in serum. *Eur J Pharm Biopharm* 56:469–477
13. Tully E, Hearty S, Leonard P, O’Kennedy R (2006) The development of rapid fluorescence-based immunoassays, using quantum dot-labelled antibodies for the detection of *Listeria monocytogenes* cell surface proteins. *Int J Biol Macromol* 39(1–3):127–134
14. Lakowicz JR (1983) Principles of fluorescence spectroscopy, 1st edn. Plenum Press, New York

---

## Fluorescent Probes

### Synonyms

Fluorophores; Luminescent labels

### Definition

Fluorescent probes are relatively small molecules that are used to label biomolecules such as proteins, antibodies, and nucleic acids. They contain functional groups and specific physical and chemical characteristics that confer suitability

for their use as detection moieties. To date, thousands of fluorescent probes are known, each with varying spectral properties. Fluorophores may be intrinsic or extrinsic in nature. Intrinsic fluorophores are naturally occurring, whereas extrinsic fluorophores are added to generate a fluorescence signal to facilitate measurement of a specific target molecule. Fluorescent labels have provided excellent sensitivity for a range of assay systems that can be applied to the determination of almost any analyte.

### Cross-References

- ▶ [DNA Microarrays](#)
- ▶ [Fluorescent Labeling](#)
- ▶ [Lab-on-a-Chip \(General Philosophy\)](#)
- ▶ [Quantum Dot](#)

---

## Fluorescent Thermometry

Vinay K. Natrajan and Kenneth T. Christensen  
Department of Mechanical Science and  
Engineering, University of Illinois, Urbana,  
IL, USA

### Synonyms

Photoluminescence; Temperature measurement using fluorescence

### Definition

Fluorescent thermometry involves the use of a fluorescent dye, whose fluorescence intensity is a strong function of temperature, to infer the temperature of a fluid or surface. The dye is dissolved in a fluid of interest, or coated on a surface, and is excited to fluoresce by incident light. The fluoresced light is recorded with a CCD camera, and variations in its intensity are proportional to variations in the local temperature.

### Overview

There exists a growing demand for the development of advanced diagnostics for high-precision temperature measurements at the microscale. This demand is driven by the ever-increasing use of complex microfluidic devices such as micro-total analysis systems ( $\mu$ -TAS) and  $\mu$ -heat exchangers. Lab-on-a-chip devices, which integrate multiple complex laboratory functions onto a single chip-sized substrate, often require precise temperature control to maximize the productivity of chemical operations like mixing, reactions, and separations. Such control becomes especially critical when electrokinetic pumping is used for driving flow through these devices, as the current flowing through the buffer solution can result in significant internal heat generation, a phenomenon known as Joule heating. Since most microfluidic-based MEMS devices utilize very high heat and mass transfer rates, a thorough understanding of their thermal transport characteristics is paramount for optimizing their design for increased performance and reliability.

While several methods exist for measurement of fluid and/or surface temperature at the macroscale, the direct application of these methods to the microscale may not be possible. In particular, the accuracy of these techniques at the microscale can be compromised because dissipation of thermal gradients occurs over extremely short time scales due to high heat transfer rates and large surface area-to-volume ratios. Therefore, obtaining accurate measurements of fluid temperature at the microscale is still a challenge. Until recently, temperature measurements in microfluidic systems were limited to measurements of bulk fluid temperature at the inlet and outlet of microfluidic sections or measurements of the substrate's temperature itself. With regard to local temperature measurements, the use of high-precision thermocouple probes to measure fluid and/or substrate temperature is generally restrictive. In addition to being physically intrusive, these probes can suffer from poor spatial resolution since most probes have a characteristic size of a few microns. Alternatively, microfluidic devices can be fabricated with integrated microscale resistance temperature

detectors (RTDs) embedded in the substrate with spatial extents on the order of a few microns (Wu et al. [1]). However, this fabrication procedure can be quite complex, and, like thermocouple probes, RTDs suffer from poor spatial resolution which limits their ability to resolve local thermal gradients. Further, while these sensors are convenient for monitoring surface temperature, they do not provide a direct measure of local fluid temperature.

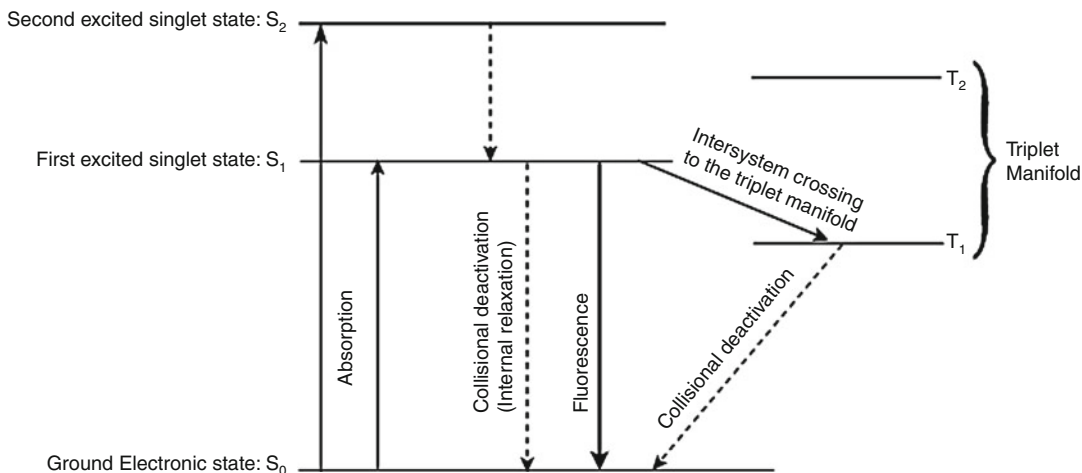
In contrast, fluorescent thermometry (a specific application of the more general laser-induced fluorescence (LIF) technique) represents one of the most accurate temperature measurement techniques at the macroscale. In this technique, a fluorescent dye whose fluorescence intensity is a strong function of temperature is dissolved in a fluid of interest or is coated on a surface of interest. In the case of fluid temperature measurement, the fluid in a plane of interest is illuminated with incident light (typically a sheet of laser light), and the dye is excited to fluoresce. In the case of surface temperature measurement by fluorescence, the surface coated with the dye would be illuminated with incident light. In both cases, the fluoresced light is imaged with a CCD camera, and the resulting image is converted to a temperature field using an a priori temperature calibration of the dye's fluorescence intensity. Unlike macroscale LIF where multiple directions of optical access are usually available, fluorescent thermometry at the microscale is often complicated by the fact that most microfluidic devices have only one principal direction of optical access, usually in a direction normal to the plane of the network. Therefore, illumination of the test section from this direction will inherently illuminate the entire depth dimension of the domain of interest. There is no adverse effect from volume illumination in the case of surface temperature measurement since presumably only the bottom surface of the device would be coated with the dye. However, in the case of fluid temperature measurement by fluorescence, the dye is homogeneously dissolved in the solvent, meaning fluorescent molecules along the entire depth dimension are excited to fluoresce. As a result, fluid temperature measurements via

fluorescence at the microscale often suffer from significantly more out-of-focus noise than similar measurements at the macroscale where sheets of laser light minimize the volume of fluid illuminated in the depth direction. Furthermore, the extremely small thermal transport time scales at the microscale render measurements of instantaneous and unsteady temperature fields much more difficult than similar measurements at the macroscale. Nevertheless, significant progress has been made in adapting fluorescent thermometry to the microscale, and this contribution summarizes the state of the art in this regard. Single- and two-dye techniques are discussed in detail, and representative experimental results are summarized.

## Basic Methodology

As illustrated in Fig. 1, when a photon of a given energy is absorbed by a fluorophore, the energy state of the molecule transitions from the ground state,  $S_0$ , to higher electronic states ( $S_1$ ,  $S_2$ , etc.). Energy is subsequently dissipated at these excited states until the molecule reaches the lowest level of the first excited singlet state,  $S_1$ . Thereafter, the molecule at the first singlet state can return to the ground state in multiple ways. The process by which the excited molecule returns to the  $S_0$  state by a radiative decay process, wherein no further energy is dissipated by collisions and its return to the ground state occurs purely by the emission of energy, is referred to as fluorescence. In such a scenario, a portion of the remaining energy is lost by the molecule before the emission occurs, meaning that the emitted energy is of a longer wavelength than the energy it initially absorbed. The shift in wavelength of the fluoresced light relative to the absorption wavelength is known as Stokes shift.

While the emission of fluoresced light represents one possible path for the transition of a molecule from the first singlet state to the ground state, there exist other non-radiative processes, like internal conversions and intersystem crossings, by which an excited molecule can return to its ground state (Fig. 1). As such, the



**Fluorescent Thermometry, Fig. 1** Schematic illustrating the energy levels of a diatomic molecule (Adapted from Guilbault [2])

efficiency of the fluorescence emission by a dye is often quantified by its quantum efficiency

$$\phi = \frac{k_r}{k_r + k_{nr}}, \quad (1)$$

where  $k_r$  is the rate of emission of photons via fluorescence and  $k_{nr}$  represents the rate at which non-radiative relaxation to the ground state occurs. Similarly, the efficiency of a dye can also be characterized by the fluorescence lifetime of its excited species

$$\tau = \frac{1}{k_r + k_{nr}}, \quad (2)$$

which represents the average time the fluorophore remains in its excited state.

For a dye of concentration  $C$  ( $\text{kgm}^{-3}$ ) illuminated with an incident light flux of intensity  $I_0$  ( $\text{Wm}^{-3}$ ), the fluorescence energy emitted per unit volume,  $I$  ( $\text{Wm}^{-3}$ ), is

$$I = I_0 C \phi \epsilon, \quad (3)$$

where  $\epsilon$  ( $\text{m}^2 \text{kg}^{-1}$ ) is the absorption coefficient of the dye. Variations in  $I$  with temperature are predominantly attributable to a dye's quantum efficiency,  $\phi$ , which displays some degree of temperature dependence for most organic dyes.

While this temperature sensitivity is small for most dyes (typically a fraction of a percent per K), there are some dyes that exhibit significantly more temperature dependence, like rhodamine B ( $2.3 \% \text{K}^{-1}$ ). In contrast,  $\epsilon$  has a very weak temperature dependence, usually of the order of  $0.05 \% \text{K}^{-1}$  [3]. Therefore, by employing a dye whose quantum efficiency is highly sensitive to temperature variations, the temperature distribution in a fluid or on a surface can be inferred from intensity variations in the light fluoresced by the dye.

### Single-Dye Fluorescence

Temperature measurement using a single fluorescent dye is the simplest adaptation of fluorescent thermometry at the microscale. If the intensity of the illuminating light flux,  $I_0$ , is assumed constant in both space and time, then the ratio of the emitted fluorescence intensity measured at a temperature  $T$  to that measured at a reference temperature  $T_{\text{ref}}$  for a fixed dye concentration is given by the ratio of the quantum efficiencies of the fluorescent dye at these temperatures:

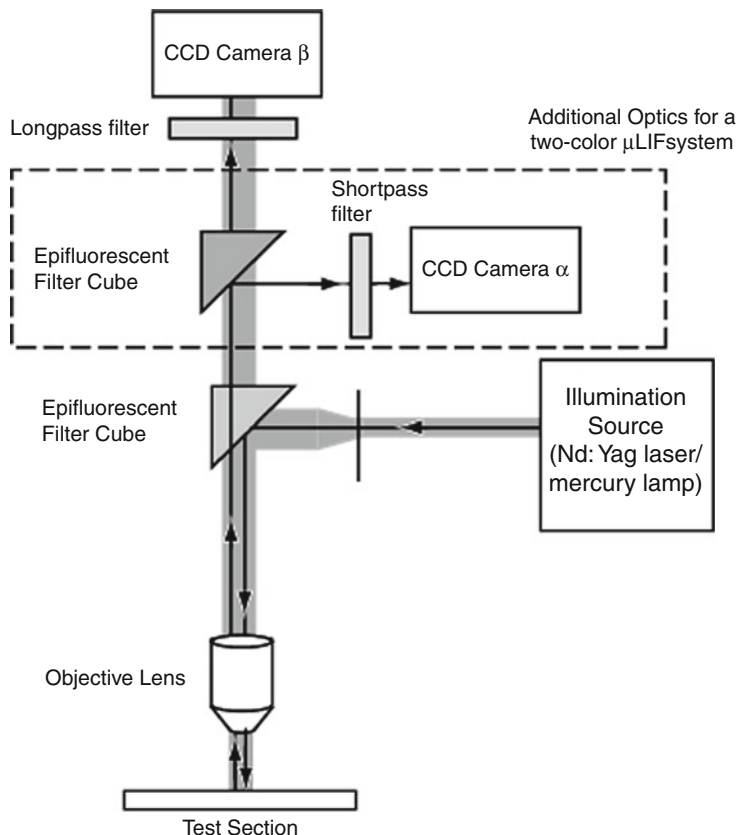
$$\frac{I}{I_{\text{ref}}} = \frac{\phi(T)}{\phi(T_{\text{ref}})} = f(T). \quad (4)$$

Therefore, assuming that the variation of the ratio of quantum efficiencies, or equivalently the

### Fluorescent Thermometry,

#### Fig. 2

Representative schematic of the optical configuration for microscale fluorescence thermometry. The *dashed box outlines* the additional optics required for a two-dye fluorescence imaging



ratio of the emitted fluorescence intensities, has been properly calibrated as a function of temperature, an estimate of the unknown temperature distribution is arrived at by comparing its fluorescence intensity to that given by the calibration. The spatial resolution of this measurement is defined by the imaging optics, while the temporal resolution is defined either by the framing rate of the imaging camera or by the illumination time of the incident light (since the fluorescence lifetime, given by Eq. 2, is quite short for most dyes – typically a few ns to a few  $\mu$ s).

A schematic of the imaging configuration used for the measurement of temperature via single-dye fluorescence is presented in Fig. 2. Light from an illumination source, like an Nd:YAG laser, argon-ion laser, or a mercury-arc lamp, is directed through an epi-fluorescent filter cube and through a microscope objective lens to excite the fluorescent dye molecules in the microfluidic

device. The filter cube allows the relatively weak fluorescent signal to pass to a CCD camera while simultaneously blocking the intense illumination wavelength. Given the relatively weak fluorescent signal from the dye, the CCD camera employed must have very low noise levels and a high sensitivity to the emitted wavelength in order to maximize the signal-to-noise ratio of the measurement. A reference image is first acquired at a known, preferably uniform, temperature, while a second image is acquired at an unknown, possibly nonuniform, temperature. A ratio of intensities is then obtained by dividing the intensity recorded at each pixel of the measurement image by the corresponding intensity at the same pixel of the reference image. This intensity ratio is then converted to temperature using an a priori calibration of the dye that tabulates the variation of the fluorescence intensity ratio with temperature (Eq. 4).

## Two-Dye Fluorescence

As outlined in single-dye fluorescence, the fluorescence intensity measured by single-dye fluorescence depends solely on temperature only if the dye concentration and the incident light flux are constant. While maintaining a constant dye concentration is quite simple, sustaining a constant incident light flux is much more difficult since all illumination sources exhibit some degree of spatial and/or temporal variability in their intensity. As such, the measured fluorescence intensity embodies not only temperature variations through  $\phi$  but also variations in the illuminating intensity through  $I_0$ . Therefore, the accuracy of temperature measurements via single-dye fluorescence is strongly dependent on the stability and homogeneity of the illuminating light source. To alleviate such issues, a two-dye methodology was introduced by Sakakibara and Adrian [3] to improve the accuracy of macroscale fluorescent thermometry. In this technique, spatial and/or temporal intensity variations within the illuminating light source are accounted for via a second fluorescent dye whose quantum efficiency exhibits little, or no, temperature dependence. Therefore, while the intensity of the fluoresced light from the temperature-dependent dye embodies both variations in temperature and illuminating intensity, any variations in the fluorescence intensity of the temperature-insensitive dye are directly attributable to variations in the illuminating intensity. Therefore, one can account for variable illumination intensity by simultaneously imaging the fluoresced light from each dye with separate CCD cameras and normalizing the fluorescence intensity of the emission from the temperature-sensitive dye by that of the temperature-insensitive dye.

Temperature measurement by two-dye fluorescence requires efficient separation of the two fluorescent emissions so that their emissions can be imaged separately over identical spatial domains at the same instant in time. Such separation is achieved by adding a second camera and additional spectral filters to the aforementioned single-dye optical arrangement (these additions are identified by the dashed bounding box in Fig. 2). In this optical arrangement, both dyes

must have similar excitation wavelengths since the same illumination source is typically used to simultaneously excite both dyes. However, the dyes must have different emission spectra so that they can be effectively separated using low- and high-pass spectral filters just upstream of the cameras. If the emission from the two dyes, labeled A (temperature sensitive) and B (temperature insensitive), is separated perfectly into cameras  $\alpha$  and  $\beta$ , the ratio of the fluorescence intensities recorded by both cameras is given by

$$\frac{V^\alpha}{V^\beta} = \frac{I_A}{I_B} = \frac{C_A \phi_A \epsilon_A}{C_B \phi_B \epsilon_B}, \quad (5)$$

where  $V^\alpha$  and  $V^\beta$  are voltage outputs from the CCDs of cameras  $\alpha$  and  $\beta$ , respectively. Note that this ratio depends on the temperature via  $\phi_A/\phi_B$  but is independent of the incident light flux,  $I_0$ . In practice, however, it is nearly impossible to obtain perfect separation of the two emissions,  $I_A$  and  $I_B$ , both because the emission spectra of most organic dyes are rather broad, meaning some overlap of their emissions is to be expected, and because spectral filters are inherently imperfect (filtering efficiencies of 90–95 % are typical). Sakakibara and Adrian [3] considered the case of imperfect separation, wherein some fractions of the fluorescent intensity of the emission from dyes A and B are imaged by cameras  $\beta$  and  $\alpha$ , respectively, and derived the expression

$$\frac{V^\alpha}{V^\beta} = \frac{I_A}{I_B} = \frac{C_A C'_B \phi_A \phi'_B V_{C_B=0}^\alpha + C_B C'_A \phi_B \phi'_A V_{C_A=0}^\alpha}{C_A C'_B \phi_A \phi'_B V_{C_B=0}^\beta + C_B C'_A \phi_B \phi'_A V_{C_A=0}^\beta}, \quad (6)$$

that accounts for this effect. Here,  $C'_A$ ,  $\phi'_A$ ,  $V_{C_B=0}^\alpha$ , and  $V_{C_B=0}^\beta$  are the measured parameters for fluorescent dye A with  $C_B = 0$ , and  $C'_B$ ,  $\phi'_B$ ,  $V_{C_A=0}^\alpha$ , and  $V_{C_A=0}^\beta$  are the measured parameters for fluorescent dye B with  $C_A = 0$ . In this context,  $V_{C_A=0}^\alpha$ ,  $V_{C_A=0}^\beta$ ,  $V_{C_B=0}^\alpha$ , and  $V_{C_B=0}^\beta$  are constants for a given optical configuration. Therefore, the intensity ratio  $I_A/I_B$  is only a function of the concentration of the two dyes,  $C_A$  and  $C_B$ , and the temperature,  $T$ .

Apart from issues related to properly imaging the light fluoresced by the two dyes, accurate determination of the temperature distribution over the chosen spatial domain in the two-camera arrangement requires that both cameras have identical fields of view. Therefore, one must ensure not only that the magnifications of the two CCD cameras are identical but also that the cameras are aligned such that each pixel location in the two CCD arrays map back to the same physical coordinate in the measurement domain. This alignment is a crucial step in the two-dye methodology because one must divide the two intensity fields pixel-by-pixel, as outlined in Eq. 6, to determine the temperature distribution over the spatial domain of interest. Therefore, any misalignment of the two CCD cameras will prevent one from properly accounting for spatial variations in the illuminating intensity, thereby reducing the overall accuracy of the measurement.

### Dye Selection

The fluorescent properties of an organic dye are governed by the chemical structure of the dye molecules and their interaction with the solvent molecules. In general, dyes whose molecules have rigid and planar structures display higher fluorescence efficiencies, meaning that their fluorescence can be imaged with very high signal-to-noise ratios. Unfortunately, such dyes seldom display a strong temperature sensitivity since the temperature dependence of a dye is often governed by the structural mobility of its functional groups. For instance, while rhodamine 101 exhibits a temperature-insensitive quantum yield close to 100 %, rhodamine B (RhB), when dissolved in ethanol, has a quantum yield of roughly 40 % at 25 °C that steadily decreases to only a few percent with increasing temperature. This RhB behavior is attributed to the increased mobility of its diethylamino groups with increasing temperature compared to the relatively rigidized diethylamino groups in rhodamine 101. Therefore, one often must sacrifice some signal-to-noise ratio during imaging for strong temperature sensitivity. In addition, when measuring fluid temperature, the fluorescent

properties of a dye can be highly dependent on the properties of the solvent itself. In most cases, solvents with higher viscosities increase the fluorescence efficiency of dyes since a higher viscosity not only restricts the mobility of the functional groups in the dye molecules but also minimizes the energy transfer between these molecules by reducing the number of molecular collisions. Rhodamine B, for instance, exhibits a quantum yield of nearly 100 % in viscous solvents like glycerol as compared to 40 % in less viscous ethanol. Further, the fluorescent efficiencies of most organic dyes also depend on other solvent properties in sometimes complicated fashions. For instance, although using water as a solvent can counteract inhomogeneities in the temperature distribution of the dye solution due to thermal energy released during the lasing process, water is known to enhance aggregation of dye molecules to form dimers and higher aggregates. These aggregates, which have different absorption spectra compared to the dye molecules themselves, can adversely affect the accuracy of the temperature measurement. Hence, the choice of fluorescent dyes and their solvents is highly dependent on the application under consideration (the reader is directed to Drexhage [4] and Guilbault [2] for a more detailed explanation of the structure and properties of fluorescent dyes).

For temperature measurement by single-dye fluorescence, the temperature sensitivity of a dye, specifically its quantum efficiency, effectively defines the temperature resolution of the measurement itself. Rhodamine B is the most common temperature-dependent fluorescent dye used in both macro- and microscale liquid applications because of its relatively strong temperature sensitivity of 2.3 % K<sup>-1</sup> in water over a temperature range of 0–120 °C. This dye is also soluble in many other organic solvents, like ethanol, making it a practical choice in a variety of microfluidic applications. Moreover, its absorption spectrum is rather broad (470–600 nm with a peak at 554 nm), meaning it can be readily excited with conventional illumination sources like mercury-arc lamps as well as argon-ion (continuous) and Nd:YAG (pulsed) lasers. Further, its emission spectrum is also

rather broad (centered at 575 nm) so a portion of its fluoresced light can be faithfully filtered from the illuminating wavelength. Pyrene is another fluorescent dye whose quantum efficiency exhibits relatively strong temperature dependence ( $0.9\% \text{ K}^{-1}$ ) in the range 20–130 °C when dissolved in decane. This dye has an excitation peak at 330 nm and a broad emission spectrum centered at 475 nm. For a more comprehensive list of temperature-sensitive fluorescent dyes, the reader is referred to Lou et al. [5].

In the case of two-dye fluorescence, the ideal choice of dyes would include one dye that has strong temperature sensitivity and one that has strong temperature insensitivity. Such a combination will maximize the temperature sensitivity of the ratio of their quantum efficiencies as given by Eq. 6. However, one must also consider other constraints on the choice of dyes, particularly their absorption and emission spectra. As noted earlier, since the two dyes are typically excited by the same illumination source, both dyes should have similar absorption spectra. In addition, both dyes should exhibit strong Stokes shifts so that the relatively weak fluoresced light from both dyes can be efficiently separated from the more intense illuminating wavelength prior to imaging. However, it is also paramount that the dyes have as different emission spectra as possible so that they can be effectively separated from one another prior to imaging. Finally, in the case of fluid temperature measurements, both dyes must also exhibit good solubility characteristics in the chosen solvent, particularly homogeneity at the molecular scale.

As in the single-dye technique, RhB (absorption and emission peaks of 554 and 575 nm, respectively) is generally chosen as the temperature-sensitive dye in two-dye fluorescence because of its broad absorption and emission spectra as well as its solubility in a number of commonly used solvents. Rhodamine-110 (Rh110) is often chosen as the temperature-insensitive dye because it exhibits a weak temperature sensitivity of  $0.13\% \text{ K}^{-1}$  in water and its emission peak of 520 nm is far enough from that of RhB to achieve efficient separation of the two emission signals. However, its absorption peak at

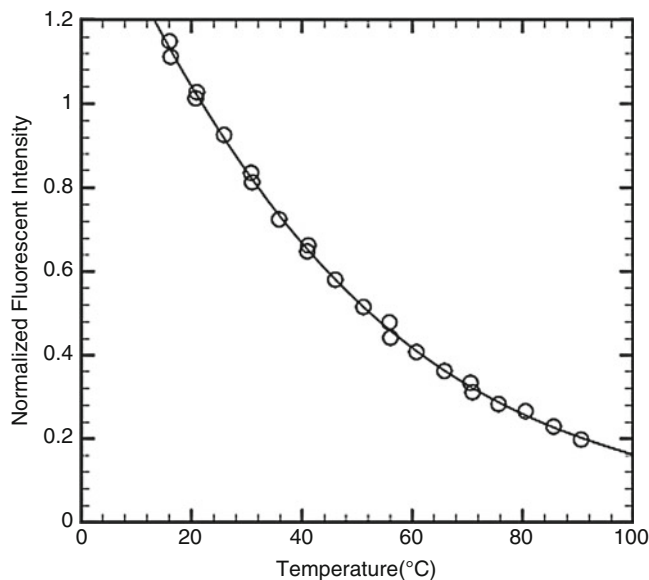
496 nm implies that its use is limited to cases where an argon-ion laser, or an alternative illumination source of similar wavelength, is employed. In situations where an Nd:YAG laser is used for illumination (which emits at 532 nm), Nile red (absorption and emission peaks of 553 and 620 nm, respectively) represents an alternative temperature-insensitive dye ( $0.1\% \text{ K}^{-1}$ ), particularly since its emission spectrum can be effectively separated from that of RhB. Unfortunately, Nile red is not soluble in water, although Nile red and RhB are both soluble in ethanol. Rhodamine-101 (Rh101; absorption and emission peaks at 575 and 635 nm, respectively) and rhodamine-6G (Rh6G; absorption and emission peaks at 520 and 566 nm, respectively), both of which are soluble in ethanol, can also be used as temperature-insensitive dyes. However, one must select a more compatible temperature-sensitive dye for use with Rh101 and Rh6G as the former has an absorption spectrum that overlaps the emission spectrum of RhB and the latter has an emission spectrum that significantly overlaps that of RhB. Finally, fluorescein, which is soluble in ethanol, represents another option as a temperature-insensitive dye because of its high quantum yield of 0.97 and its convenient absorption and emission peaks at 500 and 545 nm, respectively.

### Temperature Calibration

The exact temperature dependence of the chosen dye(s) must be known before the measured intensity ratio fields, given by Eq. 4 for single-dye fluorescence and Eq. 6 for two-dye fluorescence, can be faithfully converted to temperature fields. In the context of single-dye fluorescence, this calibration is accomplished by isolating a fixed amount of the chosen dye at a known concentration in a well-insulated reservoir whose temperature is both known and precisely controlled. One then maintains the dye solution at a known temperature, begins illuminating the dye solution, and acquires an ensemble of images of the light fluoresced by the dye using the same optical configuration outlined earlier (Fig. 2). The temperature of the dye is then varied slightly, and a new ensemble of

### Fluorescent Thermometry,

**Fig. 3** Representative calibration curve illustrating the dependence of rhodamine B on temperature (Adapted from Ross et al. [6])



images is acquired at this new temperature. This procedure is repeated until image ensembles have been acquired at several known temperatures over the range expected in a given experiment. An average over each image ensemble and/or a spatial average over neighboring pixels is often performed at a fixed temperature to minimize variations in the intensity of the recorded fluorescence due to noise (attributable to variations in the intensity of the illuminating light as well as noise from the CCD array). This procedure yields a single, average intensity value associated with each temperature. These intensities are then normalized by the intensity of the fluoresced light at a reference temperature, yielding a calibration curve of intensity ratio (or equivalently quantum efficiency ratio) versus temperature. A typical calibration curve of RhB dissolved in deionized water at a concentration of 1 mmol/l is shown in Fig. 3 (adapted from Ross et al. [6]). Note that the dependence of RhB's intensity ratio on temperature is quite nonlinear.

In the context of two-dye fluorescence, the calibration methodology is identical except that one must now assess the temperature dependence of each dye. This calibration is accomplished by applying the procedure outlined above to the temperature-sensitive and temperature-insensitive

dyes separately, yielding the temperature dependence of each dye's quantum efficiency as

$$\phi_{A(B)}(T) = \phi_{A(B)}(T = T_{\text{ref}}) \frac{I_{A(B)}(T)}{I_{A(B)}(T = T_{\text{ref}})}, \quad (7)$$

where  $T_{\text{ref}}$  is a reference temperature at which the quantum efficiency of dye  $A(B)$  is known.

### Photobleaching

As illustrated in Fig. 1, a fluorophore that is excited to higher energy levels often dissipates a portion of its energy that is in excess of the first excited singlet state,  $S_1$ . Ideally, the highest fluorescent efficiencies are obtained when a reverse transition from the  $S_1$  state to the  $S_0$  state occurs by the spontaneous emission of photons in the form of fluoresced light. However, there are other non-radiative processes that can act to compete with the emission of fluoresced light, thereby decreasing the fluorescent efficiency of the dye. These non-radiative processes include internal conversions, wherein non-radiative relaxation brings the energy state back to the ground state,  $S_0$ , and intersystem crossings, where the energy state is converted to the triplet state. As a consequence, molecules in the triplet state, as well as those that are at singlet states higher than the  $S_1$  state, are susceptible to an

irreversible alteration of their chemical structures that can yield nonfluorescent compounds. This decrease in the emitted fluorescent intensity as a result of the decay of fluorescent molecules is termed photobleaching.

Prolonged exposure of the fluorescent molecules to high-intensity incident light can raise the energy level of these molecules to energy states that are higher than the  $S_1$  excited singlet state, thereby increasing the probability of degradation via the mechanisms detailed above. As such, minimizing the number of exposures and/or the exposure time to the incident illumination in conjunction with the use of lower excitation intensities and higher exciting wavelengths can aid in delaying the effects of photobleaching. In most measurements of fluid temperature, photobleaching effects are of little concern because the fluid in which the fluorescent dye is dissolved is typically moving through the measurement domain. In cases where the average time required for a dye molecule to enter and leave the image domain,  $\tau_d$ , is small compared to the time between exposures (defined by the framing rate of the imaging system), photobleaching losses are minimal since, on average, each dye molecule will only be exposed to a single exposure of incident light. If, however,  $\tau_d$  is large compared to the time between exposures, or  $\tau_d \rightarrow \infty$  (i.e., the limiting case of a stationary fluid or dye coated on a stationary surface), photobleaching effects are inevitable and can severely compromise the accuracy of the temperature measurement. One can attempt to account for these losses by performing an a priori photobleaching calibration that embodies such effects.

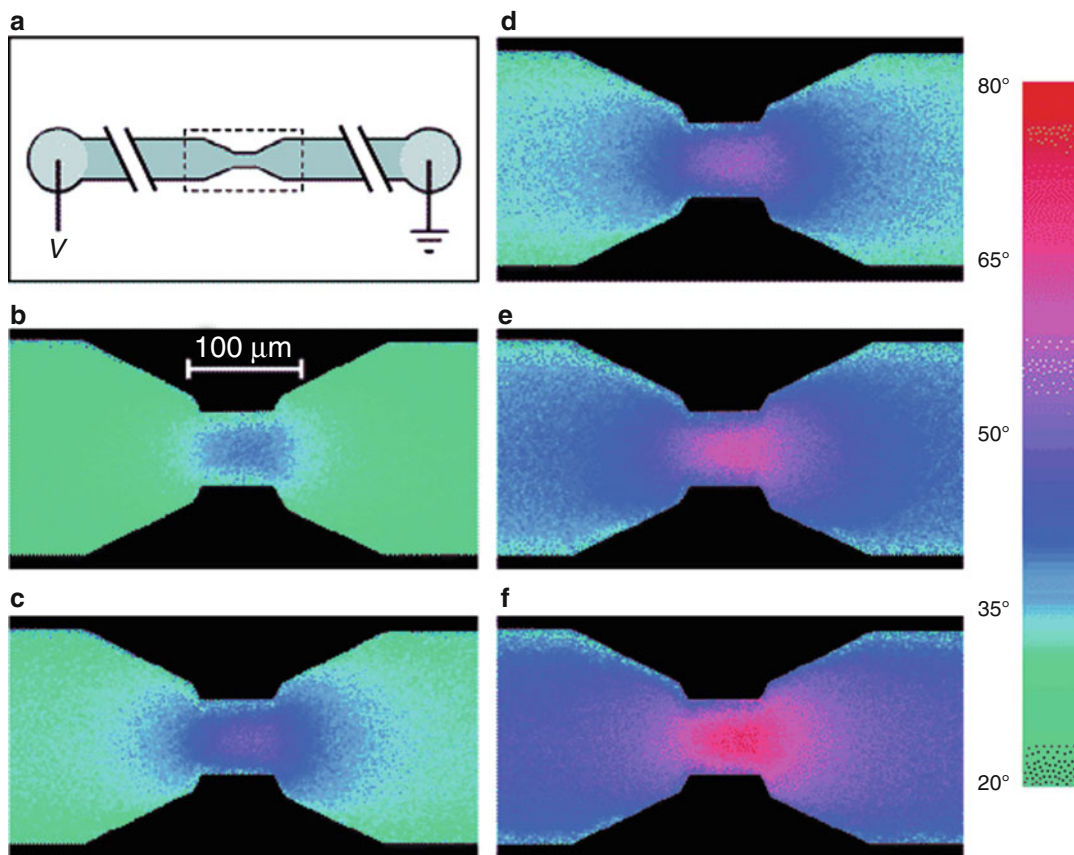
## Key Research Findings

### Single-Dye Fluorescence

Temperature measurement at the microscale by single-dye fluorescence was first accomplished by Ross et al. [6] using RhB as the temperature-dependent fluorescent dye and a mercury-arc lamp for illumination. Ross et al. [6] conducted measurements of fluid temperature distributions resulting from Joule heating in a microfluidic

circuit (Fig. 4a) due to electrokinetic pumping. Figure 4b–f present a time series of fluid temperature fields acquired by Ross et al. [6] through a constriction in the microfluidic circuit. These temperature fields clearly highlight the drastic rise in fluid temperature that can occur in the presence of electrokinetic pumping. A spatial resolution of  $1 \mu\text{m}$  and a temporal resolution of 33 ms were reported, yielding temperature uncertainties in the range  $2.4\text{--}3.5 \text{ }^\circ\text{C}$  with no spatial or temporal averaging. Improved measurement uncertainties (as low as  $0.03 \text{ }^\circ\text{C}$ ) were achieved but at a significant cost in spatial and/or temporal resolution. This single-dye methodology was also employed by Erickson et al. [7] to examine Joule heating and heat transfer in electrokinetically driven flows at the junctions of PDMS and PDMS/glass microfluidic devices. The temperature fields obtained with RhB excited by a mercury illumination source were found to agree with complementary numerical simulations to within  $\pm 3 \text{ }^\circ\text{C}$ . They also reported a repeatability of approximately  $\pm 2 \text{ }^\circ\text{C}$  and a noise level of  $\pm 1 \text{ }^\circ\text{C}$ . Improved noise levels were achieved by applying a Wiener-type filter to their raw image data.

Sato et al. [8] used single-dye fluorescence to study the two-dimensional surface temperature distributions associated with convective mixing in a T-shaped microchannel bound by a cover glass. Water at different temperatures was injected into the opposite inlets of their test section as a means of simulating a Hele-Shaw flow condition. Tris(bipyridine)ruthenium(II), with a temperature sensitivity of  $-3 \text{ } \% \text{ K}^{-1}$ , was spin coated on the interior of the cover glass of their test section and excited with a mercury illumination source as a means of measuring the wall temperature distribution. Sato et al. [8] reported a temperature resolution of  $0.26 \text{ }^\circ\text{C}$  with a measurement uncertainty of  $1.2 \text{ }^\circ\text{C}$ . They also acquired velocity fields in the same measurement domain using microscopic particle image velocimetry ( $\mu\text{PIV}$ ) which, in concert with the measured temperature fields, allowed direct evaluation of the heat fluxes due to conduction and convection. This analysis revealed that conduction effects were an order of magnitude larger than convective effects.



**Fluorescent Thermometry, Fig. 4** (a) Schematic of a microfluidic circuit through which flow is driven by electrokinetic pumping. (b–f) Temperature fields through

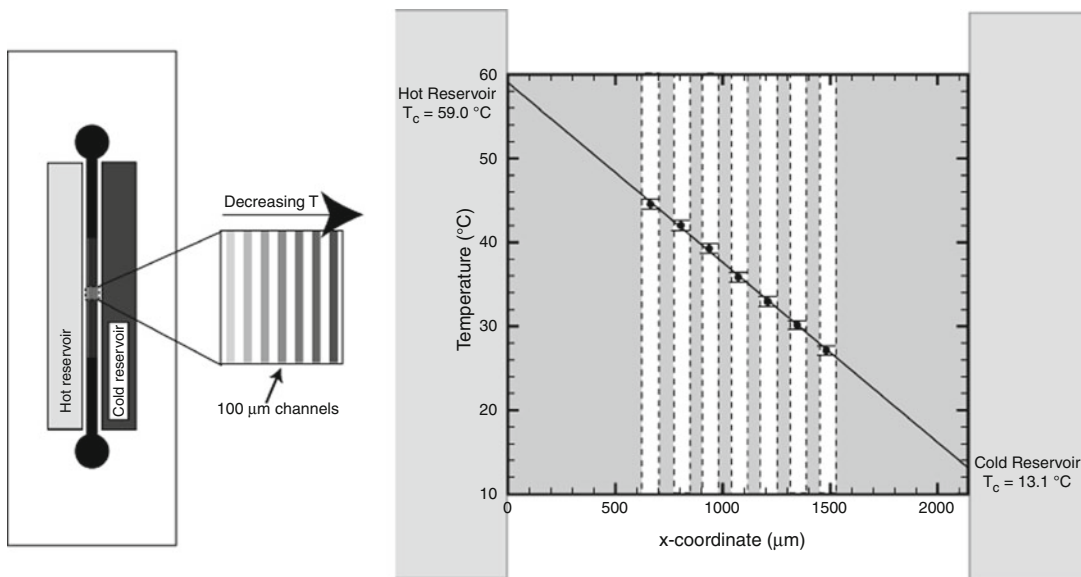
a constriction in the microfluidic circuit acquired 0.2, 0.4, 0.6, 1.4, and 3.8 s after the driving voltage was switched on (Adapted from Ross et al. [6])

### Two-Dye Fluorescence

Kim et al. [9] implemented the two-dye methodology to measure steady fluid temperature fields associated with thermal buoyancy in the interior of a 1-mm-wide closed test section at low Grashof-Prandtl numbers. Instead of employing a two-camera imaging arrangement, which requires accurate alignment of their fields of view, Kim et al. [9] instead used a single-camera arrangement to image the fluorescence emissions of RhB and Rh110 excited by a continuous Ar-ion laser. Separate imaging of the two emissions was achieved by alternating two band-pass filters just upstream of the camera, meaning that the RhB and Rh110 images were not acquired simultaneously but rather were separated in time by 50 ms as defined by the framing rate of the

CCD camera. As such, this imaging setup limited their measurements to steady-state temperature variations. The measured fluid temperature fields were found to agree well with complementary numerical simulations of the same thermal system. Kim et al. [9] cited measurement uncertainties from  $1.967^\circ\text{C}$  with a spatial resolution of  $150 \times 100 \mu\text{m}$  to  $0.412^\circ\text{C}$  with a spatial resolution of  $1,200 \times 800 \mu\text{m}$ . They also observed root-mean-square deviations of the measured temperatures from their computational predictions of  $2.3^\circ\text{C}$  and  $0.92^\circ\text{C}$  for spatial resolutions of 19 and  $76 \mu\text{m}$ , respectively.

More recently, Natrajan and Christensen [10] considered the development of a two-dye fluorescence method for temperature measurement using a pulsed, Nd:YAG laser as the illumination



**Fluorescent Thermometry, Fig. 5** (a) Schematic of the microfluidic device used by Natrajan and Christensen [10] to obtain a one-dimensional, steady-state temperature gradient. (b) Variation of temperature across the microfluidic device shown in (a). The *solid circles* represent the mean temperatures obtained via two-dye LIF measurements

while the *solid line* indicates the predicted linear temperature profile across the microchannel array. The span of the error bars represents twice the standard deviation for each mean temperature (Adapted from Natrajan and Christensen [10])

source. In this context, the Nd:YAG laser provided narrow pulse widths ( $\sim 5$  ns), enabling the measurement of instantaneous temperature fields. The experimental setup employed was a true dual-camera arrangement (identical to that illustrated in Fig. 2) implemented with two 12-bit, cooled CCD cameras with an effective chip area of  $1,392 \times 1,040$  pixels (Photometric, CoolSnap HQ2). Rhodamine B and sulforhodamine-101 were selected as the temperature-sensitive and temperature-insensitive dyes, respectively, yielding a sensitivity of 1.5 %/K for the dye mixture dissolved in ethanol. Natrajan and Christensen [10] validated this methodology via measurements of steady-state temperature in a microfluidic device specifically designed to maintain a linear temperature gradient. This device, designed in the spirit of the protocol outlined by Mao et al. [11], consisted of an array of seven parallel microchannels (width = 100  $\mu\text{m}$ , depth = 100  $\mu\text{m}$ ; made of PDMS) spaced 100  $\mu\text{m}$  apart that were fabricated between two large reservoirs (width = 3.2 mm,

depth = 3.2 mm) spaced 2 mm apart. As illustrated in Fig. 5a, one reservoir acted as a heat source and the other as a heat sink. Continuous circulation of heated and cooled water through the reservoirs ensured that they remained at constant temperatures. An independent measure of the temperature of the heated and cooled walls on either side of the channel array was obtained with two thermocouples inserted into the device through the hot and cold reservoirs. As reported by Mao et al. [11], such an arrangement generates a linear temperature gradient across the channel array which is filled with the dye mixture. When illuminated with the Nd:YAG laser, a measure of the temperature of the dye mixture in each channel was obtained by imaging the fluorescence emission from the dyes.

Figure 5b presents the measured variation of the steady-state temperature distribution across the microchannel array imposed by the hot and cold reservoirs computed from an ensemble of 60 instantaneous snapshots of the temperature field across the array as reported in Natrajan and

Christensen [10]. Note that variations of fluid temperature *within* each microchannel were not resolved, so the spatial resolution of these measurements is 100  $\mu\text{m}$  (i.e., the size of the microchannels). In this figure, the filled circles represent the mean temperatures of the dye mixture in the microchannel array obtained by averaging over the 60 samples, while the predicted linear temperature variation across the device (solid line in Fig. 5b) is obtained by fitting a line through the independently measured wall temperatures of the hot and cold reservoirs. An estimate of the uncertainty in the measurements was obtained by computing the standard deviation of the data sets comprising the ensemble. Figure 5b illustrates that the mean temperature of the dye mixture in each of the seven microchannels of the microfluidic device is in very good agreement with the predicted temperature distribution (span of error bars represent two standard deviations). The maximum deviation of the LIF-measured mean temperatures from the linear prediction is 0.4  $^{\circ}\text{C}$ , while the computed standard deviation lies in the range 0.5–0.63  $^{\circ}\text{C}$ . This range of standard deviations yields relative uncertainties (standard deviations normalized by measured temperatures) of 1.4–2.0 %, with the relative uncertainty increasing with decreasing temperature. Natrajan and Christensen [10] noted that these uncertainties are two to three times larger than those normally achieved in macroscale implementations of two-dye fluorescent thermometry, indicating that volume illumination can be a nontrivial source of error in LIF implementations at the microscale.

Chamarthy et al. [12] and Kim and Yoda [13] reported two other implementations of LIF thermometry for the measurement of steady-state fluid temperature at the microscale. Chamarthy et al. [12] used an RhB-Rh110 dye combination with mercury-arc lamp as the illumination source and reported temperature uncertainties of  $\pm 1.25$   $^{\circ}\text{C}$  for single-pixel measurements. On the other hand, Kim and Yoda [13] utilized an Ar-ion laser as the illumination source and cited uncertainties of  $\pm 1.25$   $^{\circ}\text{C}$  with an inplane resolution of 30  $\mu\text{m}$  obtained using fluorescein and

sulforhodamine-B as the temperature-sensitive and temperature-insensitive dyes, respectively. It is to be noted that while the fluorescence thermometry techniques described in Chamarthy et al. [12] and Kim and Yoda [13] are restricted to the measurement of steady-state temperature fields due to the use of continuous illumination sources, the implementation described by Natrajan and Christensen [10] utilizes a pulsed Nd:YAG laser as an illumination source and can be used for the instantaneous measurement of fluid temperature (the reader is referred to Natrajan and Christensen [14] where the authors acquire instantaneous temperature fields using the fluorescent thermometry technique described in Ref. [10] in order to characterize the convective heat transfer for laminar flow through a heated microchannel).

## Future Research Directions

While significant progress has been made in adapting fluorescent thermometry to microfluidic applications, the accuracy of the technique is still nearly an order of magnitude lower than similar implementations at the macroscale. This stark difference is attributable not only to the volume-illumination effect at the microscale but also to the relatively weak fluorescent signals that must be imaged with high signal-to-noise ratio. In the case of a stationary fluid (or equivalently a dye-coated stationary surface), the accuracy of the technique is further compromised by photobleaching effects. Therefore, significant effort must be put forth to solve such issues before fluorescent thermometry becomes a standard technique employed in a wide variety of practical applications. One promising path toward resolving the aforementioned issues involves the use of quantum dots as thermal markers, although researchers are just beginning to explore this intriguing possibility. Quantum dots are nanometer-scale semiconductors that are formed by confining the motion of electrons and/or holes (the absence of electrons) in all directions and can range in size from a few to a few hundred nanometers depending upon how

they are fabricated (typically by molecular beam epitaxy or self-assembly). Quantum dots behave similarly to fluorescent dyes in that they can be excited with an illumination source to fluoresce light with rather large Stokes shifts, and their fluorescence intensity is strongly dependent upon temperature (for instance, Walker et al. [15] and Vasudevanpillai et al. [16]). However, quantum dots are superior to fluorescent dyes in several respects. First, they have extremely broad absorption spectra, meaning a wider variety of illumination sources can be employed (like diode lasers). In addition, the wavelength of the light fluoresced by a quantum dot is a function of its size, so one can tailor the spectral characteristics of the thermal marker by simply altering its size. In this regard, smaller dots fluoresce toward the blue end of the spectrum, while larger dots fluoresce toward the red. This spectral behavior is attributable to the fact that larger dots are more efficient at absorbing weaker photons which tend to reside in the red portion of the spectrum. Finally, of critical importance is the fact that quantum dots display significantly higher quantum yields compared to fluorescent dyes and yet do not suffer from photobleaching effects. Therefore, not only is the signal-to-noise ratio of the fluorescence imaging greatly enhanced by using quantum dots as thermal markers, but their viability is not compromised by continued exposure to illuminating light as is unfortunately the case with fluorescent dyes. Of particular relevance is the work by Guasto and Breuer [17], where the authors use quantum dots as simultaneous temperature and velocity probes at the microscale. While the intensity distribution of the quantum dots are mapped to fluid temperature, the tracking of individual quantum dots yields particle displacement (and hence velocities). As such, all of these characteristics make quantum dot-based fluorescent thermometry an intriguing possibility for applications ranging from mesoscale surface temperature monitoring in electronics cooling, whereby the surface would be coated with a single layer of quantum dots, to temperature monitoring of microscale biological processes wherein precise temperature control is of critical importance.

## Cross-References

- ▶ [Fluorescence Measurements](#)
- ▶ [Fluorescent Labeling](#)
- ▶ [Laser-Induced Fluorescence](#)
- ▶ [Liquid Crystal Technique for Measuring Temperature](#)
- ▶ [Quantum Dot](#)
- ▶ [Resistance Temperature Detectors](#)
- ▶ [Temperature Measurement, Methods](#)
- ▶ [Thermocouples](#)

## References

1. Wu S, Mui J, Tai YC, Ho CM (1999) Micro heat exchanger by using MEMS impinging jets. In: Proceedings of the IEEE micro electro mechanical systems. Orlando, FL, USA
2. Guilbault GG (1990) General aspects of luminescence spectroscopy. In: Guilbault GG (ed) Practical fluorescence. Dekker, New York, pp 1–40
3. Sakakibara J, Adrian RJ (1999) Whole field measurement of temperature in water using two-color laser induced fluorescence. *Exp Fluids* 26:7–15
4. Drexhage KH (1990) Structure and properties of laser dyes. In: Schaefer FP (ed) Dye lasers. Springer, New York, pp 154–200
5. Lou J, Finegan TM, Mohsen P, Hatton TA, Laibinis PE (1999) Fluorescence-based thermometry: principles and applications. *Rev Anal Chem* 18:235–283
6. Ross D, Gaitan M, Locascio LE (2001) Temperature measurement in microfluidic systems using a temperature-dependent fluorescent dye. *Anal Chem* 73:4117–4123
7. Erickson D, Sinton D, Li D (2003) Joule heating and heat transfer in poly(dimethylsiloxane) microfluidic systems. *Lab Chip* 2:141–149
8. Sato Y, Irisawa G, Ishizuka M, Hishida K, Maeda M (2003) Visualization of convective mixing in microchannel by fluorescence imaging. *Meas Sci Technol* 14:114–121
9. Kim HJ, Kihm KD, Allen JS (2003) Examination of ratiometric laser induced fluorescence thermometry for microscale spatial measurement resolution. *Int J Heat Mass Transf* 46:3967–3974
10. Natrajan VK, Christensen KT (2009) Two-color laser-induced fluorescent thermometry for microfluidic systems. *Meas Sci Technol* 20:015401
11. Mao H, Yang T, Cremer PS (2002) A microfluidic device with a linear temperature gradient for parallel and combinatorial measurements. *J Am Chem Soc* 124:4432–4435
12. Chamarthy P, Garimella SV, Wereley ST (2010) Measurement of the temperature non-uniformity in

a microchannel heat sink using microscale laser-induced fluorescence. *Int J Heat Mass Transf* 53:3275–3283

13. Kim M, Yoda K (2010) Dual-tracer fluorescence thermometry measurements in a heated channel. *Exp Fluids* 49:257–266
14. Natrajan VK, Christensen KT (2010) Non-intrusive measurements of convective heat transfer in smooth- and rough-wall microchannels: laminar flow. *Exp Fluids* 49:1021–103710
15. Walker GW, Sundar VC, Rudzinski CM, Aetna WW (2003) Quantum-dot optical temperature probes. *Appl Phys Lett* 83:3555–3557
16. Vasudevanpillai B, Makita Y, Sonoda A, Yokoyama H, Bana Y, Ishikawa M (2005) Temperature-sensitive photoluminescence of CdSe quantum dot clusters. *J Phys Chem* 109:13899–13905
17. Guasto JS, Breuer KS (2008) Simultaneous, ensemble-averaged measurement of near-wall temperature and velocity in steady micro-flows using single quantum dot tracking. *Exp Fluids* 45:155–166

---

## Focused Ion Beam Milling (FIB)

### Definition

This is a fabrication procedure used to machine or modify materials on the microscale. A focused beam of high-energy ions is targeted at a material, and the impacting ions sputter atoms from the surface; a prescribed scanning of the ion beam thus has the effect of a milling procedure.

### Cross-References

- ▶ [Supersonic Micro-nozzles](#)

---

## Free Boundary Reflection

### Definition

A virtual boundary (interface) exists between a gas jet exhausting from a nozzle and the surrounding quiescent medium. Compression and/or expansion pressure waves propagating within the jet will undergo a reflection at the

virtual boundary in such a way as to maintain a continuity in pressure across the interface.

### Cross-References

- ▶ [Supersonic Micro-nozzles](#)

---

## Free-Surface Atomization

### Definition

Formation of droplets from a fluid–fluid interface of a scale at least an order of magnitude smaller than the characteristic scale of the interface. Acoustic atomizers are typical examples of free-surface atomization.

### Cross-References

- ▶ [Piezoelectric Microdispenser](#)

---

## Frequency Response

### Definition

The frequency response (although called transfer function) is a common function in signal analysis and control engineering when the dynamic behavior of a system must be analyzed. Therefore, the input and output parameters of the system will be compared as a function of frequency. For example, when the system is stimulated with a harmonic input signal of a certain frequency, the system will answer with the same frequency, but with attenuated amplitude and a shifted phase. Since the amplitude attenuation and the phase shift are both functions of the stimulation frequency, it is common to plot them in Bode diagrams, where the amplitude response and the phase response are displayed separately over the frequency.

---

## Fuel Cell

### Definition

Conceptually similar to a battery, a fuel cell is an electrochemical device that converts chemical energy stored in a fuel and an oxidant into electrical energy. The fundamental difference between a fuel cell and a battery is that fuel and oxidant are supplied from outside the reaction chamber and waste products are removed. The heart of the fuel cell contains an anode and a cathode, separated by an ion-conducting electrolyte. Its operation is conceptually straightforward. The fuel is oxidized at the anode, releasing protons ( $H^+$  ions) and electrons. The protons travel through the electrolyte, which conducts ions but is electrically insulating, and recombine with the oxidant at the cathode. The electrons, which are required for the cathodic reaction, are conducted from the anode to the cathode through external wiring, thereby generating an electrical current used to drive a load. Most fuel cells operate at low temperatures and therefore require an electrochemical catalyst such as platinum to reduce the activation energy of the chemical reactions and generate useful electrical power.

### Cross-References

- ▶ [Micro Energy Conversion Devices](#)
- ▶ [Microfluidic Fuel Cells](#)
- ▶ [Microstructured Hydrogen Fuel Cells](#)

---

## Full-Width Half-Maximum (FWHM)

### Definition

The FWHM is the width of the narrow transmitted peaks, by an optical filter, at half-height.

### Cross-References

- ▶ [Lab-on-a-Chip Devices for Chemical Analysis](#)
- ▶ [Optofluidics: Optics Enabling Fluidics](#)
- ▶ [Sputtering for Film Deposition](#)

---

## Fundamentals of Diffusion in Microfluidic Systems

Pramod Chamrathy<sup>1</sup>, Alope Kumar<sup>2</sup>, Jinhua Cao<sup>1</sup> and Steven T. Wereley<sup>3</sup>

<sup>1</sup>Department of Mechanical Engineering, Purdue University, West Lafayette, IN, USA

<sup>2</sup>Biosciences Division, Oak Ridge National Laboratory, Oak Ridge, TN, USA

<sup>3</sup>Department of Mechanical Engineering, Purdue University, Birck Nanotechnology Center, West Lafayette, IN, USA

### Synonyms

Self-diffusion

### Definition

Brownian motion is defined as the irregular motion of microscopic particles suspended in a fluid due to collisions with the surrounding fluid molecules. The mean square displacement of a particle executing Brownian motion is directly proportional to the temperature of the fluid and inversely proportional to the viscosity of the fluid and the diameter of the particle.

### Chemical and Physical Principles

In the latter half of the nineteenth century and the beginning of the twentieth century, Brownian motion played an important role in the debate about the molecular reality of nature. The random movement of microscopic particles suspended in

a liquid is named after the botanist Robert Brown, who discovered this phenomenon while observing pollen grain suspended in water. Though Brown himself states that this motion was observed by other researchers before him such as Leeuwenhoek (1632–1723), Buffon (1800s), Spallanzani (1800s), and Bywater (1819), he is credited with conducting the first systematic experiments to study the nature of this motion. He observed that both organic and inorganic particles exhibited this motion and that it was not caused by local currents in the fluid or any other such disturbances; he concluded that the motion originated in the particles themselves and called them *active molecules*.

Several investigations [1] were carried out to study this motion between 1860 and 1900, and it was established that external factors such as vibration, temperature, surface tension, and incident light were not the cause of Brownian motion. It was proposed that the random movement of these particles was caused due to the bombardment by the molecules of the fluid, as predicted by kinetic theory. This hypothesis was open to a simple test. On the basis of the law of equipartition of energy, it was known that the mean kinetic energy of the molecules in a fluid in any one direction was

$$\frac{1}{2}m\langle v_x^2 \rangle = \frac{1}{2}kT, \quad (1)$$

where  $m$  is the mass of a molecule,  $v_x$  is the velocity of a molecule in the  $x$ -direction,  $k$  is Boltzmann's constant, and  $T$  is the temperature of the fluid. On the basis of statistical mechanics, it was proposed that a particle suspended in a fluid should have the same kinetic energy. Several experiments were attempted to verify this theory, but the values of the kinetic energy differed by a factor of up to 100,000 [2].

The theoretical explanation of Brownian motion was derived independently by Einstein [3] and Smoluchowski around the same year. Later, Paul Langevin [4] derived the same expression through a completely different approach. Einstein's derivation will be discussed in the following Section.

### Einstein's Derivation

In the first part of the argument, Einstein derived a relationship between the diffusion coefficient and other physical quantities. On the basis of the molecular kinetic theory of heat, he asserted that particles suspended in a liquid will experience the same osmotic pressure that molecules do. If an external force  $K$  acts on a suspension of Brownian particles, then in equilibrium this force will be balanced by osmotic pressure forces given by the relation

$$K = kT \frac{\nabla \cdot c}{c}, \quad (2)$$

where  $c$  is the number of particles per unit volume. Here, the force  $K$  can be any external force, such as gravity. The Brownian particles moving in the fluid because of this force will experience a resistance from the fluid of the form

$$\frac{K}{m\beta}, \quad (3)$$

where  $\beta$  is a constant with dimensions of frequency, and  $m$  is the mass of the particle. Therefore, the number of particles that pass through a unit area per unit time owing to the action of the force  $K$  is given by

$$\frac{cK}{m\beta}. \quad (4)$$

The number of particles that pass through a unit area per unit time  $t$  owing to diffusion is given by the diffusion equation

$$\frac{\partial c}{\partial t} = D(\nabla \cdot c). \quad (5)$$

Since the system is in dynamic equilibrium, the number of particles displaced owing to  $K$  will be restored by diffusion, giving the relation

$$\frac{cK}{m\beta} = D(\nabla \cdot c). \quad (6)$$

Using Eqs. 2 and 6,  $K$  and  $c$  can be eliminated, giving the relation

$$D = \frac{kT}{m\beta}. \quad (7)$$

If the Brownian particles are spheres of radius  $a$ , then the frictional resistance is given by Stokes's theory as

$$m\beta = 6\pi\eta a, \quad (8)$$

where  $\eta$  is the dynamic viscosity of the fluid. Combining Eqs. 7 and 8, we obtain Einstein's equation for the diffusion coefficient

$$D = \frac{kT}{6\pi\eta a}. \quad (9)$$

In the second part of his argument, Einstein relates the diffusion coefficient to a measurable property of Brownian motion such as the mean displacement of the particles. Let  $c(x, t)$  denote the probability for a Brownian particle to be at position  $x$  at time  $t$ . By following a probabilistic argument, the spatial and temporal changes in the concentration of the particles were shown to be related to the diffusion coefficient by

$$\frac{\partial c}{\partial t} = D \frac{\partial^2 c}{\partial x^2}. \quad (10)$$

This equation was established by Adolf Fick, but was reinterpreted and applied to the problem of Brownian motion by Einstein. Integrating Eq. 10, we obtain

$$c(x, t) = \frac{n}{\sqrt{4\pi D}} \frac{e^{-\frac{x^2}{4Dt}}}{\sqrt{t}}, \quad (11)$$

where  $n$  is the total number of particles suspended in the fluid. The mean square of the displacement  $x^2$  of the particles along the  $x$ -axis in a time  $\Delta t$  can be obtained by solving the integral equation

$$\langle x^2 \rangle = \left( \frac{1}{n} \right) \int_{-\infty}^{+\infty} x^2 c(x, t) dx, \quad (12)$$

which gives the final result:

$$\langle x^2 \rangle = 2D\Delta t. \quad (13)$$

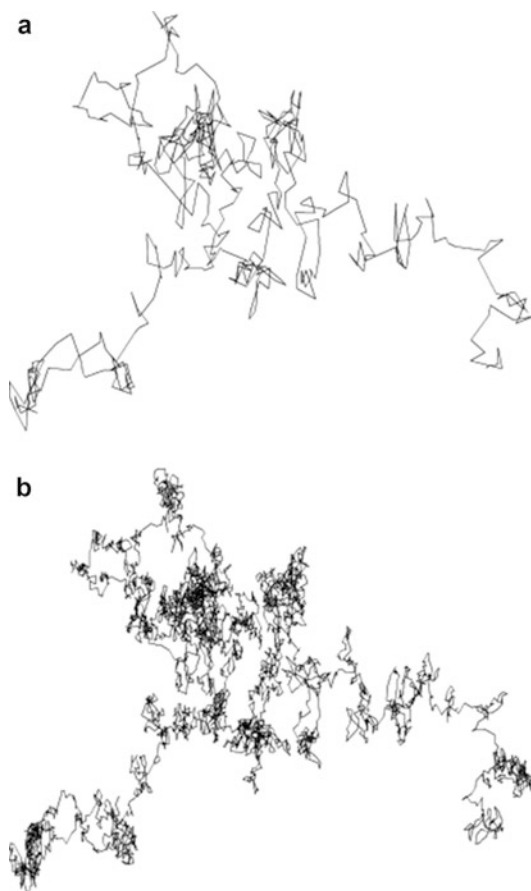
If the displacements along all three dimensions are considered,

$$\langle r^2 \rangle = \langle x^2 + y^2 + z^2 \rangle = 6D\Delta t. \quad (14)$$

### Mathematical Foundation

The theory of Brownian motion has grown far beyond the domain of its initial application and has benefited enormously from the contributions made by mathematicians. An interesting aspect of Brownian motion is its interpretation as a particular limiting case of a random walk, which is the motion generated by taking successive steps, of a fixed length, in a random direction. Hence, Brownian motion is often stated to be the random-walk motion of small particles suspended in a fluid due to bombardment by molecules obeying a Maxwellian velocity distribution. Such a motion can be easily demonstrated experimentally by taking a sequence of images of a Brownian particle. Figure 1 shows a simulated random walk of a particle undergoing Brownian motion in two dimensions. Figure 1a shows the motion of a particle on a large timescale, and Fig. 1b shows the same motion recorded on a smaller timescale. It can be seen that the path of the Brownian motion contains fine details. More and more details emerge as smaller timescales are chosen to sample the data. The assumption that the mean square displacement of the particles is proportional to the time interval becomes invalid at very small timescales [5]. As soon as a particle receives momentum from the fluid molecules, the fluid in the immediate vicinity of the particle is disturbed. Owing to the inertial effect of the surrounding fluid, there is a time delay in the transition from ballistic motion to a purely diffusive motion. This effect is called the hydrodynamic memory effect and becomes important at timescales much less than  $1 \mu\text{s}$  [6, 7].

In a strict mathematical sense, Brownian motion can be classified as a Wiener process.



**Fundamentals of Diffusion in Microfluidic Systems, Fig. 1** Simulated paths of a Brownian particle. (a) Path recorded on a large timescale and (b) same path recorded on a smaller timescale. More details emerge as we use smaller timescales

A Wiener process is a class of stochastic processes which satisfies the following conditions [8]:

1.  $X(0) = 0$ .
2.  $\{X(t), t \geq 0\}$  has stationary and independent increments.
3. For every  $t > 0$ ,  $X(t)$  is normally distributed with mean 0 and variance  $\sigma^2 t$ .

This definition shows that Brownian motion is closely linked to the Gaussian/normal distribution. The formalism of Wiener processes opens stochastic processes to rigorous mathematical analysis and has enabled the use of Wiener processes in the field of stochastic differential equations. Stochastic differential equations are analogs of classical differential equations where

the coefficients are stochastic variables rather than constants or deterministic variables. The field of stochastic differential equations finds wide application in many practical situations where modeling using stochastic models becomes a necessity. Examples of such situations include population growth models where *noise* is present and electrical circuits with noise. The non-differentiability of the Wiener process requires the introduction of concepts of white noise; an appropriate text may be referred to for a deeper understanding [9].

## Key Research Findings

### Influence of Brownian Motion on Particulate Flows

In the past two decades, the biological and medical fields have seen great advances in the development of biochips capable of characterizing and quantifying biomolecules. Biochips, also known as labs on a chip or  $\mu$ TAS (micro-total analysis systems), are microscale systems that interact with biological components on their characteristic length scale. Many biochips work with *particles* (cells, bacteria, DNA, etc.) suspended in fluids.

Generally, two major phenomena act on suspended neutrally buoyant particles to determine their spatial distribution: particle migration due to hydrodynamic forces and Brownian motion. Bulk migration of particles has been shown in non-Brownian suspension flows both theoretically and experimentally in many studies since Segré and Silberberg's pioneering reports [10, 11] on the inertial migration of particles in tube flow and Leighton and Acrivos's report [12] on particle-particle interaction in concentrated suspensions. Considering the characteristic length scale (several microns or less) of biological components and their typical speed in both biomedical devices, Brownian motion cannot be neglected.

### Concentrated Suspensions

Frank et al. [13] investigated particle migration in concentrated Brownian suspensions both by

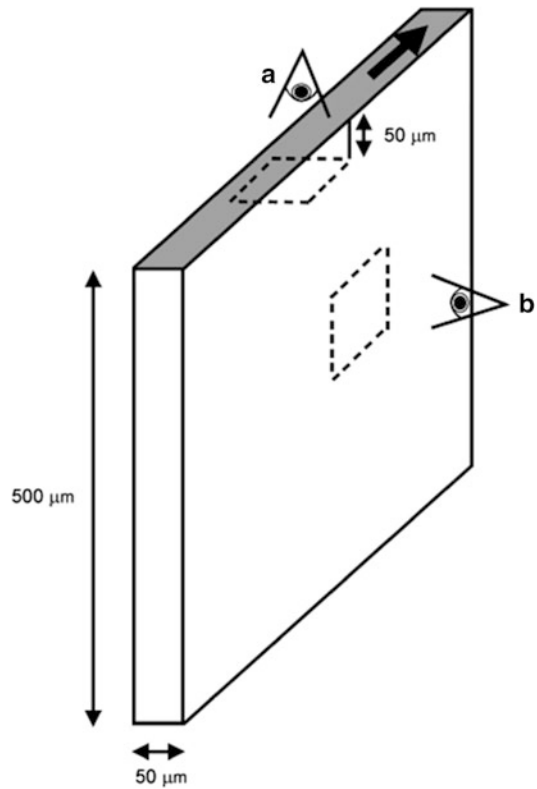
experiment and by modeling of flow in a mixer. The flow rate was quantified by the dimensionless Péclet number, which, conceptually, is the ratio of the time required for Brownian diffusion to move a particle by its own size,  $a^2/D = a^2/(kT/6\pi\eta a)$ , to the time required for shear flow to move it by the same distance,  $\gamma^{-1}$  (where  $\gamma$  is the shear rate of the surrounding flow field), yielding

$$\text{Pe} = \frac{6\pi\eta\gamma a^3}{kT}. \quad (15)$$

Confocal microscopy was used to study the flow of Brownian particles experimentally by directly imaging the particle motion and concentration. The experimental setup was a long, rectangular glass channel of cross section  $50 \times 500 \mu\text{m}^2$ , connected on each side to a Teflon tube. Concentration profiles were measured across the narrow dimension of the glass channel as shown in Fig. 2. The results are shown in Fig. 3. It can be seen that there is an increase in concentration in the center, which shows that at high volume fractions particles migrate toward the centerline, with the migration becoming progressively stronger as  $\text{Pe}$  increases. Comparisons of the experimental data with the modeling indicate that the dependence of the extent of migration on  $\text{Pe}$  is captured well but that discrepancies arise, at least in part because the assumption of fully developed flow is not valid for these experiments.

#### Dilute Suspensions

In Poiseuille flow, rigid, spherical, non-Brownian particles are subjected to lateral forces that result in migration to an equilibrium radial region located at approximately 60 % of the distance from the tube axis to the tube wall, which is called the *Segré and Silberberg effect* [10, 11]. The migration of Brownian particles in a Poiseuille flow for a range of particle volume fractions  $\phi$  much less than 0.01 has been investigated using epifluorescent microscopy and microparticle image velocimetry [14]. When  $\text{Pe}$  is smaller than 1,000, particles migrate away from the channel wall, with a nearly uniform particle concentration everywhere else in the channel, as shown



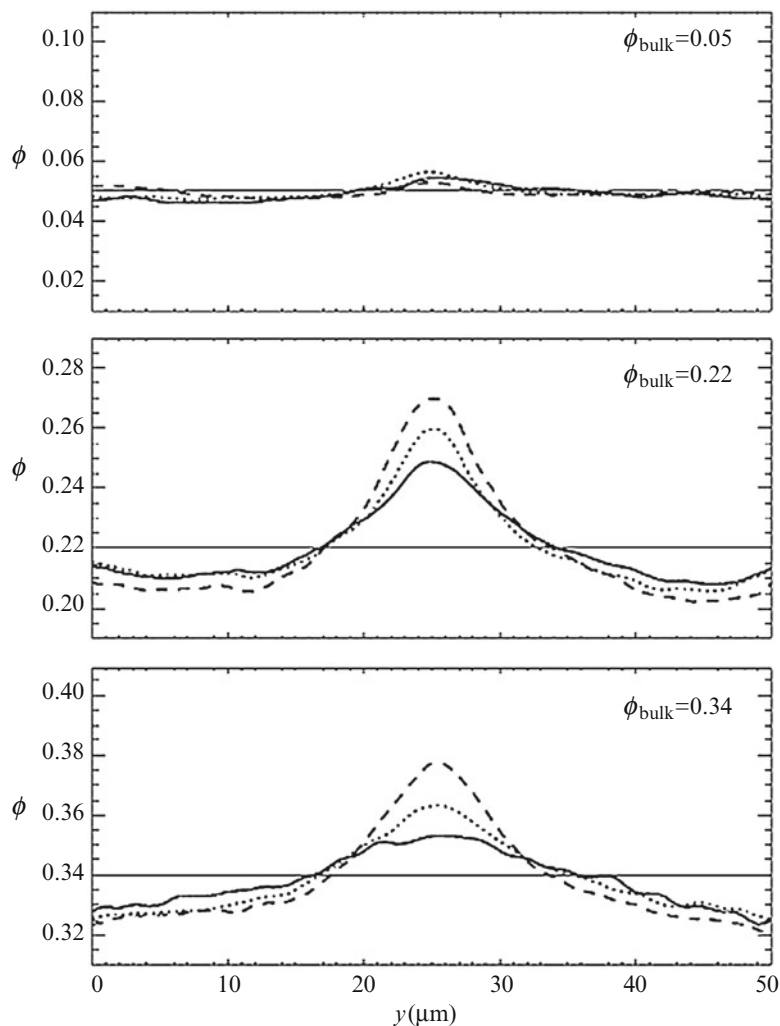
**Fundamentals of Diffusion in Microfluidic Systems, Fig. 2** Sketch of an experimental flow chamber; the bold arrow indicates the flow direction. Concentration profiles were obtained by looking through the top (a) at a fixed distance ( $50 \mu\text{m}$ ) from the top wall. Velocity profiles were taken by scanning a horizontal plane through the side (b) of the chamber, across the  $50 \mu\text{m}$  width of the channel

in Fig. 4. When  $\text{Pe}$  is greater than 1,000, the Segré and Silberberg effect is observed: particles move toward a preferred position, with the migration effect becoming progressively stronger as  $\text{Pe}$  increases, which results in an increase in the concentration profile between the channel center and channel wall.

#### Influence of Brownian Motion on Velocity Measurements

In typical particle image velocimetry (PIV) analysis, the correlation of an image with itself is called an autocorrelation, and the correlation of an image with another image is called a cross-correlation. The location of the correlation peak gives the average displacement of the particles,

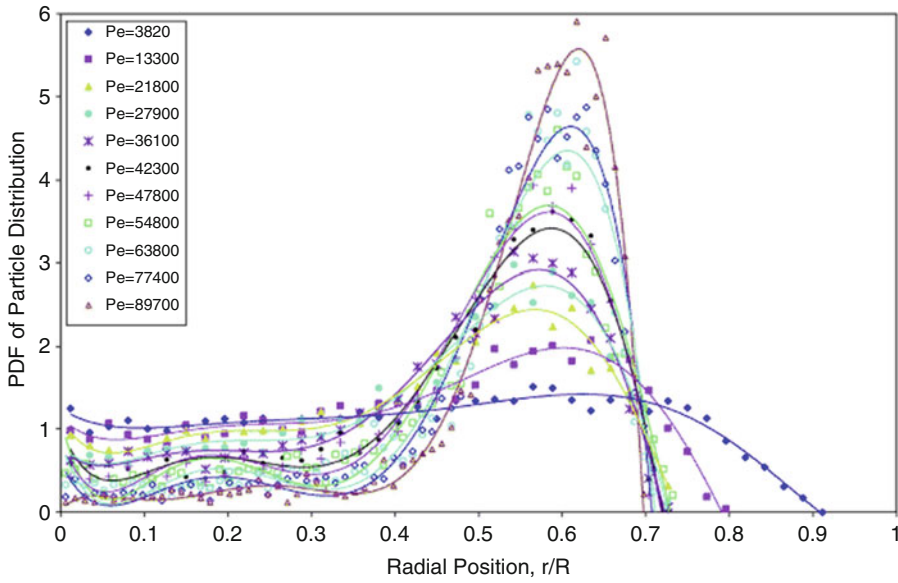
**Fundamentals of Diffusion in Microfluidic Systems, Fig. 3** Plots of the local volume fraction  $\phi$  as a function of the distance across the channel for an average volume fraction  $\phi_{\text{bulk}} = 0.05, 0.22,$  and  $0.34$  at flow rates of  $0.125 \mu\text{min}^{-1}$  (solid line,  $\text{Pe} = 69$ ),  $1.0 \mu\text{min}^{-1}$  (dotted line,  $\text{Pe} = 550$ ), and  $8.0 \mu\text{min}^{-1}$  (dashed line,  $\text{Pe} = 4,400$ ) [13]



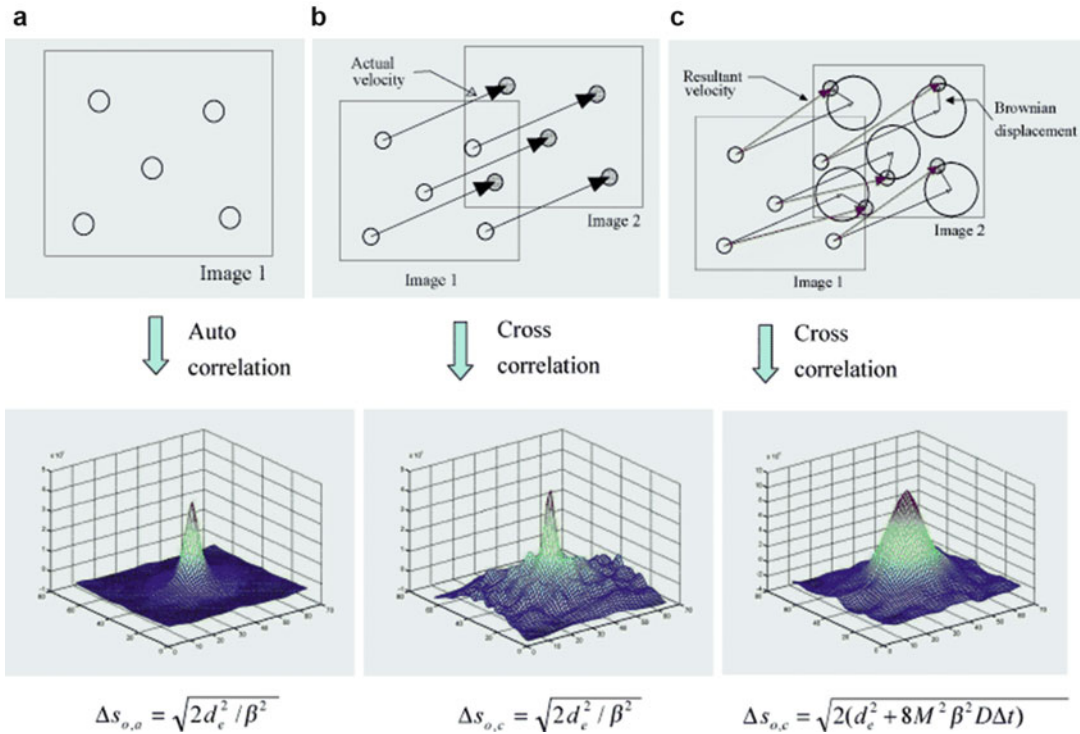
and the shape of the correlation peak depends on the particle size and on the imaging optics. It has been observed that for low velocities ( $<10 \mu\text{m/s}$ ), the submicron-sized particles used to seed the flow undergo enough Brownian motion to introduce significant errors in velocity measurements made by microparticle image velocimetry ( $\mu\text{PIV}$ ) [15]. This uncertainty in locating the peak center was, however, substantially minimized through ensemble averaging over multiple images. This had the effect of causing a widthwise spreading of the correlation function. The effect of Brownian motion on the cross-correlation function is illustrated in Fig. 5. Figure 5a shows a typical auto-correlation peak, Fig. 5b shows a typical

cross-correlation peak without any Brownian motion, and Fig. 5c shows a typical cross-correlation peak in the presence of Brownian motion. It can be seen that the peak width of the correlation function in the presence of Brownian motion is broader, and the peak is lower than for the correlation function without any Brownian motion.

Olsen and Adrian [16] performed a theoretical study of the effect of Brownian motion on the  $\mu\text{PIV}$  correlation signal peak and derived a function quantifying the broadening of the correlation function. They postulated that this widthwise broadening of the correlation function could be used to calculate the temperature of the fluid, since Brownian motion has a direct



**Fundamentals of Diffusion in Microfluidic Systems, Fig. 4** Plot of the relative concentration (probability density function of the particle distribution) as a function of the radial position in a round capillary tube



**Fundamentals of Diffusion in Microfluidic Systems, Fig. 5** Broadening of cross-correlation function in the presence of Brownian motion. (a) Autocorrelation

function. (b) Cross-correlation function. (c) Cross-correlation function with Brownian motion

dependence on temperature. This method would utilize the same data as that obtained for making  $\mu$ PIV measurements, eliminating the need to set up an entirely different experiment for measuring the temperature [15]. This idea was further developed by Hohreiter et al. [17], where the measurement technique was demonstrated with an experimental uncertainty of  $\pm 3$  °C.

### Measurement of Brownian Motion

Several attempts have been made to experimentally verify the theory of Brownian motion proposed by Einstein. Svedberg's results [18] were close to the expected values, but several researchers remained skeptical. Henri [19] used the recently invented film camera, attached to a microscope, to record the trajectories of latex particles suspended in water, but could not find quantitative agreement with Einstein's formula. The theory was finally verified by Perrin [20] by a series of experiments. In these experiments, the data was obtained using a microscope and a camera, while the displacements and the number of particles were measured manually.

At present, several different methods can be used to measure diffusion. The commonly used techniques to measure Brownian motion are briefly discussed below.

### Light Scattering

When a beam of light is incident on a particle, it is partially reflected, refracted, and transmitted, depending on the size and properties of the particle. Light scattering can be broadly classified into classical light scattering and dynamic light scattering. In classical light scattering, if the particle size is of the order of or smaller than the wavelength of light, the light is scattered in all directions (Rayleigh scattering) and is a function of the molar mass and of the size of the particle. If the particle size is much greater than the wavelength of light, the intensity of the scattered light is dependent on the angle (Mie scattering). Classical light-scattering techniques are commonly used to study the size, shape, and structure of biological molecules in cells.

Dynamic light scattering involves the study of time-dependent fluctuations in the intensity of

scattered light which are the result of the Brownian motion of the particles. The random movement of the particles causes the distances between the particles to fluctuate, causing constantly varying constructive and destructive interference patterns. This time-dependent fluctuation in the intensity can be correlated with itself to obtain the diffusion coefficient of the particles. This method is also called photon correlation spectroscopy (PCS) and quasi-elastic light scattering (QELS) [21, 22].

### Fluorescence Correlation Spectroscopy

In fluorescence correlation spectroscopy (FCS), the fluorescence intensity of molecules within a small volume is statistically correlated to measure the concentration and the particle size. Typically, the sample is illuminated with a laser beam, and the intensity, which is dependent on the number of fluorescent molecules, is measured. Since these fluorescent molecules exhibit Brownian motion, the number of particles present in the region will be constantly changing, resulting in a fluctuating intensity signal. If the time series of the intensity is correlated with itself, the resulting plot gives a measure of the number of fluorescent molecules present in that volume, as well as the diffusion coefficient of the molecules. By using a confocal microscope, the background noise can be eliminated, and the fluorescence intensity of a single molecule can be measured [23].

### Fluorescence Recovery After Photobleaching (FRAP)

If a fluorescent molecule is irradiated with a high-intensity laser, the molecule undergoes a permanent chemical reaction, as a result of which it loses its fluorescent capability. This phenomenon is called photobleaching. In this method, high-intensity laser light is used to photobleach a small volume of the sample, and low-intensity laser light is used to image the sample. Immediately after photobleaching, there is a dark region, where the fluorescent molecules have been inactivated, surrounded by a bright region containing unaffected fluorescent molecules. But, as time progresses, the fluorescent

molecules from the bright region diffuse into the dark region. By measuring this fluorescence recovery after photobleaching, the mobile fraction and the rate of motion of the molecules in a region can be measured. The rate of motion can be used to calculate the diffusion coefficient.

The spatial resolution in FRAP (also known as fluorescence photobleaching recovery, FPR) measurements is limited by the minimum diffraction-limited size of the laser beam [24, 25].

### Single-Particle Tracking

The most straightforward method of measuring diffusion is by tracking the movement of individual particles. Particles executing Brownian motion are imaged at fixed time intervals with the help of a video camera or CCD camera attached to a microscope. The images are then processed to locate the centers of the particles and to measure the distance that each particle travels within each time interval. The diffusion coefficient is obtained directly by plotting the mean square of the displacement as a function of time, as given by Eq. 14.

Several researchers have studied the Brownian motion of submicron-sized particles suspended in a fluid using digital video microscopy. Crocker and Grier [26] made use of optical tweezers to study the hydrodynamic correction to Brownian motion in the case of two spheres in close proximity. They argued that with careful experiments, diffusion coefficients can be experimentally measured to an accuracy of  $\pm 1\%$ . Nakrohis et al. [27] measured Boltzmann's constant, and Salmon et al. measured Avogadro's number by studying the Brownian motion of submicron-sized particles. Park et al. used optical serial-sectioning microscopy (OSSM) to measure Brownian particle displacements in all three dimensions and deduced temperature information with uncertainty differentials of 5.54 %, 4.26 %, and 3.19 % for the 1D, 2D, and 3D cases. Kihm et al. used 3D ratiometric total internal reflection fluorescence microscopy (3D R-TIRFM) to measure Brownian displacements near a wall and calculated the hindered diffusion constant of 200 nm particles in the lateral and normal directions relative to the wall.

## Examples of Application

Brownian motion is a rich field in terms of the attention it has received from both physicists and mathematicians, and various models exist which incorporate other physical features. The study of Brownian motion is now being applied in fields as varied as financial modeling, protein-DNA interactions, fractal analysis in medical imaging, and estimation of floods.

## Cross-References

- ▶ [Optical Tweezers for Manipulating Cells and Particles](#)
- ▶ [Particle Image Velocimetry \(PIV\)](#)

## References

1. Haw MD (2002) Colloidal suspensions, Brownian motion, molecular reality: a short history. *J Phys Condens Matter* 14(33):7769–7779
2. Nelson E (1967) *Dynamical theories of Brownian motion*. Princeton University Press, Princeton, p 142
3. Einstein A (1905) The motion of elements suspended in static liquids as claimed in the molecular kinetic theory of heat. *Ann Phys* 17(8):549–560
4. Langevin P (1908) The theory of Brownian movement. *CR Hebd Seances Acad Sci* 146:530–533
5. Hinch EJ (1975) Application of Langevin equation to fluid suspensions. *J Fluid Mech* 72:499–511
6. Lukic B, Jeney S, Tischer C, Kulik AJ, Forro L, Florin EL (2005) Direct observation of nondiffusive motion of a Brownian particle. *Phys Rev Lett* 95(16):160601-1–160601-4
7. Kao MH, Yodh AG, Pine DJ (1993) Observation of Brownian-motion on the time scale of hydrodynamic interactions. *Phys Rev Lett* 70(2):242–245
8. Ross SM (2003) *Introduction to probability models*, 8th edn. Academic, San Diego
9. Øksendal BK (1998) *Stochastic differential equations: an introduction with applications*, 5th edn. Springer, Berlin
10. Segré G, Silberberg A (1962) Behaviour of macroscopic rigid spheres in poiseuille flow. 1. Determination of local concentration by statistical analysis of particle passages through crossed light beams. *J Fluid Mech* 14(1):115–135
11. Segré G, Silberberg A (1962) Behaviour of macroscopic rigid spheres in poiseuille flow. 2. Experimental results and interpretation. *J Fluid Mech* 14(1):136–157

12. Leighton D, Acrivos A (1987) The shear-induced migration of particles in concentrated suspensions. *J Fluid Mech* 181:415–439
13. Frank M, Anderson D, Weeks ER, Morris JF (2003) Particle migration in pressure-driven flow of a Brownian suspension. *J Fluid Mech* 493:363–378
14. Cao J, Wereley ST (2004) Brownian particle distribution in tube flows. In: Proceedings of the ASME international mechanical engineering congress and exposition, Anaheim
15. Santiago JG, Wereley ST, Meinhart CD, Beebe DJ, Adrian RJ (1998) A particle image velocimetry system for microfluidics. *Exp Fluid* 25(4):316–319
16. Olsen MG, Adrian RJ (2000) Brownian motion and correlation in particle image velocimetry. *Opt Laser Technol* 32(7–8):621–627
17. Hohreiter V, Wereley ST, Olsen MG, Chung JN (2002) Cross-correlation analysis for temperature measurement. *Meas Sci Technol* 13(7):1072–1078
18. Svedberg T (1906) Concerning the proper motion of particles in colloidal solutions. *Z Angew Elektrochem Angew Phys Chem* 12:853–860
19. Henri V (1908) Cinematographic study of Brownian movements. *CR Hebd Seances Acad Sci* 146:1024–1026
20. Perrin J (1910) Brownian movement and molecular science. *Phys Z* 11:461–470
21. Berne BJ, Pecora R (2000) *Dynamic light scattering: with applications to chemistry, biology, and physics*. Dover Publications, Mineola
22. Schmitz KS (1990) *An introduction to dynamic light scattering by macromolecules*. Academic, Boston
23. Rigler R, Elson E (2001) *Fluorescence correlation spectroscopy: theory and applications*. Springer, New York
24. Klonis N, Rug M, Harper I, Wickham M, Cowman A, Tilley L (2002) Fluorescence photobleaching analysis for the study of cellular dynamics. *Eur Biophys J Biophys Lett* 31(1):36–51
25. Elson EL (1985) Fluorescence correlation spectroscopy and photobleaching recovery. *Annu Rev Phys Chem* 36:379–406
26. Crocker JC, Grier DG (1996) Methods of digital video microscopy for colloidal studies. *J Colloid Interface Sci* 179(1):298–310
27. Nakroshis P, Amoroso M, Lagere J, Smith C (2003) Measuring Boltzmann's constant using video microscopy of Brownian motion. *Am J Phys* 71(6):568–573